Computational Models of Intracellular Signalling and Synaptic Plasticity Induction in the Cerebellum

Thiago Matos Pinto

May 2013

Submitted to the University of Hertfordshire in partial
fulfilment of the requirements of the degree of

Doctor of Philosophy

Abstract

Many molecules and the complex interactions between them underlie plasticity in the cerebellum. However, the exact relationship between cerebellar plasticity and the different signalling cascades remains unclear. Calcium-calmodulin dependent protein kinase II (CaMKII) regulates many forms of synaptic plasticity, but very little is known about its function during plasticity induction in the cerebellum. The aim of this thesis is to contribute to a better understanding of the molecular mechanisms that regulate the induction of synaptic plasticity in cerebellar Purkinje cells (PCs). The focus of the thesis is to investigate the role of CaMKII isoforms in the bidirectional modulation of plasticity induction at parallel fibre (PF)-PC synapses. For this investigation, computational models that represent the CaMKII activation and the signalling network that mediates plasticity induction at these synapses were constructed.

The model of CaMKII activation by calcium-calmodulin developed by Dupont et al (2003) replicates the experiments by De Koninck and Schulman (1998). Both theoretical and experimental studies have argued that the phosphorylation and activation of CaMKII depends on the frequency of calcium oscillations. Using a simplified version of the Dupont model, it was demonstrated that the CaMKII phosphorylation is mostly determined by the average calcium-calmodulin concentration, and therefore depends only indirectly on the actual frequency of calcium oscillations. I have shown that a pulsed application of calcium-calmodulin is, in fact, not required at all. These findings strongly indicate that the activation of CaMKII depends on the average calcium-calmodulin concentration and not on the oscillation frequency per se as asserted in those studies.

This thesis also presents the first model of AMPA receptor phosphorylation that simulates the induction of long-term depression (LTD) and potentiation (LTP) at the PF-PC synapse. The results of computer simulations of a simple mathematical model suggest that the balance of CaMKII-mediated phosphorylation and protein phosphatase 2B (PP2B)-mediated dephosphorylation of AMPA receptors determines whether LTD or LTP occurs in cerebellar PCs. This model replicates the experimental observations by Van Woerden et al (2009) that indicate that βCaMKII controls the direction of plasticity at PF-PC synapses. My computer simulations support Van Woerden et al's original suggestion that filamentous actin binding can enable βCaMKII to regulate bidirectional plasticity at these synapses.

The computational models of intracellular signalling constructed in this thesis advance the understanding of the mechanisms of synaptic plasticity induction in the cerebellum. These simple models are significant tools for future research by the scientific community.

Contents

Chapter 1

Introduction

Contents

1.1 Motivation

The cerebellum is a brain structure involved in motor control and reflex adjustments. A large number of studies have been performed in order to understand the principles of the function and the structure of the cerebellum. Although the cerebellar structure is well-known, the role of the cerebellum in motor learning, motor control, emotions, and higher cognitive functions still remains obscure [Glickstein 2009, Beaton 2010].

It is generally accepted in neuroscience that activity-dependent changes in synapses represent a system for storing information in the brain [Steuber 2004, Steuber 2007]. Synaptic plasticity, which is the ability to strengthen and weaken synaptic connections, has been described as a crucial cellular mechanism for learning and memory formation in neuronal circuits of the brain [Ito 2002].

Different intracellular signalling pathways allow the cell to receive, process, store, and recall information. The compounds of distinct pathways interact and form signalling networks. It is thought that the molecular mechanisms of intracellular biochemical networks underlie learning in biological systems [Bhalla 1999]. During the past decades a multitude of signal transduction processes that underlie different forms of plasticity in the cerebellum were revealed [Ito 2002], but a better comprehension of this phenomenon is inhibited by the complexity of the interactions between intracellular signalling compounds involved in synaptic plasticity [Kotaleski 2010].

Many biochemical compounds are involved in the signalling networks that govern synaptic plasticity in the cerebellum. In particular, calcium-calmodulin dependent protein kinase II (CaMKII), which is highly concentrated in the brain, regulates forms of synaptic plasticity. Although significant progress has been made in understanding the role of postsynaptic CaMKII in plasticity in other brain areas, very little is known about its function during plasticity induction in the cerebellum [Hansel 2006, van Woerden 2009, Kawaguchi 2011].

Cerebellar Purkinje cells (PCs) receive strong inputs from parallel fibre axons (PFs). Cerebellar long-term depression (LTD) and potentiation (LTP) are calcium-dependent forms of synaptic plasticity that weaken and strengthen synapses between PFs and PCs. LTD and LTP are regulated by intracellular calcium concentrations. Large increases in calcium concentrations in response to paired PF and climbing fibre (CF) input lead to LTD, while the induction of LTP is mediated by smaller calcium concentration increases that result from PF input alone.

The CaMKII holoenzyme is composed of different isoforms, such as αCaMKII and βCaMKII, which is the predominant CaMKII isoform in the cerebellum. Recent experiments demonstrated that βCaMKII controls the direction of plasticity at the PF-PC synapse [van Woerden 2009]. More specifically, protocols that induce LTD in wild-type mice result in LTP in knockout mice that lack βCaMKII, and vice versa. However, the mechanism that underlies these experimental findings is not clear.

Mathematical analyses and computational simulations have been established as valuable approaches to understanding complex systems such as biological cells [Kier 2005, Schilstra 2008]. The computational simulation of kinetic models is a powerful tool for analysing and exploring the behaviour of complex signal transduction pathways involved in synaptic plasticity.

Various computational models of intracellular signalling networks underlying LTD induction have been proposed [Fiala 1996, Wang 2000, Kuroda 2001, Ito 2002, Doi 2005]. However, the relationship between the known signalling pathways and LTD still remains obscure. Interestingly, these models do not take LTP induction into account, and CaMKII has never been included in their signalling cascades. Moreover, existing kinetic models of the activation of CaMKII are surprisingly diverse and there is little general consensus on which processes should be included or how detailed the modelling needs to be.

The development of a kinetic model of PF LTD and LTP that includes CaMKII is the key to unravelling processes that underlie the regulation of bidirectional plasticity at the PF-PC synapse [van Woerden 2009]. This new computational model would significantly advance the understanding of synaptic plasticity induction in the cerebellum.

1.2 Aims of the Thesis

The aim of this thesis is to contribute to a better understanding of the molecular mechanisms that regulate the induction of synaptic plasticity in cerebellar PCs. In particular, the thesis addresses the role of the βCaMKII isoform in bidirectional plasticity at PF-PC synapses.

To understand the mechanisms of cerebellar LTD and LTP at the PF-PC synapse, a new kinetic model of signalling pathways in PCs that includes CaMKII is needed. At first, the present research was based on a well-known cerebellar LTD model of

[Kuroda 2001]. Kuroda and collaborators have simulated the phosphorylation of AMPA receptors, an important process in cerebellar LTD and LTP. Many errors in the original implementation of the Kuroda model were identified, and its reimplementation was completed.

Because this thesis focuses on studying how different isoforms of CaMKII contribute to cerebellar plasticity, a simplified version of a commonly used model of CaMKII phosphorylation [Dupont 2003] was developed. The model by Dupont and collaborators reproduced experiments of [De Koninck 1998]. Both the experimental and modelling studies demonstrated the sensitivity of CaMKII to the frequency of calcium oscillations. The first aim of the implementation of the Dupont model in this thesis was to include the CaMKII phosphorylation pathway in the existing cerebellar LTD model, but while developing the new CaMKII model interesting issues arose. A series of simulations under the conditions that were used in [Dupont 2003] to explain the key experimental observations of [De Koninck 1998] were carried out. These simulations gave rise to new insights about the decoding of calcium oscillations by CaMKII.

The CaMKII model was ultimately incorporated into the reimplemented version of the biochemical LTD model. However, the complexity of the intracellular signalling network of the existing cerebellar LTD model [Kuroda 2001] prohibited a better understanding of the actual role of CaMKII in synaptic plasticity in PCs. Therefore, a simple model of the phosphorylation and dephosphorylation of AMPA receptors by CaMKII and protein phosphatase 2 B (PP2B) was proposed. This kinetic model was crucial to understand how the βCaMKII isoform regulates the direction of synaptic plasticity in a cerebellar Purkinje cell.

The following questions are addressed in this thesis:

- What are the mechanisms that determine the sensitivity of CaMKII to the frequency of calcium oscillations?
- Does CaMKII decode the frequency of calcium oscillations?
- How does the network of intracellular signalling molecules in cerebellar PCs implement the induction of LTD and LTP at the PF-PC synapse?
- In particular, how do different isoforms of CaMKII contribute to the bidirectional modulation of synaptic plasticity at this synapse?

1.3 Contributions to Knowledge

The research presented in this thesis led to the following main findings that contribute significantly to neuroscience:

- The CaMKII phosphorylation rate during the application of calcium-calmodulin pulses is determined by the average concentration of calcium-calmodulin in the system, and not by the pulse frequency itself.

- The application of pulsed and constant levels of calcium-calmodulin with the same mean concentration results in the same level of CaMKII phosphorylation.
- Thus, the notion of CaMKII as a decoder of the calcium oscillation frequency is misleading, and experimental tests with rescaled concentrations of calcium-calmodulin are suggested.
- The first kinetic model of the induction of cerebellar LTD and LTP in PCs that includes CaMKII is proposed.
- Computational simulations replicate recent experimental findings that demonstrated that βCaMKII controls the direction of plasticity at the PF-PC synapse [van Woerden 2009].
- The binding of filamentous actin to CaMKII can contribute to the regulation of bidirectional plasticity in PCs.

1.4 Overview of the Thesis

The following is a brief overview of each subsequent chapter of this thesis:

- **Chapter 2** gives an introduction to cerebellar neuroscience, focusing on the long-term forms of synaptic plasticity in cerebellar PCs. In the first half of Chapter 2, the structure, functions and the basic circuit of the cerebellum are summarised. In the second half of the chapter, the long-term forms of cerebellar plasticity and the molecular mechanisms involved in cerebellar LTD are discussed.
- **Chapter 3** contains a review of CaMKII, with particular focus on the CaMKII frequency sensitivity, and on the role of CaMKII isoforms in cerebellar plasticity. The chapter begins with a description of the structure and the mechanism of activation of CaMKII.
- **Chapter 4** describes how to model intracellular signalling pathways. The kinetics of biochemical compounds of signalling networks can be described by ordinary differential equations (ODEs). In the first half of the chapter, the mathematical modelling of kinetics of biochemical reactions is summarised. The second half of Chapter 4 presents software packages for implementing the biochemical models described in this thesis, such as GENESIS (GEneral NEural SImulation System), including the GENESIS/kinetikit library for the simulation of biochemical reactions [Bower 2008], and XPPAUT (X-Windows Phase Plane plus Auto) [Ermentrout 2002].
- **Chapter 5** presents the reimplementation of an existing model of signalling in cerebellar LTD. The complex model of [Kuroda 2001] is described in detail in the chapter. This model was originally implemented in GENESIS/kinetikit.

Various inconsistencies were identified in the original implementation of the Kuroda model, and its reimplementation in XPPAUT was performed. All discrepancies of the cerebellar LTD model were corrected, and results from the prior research were ultimately reproduced.

- **Chapter 6** gives a description of the investigation of the CaMKII frequency sensitivity. CaMKII is activated by calcium-calmodulin. Based on prior experiments [De Koninck 1998] and computational simulations [Dupont 2003] the phosphorylation of CaMKII was thought to be sensitive to the frequency of calcium oscillations. A rationalized version of the earlier model [Dupont 2003] was proposed to re-evaluate the experimental findings of [De Koninck 1998]. Computational simulations reveal one of the major findings of this thesis: the CaMKII phosphorylation depends on the average concentration of calcium-calmodulin, rather than on the actual pulse frequency. As a corollary, equal phosphorylation levels are achieved in response to pulsed and constant applications of equal mean concentrations of calcium-calmodulin.

- **Chapter 7** presents the study of bidirectional plasticity in cerebellar PCs. The model of CaMKII activation described in Chapter 6 was incorporated into a simple kinetic simulation of the phosphorylation of AMPA receptors. A description of the proposed model is presented in the chapter. The bidirectional plasticity model was created to understand the mechanisms underlying the role of βCaMKII in regulating the direction of plasticity at PF-PC synapses [van Woerden 2009]. Simulation results replicate the experimental observations of [van Woerden 2009] and indicate that the binding of βCaMKII to filamentous actin can contribute to the regulation of the bidirectional plasticity at this synapse.

- **Chapter 8** reviews the main contributions of this thesis to knowledge, and highlights potential avenues for future research that should now be explored. In the end of this thesis, a list of publications, talks and participations in conferences during the three years of this research is presented.

Chapter 2

The Cerebellum

Contents

The cerebellum, whose name comes from the Latin meaning “the little brain”, lies above the brain stem and toward the back of the brain (Figure 2.1). The cerebellar structure has been studied for many years due to its unique anatomical organisation composed of regular and repetitive structures. Although the volume of the cerebellum is small, it contains most of neurons in the brain.

This chapter begins with a summary of the anatomy of the cerebellum. Although its structure is well understood, the functions of the cerebellum remain unclear. The cerebellar function is discussed in the second section of this chapter. Following on from this, a description of the well-established cerebellar circuit is given. One of the most important issues in cerebellar research is the role of synaptic plasticity in the cerebellar cortex. This chapter ends with a discussion of the long-term forms of synaptic plasticity in the cerebellum, and describes the molecular mechanisms underlying cerebellar long-term depression.

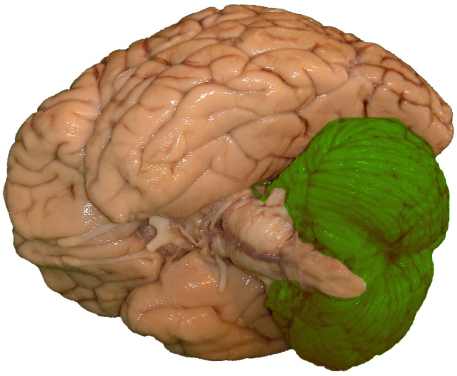

Figure 2.1: **The human brain.** View of a human brain which highlights the location of the cerebellum (green). Adapted from [Marino 2012].

2.1 Structure of the Cerebellum

The cellular structure of the *cerebellar cortex* is nearly identical throughout. The cerebellum has been divided into many regions and comprises three uniform layers throughout the entire cortex. Like the cerebral cortex, the cortex of the cerebellum, a highly elaborated area, is located outside a centrally located mass of *white matter* composed of afferent and efferent fibres (Figure 2.2) (see for example [Kandel 1991]). The outer mantle of the cerebellar cortex consists of a mass of *grey matter*.

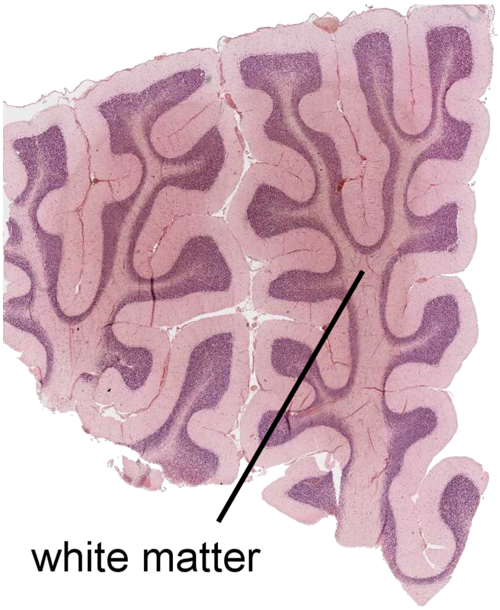

Figure 2.2: **Midsagittal section through the cerebellum.** The figure shows the tree shaped white matter and the surrounding grey matter of the cerebellar cortex. Adapted from [Spitalnik 2012].

Three pairs of *deep cerebellar nuclei* project out of the cerebellum, the *interposed*, the *fastigial* and the *dentate nucleus* (Figure 2.3). Each of the three nuclei is involved in different functions and sends projections to different areas of the brain.

The cerebellum is linked to the medulla by three thick connectives, the *inferior*, *middle*, and *superior cerebellar peduncles*, where the efferent fibres leave and the afferent fibres enter the cerebellar structure.

The cortex is divided into three zones: the *vermis*, the *cerebellar hemispheres*, and the *flocculonodular lobe*. The flocculonodular lobe is phylogenetically the oldest part of the cerebellum. The vermis constitutes the majority of the cerebellum in most animals, but it is overshadowed by the cerebellar hemispheres in humans. Anatomists divide the vermis into many parts, while the cerebellar hemispheres are divided into intermediate and lateral zones.

Because of the precision and geometric beauty of the neuronal arrangement of the cerebellum, neuroanatomists have recognised that this part of the brain provides an ideal opportunity to determine its function [Eccles 1967, Ito 2006].

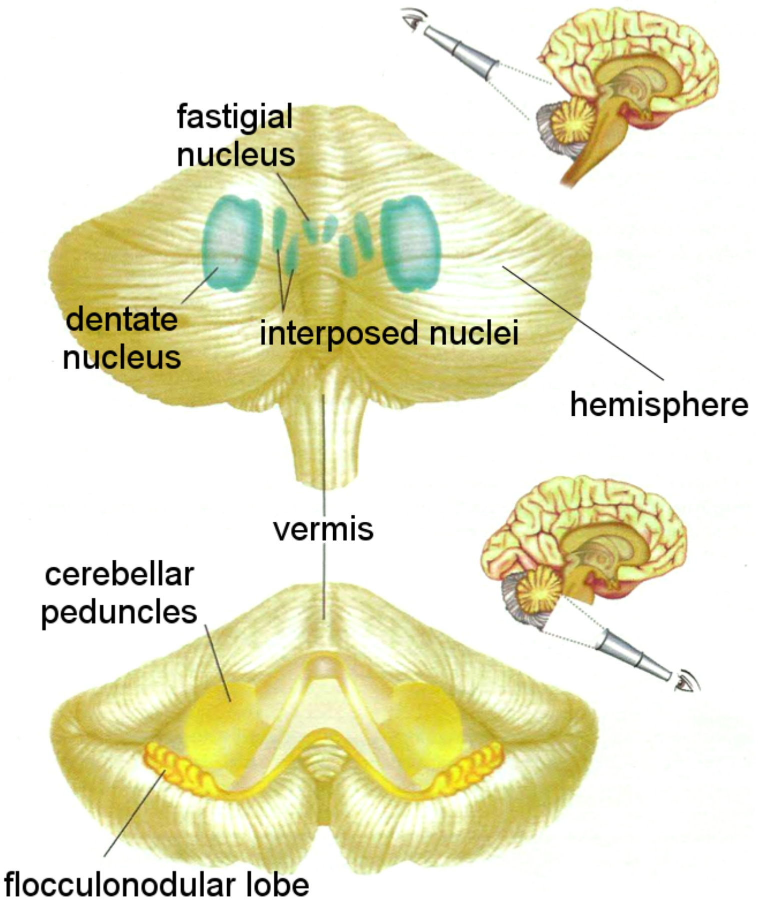

Figure 2.3: **The major anatomical subdivisions of the human cerebellum.** The cerebellar dorsal and ventral views are represented in the figure. The cerebellum contains a cortex on its surface and deep nuclei in its internal region. Adapted from [Lent 2005].

2.2 Functions of the Cerebellum

Because cerebellar lesions lead to impairments in motor control and posture, and most of the cerebellar output leads to the motor system, the cerebellum has been considered to play a role in motor control. It is also thought to control balance and regulate muscle tone [Kandel 1991]. It is generally accepted in neuroscience that the cerebellum is important for motor learning, but the nature of its involvement is unclear. Important questions are still unanswered as to how and where cerebellar-dependent motor memories are stored. Other studies point to a role of the cerebellum in cognition and emotion (for review, see [D'Angelo 2012]).

To achieve a better comprehension of cerebellar function, scientists have focused on studying information processing in the basic circuit of the cerebellum.

2.3 The Basic Cerebellar Circuit

Most of the work on information processing in cerebellar cortex has focused on five different types of neurons: *Purkinje*, *granule*, *basket*, *stellate* and *Golgi cells*, while much less is known about the role of Lugaro cells and unipolar brush cells. The cerebellar cortical neurons are organized into a three-layered structure composed of the *molecular*, *Purkinje cell* and *granular layers* (Figure 2.4).

The outer layer of the cerebellar cortex, the *molecular layer*, contains the axons of granule cells, the dendrites of Purkinje cells, and basket and stellate cells, which are often grouped together as *molecular layer interneurons*. The cerebellar *granule cells* are the most abundant class of neurons in the human brain. They give rise to specialized axons called *parallel fibres* due to their parallel orientation along the axis of the folia.

Directly beneath the molecular layer, a single layer of Purkinje cell bodies forms the *Purkinje cell layer*. The *Purkinje cells* are large neurons with a fan-like dendritic tree that extends upwards through the molecular layer. These neurons receive *excitatory* synaptic inputs from approximately 200,000 different parallel fibres and a single climbing fibre, and *inhibitory* inputs from stellate and basket cells, and recurrent collaterals of the axons of Purkinje cells. The Purkinje cell axons run through the granular layer and the white matter and form inhibitory synapses with the neurons in the deep cerebellar nuclei. The innermost layer of the cerebellar cortex, the *granular layer*, is composed of a large number of small granule cells and a few large Golgi cells.

The basic cerebellar circuit is relatively simple and well established. The cerebellum receives input from two major excitatory afferents, the *mossy fibres* and the *climbing fibres*, which form glutamatergic synapses with cerebellar neurons. Interestingly, the two types of fibres produce different patterns of firing in the single output neuron of the cerebellar cortex: the Purkinje cell (Figure 2.5).

The *mossy fibres* are the major input to the cerebellum. These fibres originate from neurons in the spinal cord and brain stem, and project to the neurons in the deep cerebellar nuclei, and to granule and Golgi cells in the cerebellar cortex.

Climbing fibres, which are unique to the cerebellum [Ito 2002], originate in the inferior olivary nucleus in the medulla. Like the mossy fibres, the climbing fibres send collaterals to the neurons in the deep cerebellar nuclei. Purkinje cells receive a powerful synaptic input from a single climbing fibre, whereas climbing fibres contact the Purkinje cells with a divergence ratio of 1:10.

The organisation of the cerebellar output is simple. Purkinje cell axons form inhibitory synapses with neurons in the deep cerebellar nuclei which also receive excitation through mossy fibre and climbing fibre collaterals. The spike output of the Purkinje cells is modulated by excitatory input from parallel fibres and a single climbing fibre, and by inhibitory input from stellate cells, basket cells, and recurrent Purkinje cell collaterals.

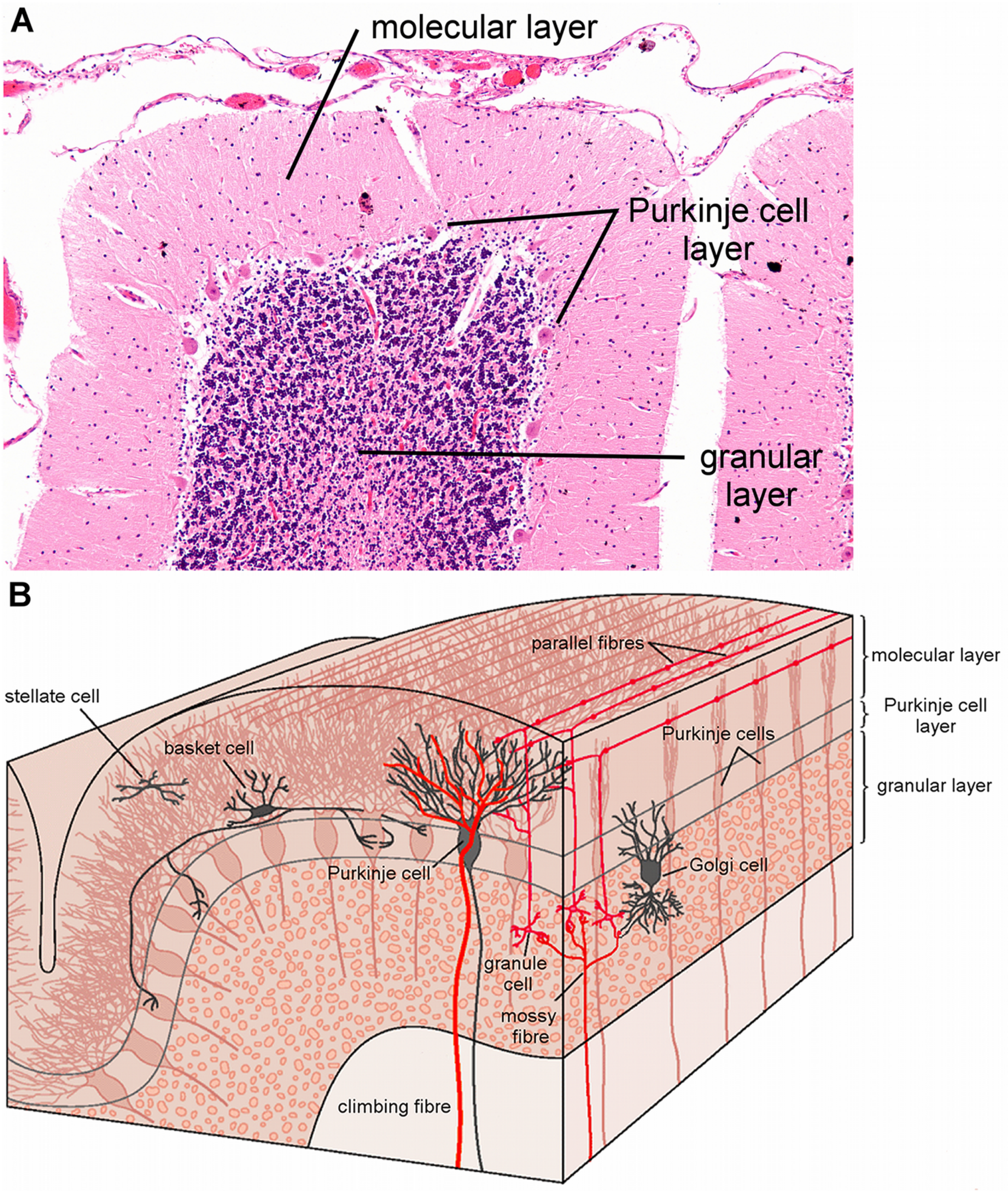

Figure 2.4: **Organisation of the cerebellar cortex. A.** Micrograph of the cerebellar cortex showing its three layers. The figure indicates the location of the cell bodies and shows the large number of neurons in the granular layer. Adapted from [Nephron 2012]. **B.** Three-dimensional view of the cerebellar cortex. Adapted from [Kandel 1991].

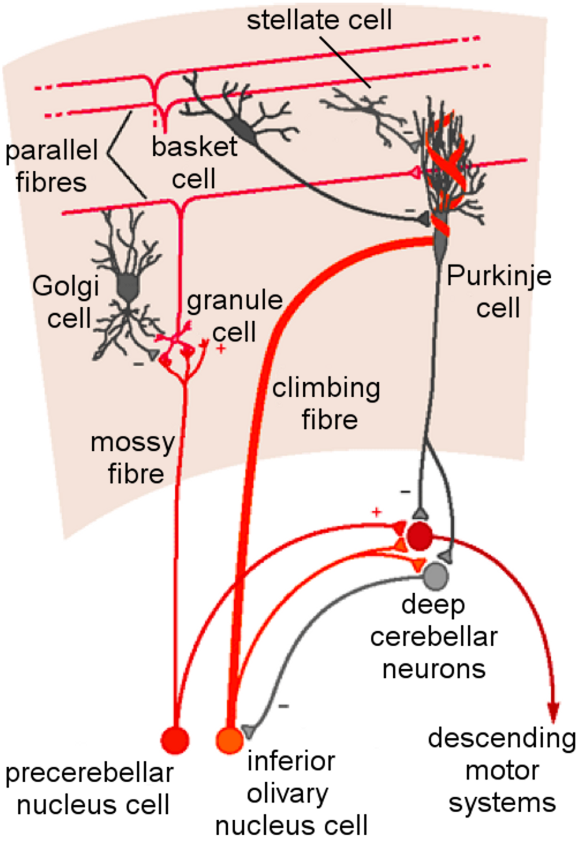

Figure 2.5: **The basic cerebellar circuit.** The figure indicates the excitatory (+) and inhibitory (−) synapses between the cell types. Adapted from [Kandel 1991].

2.4 Cerebellar Long-term Plasticity

Synaptic plasticity is an activity-dependent change in the strength of the synaptic connection between pre and postsynaptic neurons. Changes in synaptic plasticity can occur at timescales of milliseconds to seconds, known as *short-term plasticity*, or within minutes, which is then called *long-term plasticity*.

The long-term strengthening and weakening of synapses are known as *long-term potentiation* and *long-term depression*, respectively. Long-lasting changes in synaptic strength are assumed to be the basis of learning and the formation of memories (for review, see for example [Manninen 2010]). In particular, these forms of plasticity are involved in learning processes in cerebellar Purkinje cells.

Many types of cerebellar plasticity have been studied, but a major focus of cerebellar research is the long-term depression (LTD) at excitatory synapses between parallel fibres (PF) and Purkinje cells (PCs). PF LTD (often called cerebellar LTD) is a process in which the strength of the PF-PC synapse is depressed in response to the coincident activation of PF and CF input onto the PC [Ito 1982, Ito 1989, Ito 2002].

Some studies concerning cerebellar learning have revealed that PFs convey information required for movement generation, and CFs carry error signals, which are delayed relative to the PF activation. Accordingly, it has been shown that PF activation preceding CF activation is more effective in inducing LTD than CF activation preceding PF activation [Wang 2000, Doi 2005].

In addition to undergoing LTD, PF synapses can also exhibit long-term potentiation (LTP). The strengthening of excitatory synapses between PFs and PCs by PF LTP occurs after the activation of PFs without any coincident CF input to the PC. LTP is necessary to balance LTD at cerebellar PF-PC synapses to prevent saturation and to allow reversal of motor learning [Belmeguenai 2005]. Cerebellar research has little explored the mechanisms underlying cerebellar LTP.

2.5 Molecular Mechanisms of Cerebellar LTD

Research has pointed out that many molecules and the complex interactions between them underlie cerebellar plasticity (see for example [Kotaleski 2010]). In particular, multiple signalling pathways involving more than 30 molecules have been shown to contribute to cerebellar LTD [Fiala 1996, Kuroda 2001]. However, the exact relationship between cerebellar LTD and the different signalling cascades remains unclear. Computational models have been developed to investigate the information processing performed by the signalling networks underlying synaptic plasticity in the cerebellum.

Kuroda and collaborators have simulated the phosphorylation of AMPA receptors, an important process in cerebellar LTD and LTP [Kuroda 2001]. They have developed a kinetic simulation to study the behaviour of the complex signal transduction pathways involved in cerebellar LTD (Figure 2.6). Their model predicts that the activation of protein kinase C (PKC) can underlie the initial phase of the phosphorylation of AMPA receptors, and that a positive feedback loop through mitogen-activated protein (MAP) kinase can mediate the intermediate phase (with a late phase that depends on protein synthesis and that is not modelled). The LTD induction model of [Kuroda 2001] is studied in Chapter 5 of the present thesis. The underlying mechanisms are described below and summarised in Figure 2.6.

As mentioned earlier, the paired activation of PF and CF input leads to the induction of cerebellar LTD, by activating various signalling pathways that modulate the phosphorylation of AMPA receptors. Glutamate and nitric oxide (NO) are involved in PF signal transmission, and the CF signal is mediated by glutamate and corticotropin-releasing factor (CRF). The release of glutamate from PFs results in the activation of type-1 metabotropic receptors (mGluR) that are bound to G_q protein complexes, which in turn leads to the release of the GTP-binding protein subunit GTP-G_α. GTP-G_α activates phospholipase C (PLC). Diacylglycerol (DAG) and inositol trisphosphate (IP_3) are the products of the hydrolysis of the phospholipid phosphatidylinositol 4,5-bisphosphate (PIP_2) by active PLC. Calcium, DAG and PIP_2 activate cytosolic phospholipase A_2 (PLA_2), which results in the production of arachidonic acid (AA). The subsequent activation of PKC is regulated by calcium, DAG and AA. PKC phosphorylates AMPA receptors and plays an important role in the induction of cerebellar LTD.

Moreover, PFs produce NO that diffuses into the PC. NO binds to soluble guanylate cyclase (GC), which in turn catalyses the conversion of GTP into cyclic guanosine monophosphate (cGMP). cGMP binds to cGMP-dependent protein kinase G (PKG). PKG phosphorylates its substrate (G-substrate), which inhibits protein phosphatase 2A (PP2A). The resulting inhibition of PP2A causes a reduced dephosphorylation of AMPA receptors, and reduced dephosphorylation of two kinases that form part of a positive feedback loop (see below).

The coincident activation of CF and PF synapses leads to an increase in the intracellular calcium concentration in the PC. In the Kuroda model, this increase in calcium is based on experimental measurements [Wang 2000] and given by an explicit function of time, rather than being modelled by the kinetic simulation.

The CRF that is released from CF synapses activates corticotropin-releasing hormone receptor (CRHR). Activated CRHR and the protein tyrosine kinase Lyn phosphorylate Raf. Phosphorylated forms of Raf mediate the phosphorylation of mitogen-activated ERK-activating kinase (MEK), while phosphorylated MEK regulates the phosphorylation of MAP kinase. PP2A dephosphorylates Raf, MEK and AMPA receptors. Activated MAP kinase phosphorylates PLA_2 which catalyses the production of AA and the subsequent activation of PKC. These interactions result in a positive feedback loop. The consequence of this feedback loop is the sustained phosphorylation of AMPA receptors by PKC, which underlies the intermediate phase of LTD induction.

2.6 Chapter Conclusions

The structure of the cerebellum is well understood. The precision of the cerebellar anatomy has instigated the development of many theories that attempt to unravel cerebellar function. Although it is known that the cerebellum contributes to motor learning and cognition, there is still no general agreement about its exact functional role.

It is thought that modifications in the strength of synaptic connections onto cerebellar PCs such as LTD and LTP contribute to learning. Repeated conjunctive stimulations of PFs and CF lead to LTD of PF induced responses in PCs, while LTP is induced as a result of PF stimulation alone.

Cerebellar LTD is considered as the basis of cerebellum-dependent motor learning, and has been studied extensively. The events following the paired stimulation of PF and CF inputs that induce LTD are becoming clearer, however the precise interactions of the molecular machinery underlying LTD induction remain something of an enigma.

Many signalling cascades have been demonstrated to be involved in cerebellar LTD. However, the relationship between the known signalling pathways and cerebellar LTD is still not completely known. Kuroda and colleagues have proposed a complex intracellular signalling model that simulates the phosphorylation of AMPA receptors, which is crucial for the induction of LTD at PF-PC synapses. The reimplementation and test of this model are presented in Chapter 5 of the thesis.

It has recently been shown that calcium-calmodulin dependent protein kinase II (CaMKII) is an important component of the signalling network that is responsible for LTD at PF-PC synapses. The involvement of CaMKII in cerebellar plasticity will be discussed in the next chapter.

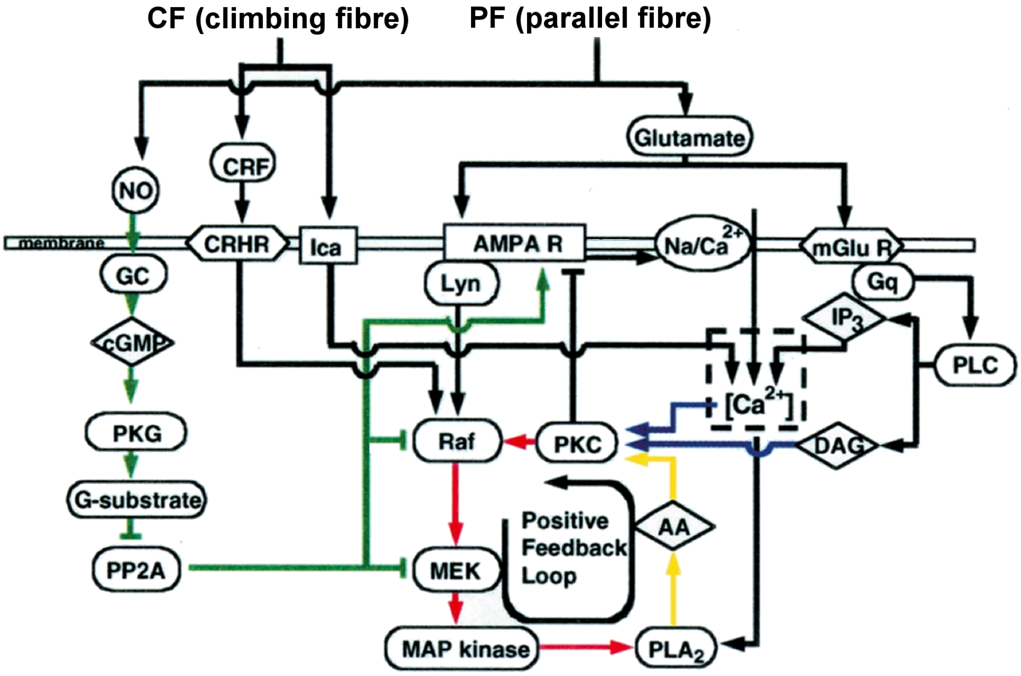

Figure 2.6: **Signalling pathways underlying cerebellar LTD.** The phosphorylation and dephosphorylation of AMPA receptors are mediated by the activation of PKC (blue, pink and yellow lines) and the inhibition of PP2A (green line), respectively. The intracellular calcium concentration (Ca^{2+}, in the figure) is indicated in the dashed-line box. However, in the model, the increase in calcium concentration that results from paired stimulation of PF and CF is based on experimental observations [Wang 2000], and not modelled by kinetic simulation. The symbols for the biochemical compounds are explained in the text. Adapted from [Kuroda 2001].

Chapter 3

CaMKII

Contents

Calcium-calmodulin dependent protein kinase II (CaMKII), which is one of the most abundant proteins in the brain, is a multifunctional enzyme that phosphorylates a wide range of substrates. CaMKII is a critical mediator of calcium signalling systems that underlie the induction of synaptic plasticity. Although significant progress has been made in understanding the role of CaMKII in synaptic plasticity in other brain areas, very little is known about its function during plasticity induction in the cerebellum.

This chapter begins with a summary of the structure and function of CaMKII. Following on from this, a description of the unique processes involved in the kinase activation is given. The third section of this chapter presents the idea that the CaMKII phosphorylation may respond to repetitive calcium signals based on their frequency. This chapter finishes with a discussion of the involvement of CaMKII isoforms in the induction of cerebellar plasticity.

3.1 Structure and Function of CaMKII

The CaMKII holoenzyme consists of 12 subunits that oligomerise into a double layer of hexameric rings (Figure 3.1). The kinase comprises a family of nearly 30 similar isoforms derived from the α, β, γ and δ genes. CaMKII is found in most types of cells, and the predominant isoforms in neurons are the α and β subunits [Fink 2002, Lisman 2002].

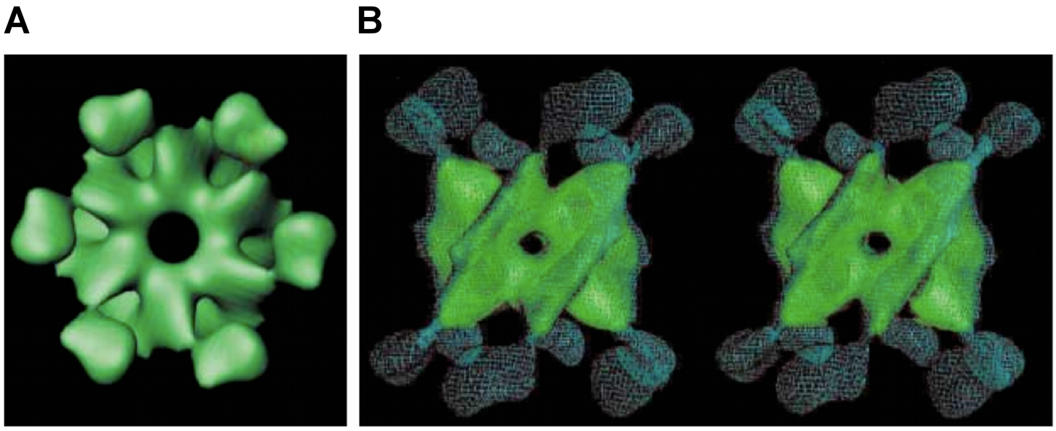

Figure 3.1: **Multimeric structure of CaMKII.** Three-dimensional views of the surfaces of the holoenzyme. **A.** Aspects of one of the CaMKII rings composed of 6 subunits. **B.** Perpendicular perspectives to the view shown in **A** that illustrate the 12 subunits of a CaMKII holoenzyme, distributed in two coupled hexameric rings. Adapted from [Lisman 2002].

The structures of αCaMKII and βCaMKII isoforms are similar. Each subunit is composed of catalytic, regulatory and oligomerisation domains whose functions are well known (Figure 3.2A). The *catalytic domain* contains sites for interactions with adenosine triphosphate (ATP), substrates and anchoring proteins. Under resting conditions, CaMKII has no catalytic activity since the regulatory domain inhibits its own catalytic region. The *regulatory domain*, also known as autoinhibitory domain, acts as a pseudosubstrate that binds to the catalytic segment and prevents substrates from binding to CaMKII, inhibiting the enzyme activity. Each CaMKII subunit can be activated by the binding of calcium-calmodulin to a region that overlaps with the pseudosubstrate segment [Lisman 2002]. The *oligomerisation domain*, also known as association domain, is the site by which subunits bind to each other to form the holoenzyme.

The oligomerisation segment is connected to the catalytic and regulatory domains by a variable region, which is responsible for the main difference between the kinase isoforms (red, Figure 3.2A). βCaMKII is longer than αCaMKII, presenting a sequence of amino acids that contains a binding site for the filamentous actin cytoskeleton (F-actin). Accordingly, βCaMKII but not αCaMKII can bind to F-actin.

The α and β kinase isoforms can form holoenzymes that consist of either one or both isoform types (Figure 3.2B). The cerebellum contains about four times as much βCaMKII as αCaMKII [Fink 2002].

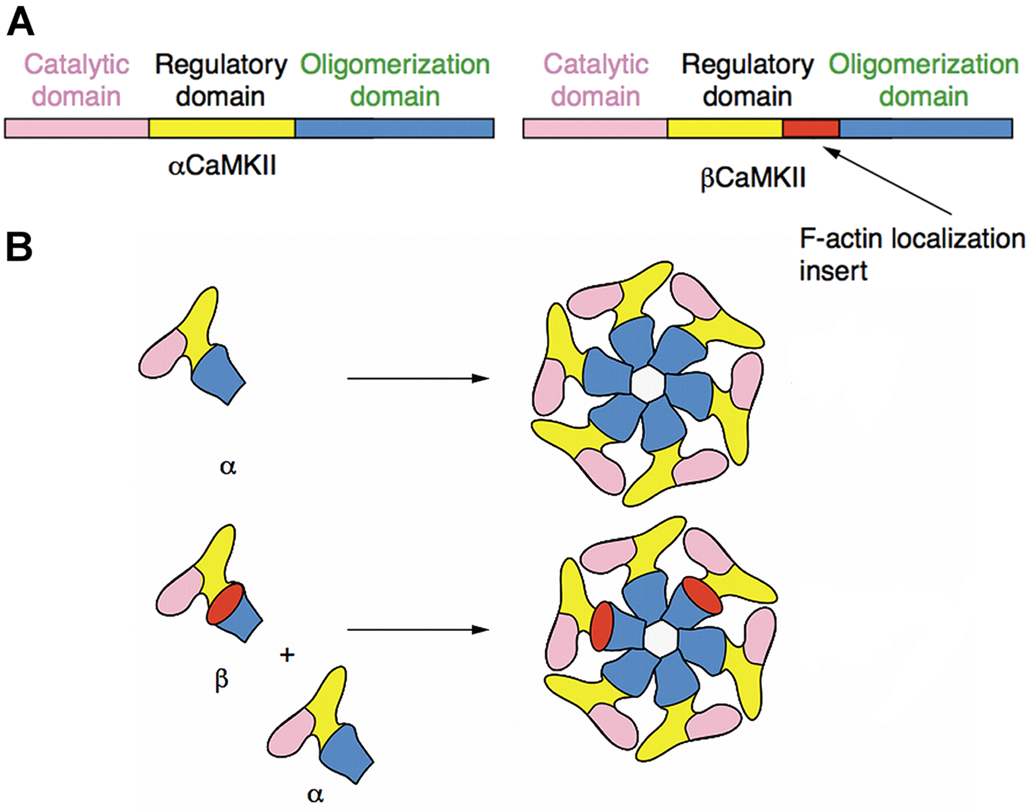

Figure 3.2: **Organisation of CaMKII subunits. A.** Schematic representation of the catalytic, regulatory and oligomerisation domains of αCaMKII and βCaMKII isoforms. The main difference between these genes is a region that appears in βCaMKII isoforms only (red). This segment functions as a target for filamentous actin (F-actin). **B.** The CaMKII isoforms oligomerise into a double layer of hexameric rings. They can form homooligomers of either αCaMKII or βCaMKII isoforms (top), or heterooligomers comprised of both αCaMKII and βCaMKII subunits (bottom). Adapted from [Fink 2002].

The meaning of the structural design of the CaMKII holoenzyme is still not completely understood [Lisman 2002]. Its ring-like structure, however, directly contributes to the regulation of the kinase activation.

3.2 Activation of CaMKII

Calcium, crucial for the learning process, mediates the activation of CaMKII subunits. Extracellular stimulation elevates the concentration of intracellular free calcium, which then binds to calmodulin. Binding of calcium-calmodulin is thought to disrupt the complex between the autoinhibitory and catalytic domains, thereby exposing the catalytic site of CaMKII and allowing it to phosphorylate its targets [Fink 2002]. Thus, this process results in activation of the kinase activity of CaMKII. One of the phosphorylation targets of an activated CaMKII subunit is its unphosphorylated neighbouring subunit in the multimer.

The requirement for initiating subunit phosphorylation within the CaMKII multimer is that two molecules of calcium-calmodulin bind to two neighbouring CaMKII subunits (Figure 3.3). A kinase subunit is phosphorylated in the regulatory domain at the Thr^{286} site for the αCaMKII isoform, and at the Thr^{287} site for βCaMKII [Brocke 1999]. The catalytic domain of an activated subunit in the CaMKII multimer phosphorylates $\mathrm{Thr}^{286/287}$ of a neighbouring subunit that must also be active. Once one subunit is phosphorylated, the propagation of phosphorylation around the multimer can proceed in a unidirectional process. This mechanism is named *CaMKII autophosphorylation*, and has a critical role in calcium signalling systems. Dissociation of calcium-calmodulin from an autophosphorylated subunit yields an autonomous form of CaMKII that retains kinase activity, a calcium-calmodulin independent activity.

The structure and the mechanism of activation of CaMKII are crucial for its autoregulatory behaviour, which is thought to underlie the kinase ability to become differentially phosphorylated at distinct frequencies of calcium pulses [Hudmon 2002].

3.3 CaMKII Frequency Sensitivity

Extracellular stimulation and the release of calcium from reticulum stores produce oscillations of intracellular calcium concentration of different frequencies [Meyer 1992, Hudmon 2002, Colbran 2004]. It is thought that information may be “encoded” by the frequency of calcium spikes and “decoded” by effector systems [Hanson 1994]. Based on this idea, Hanson et al have introduced the notion that CaMKII may act as a “decoder” of calcium pulse frequencies, i.e. the CaMKII autophosphorylation would depend on the frequency of calcium spikes.

Following on from this suggestion, many studies have investigated the involvement of CaMKII in the frequency-dependent information processing of calcium oscillations. Computer simulations have indicated that the CaMKII activation should be sensitive to the calcium oscillation frequency [Hanson 1994, Michelson 1994, Dosemeci 1996]. *In vitro* experiments with immobilized CaMKII demonstrated that the kinase does indeed respond differentially to many frequencies of calcium spikes, i.e. the oscillation frequency is translated to different levels of CaMKII activity [De Koninck 1998] (Figure 3.4A).

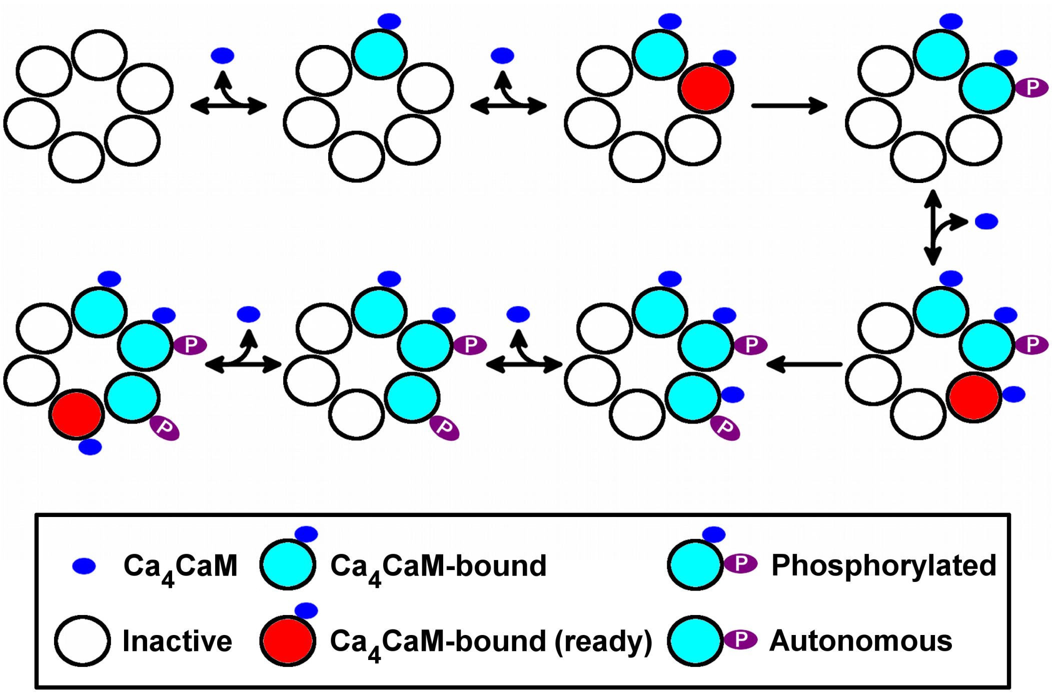

Figure 3.3: **Trajectories for the activation of CaMKII.** CaMKII holoenzymes are represented by rings with 6 subunits each. The kinase subunits can be in the following states: inactive, bound to calcium-calmodulin (Ca_4CaM), phosphorylated and bound to Ca_4CaM, and autonomous: phosphorylated, but dissociated from Ca_4CaM. A possible trajectory for the CaMKII autophosphorylation is represented in this figure. Initially, all CaMKII subunits are inactive. The activation of a CaMKII multimer initiates by the binding of Ca_4CaM to a kinase subunit. The Ca_4CaM-bound subunit is "ready" for phosphorylation (red) when its left neighbour within the CaMKII ring is an active subunit (cyan): Ca_4CaM-bound, phosphorylated or autonomous. A possible dephosphorylation of CaMKII is not considered in this scheme.

Dupont and collaborators [Dupont 2003] have proposed a simple biophysical model of activation of CaMKII by calcium-calmodulin to quantitatively reproduce the experiments by De Koninck and Schulman [De Koninck 1998]. It was demonstrated that the kinase presents different phosphorylation levels in response to square calcium pulses with the same amplitude and duration, applied at different frequencies (Figure 3.4B). Both theoretical and experimental studies have argued that CaMKII depends on the frequency of calcium oscillations.

The stimulation protocols adopted in those earlier studies are investigated in details in this thesis. With a rationalized version of the earlier computational model of CaMKII activation [Dupont 2003], it was demonstrated that the kinase autophosphorylation kinetics are independent of the pulse frequency itself (Chapter 6). This is one of the major findings of the thesis and my main contribution to knowledge.

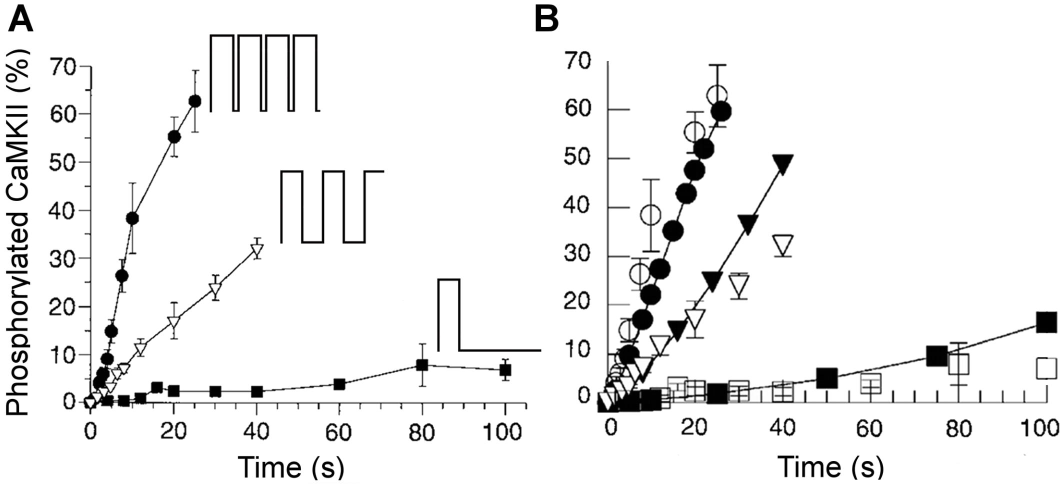

Figure 3.4: **Sensitivity of CaMKII to the frequency of calcium-calmodulin oscillations.** Experimental observations (**A**) and computer simulations (**B**) demonstrate the temporal evolution of the phosphorylation levels of CaMKII in response to one hundred 200 ms square pulses of calcium-calmodulin (100 nM) at frequencies of 1 (squares), 2.5 (triangles) and 4 Hz (circles). **A.** Adapted from [De Koninck 1998]. **Insets.** Representations of the calcium-calmodulin oscillations with identical amplitude at frequencies of 1, 2.5 and 4 Hz for 1 s. **B.** Filled symbols represent results from computer simulations [Dupont 2003], while open symbols denote the experimental results shown in **A**. Adapted from [Dupont 2003].

3.4 CaMKII Isoforms and Cerebellar Plasticity

The αCaMKII and βCaMKII isoforms have recently been shown to mediate synaptic plasticity in the cerebellum, and therefore to be essential for learning and memory formation.

Because Purkinje cells (PCs) are the only cells in the cerebellum that contain αCaMKII, Hansel and co-workers have investigated the role of this isoform in cerebellar plasticity and motor learning [Hansel 2006]. They have performed experiments with αCaMKII knockout mice, a mutation that deletes the α isoform of CaMKII. Experimental observations have revealed that αCaMKII knockout mice were impaired in cerebellar long-term depression (LTD) induction, whereas the induction of long-term potentiation (LTP) was unaffected (Figure 3.5). For the first time, it has been shown that αCaMKII is required for LTD but not for LTP at the parallel fibre (PF)-PC synapse and that αCaMKII is important for cerebellar motor learning.

Although βCaMKII is the predominant isoform of CaMKII in the cerebellum, the role of βCaMKII in cerebellar learning and memory has yet to be established. The β isoform of CaMKII received more attention since Meyer and collaborators have shown the unique F-actin binding properties of βCaMKII [Shen 1998], but little is known about the function of this isoform in synaptic plasticity.

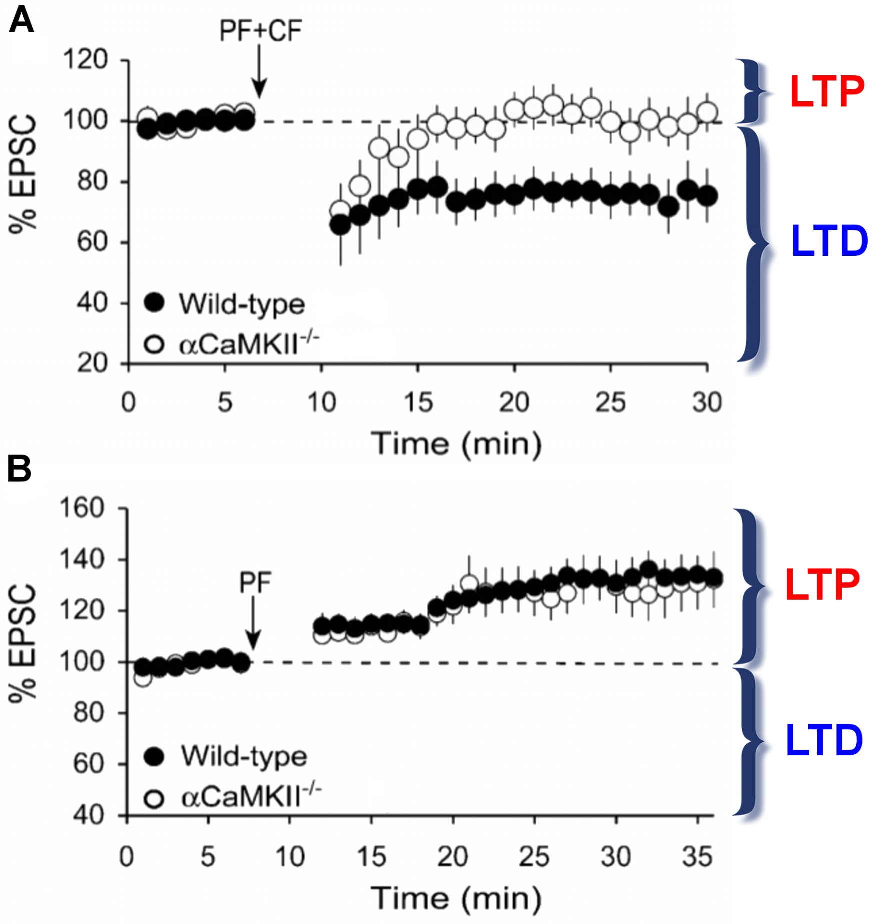

Figure 3.5: **αCaMKII is necessary for LTD induction but not for LTP in cerebellar PCs.** Temporal evolution of amplitudes of excitatory postsynaptic current (EPSC) in response to conjunctive PF and CF stimulation (**A**) and PF stimulation alone (**B**). The wild-type mice contain both αCaMKII and βCaMKII isoforms (filled circles), while αCaMKII$^{-/-}$ represents mice that lack αCaMKII (open circles). Cerebellar LTD is induced by paired stimulation of PF and CF at 1 Hz for 5 min, whereas PF stimulation alone induces LTP. Values for EPSC $>$ 100% indicate LTP induction, whereas the generation of LTD is expressed by EPSC $<$ 100%. **A.** Conjunctive stimulation of PF and CF leads to the impairment of LTD in αCaMKII knockout mice. **B.** The lack of the αCaMKII isoform does not affect the LTP induction in response to PF stimulation alone. Adapted from [Hansel 2006].

Recent experiments with *Camk2b* knockout mice, which suffer a mutation that deletes the β isoform of CaMKII, have addressed the role of βCaMKII in plasticity in cerebellar PCs. Those studies have revealed that βCaMKII controls the direction of plasticity at PF-PC synapses [van Woerden 2009]. More specifically, protocols that induce LTD in wild-type mice result in LTP in knockout mice that lack βCaMKII, and vice versa (Figure 3.6).

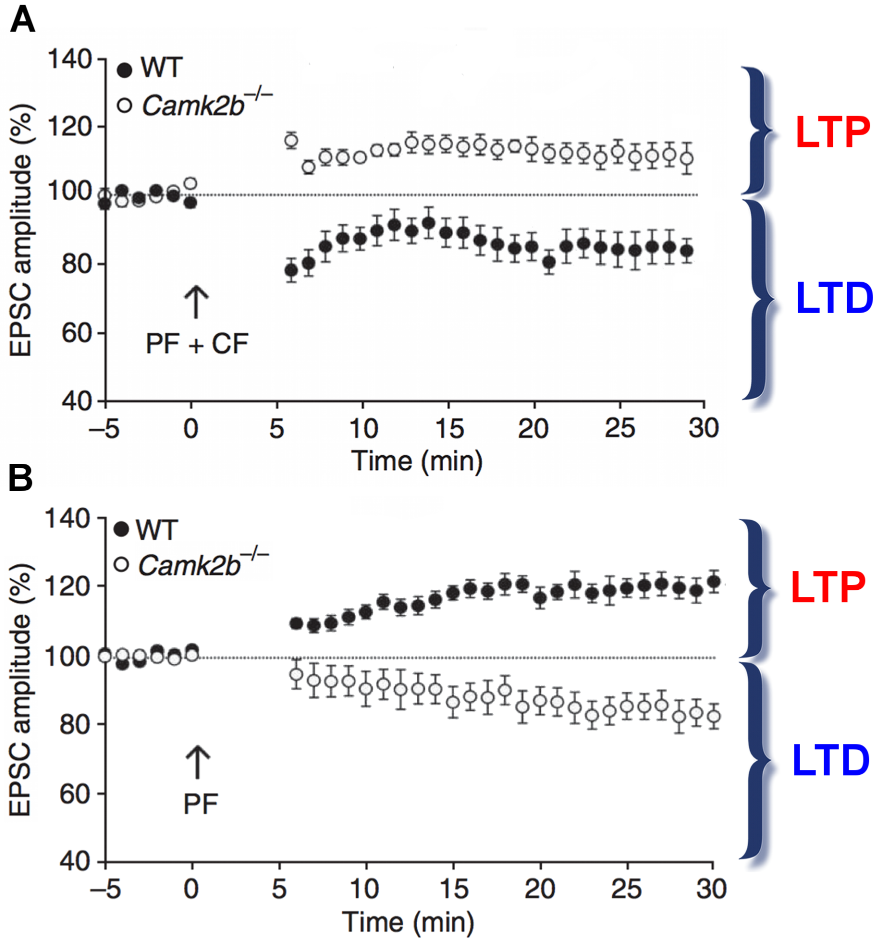

Figure 3.6: **βCaMKII regulates the direction of cerebellar plasticity in PCs.** Time-evolution of amplitudes of EPSC in response to conjunctive PF and CF stimulation (**A**) and PF stimulation alone (**B**). WT represents the wild-type mice that contain both αCaMKII and βCaMKII isoforms (filled circles), while *Camk2b*$^{-/-}$ denotes mice that lack βCaMKII (open circles). **A.** Paired stimulation of PF and CF leads to the induction of LTP in βCaMKII knockout mice, rather than LTD. **B.** The lack of the βCaMKII isoform leads to LTD induction in response to PF stimulation alone that should induce LTP. Adapted from [van Woerden 2009].

However, the underlying mechanism that may explain those experimental findings was not clear. Van Woerden et al have suggested that a biochemical difference between the αCaMKII and βCaMKII isoforms would underlie the switch of the direction of synaptic plasticity. The βCaMKII, but not αCaMKII, isoforms can bind to F-actin, which could result in recruitment of CaMKII to F-actin, making it unavailable for AMPA receptor phosphorylation.

To investigate the proposed function of βCaMKII in cerebellar plasticity, a kinetic model of the phosphorylation of AMPA receptors by CaMKII was built (Chapter 7). The simulation results show that the βCaMKII isoform could indeed control the direction of plasticity at PF-PC synapses in the manner proposed by van Woerden et al.

3.5 Chapter Conclusions

One of the most vexing questions in cerebellar research is whether or not the cerebellum contributes to motor learning and memory formation. It is known that CaMKII is a crucial molecule for synaptic plasticity, a process believed to be responsible for memory and learning. However, little is known about the role of the αCaMKII and βCaMKII isoforms in cerebellar plasticity.

The oscillatory intracellular calcium signals mediate several cellular mechanisms such as plasticity in the cerebellum. It is thought that the frequency of calcium oscillations may influence many of these processes. Computer simulations [Dupont 2003] and experimental observations [De Koninck 1998] have indicated that frequencies of oscillatory calcium signals can determine different levels of CaMKII activation by calcium-calmodulin. A kinetic model of the activation of CaMKII to study the stimulation protocols adopted in those earlier studies was developed in the thesis (Chapter 6). Simulation results lead to findings of high interest to neuroscience.

It has been found that the βCaMKII isoform regulates the direction of cerebellar plasticity at PF-PC synapses [van Woerden 2009]. However, a plausible quantitative model of the molecular mechanisms underlying their observations did not exist. This thesis presents a simple model of signalling pathways to study the role of βCaMKII in the bidirectional plasticity at the PF-PC synapse (Chapter 7). Computer simulations predict how βCaMKII may mediate the reversal of plasticity at this cerebellar synapse. This is the first data-driven model of intracellular signalling pathways that includes CaMKII and that is able to replicate the induction of cerebellar LTD and LTP in cerebellar PCs.

The kinetic models described in this thesis represent molecular interactions that occur in intracellular signalling. The processes involved in modelling biochemical reactions of signalling pathways are described in details in the next chapter.

Chapter 4

Computational Modelling of Intracellular Signalling

Contents

Biochemical *reaction kinetics* is the study of the velocity of biochemical reactions. Kinetics simulation of biological signalling pathways has received much attention from experimental and theoretical researchers. Modelling of signalling networks can contribute to testing or supporting experimental hypotheses about underlying biological processes, and may suggest new experiments. Computational modelling of biochemical reactions regulating intracellular signalling is, in many cases, crucial to understanding the complex signalling mechanisms involved in cerebellar plasticity.

This chapter highlights the fundamental concepts of reaction kinetics that are crucial for building signalling computational models. It includes a presentation of the Law of Mass Action for representing biochemical kinetics, a description of models for expressing enzymatic reactions, such as the Michaelis-Menten model and the kinetics of explicit enzyme-substrate complex, and a discussion about the thermodynamics of reactions. This chapter also presents features of the computational tools used in this thesis for kinetics simulation of signalling.

4.1 Kinetics of Biochemical Reactions

A *biochemical reaction* is the process in which a set of compounds called *reactants* is transformed into one or more *products*. A general biochemical reaction can be expressed as

$$\mathrm{A} + \mathrm{B} \underset{\mathrm{k_{off}}}{\overset{\mathrm{k_{on}}}{\rightleftharpoons}} \mathrm{AB} \quad , \tag{4.1}$$

where the reactant A binds to another reactant B and forms the product AB. This reaction presents a reversible transformation, i.e. AB can dissociate and result in substances A and B.

The reaction kinetics describes the *rate*, or velocity, of biochemical reactions, determining how fast these transformations occur over a period of time. For instance, in Reaction 4.1, k_{on} is the rate constant for A binding to B, and k_{off} is the rate for AB dissociation.

The temporal evolution of biological systems governed by biochemical reactions can be described by ordinary differential equations (ODEs). Each ODE denotes variations in the concentration of a certain substance (ξ) evolved over time, and may be expressed as follows [Cornish-Bowden 2004, Atkins 2009]

$$\frac{d\,[\xi]}{dt} = \sum v_{production} - \sum v_{consumption} \quad , \tag{4.2}$$

where $[\xi]$ represents the concentration of ξ, $\sum v_{production}$ is the total velocity of production of ξ, and $\sum v_{consumption}$ is the sum of the reaction rates consuming ξ.

Rates of biochemical reactions depend on many factors such as the concentration of reactants. The kinetics of reactions in signalling pathways may be modelled at different levels of abstraction or simplification. Most approaches, including the Michaelis-Menten model for simple enzyme reactions, are derived from the Law of Mass Action, explained below.

4.1.1 Mass action Kinetics

Waage and Guldberg have postulated the Law of Mass Action to demonstrate observations about the kinetics of chemical reactions [Waage 1864, Atkins 2009]. This law describes the velocity at which chemical substances collide and interact to form different chemical combinations. Those authors have related the velocities of reactions to the amounts of reacting substances. More specifically, the *mass action kinetics* states that the rate of a reaction is proportional to the product of the concentrations of compounds reacting in this transformation. For example, assuming the Law of Mass Action and considering Equation 4.2, variations in the concentration of the substances of Reaction 4.1 may be calculated as

$$\frac{d[A]}{dt} = k_{off}[AB] - k_{on}[A][B] \quad , \tag{4.3}$$

$$\frac{d[B]}{dt} = k_{off}[AB] - k_{on}[A][B] \quad , \quad \text{and} \tag{4.4}$$

$$\frac{d[AB]}{dt} = k_{on}[A][B] - k_{off}[AB] \ , \tag{4.5}$$

where $[A]$, $[B]$ and $[AB]$ denote the concentrations of substances A, B and AB, respectively.

Most biochemical reactions exhibit a linear dependence of the transformation rate upon the concentrations of the reactants. However, the reactions that involve enzymes mostly present a nonlinear dependence of the initial reaction rate on the reactant concentration. In the following, the kinetics of enzymatic reactions is discussed in detail.

4.1.2 Kinetics of Enzymatic Reactions

Enzymes are proteins that speed up the velocity of biochemical reactions without being consumed in the transformation. Because enzymes change the *rate* of reactions, these proteins act as catalysts on selected reactions and substances.

A free enzyme (E) can act on a compound called *substrate* (S), catalysing a specific biochemical reaction. The substrate binds to the active site of the enzyme and forms an intermediate *enzyme-substrate* complex (ES), and the enzyme catalyses the transformation of S into one or more *products* (P). The *enzyme-product* complex (EP) then breaks down to form one or more products. For simplicity, the EP complex and the transformation step $ES \to EP$ are usually not explicitly included in the reaction scheme. This simplified reaction scheme, depicted in Figure 4.1, is denoted as

$$\mathrm{E} + \mathrm{S} \underset{\mathrm{k_b}}{\overset{\mathrm{k_f}}{\rightleftharpoons}} \mathrm{ES} \xrightarrow{\mathrm{k_{cat}}} \mathrm{E} + \mathrm{P} \ , \tag{4.6}$$

where k_f is the rate constant of formation of the ES complex, also called *forward* rate, k_b is the rate of dissociation of ES, or the *backward* rate, and k_{cat} is the *catalytic* rate constant, which in this simplified model includes the S to P transformation itself as well as the dissociation of the EP complex.

The kinetics of enzymatic reaction above can be modelled explicitly, or using the simplified approaches proposed by Michaelis and Menten [Michaelis 1913] or Briggs and Haldane [Briggs 1925].

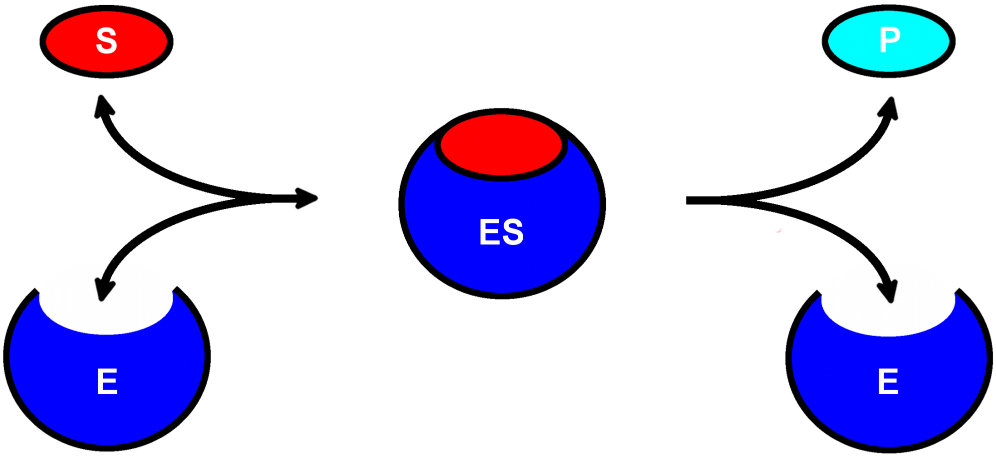

Figure 4.1: **Mechanisms of enzymatic reactions.** The active site of an enzyme (E, blue) binds to a substrate compound (S, red) forming an enzyme-substrate complex (ES, red & blue). In such a scheme, this is a reversible transformation in which the ES complex can dissociate and result in E and S. However, the enzymatic reaction can also result in a breakdown of the substrate into one or more products (P, magenta). The product then diffuses away and the enzyme is again available for binding to another substrate.

4.1.2.1 Explicit Enzyme-substrate Complex Kinetics

Considering the Law of Mass Action described in Section 4.1.1 and Equation 4.2, the time evolution of concentrations of the substances of Reaction 4.6 may be calculated by evaluating four nonlinear ODEs

$$\frac{d[E]}{dt} = -k_f[E][S] + (k_b + k_{cat})\,[ES] \enspace , \tag{4.7}$$

$$\frac{d[S]}{dt} = -k_f[E][S] + k_b[ES] \enspace , \tag{4.8}$$

$$\frac{d[ES]}{dt} = k_f[E][S] - (k_b + k_{cat})\,[ES] \enspace , \quad \text{and} \tag{4.9}$$

$$\frac{d[P]}{dt} = k_{cat}[ES] \enspace , \tag{4.10}$$

where $[E]$, $[S]$, $[ES]$ and $[P]$ are the concentration levels of compounds E, S, ES and P. In the thesis, this modelling approach for enzymatic reactions is called *explicit ES complex kinetics* (Figure 4.2).

Because complex signalling pathways comprise many enzymatic reactions, the major problem with the explicit modelling described above is the large amount of ODEs to simulate those signalling processes. Simpler methods for modelling enzymatic reactions, such as Michaelis-Menten kinetics, do not simulate concentration variations of E and ES (Equations 4.7 and 4.9, respectively). This reduces the number of ODEs, which in turn decreases the complexity of those mathematical systems.

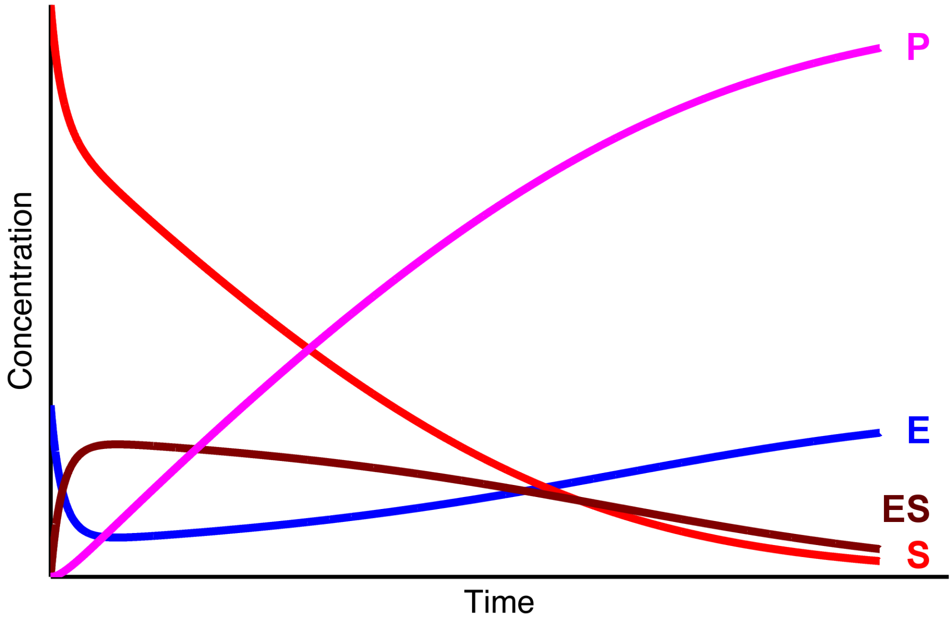

Figure 4.2: **Kinetics of enzymatic reactions.** Temporal evolution of concentrations of the substances that compose the general enzyme-catalysed Reaction 4.6, according to the explicit ES complex kinetics. This graph results from the numerical solution of the system of Equations 4.7, 4.8, 4.9 and 4.10 that represents variations in the concentrations of the free enzyme E (blue), the substrate S (red), the enzyme-substrate ES (brown), and the product P of the reaction (magenta), respectively. Values for the kinetic constants were arbitrarily chosen for demonstration purposes.

4.1.2.2 Michaelis-Menten Kinetics

Michaelis and Menten have proposed a model to explain the enhancement of reaction rates caused by enzymes [Michaelis 1913] (see also [Briggs 1925, Cornish-Bowden 2004]). The *Michaelis-Menten kinetics* is the best-known model that accounts for the kinetic properties of enzymatic reactions.

The product of an enzymatic reaction is formed faster than uncatalysed reactions, reaching equilibrium more rapidly. In enzyme kinetics, the concentrations of intermediates quickly approach a steady state, i.e. after an initial burst phase, the ES concentration remains nearly constant through much of the reaction (brown in Figure 4.2), while the concentrations of substrates and products are changing [Briggs 1925]. This phase is called *quasi-steady-state approximation* and lasts until a significant amount of substrate has been consumed.

Because the velocities of formation and breakdown of the enzyme-substrate complex are equal in a steady state, the concentration of the intermediate ES shown in Reaction 4.6 may be assumed as constant [Berg 2002, Cornish-Bowden 2004], and

$$\frac{d[ES]}{dt} = 0 \ . \tag{4.11}$$

Substituting Equation 4.11 in Equation 4.9, the concentration of the ES complex can be written as

$$[ES] = \frac{[E][S]}{K_M} \ , \tag{4.12}$$

where K_M is the Michaelis-Menten constant defined by

$$K_M = \frac{k_b + k_{cat}}{k_f} \ . \tag{4.13}$$

Provided that the concentration of the substrate S is much greater than the concentration of the free enzyme E [Berg 2002], the fraction of S that binds to E to form the ES complex is negligible. Therefore, the total enzyme concentration $[E_t]$ is

$$[E_t] = [E] + [ES] \ . \tag{4.14}$$

Rearranging Equation 4.14 and substituting the expression for $[E]$ in Equation 4.12, the ES concentration can be rewritten as

$$[ES] = [E_t] \, \frac{[S]}{[S] + K_M} \ . \tag{4.15}$$

In order to determine the catalytic rate (v) of Reaction 4.6, it is possible to substitute Equation 4.15 in Equation 4.10 to obtain

$$v = \frac{d[P]}{dt} = k_{cat} \, [E_t] \, \frac{[S]}{[S] + K_M} \ . \tag{4.16}$$

The maximum speed of the reaction is reached when the concentration of the substrate is much greater than K_M. Thus

$$\frac{[S]}{[S] + K_M} \rightarrow 1 \ , \tag{4.17}$$

and the maximal reaction rate (V_{max}) is

$$V_{max} = k_{cat} \, [E_t] \ . \tag{4.18}$$

Substituting Equation 4.18 in Equation 4.16, the *Michaelis-Menten equation* is then obtained

$$v = V_{max} \frac{[S]}{[S] + K_M} \ . \tag{4.19}$$

Therefore, using the Michaelis-Menten model, the system of Equations 4.7, 4.8, 4.9 and 4.10 that simulates the kinetics of Reaction 4.6 can be reduced to

$$\frac{d[S]}{dt} = -k_{cat} \, [E_t] \, \frac{[S]}{[S] + K_M} \ , \quad \text{and} \tag{4.20}$$

$$\frac{d[P]}{dt} = k_{cat} \, [E_t] \, \frac{[S]}{[S] + K_M} \ , \tag{4.21}$$

and here the concentrations of E and ES are unchangeable over time, i.e. Equations 4.7 and 4.9 are equal to zero.

Enzyme-catalysed reactions exhibit *saturation kinetics*, which is the kinetics of a reaction whose velocity approaches a maximal value, as the concentration of substrate increases (Figure 4.3). At low substrate concentrations, the reaction rate increases linearly with the concentration of the substrate, while at high amounts of substrate, the speed of the reaction approaches a maximal rate, and the enzyme is said to be *saturated* with respect to the substrate. In Equation 4.19, V_{max} represents the theoretical maximal velocity that the reaction achieves, while K_M denotes the substrate concentration at which the reaction rate is half V_{max}.

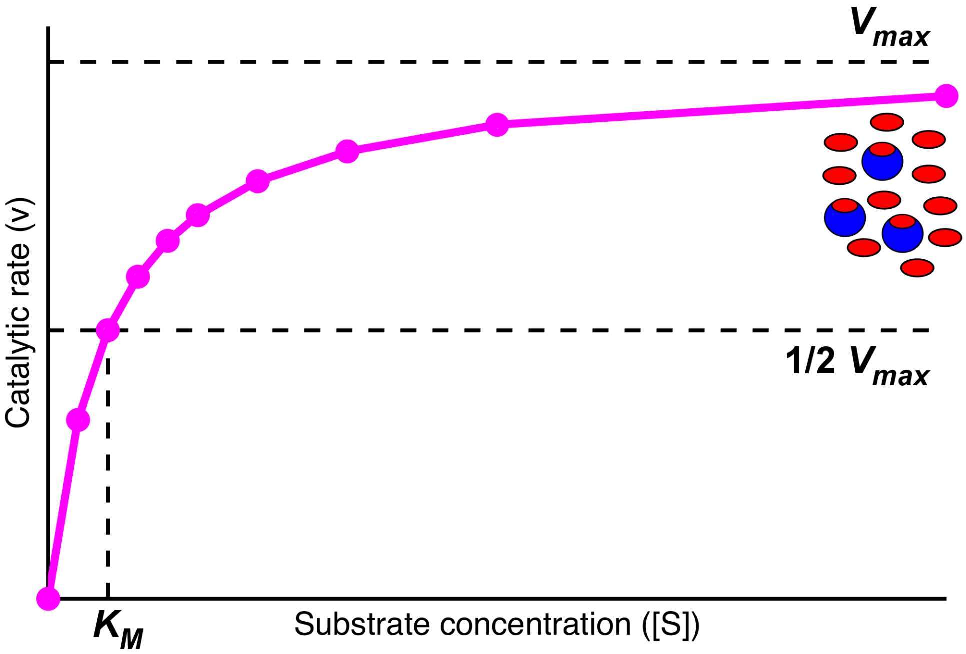

Figure 4.3: **Enzymatic reactions exhibit saturation kinetics.** This figure illustrates the effect of substrate concentrations on the enzymatic reaction velocity, according to Michaelis-Menten Equation 4.19. The reaction has half its maximum velocity (V_{max}) when the substrate concentration is K_M. The catalytic rate approaches V_{max} but never reaches it. **Inset.** Enzymes (blue) become saturated at high concentrations of substrate (red), i.e. all active sites are bound to substrate molecules, and enzymes are operating at full capacity.

4.1.3 Thermodynamics of Reactions

Many cellular activities require energy. *Thermodynamics* is the science that studies energy transformations [Haynie 2001]. The kinetic model built in Chapter 7 contains a few reaction rates whose values have, as yet, not been experimentally determined. Thus, those parameter values were assumed in this thesis.

To determine hypothetical values for reactions rates under certain conditions, calculations are needed not to violate principles of chemical thermodynamics in biological systems. In the following, the concepts underlying those mathematical calculations are briefly discussed.

4.1.3.1 Gibbs Free Energy

The *Gibbs free-energy change* ΔG, also called the chemical potential, is the variation of energy suffered by a reaction when moving from its initial state to equilibrium, with no alteration in pressure or temperature [Nelson 2005, Atkins 2009]. For instance, considering the following biochemical reaction

$$\mathrm{A} + \mathrm{B} \underset{\mathrm{k_b}}{\overset{\mathrm{k_f}}{\rightleftharpoons}} \mathrm{C} + \mathrm{D} \ , \tag{4.22}$$

where C and D are products of the reaction. Changes in its Gibbs free energy are given by

$$\Delta G = \Delta G'^{o} + RTln\frac{[C][D]}{[A][B]} \ , \tag{4.23}$$

where $\Delta G'^{o}$ is the standard Gibbs free-energy change, R is the gas constant, T is the absolute temperature, and $[A]$, $[B]$, $[C]$ and $[D]$ denote the respective concentrations of reactants A and B, and products C and D.

A chemical reaction tends to occur in the forward direction when ΔG is large and negative, while for a large and positive ΔG, the reaction tends to go in the backward direction. However, if $\Delta G = 0$, the reaction has reached equilibrium.

4.1.3.2 The Equilibrium Constant

The tendency of a reaction to move toward equilibrium can be calculated by the equilibrium constant K_{eq}. For Reaction 4.22, the equilibrium constant is expressed as [Atkins 2009]

$$K_{eq} = \frac{k_f}{k_b} = \frac{[C][D]}{[A][B]} = e^{-\frac{\Delta G'^{o}}{RT}} \ . \tag{4.24}$$

High K_{eq} values indicate that reactants have been almost completely converted into products.

Considering another scenario, signal transduction pathways can comprise coupled biochemical reactions forming multiple pathways from one compound to another (Figure 4.4). As described in Section 4.1.3.1, each reaction i contains its specific free-energy change ΔG_i. For instance, in Figure 4.4, ΔG_{AB}, ΔG_{BC}, ΔG_{AD} and ΔG_{DC} are the respective free-energy changes for reactions A $\rightleftharpoons$ B, B $\rightleftharpoons$ C, A $\rightleftharpoons$ D and D $\rightleftharpoons$ C.

Based on the *First Law of Thermodynamics* which says that energy is neither created nor destroyed but converted from one form to another, Hess has proposed a law that relates this principle to chemical reactions [Hess 1840]. *Hess's law* states that the free-energy change depends only on the initial and final states of a reaction, and is independent of the route by which the reaction may occur. For example, in the case of Figure 4.4, the overall free-energy change from A to C can be expressed as

$$\Delta G_{AB} + \Delta G_{BC} = \Delta G_{AD} + \Delta G_{DC} \ . \tag{4.25}$$

From Equations 4.23 and 4.24, and after some calculations, Equation 4.25 can be rewritten as

$$K_{eq_{AB}} K_{eq_{BC}} = K_{eq_{AD}} K_{eq_{DC}} \ , \tag{4.26}$$

where

$$K_{eq_{AB}} = \frac{k_{f_{AB}}}{k_{b_{AB}}} \ , \ K_{eq_{BC}} = \frac{k_{f_{BC}}}{k_{b_{BC}}} \ , \ K_{eq_{AD}} = \frac{k_{f_{AD}}}{k_{b_{AD}}} \ , \text{ and } K_{eq_{DC}} = \frac{k_{f_{DC}}}{k_{b_{DC}}} \ . \tag{4.27}$$

Equation 4.26 was adopted to estimate values for kinetic constants whose reactions form thermodynamic cycles in the model developed in Chapter 7.

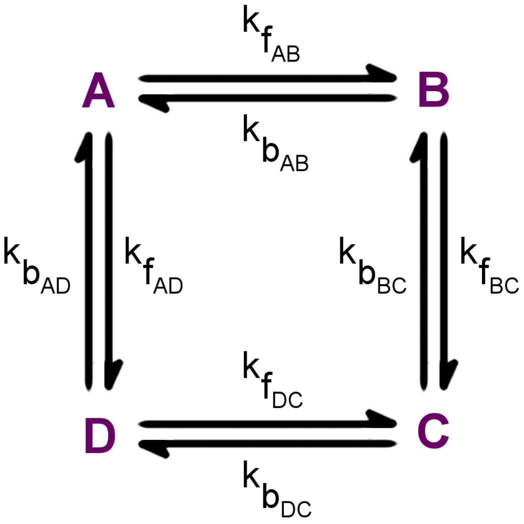

Figure 4.4: **A biochemical reaction "loop".** This figure portrays a set of coupled biochemical reactions that forms a "loop". The kinetic constants $k_{f_{AB}}$ and $k_{b_{AB}}$, $k_{f_{BC}}$ and $k_{b_{BC}}$, $k_{f_{AD}}$ and $k_{b_{AD}}$, $k_{f_{DC}}$ and $k_{b_{DC}}$ represent the forward and backward reaction rates for A $\rightleftharpoons$ B, B $\rightleftharpoons$ C, A $\rightleftharpoons$ D and D $\rightleftharpoons$ C, respectively.

4.2 Simulators for Signalling Pathways in this Thesis

All models built in this thesis were implemented in XPPAUT (X-Windows Phase Plane plus Auto). However, this document also presents the study of an existing signalling model [Kuroda 2001], which was originally implemented in GENESIS (GEneral NEural SImulation System) that uses the GENESIS/kinetikit library for the simulation of reaction kinetics (Chapter 5). In the following, the features of GENESIS/kinetikit and XPPAUT are summarised.

4.2.1 GENESIS/kinetikit

In 1988, Bower and Beeman released a simulator for the realistic modelling of biological and neural systems called GENESIS [Bower 2008]. This software platform allows modellers to simulate a wide range of biological scenarios, ranging from simple intracellular components to large complex networks.

GENESIS contains libraries from which different types of simulations can be developed. For instance, Bhalla has developed a library named *kinetikit* whose environment provides a graphical interface for modelling a wide number of biochemical reactions underlying signalling pathways [Vayttaden 2004, Bower 2008]. *Kinetikit* shows a user-friendly interface in which compounds and reactions can be clicked and dragged in a simple way, forming biochemical reactions that occur in signal transduction processes (Figure 4.5).

4.2.2 XPPAUT

XPPAUT is a numerical tool developed by Bard Ermentrout for simulating dynamical systems [Ermentrout 2002]. This simulator numerically solves linear and nonlinear ODEs, providing powerful analytical tools. To model biochemical reactions using XPPAUT, it is necessary to create an input file that informs the initial concentration of each compound, the rate constants of reactions, and the ODEs. For example, Figure 4.6 represents the XPPAUT input file for solving Equations 4.7, 4.8, 4.9 and 4.10 that represent the kinetics of Reaction 4.6.

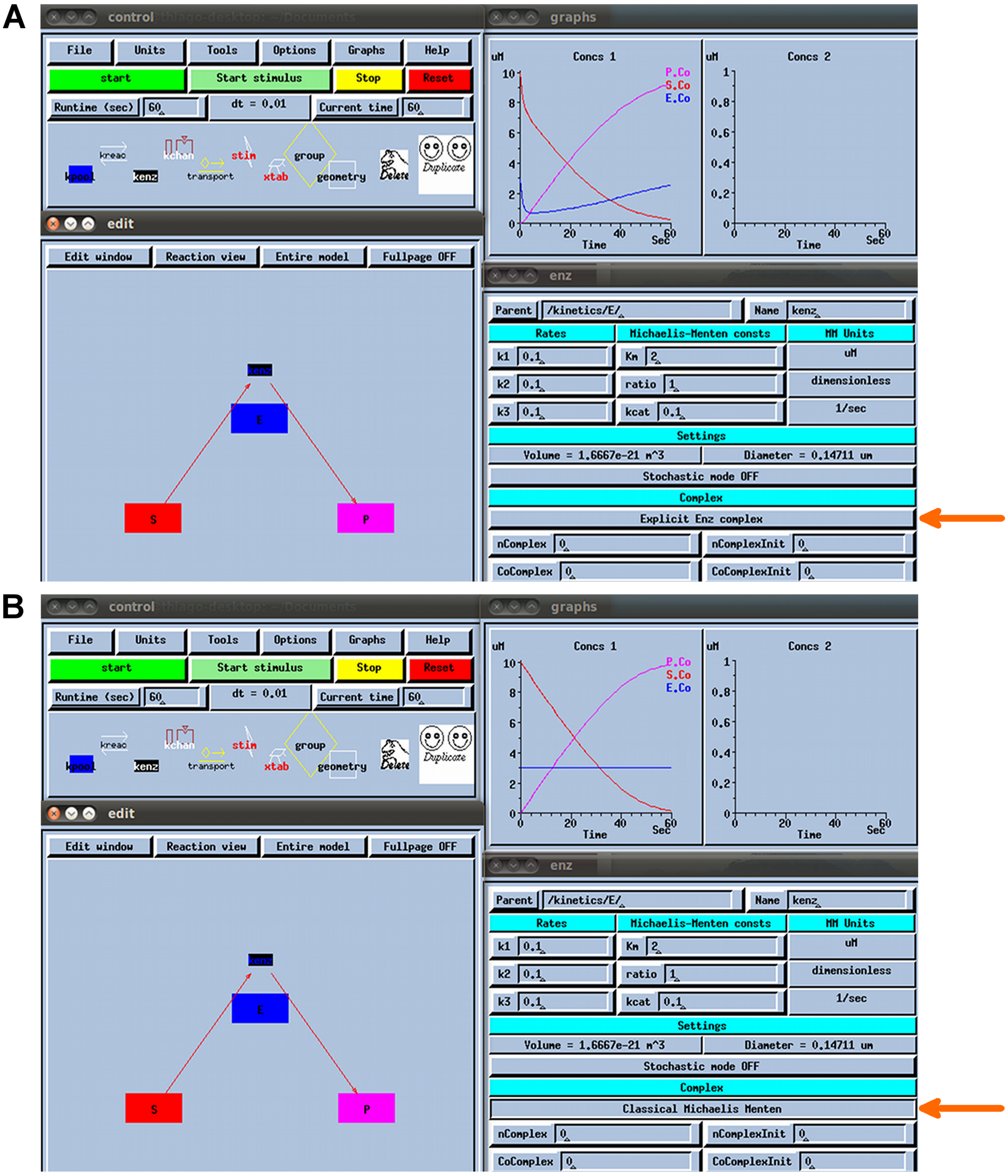

A.

Runtime (sec) 60
dt = 0.01
Current time 60

Parent /kinetics/E/
Name kenz
k1 0.1
Km 2
uM
k2 0.1
ratio 1
dimensionless
k3 0.1
kcat 0.1
1/sec
Volume = 1.6667e-21 m^3
Diameter = 0.14711 um
Stochastic mode OFF
Explicit Enz complex
nComplex 0
nComplexInit 0
CoComplex 0
CoComplexInit 0

B.

Runtime (sec) 60
dt = 0.01
Current time 60

Parent /kinetics/E/
Name kenz
k1 0.1
Km 2
uM
k2 0.1
ratio 1
dimensionless
k3 0.1
kcat 0.1
1/sec
Volume = 1.6667e-21 m^3
Diameter = 0.14711 um
Stochastic mode OFF
Classical Michaelis Menten
nComplex 0
nComplexInit 0
CoComplex 0
CoComplexInit 0

Figure 4.5: **GENESIS/kinetikit simulation of enzyme kinetics.** These panels illustrate the graphical interface of GENESIS/kinetikit after simulating the kinetics of enzymatic Reaction 4.6, using the explicit *ES* complex kinetics (**A**) and the Michaelis-Menten kinetics (**B**). In such a case, both kinetic models are identical in GENESIS/kinetikit. However, a single button is responsible for switching the reaction modelling approach (orange arrows). **A.** *Explicit Enz complex* indicates that the simulated enzymatic reaction is modelled by explicit *ES* complex kinetics (Section 4.1.2.1). This kinetic simulation replicates the results shown in Figure 4.2 (see graph in *Concs 1*). **B.** After pressing the button highlighted in **A**, *Classical Michaelis Menten* shows that the Michaelis-Menten model is adopted for enzyme-catalysed reactions (Section 4.1.2.2).

```
init E=3 S=10

parameters kf=0.1 kb=0.1 kcat=0.1

dE/dt=-kf*E*S+(kb+kcat)*ES

dS/dt=-kf*E*S+kb*ES

dES/dt=kf*E*S-(kb+kcat)*ES

dP/dt=kcat*ES

@ Total=60 dt=0.01 meth=euler, xlo=0 xhi=60 \
ylo=0 yhi=10 maxstor=10000 BACK=white

done
```

Figure 4.6: **XPPAUT source code for the simulation of enzyme kinetics.** This XPPAUT code simulates the kinetics of enzyme-catalysed Reaction 4.6, using the explicit *ES* complex kinetics (Section 4.1.2.1). This is the source code that generates the results shown in Figure 4.2. The initial concentrations of compounds are presented after *init*. The command *parameters* initiates the definition of rate constants. Following on from this, the ODEs that represent Equations 4.7, 4.8, 4.9 and 4.10 are listed. *Total* indicates the total time of the simulation, *dt* is the simulation step size, and *meth* presents the numerical method adopted. Commands *xlo*, *xhi*, *ylo* and *yhi* denote the axis limits on graphs, *maxstor* indicates the maximum number of stored data points, and *BACK* defines the background colour of generated graphs. The source code is finalised with *done*.

4.3 Chapter Conclusions

Computational modelling of signalling pathways is an important tool to study the biological mechanisms that regulate cellular functions. These models simulate aspects of entire signalling networks and do not only focus on the behaviour of isolated components, as in many experiments.

This chapter summarised the theory adopted for the development of all signalling models presented in this thesis. Signal transduction processes involve many biochemical reactions, and ODEs can express how the concentration of reaction substances evolves over time. For instance, the Law of Mass Action presented here is the basis for simulating velocities of all types of biochemical reactions.

Enzymes act in particular biochemical transformations and play an important role in many cell signalling processes. Based on the Law of Mass Action, velocities of enzymatic reactions may be modelled by either the explicit ES kinetics that simulates concentration variations of enzyme-substrate complexes, or the Michaelis-Menten kinetics which assumes that the concentrations of enzymes and enzyme-substrate complexes are unchangeable. Despite of the fact that the Michaelis-Menten approach is widely adopted for simulating enzyme kinetics, the explicit ES modelling is used to simulate all enzymatic reactions in the thesis. However, the Michaelis-Menten kinetics is crucial to understanding a few aspects of the original implementation of the signalling model [Kuroda 2001] analysed in Chapter 5.

Concepts underlying the thermodynamics of biochemical reactions were also summarised here. Chapter 7 presents a kinetic model whose reactions may form multiple pathways from one compound to another. In such a case, it is important to ensure that the kinetic constants involved in those reactions do not alter the equilibrium of the biological system. Equation 4.26 was crucial to determine values for the assumed rate constants which participate in reactions that form thermodynamic cycles.

Furthermore, two computational tools were adopted for simulating the mathematical modelling of intracellular signalling presented in this chapter: GENESIS/kinetikit and XPPAUT. Simulations with GENESIS/kinetikit were used to study the original implementation of the existing model presented in Chapter 5. However, all models developed in this thesis were implemented in XPPAUT.

To build the first kinetic model of signalling pathways that regulate the induction of long-term depression (LTD) and long-term potentiation (LTP) in cerebellar Purkinje cells including calcium-calmodulin dependent protein kinase II (CaMKII), the rest of the thesis begins with an exploration of a widely-known cerebellar LTD model [Kuroda 2001]. In the next chapter, a reimplementation of this kinetic simulation is proposed, and various discrepancies in its original implementation are unravelled.

CHAPTER 5

Reimplementation of Cerebellar LTD Models

Contents

PREVIOUS chapters have described experimental observations that indicate the importance of calcium-calmodulin dependent protein kinase II (CaMKII) for cerebellar plasticity. However, the exact role of CaMKII in the signalling cascades underlying plasticity induction is yet to be unravelled. A kinetic model that simulates the induction of long-term depression (LTD) and long-term potentiation (LTP) is crucial to investigate how CaMKII regulates bidirectional plasticity in cerebellar Purkinje cells. Interestingly, although many molecules have been characterised in the signal transduction network that underlies cerebellar plasticity, CaMKII has not been included in previous models of these signalling pathways.

My initial intention was to incorporate CaMKII into a commonly used model of signalling in cerebellar LTD [Kuroda 2001]. A reimplementation of the Kuroda model is therefore proposed in this chapter. The main results obtained by Kuroda and collaborators are briefly summarised in the following section. The second section of the chapter presents a study of the original implementation of the Kuroda model in GENESIS/kinetikit, and demonstrates the replication of its results in XPPAUT. Various inconsistencies were identified in their original implementation. The last section summarises the corrections for all these discrepancies, and describes the adjustments in kinetic parameters that were needed to eventually reproduce the results in [Kuroda 2001].

5.1 Results of the Study by Kuroda and Collaborators

At excitatory synapses in the hippocampus, LTD induction requires the activation of protein phosphatases, whereas LTP depends on the activation of kinases [Din 2010, Henley 2011]. In contrast, at cerebellar parallel fibre (PF) synapses onto Purkinje cells, kinases are required for LTD induction, whereas protein phosphatases are required for LTP induction.

Kuroda et al (2001) developed a model for the phosphorylation and dephosphorylation of AMPA receptors based on the activation of protein kinase C (PKC) and the inhibition of protein phosphatase 2A (PP2A) (Figure 5.1). The molecular mechanisms that are represented by this kinetic model were described in detail in Section 2.5.

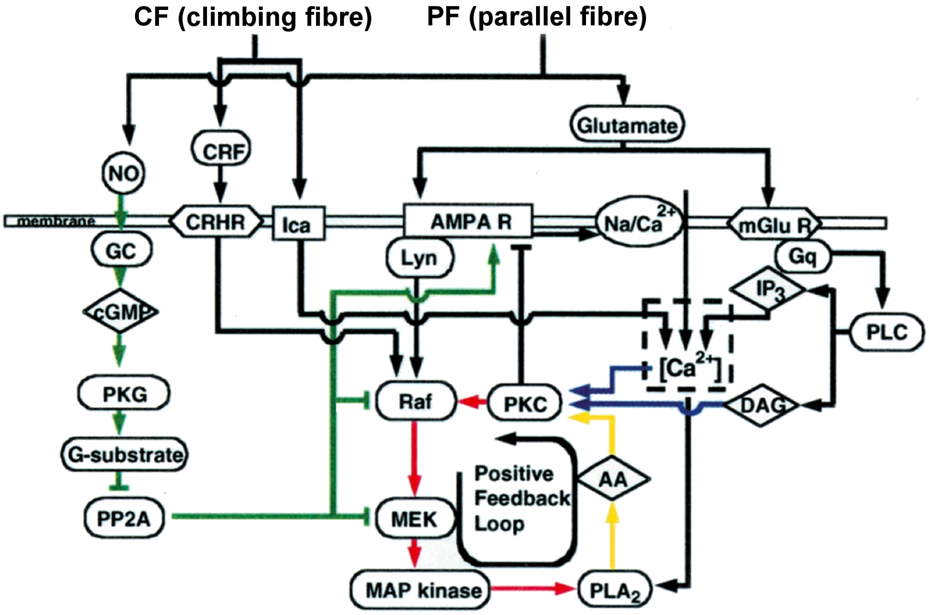

Figure 5.1: **Signalling pathways underlying cerebellar LTD.** The respective phosphorylation and dephosphorylation of AMPA receptors are mediated by PKC and PP2A. Adapted from [Kuroda 2001].

According to the results in [Kuroda 2001], the phosphorylation of AMPA receptors in cerebellar LTD occurs in three phases: an initial peak, an intermediate phase, and a late stage (Figure 5.2A). The paired activation of PF and climbing fibre (CF) for 5 min evoked increases in the concentration of phosphorylated AMPA receptors that are caused by the activation of PKC.

The time course of PKC activation also consists of three stages that result from the following molecular mechanisms: (i) the activation of PKC by calcium, arachidonic acid (AA) and diacylglycerol (DAG) that leads to its initial peak, (ii) the activation of the positive feedback loop mediated by mitogen-activated protein (MAP) kinase that determines the intermediate phase of PKC activation, and (iii) a late stage caused by the inactivation of PKC activity (Figure 5.2B).

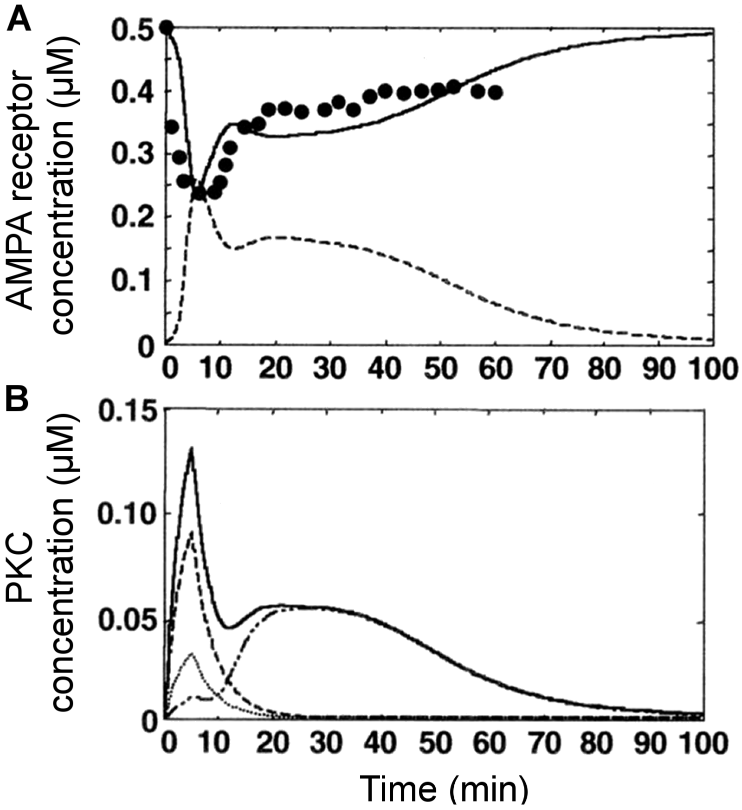

Figure 5.2: **Phosphorylation of AMPA receptors in cerebellar LTD induction.** Temporal evolution of the concentrations of biochemical species in response to paired activation of PF and CF at 1 Hz for 5 min. **A.** Concentrations of unphosphorylated and phosphorylated AMPA receptors (solid and dashed, respectively). **B.** Concentrations of complexes of PKC that express its activity: total PKC activity (solid), calcium-activated PKC (dashed), DAG-activated PKC (dotted), and AA-activated PKC (dashed-dotted). Adapted from [Kuroda 2001].

The cerebellar LTD model in [Kuroda 2001] was originally implemented in GENESIS/kinetikit. However, this simulation tool does not provide easy options to visualise the underlying ordinary differential equations (ODEs), to edit them by hand, or to analyse the behaviour of the signalling network using dynamical systems techniques. It was therefore decided to reimplement the Kuroda model in XPPAUT; this reimplementation is described in the following section.

5.2 Reimplementation of Kuroda Model

The original code of the Kuroda model in GENESIS/kinetikit was not available online. However, it was possible to obtain a version of the original implementation from Kuroda's collaborators. This code produced very similar results as in

[Kuroda 2001] and facilitated the analysis and understanding of many details of the model implementation.

The Kuroda model was reimplemented from scratch by coding the ODEs that represent the kinetics involved in the LTD signalling in XPPAUT to numerically solve these equations. The development of this new implementation was based on the GENESIS/kinetikit code obtained, and on the supplementary information in [Kuroda 2001] which gives details for signalling pathways and kinetic parameters. The reimplementation of the Kuroda model in XPPAUT is called the *Pinto implementation*, while the original code of the model in GENESIS/kinetikit is referred to as the *Kuroda implementation*.

The results for the phosphorylation of AMPA receptors obtained from both implementations initially did not match (data not shown). Therefore, the Kuroda and Pinto implementations were debugged using a *bottom-up approach*, that is, results were compared starting from simple reactions and moving on to larger signalling cascades. This investigation unveiled many issues in the Kuroda implementation. The following sections describe the discrepancies found in the original code and eventually present the replication of the Kuroda model.

5.2.1 Interpolation of Input Tables

Temporal waveforms representing concentrations of calcium, nitric oxide (NO) and glutamate were adopted as input stimuli to the model in [Kuroda 2001]. These concentration values were based on experimental observations. However, the initial phase of the calcium and NO stimulations showed spurious concentration peaks (Figure 5.3). Because these peaks did not correspond to the actual stimuli shown in Figure 6 of [Kuroda 2001], the calcium and NO inputs were adjusted in this thesis. These corrections caused no alteration to the LTD results.

A further investigation of the input tables in the Kuroda implementation revealed that the data points of the Kuroda tables were not interpolated during the simulation (Figure 5.3). *Interpolation* is an important method for creating new data points between the values provided in the tables. Therefore, linear interpolation was applied to the calcium, NO and glutamate tables in the Kuroda implementation. Following suggestions from the creator of *kinetikit*, Upi Bhalla, the command line *table−>calc_mode 1* was added to the GENESIS/kinetikit code to activate the linear interpolation.

These modifications slightly affected the original results obtained from the Kuroda implementation (Figure 5.4). However, these small changes in concentration levels of AMPA receptors during the intermediate phase were considered unimportant as the same qualitative LTD behaviour was achieved. The precise concentration of AMPA receptors over time in cerebellar LTD is not known. All further simulations were compared to the results obtained from the interpolated Kuroda implementation.

After having set all input values to the model, its biochemical reactions were incrementally simulated in both the Kuroda and Pinto implementations. New issues arose that were related to the modelling of enzyme kinetics.

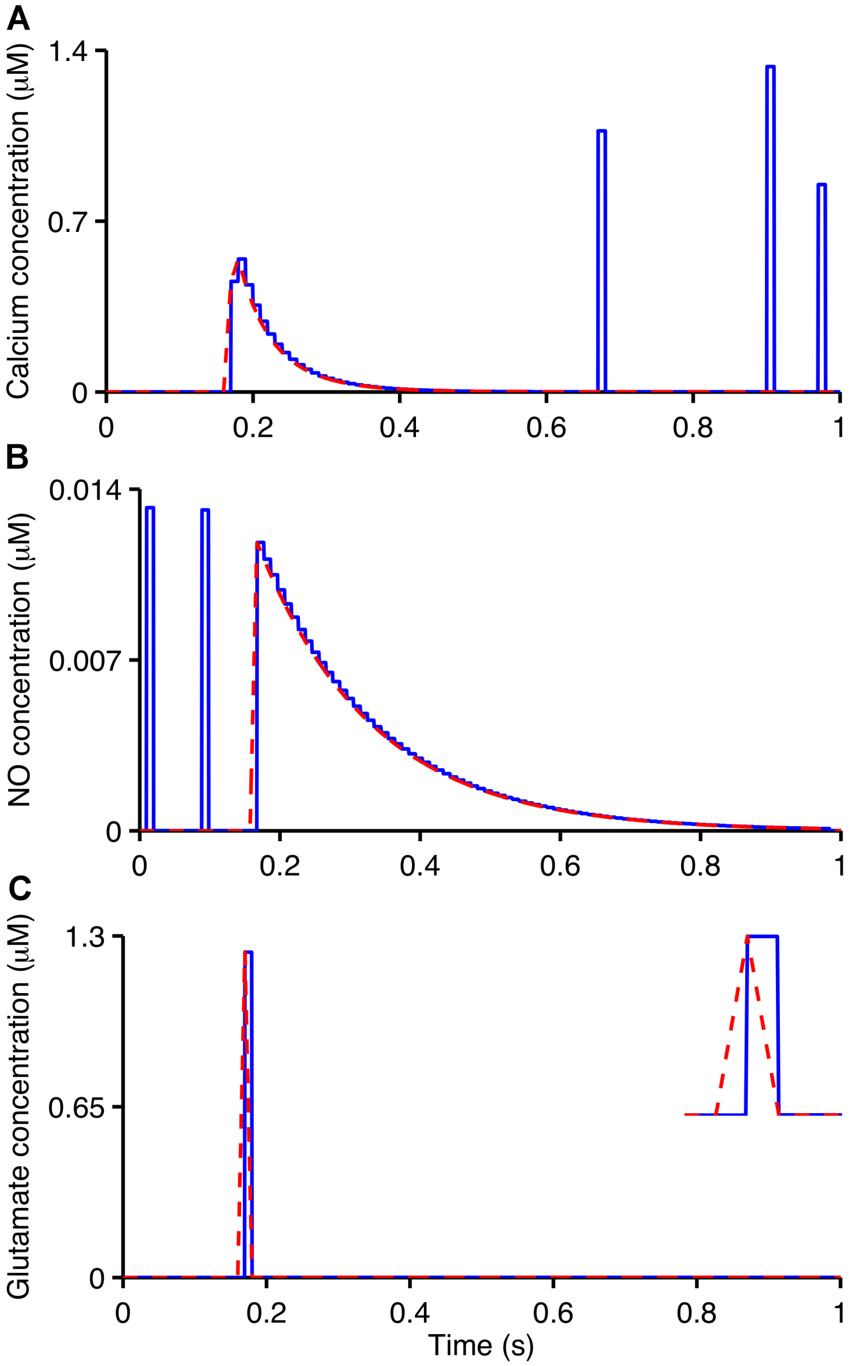

Figure 5.3: **Correction of inputs to the Kuroda model.** Stimuli of calcium (**A**), NO (**B**) and glutamate (**C**) at 1 Hz for 5 min were used as inputs to the Kuroda model [Kuroda 2001]. The new input tables (red) correct the spurious concentration peaks in the calcium and NO stimuli, and implement the linear interpolation in the original tables from the Kuroda implementation (blue). **Inset.** Larger view of a glutamate concentration peak that highlights the non-interpolated (blue) and interpolated stimuli (red). All curves were integrated and plotted using a 5×10^{-4} s time step.

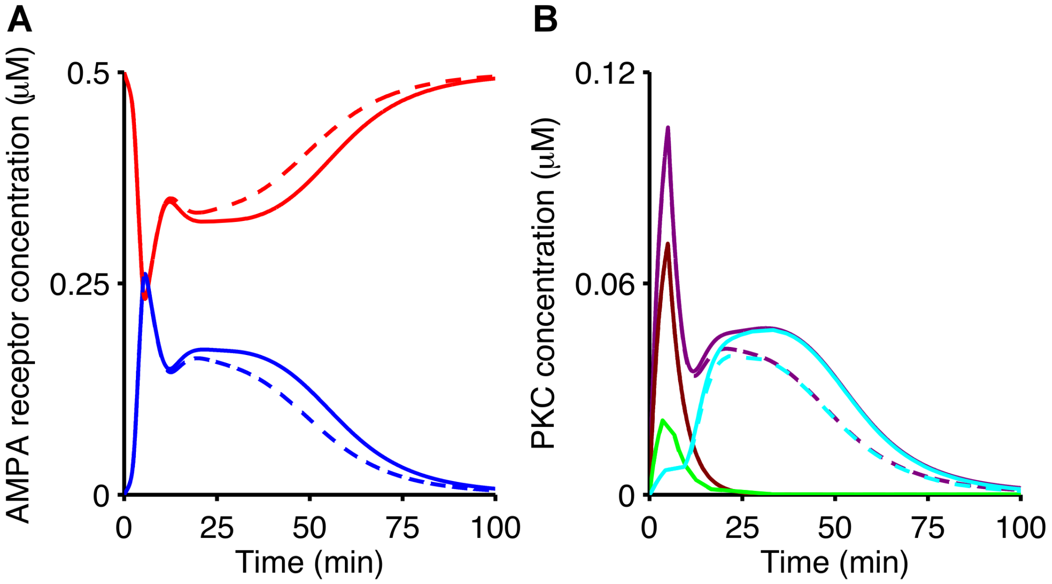

Figure 5.4: **Effect of linear interpolation in the Kuroda implementation.** Time-evolution of the phosphorylation of AMPA receptors (**A**) and the activation of PKC (**B**) obtained from the Kuroda implementation that replicates Figure 5.2 [Kuroda 2001]. Here, the GENESIS/kinetikit simulation responds to the calcium, NO and glutamate input tables in two distinct conditions: originally non-interpolated (solid) and interpolated (dashed). **A.** Unphosphorylated and phosphorylated AMPA receptors (red and blue, respectively). **B.** Active forms of PKC: total PKC activity (purple), calcium-activated PKC (brown), DAG-activated PKC (green), and AA-activated PKC (cyan).

5.2.2 Kinetics of Enzymatic Reactions

According to Kuroda and co-authors (2001), all enzymatic reactions in their model were described by Michaelis-Menten kinetics. However, results from the Kuroda and Pinto implementations differed when enzymatic reactions were included (Figure 5.5A). A detailed analysis of the Kuroda implementation unveiled that the actual concentration of enzyme-substrate (ES) complexes varied during model simulations. This suggested that the ES species were expressed by ODEs in their model and that enzymatic reactions were not modelled according to Michaelis-Menten principles.

The GENESIS/kinetikit interface for Kuroda's enzymatic reactions revealed that the button that allows users to switch from the explicit ES complex modelling to the Michaelis-Menten kinetics was not pressed (example in Figure 4.5). This demonstrated that none of the reactions in the Kuroda implementation were modelled as Michaelis-Menten equations, even though [Kuroda 2001] states they are. The Pinto implementation was therefore modified and enzymatic reactions were represented by explicit ES kinetics. These alterations led to identical results for both implementations (Figure 5.5B).

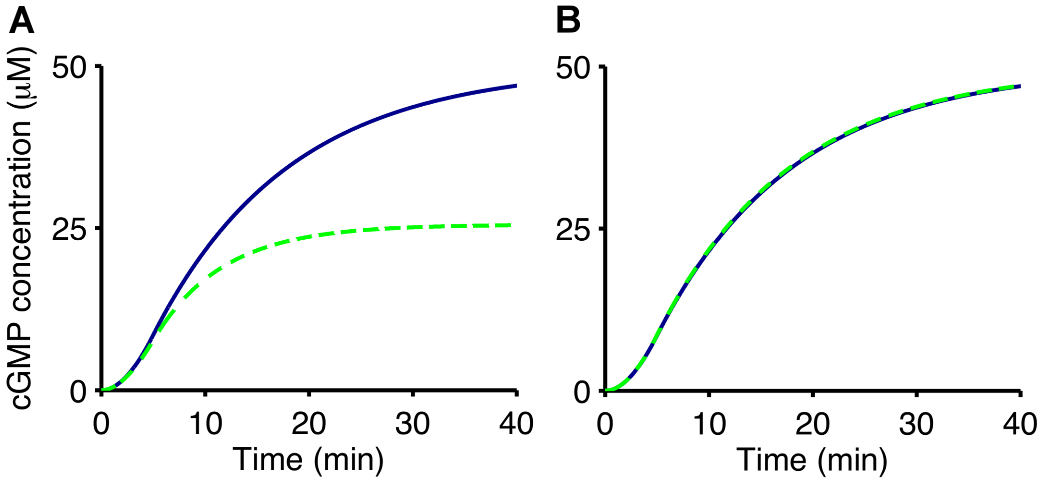

Figure 5.5: **Enzymatic reactions are not modelled by Michaelis-Menten kinetics in [Kuroda 2001].** The Kuroda and Pinto implementations simulate the kinetics of the enzymatic reaction that produces cyclic guanosine monophosphate (cGMP). **A.** The Pinto implementation initially modelled enzymatic reactions using Michaelis-Menten kinetics, as stated in [Kuroda 2001] (dashed). However, results from the original Kuroda implementation suggest that these reactions are modelled by explicit ES complex kinetics (solid). **B.** After modifying the Pinto implementation to use kinetics of explicit ES complexes, both implementations demonstrate identical results. This figure simulates Reactions A.37 and A.39.

The original speed of catalysis for a few enzymatic reactions also provoked discrepancies between the results from both implementations (Figure 5.6). These rate constants were set to zero in the Pinto implementation to replicate the results in [Kuroda 2001] (Appendix B.1).

Still, the ODE for the enzymatic activity of PKC in the phosphorylation of Raf and AMPA receptors was not included in the new implementation at this stage. The kinetics of these reactions resulted in a PKC activity slightly different from the original study (data not shown).

While several errors in the Kuroda implementation did not affect the outcome of the simulations to a significant extent, more substantial problems were identified in the signalling network modelling.

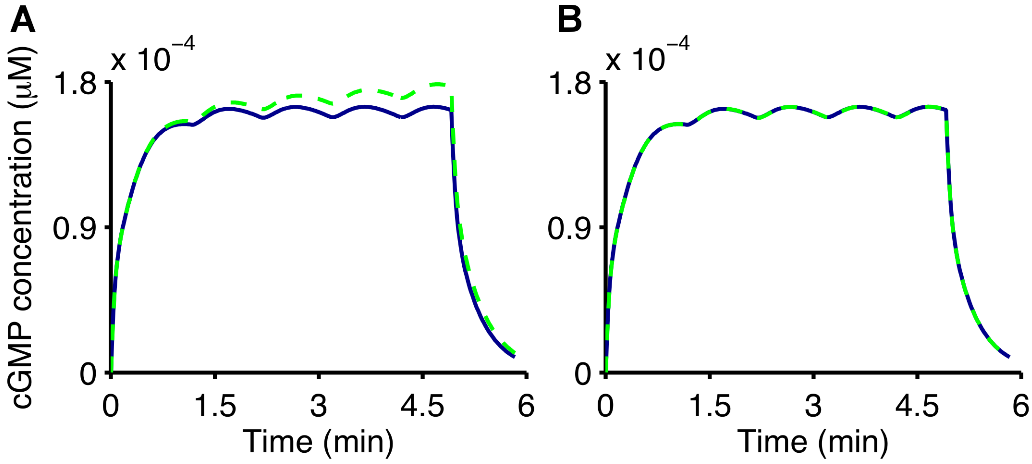

Figure 5.6: **Catalytic rate constants lead to inconsistencies in the Pinto implementation. A.** The adoption of original parameter values for a few catalytic rate constants causes different results between the Kuroda and Pinto implementations (solid and dashed, respectively). **B.** Results from both simulations are identical after setting these kinetic parameters to zero in the Pinto implementation. The figure illustrates the temporal evolution of cGMP when modelling Reactions A.37-A.41. The original catalytic rate constant for Reaction A.40 in the Pinto implementation in **A** is $k_{cat_{40}} = 3.87$ s^{-1}, while $k_{cat_{40}} = 0$ in **B**.

5.2.3 Significant Errors

All molecules of the LTD model analysed here reside in a single compartment [Kuroda 2001]. This means that all species should be implemented in a spherical volume with the same diameter. However, for some reason, MAP kinase, MAP kinase phosphatase-1 (MKP_1) and phosphorylated Raf had been assigned to a smaller compartment that differs from the other compounds (diameter 0.10839 μm rather than 0.14711 μm). Differences in the diameter of compartments influence the concentrations of the substances and, in turn, the reaction rates in the Kuroda implementation. As a result, the MAP kinase, MKP_1 and phosphorylated Raf reactions were about 25% slower than the other reactions involved in the signalling network. The Pinto implementation was therefore modified to reproduce these errors and replicate the results in [Kuroda 2001]. All rate constants in the ODEs for these compounds were multiplied by 2.5, and their concentration values were then multiplied by 0.4. Based on this correction, MAP kinase, MKP_1 and phosphorylated Raf had the same concentrations as in the Kuroda implementation.

In addition to this significant error, a spare arrow from phosphorylated cytosolic phospholipase A_2 (PLA_2P) to its enzymatic reaction was found in Kuroda's code. The detection of this error was not trivial because this arrow was hidden in the original implementation (Figure 5.7). This inconsistency created two instances of

$\mathrm{PLA_2P}$ rather than one in Reaction A.25

$$2\,\mathrm{PLA_2P} + \mathrm{APC} \rightleftharpoons \mathrm{PLA_2P\_APC} \longrightarrow \mathrm{PLA_2P} + \mathrm{AA}\ .$$

Although modelling two phosphorylated $\mathrm{PLA_2}$ enzymes makes no sense, the Pinto implementation still accounts for this discrepancy to replicate the results in [Kuroda 2001].

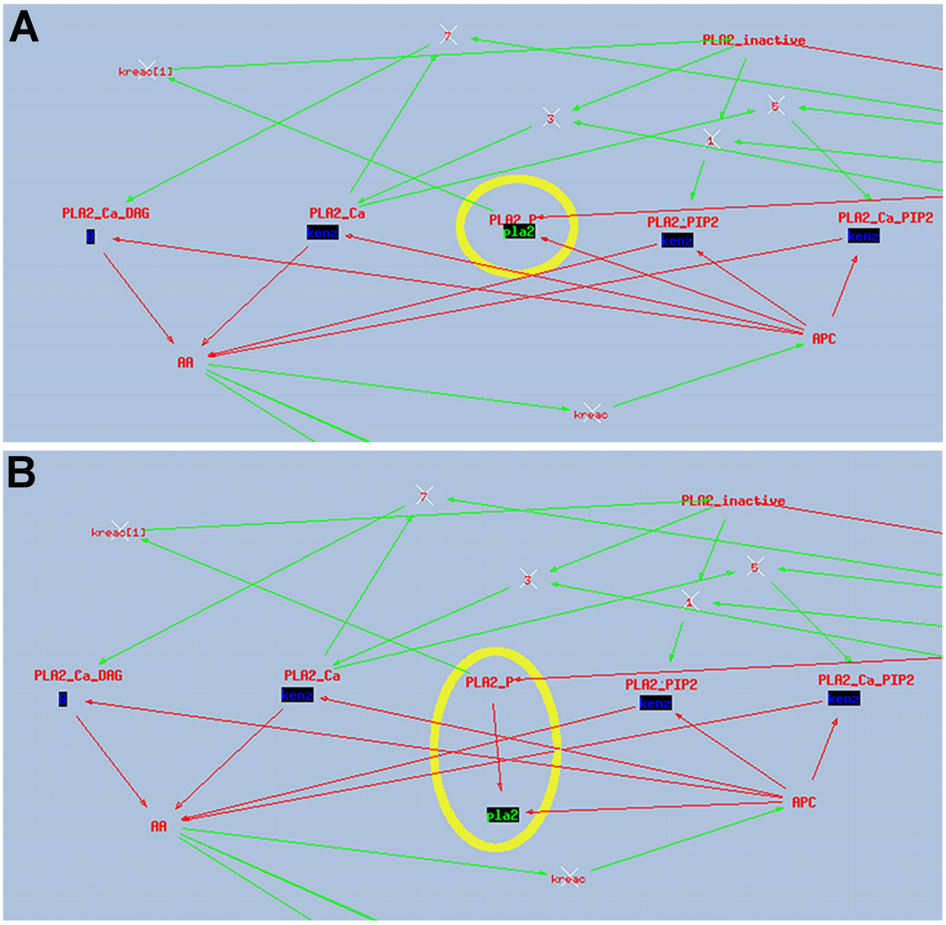

Figure 5.7: **A spare arrow is unveiled in the Kuroda implementation.** This figure illustrates part of the visual interface of the Kuroda implementation. **A.** The yellow ellipse highlights the $\mathrm{PLA_2}$ enzymatic Reaction A.25. **B.** An arrow that points from phosphorylated $\mathrm{PLA_2}$ to this enzymatic reaction was hidden in the Kuroda implementation. The spare arrow is unveiled after dragging the $\mathrm{PLA_2}$ reaction button.

The Kuroda model comprises a few reactions whose compounds bind to the cell membrane (Reactions A.32-A.35). The speed of formation of these reactions is much faster than those of the biochemical reactions of the entire model. Due to these larger parameter values, the integration of ODEs in the Pinto implementation crashed as soon as the simulation was started. This problem occurred as a consequence of an unsuccessful integration of the Euler numerical method which was originally used. To solve the problem in the numerical integration, the CVODE numerical method was adopted. This method is provided by the XPPAUT analytical tool, and uses a variable time step size. CVODE was chosen here based on a suggestion of the XPPAUT creator, Bard Ermentrout.

The results from the original implementation of the Kuroda model were eventually replicated in XPPAUT (Figure 5.8). At this stage, the Pinto implementation included the errors encountered in the Kuroda implementation to reproduce the model in [Kuroda 2001] (Appendices B.1 and B.2). Various inconsistencies were also detected in the supplementary information of the paper by Kuroda and coauthors ([Kuroda 2001]; Appendix B.3). The biochemical reactions, ODEs, initial concentrations and kinetic constants of the Pinto implementation that reproduces the original results in [Kuroda 2001] are described in Appendix A.

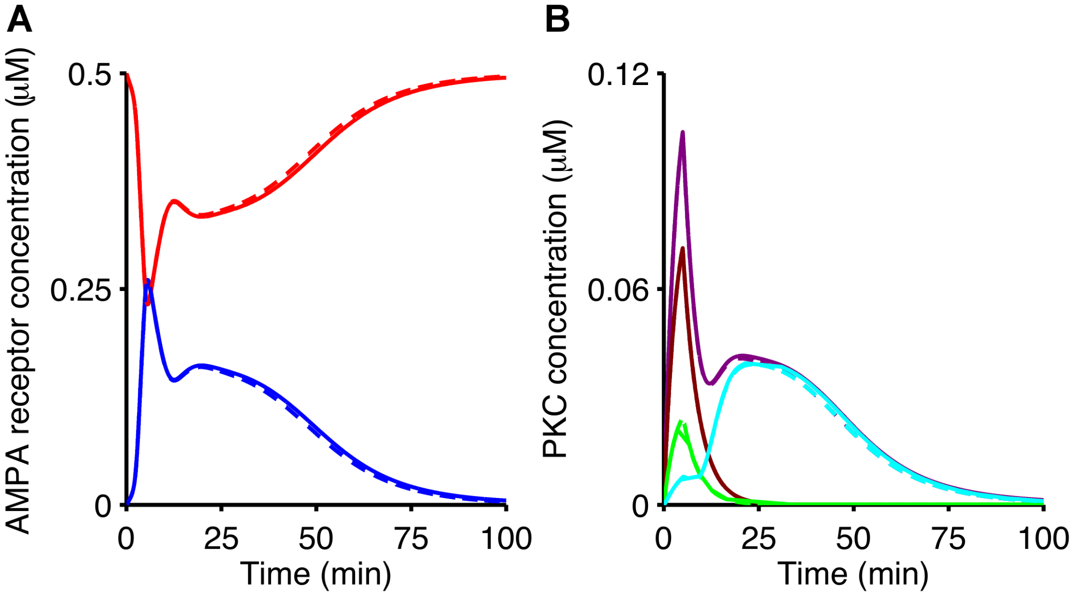

Figure 5.8: **Replication of [Kuroda 2001] in the Pinto implementation.** Simulation results from the Pinto implementation (dashed) reproduce the phosphorylation of AMPA receptors in [Kuroda 2001] obtained from the interpolated version of the Kuroda implementation (solid). Here, the Pinto implementation mimics the errors encountered in Kuroda's code. **A.** Time-evolution of unphosphorylated and phosphorylated AMPA receptors (red and blue, respectively). **B.** The active forms of PKC over time: total PKC activity (purple), calcium-activated PKC (brown), DAG-activated PKC (green), and AA-activated PKC (cyan).

Although the Pinto implementation replicated the Kuroda model, it mimicked several issues identified in the original implementation. The following section describes how these errors were corrected in the Pinto implementation, while still producing very similar results to those published in [Kuroda 2001].

5.3 Correction of Errors from the Original Implementation

The discrepancies that had been included in the Pinto implementation to replicate the LTD model were eventually corrected as follows (Appendix B.4)

1. All kinetic constants that had been set to zero were replaced according to the original parameter values published in [Kuroda 2001];
2. The ODE that models changes in the PKC concentration resulting from its enzymatic activity in the phosphorylation of Raf and AMPA receptors was included in the XPPAUT code;
3. Phosphorylated PLA_2 was implemented as a single instance in its enzymatic reaction rather than two;
4. The concentrations of MAP kinase, MKP_1 and phosphorylated Raf were readjusted to simulate all compounds within the same volume.

The results from the Pinto implementation after correcting these errors initially did not match those published in [Kuroda 2001] (Figure 5.9A). The reduction of the stoichiometry of phosphorylated PLA_2 from 2 to 1 caused an increase in the production of AA. Therefore, higher amounts of AA mediated a greater activation of PKC during the intermediate phase which, in turn, led to alterations in the phosphorylation of AMPA receptors. To compensate the loss of the duplicated phosphorylated PLA_2, the speed of PLA_2 dephosphorylation was nearly doubled (0.39 s^{-1} rather than 0.17 s^{-1} as in the original research). This modification led to similar results as in [Kuroda 2001] (Figure 5.9B).

Although Kuroda et al state that the concentration levels of calcium in their model were based on experimental observations in [Wang 2000], their calcium concentration peaks did not correspond to the results shown in the experimental paper. Furthermore, the actual basal calcium concentration between pulses is not zero as in their input tables (Figure 5.3). The following section gives the details for correcting the calcium stimulus, and describes the new adjustments in kinetic constants for the final replication of the results in [Kuroda 2001].

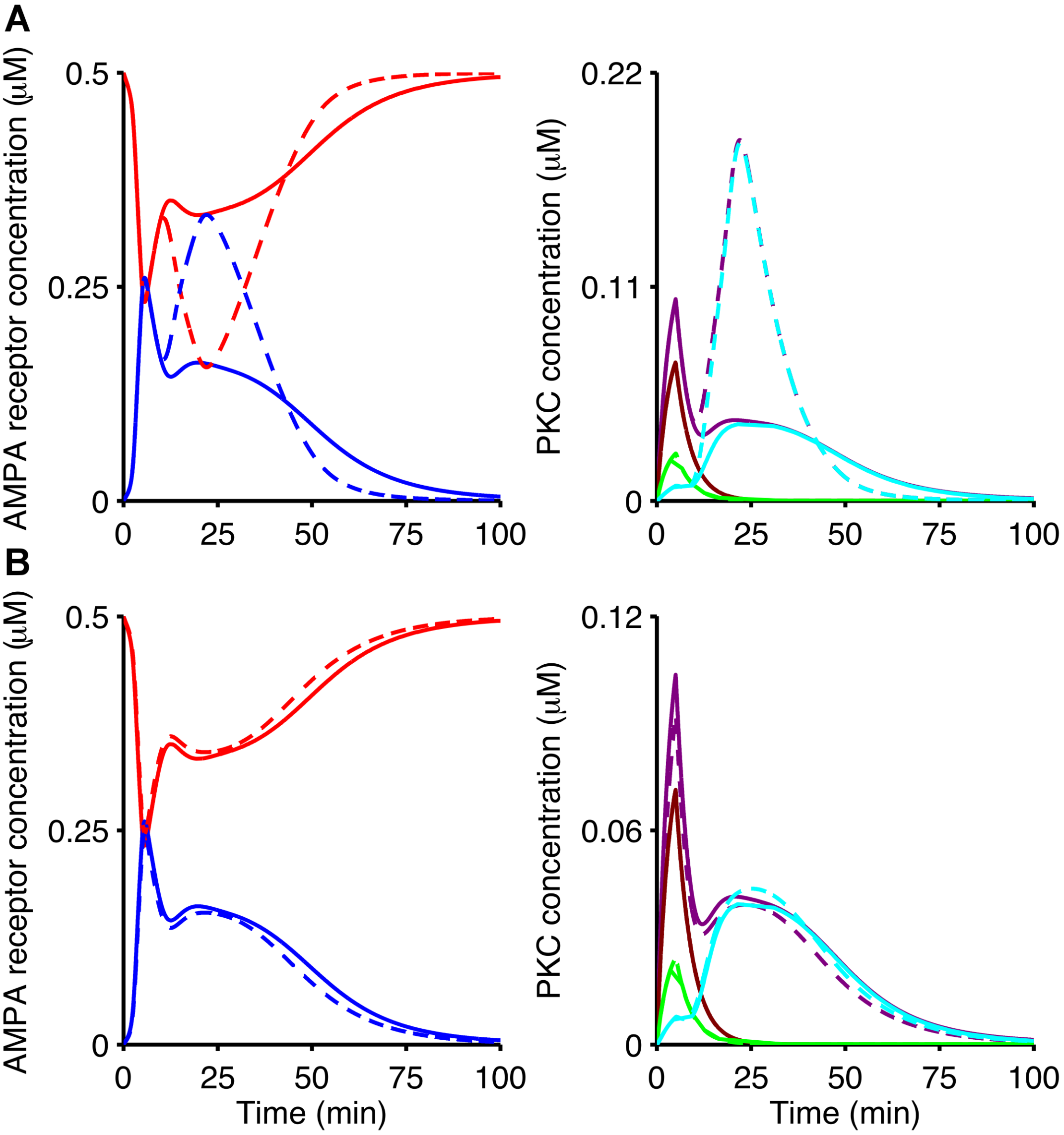

Figure 5.9: **Effect of the correction of errors from the Kuroda implementation.** Temporal evolution of unphosphorylated and phosphorylated AMPA receptors (red and blue, respectively) and active forms of PKC: total PKC activity (purple), calcium-activated PKC (brown), DAG-activated PKC (green), and AA-activated PKC (cyan). **A.** All errors from Kuroda's code (solid) were corrected in the Pinto implementation (dashed). The correction of errors provoked concentration increases of active PKC and phosphorylated AMPA receptors in the intermediate phases. **B.** The rate of PLA_2 dephosphorylation was then increased to compensate the removal of the spare arrow illustrated in Figure 5.7. This alteration led to the replication of [Kuroda 2001].

5.3.1 Adoption of New Calcium Levels

The basal concentration of calcium within Purkinje cells is about 0.1 μM, and its maximum concentration in response to the paired activation of PF and CF is nearly 10 μM [Wang 2000]. The sequence of calcium stimuli in the Pinto implementation was therefore adjusted according to these values (Figure 5.10). To this aim, the data in the original calcium table were transformed as follows

$$y_{new} = y_{old}\left(\frac{max - min}{max}\right) + min \ , \tag{5.1}$$

where y_{new} is the new data point in the calcium input table, y_{old} is the original data point in the Kuroda table, min denotes the basal calcium concentration, and max is the calcium concentration peak at each stimulus.

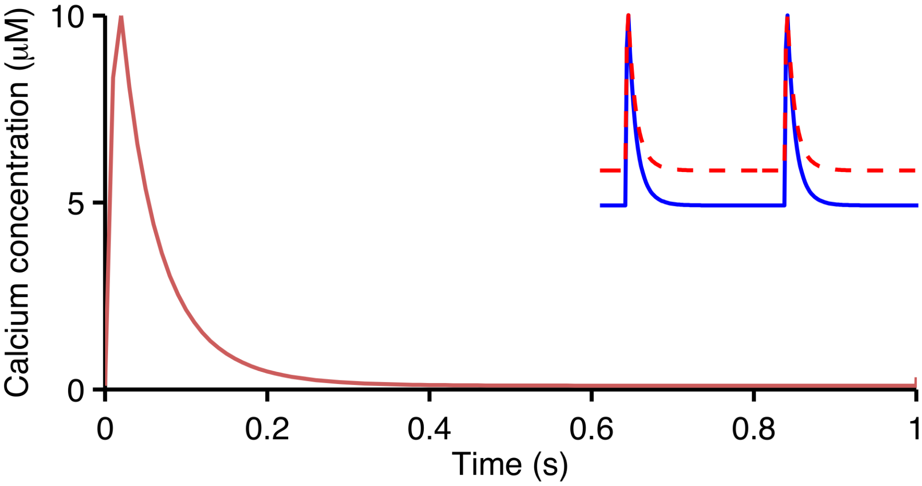

Figure 5.10: **Calcium stimulus transformation by changing the basal and maximum concentrations.** The new calcium input to the Kuroda model in response to coincident PF and CF activation comprises a resting concentration of 0.1 μM and a maximum amount of 10 μM for each pulse. The total calcium stimulation in the model lasts 5 min. **Inset.** Illustration of the calcium stimuli in the Pinto implementation (dashed) after adjusting only the basal concentration in the Kuroda implementation (solid).

The adoption of calcium levels that were 1,852% higher than in [Kuroda 2001] drastically increased the rate of calcium-activated reactions (Figure 5.11B). This resulted in a high initial peak for calcium-activated PKC and the disappearance of the LTD intermediate phase. The lack of an LTD intermediate phase was due to the fact that the high levels of calcium converted all available inactive PKC into calcium-activated PKC, so that the also increased production of AA by calcium-activated PLA$_2$ could not result in PKC activation during the LTD intermediate phase.

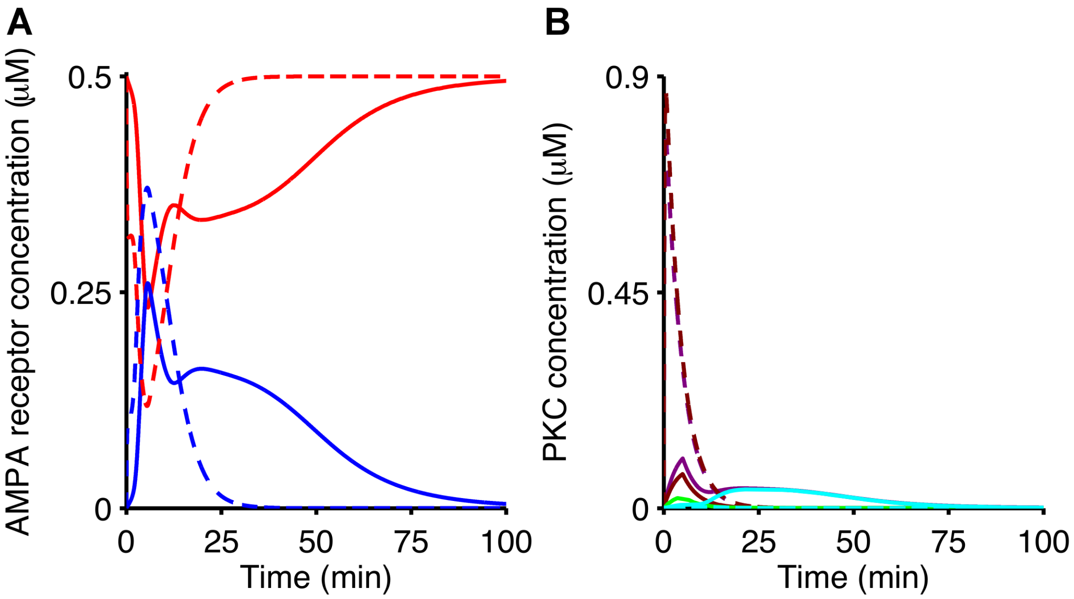

Figure 5.11: **Effect of the adoption of new calcium levels.** Comparison of the simulation results from the Kuroda and Pinto implementations (solid and dashed, respectively) after adopting the new calcium levels illustrated in Figure 5.10. **A.** Time course of unphosphorylated and phosphorylated AMPA receptors (red and blue, respectively). **B.** Temporal evolution of the active forms of PKC: total PKC activity (purple), calcium-activated PKC (brown), DAG-activated PKC (green), and AA-activated PKC (cyan).

To reproduce the results from the Kuroda model after modifying the calcium input table, a few rates of calcium-mediated reactions were adjusted. These include much slower rates of (i) production of AA via calcium-activated PLA_2, (ii) activation of PKC by calcium, and (iii) binding of calcium-activated PKC to the cell membrane. In addition to these, the velocity of PLA_2 dephosphorylation was again altered, demonstrating that this kinetic parameter is crucial for the Kuroda model. The dephosphorylation of PLA_2 affects the concentration levels of the AMPA receptors during the intermediate phase in [Kuroda 2001].

Similar results to those in [Kuroda 2001] were obtained after altering these reaction rates (Figure 5.12) (Appendix B.5). Although the same qualitative behaviours for the phosphorylation of AMPA receptors and the activation of PKC are obtained in the Pinto implementation as in the Kuroda one, the concentration levels of these compounds differ from those presented in [Kuroda 2001]. However, the true amounts of AMPA receptors and PKC within cerebellar Purkinje cells are unknown.

After debugging the Kuroda implementation, another GENESIS/kinetikit implementation was obtained that is mentioned in [Doi 2006]. This latest GENESIS/kinetikit version of the Kuroda LTD model was implemented by Tomokazu Doi, who is one of Kuroda's collaborators but not a co-author in [Kuroda 2001]. The Doi implementation is briefly examined in the next section.

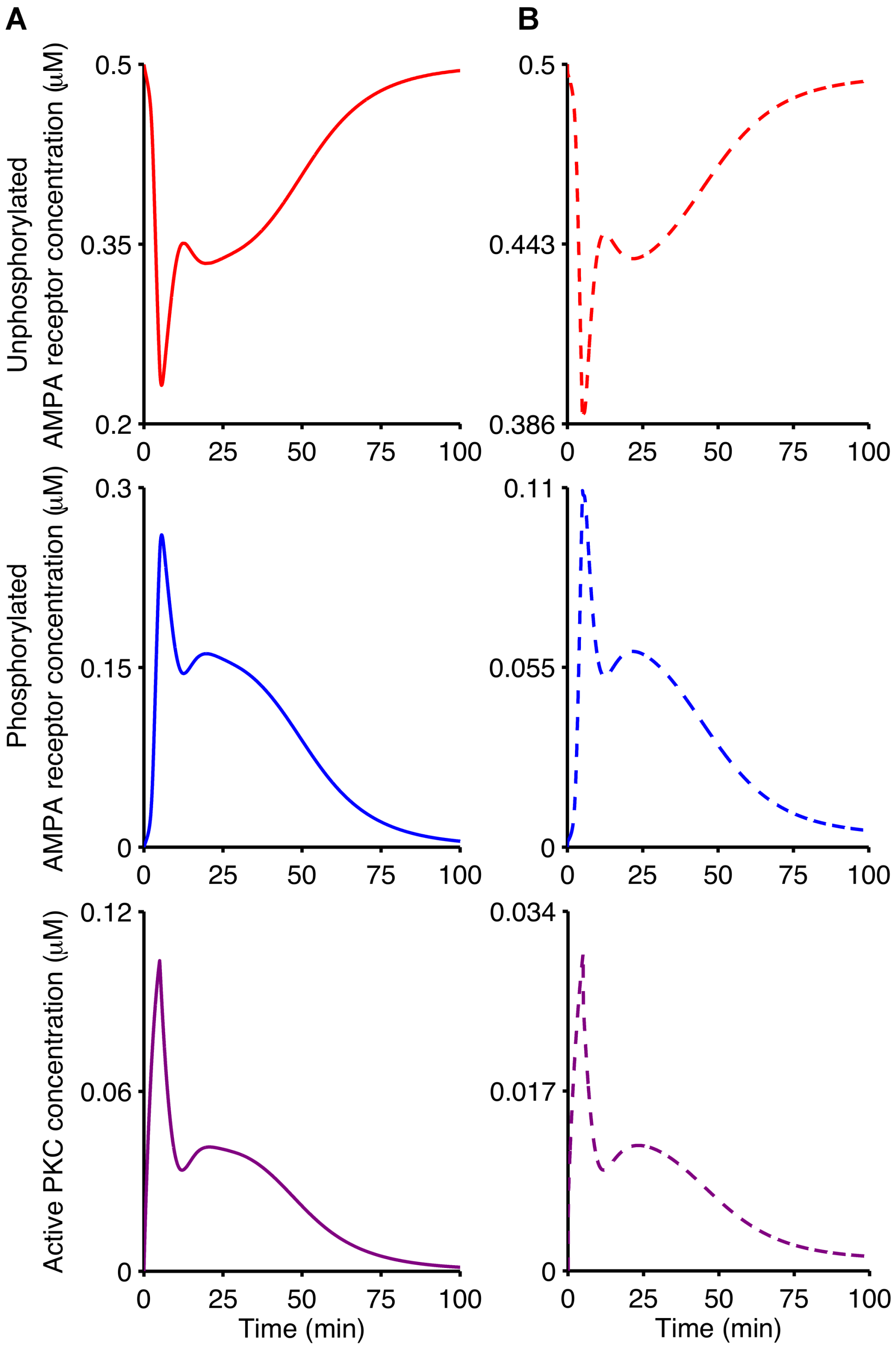

Figure 5.12: **Final replication of [Kuroda 2001] after adopting new calcium levels.** The Pinto implementation (**B**, dashed) qualitatively reproduces the results obtained from the Kuroda implementation (**A**, solid) after adjusting the calcium levels shown in Figure 5.10. Although the concentration levels of the unphosphorylated and phosphorylated AMPA receptors (red and blue, respectively) and active PKC (purple) differ in both implementations, their behaviours over time are similar.

5.3.2 Comparison with Doi Implementation

The Doi implementation [Doi 2006] proposes the correction of significant errors in the Kuroda implementation. Their GENESIS/kinetikit code uses a uniform volume for all compounds in the signalling network rather than different compartment volumes for MAP kinase, MKP_1 and phosphorylated Raf. It also corrects the spare arrow that creates two instances of phosphorylated PLA_2. However, the results from this implementation are slightly different from the published data in [Kuroda 2001].

The time step size of the Doi implementation is smaller than that of the Kuroda implementation and indeed corroborates the adoption of a smaller time step size to match Pinto's results (Appendix B.2). The arrow from glutamate to protein tyrosine kinase Lyn is now deleted. However, for some reason, a new Lyn stimulus was created and contains identical values as those in the glutamate stimulation.

Although the arrows from Ca_basal, Ca_pump, Ca_ext, Cachannel, and Ca_store were corrected in the Doi implementation, these still have no role in the model (Appendix B.2). The input tables are still not interpolated, and the calcium stimulus is identical to the original Kuroda table. Furthermore, a few values of kinetic constants are different from the original data published in [Kuroda 2001]. Similar results are obtained from the final implementations of Kuroda, Pinto and Doi (Figure 5.13).

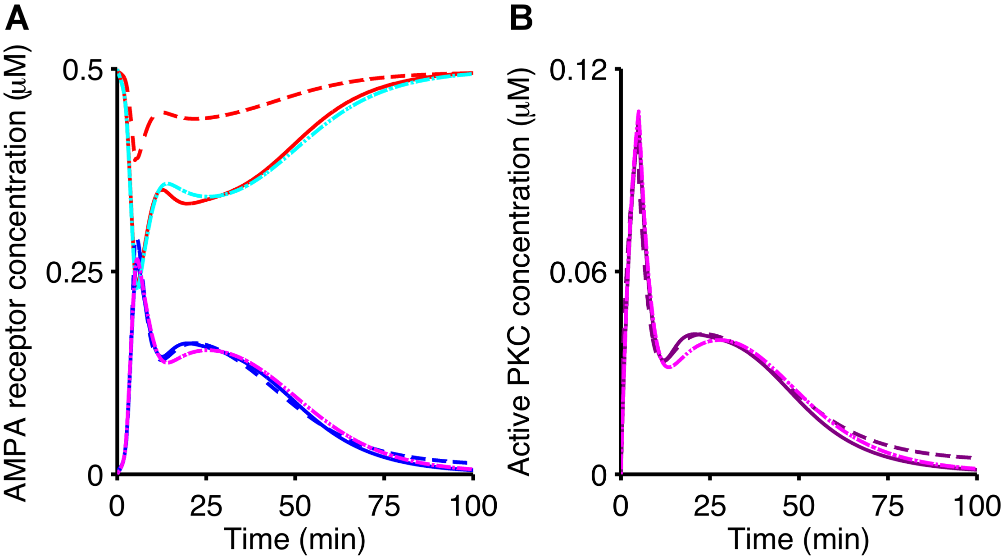

Figure 5.13: **Comparison of different implementations of the Kuroda model.** Results from the Doi implementation (dashed-dotted) are similar to those obtained from the interpolated Kuroda simulation (solid) and the final Pinto implementation (dashed). **A.** AMPA receptors in different states: unphosphorylated (red and cyan) and phosphorylated (blue and magenta). **B.** Total activity of PKC. The respective concentrations of phosphorylated AMPA receptors (dashed blue) and active PKC (dashed purple) in the Pinto implementation are multiplied by 2.7 and 3.5 to fit the results in [Kuroda 2001].

5.4 Chapter Conclusions

The biochemical model published in [Kuroda 2001] is an important kinetic simulation of the signalling processes underlying cerebellar LTD. It models a key step in the plasticity induction in Purkinje cells: the phosphorylation of AMPA receptors. This chapter demonstrated the processes involved in the replication of the Kuroda model. It described a new implementation of this model in a simulation tool different from that used in the original study. Kinetic models developed in XPPAUT provide an easier understanding of the mathematical processes involved in the reaction kinetics.

Several errors were identified in the GENESIS/kinetikit implementation described in [Kuroda 2001]. Some of these discrepancies such as the double instance of phosphorylated PLA_2 might have occurred due to the occasional instability of this kinetic tool. The drag-and-drop inclusion of reactions sometimes provokes the appearance of spurious arrows from species to reactions. Other issues in these models may also emerge given that the developer is not always aware of all features provided by GENESIS/kinetikit. This may be the case for the lack of interpolation in the input tables and for the adoption of a modelling approach for enzymatic reactions different from that stated in [Kuroda 2001]. The resources for implementing these features are not easily identified in this simulator. However, the modification of the cell diameter for some species in the Kuroda model was indeed included by the authors for an unknown reason.

The correction of the errors in the Kuroda implementation involved the adjustment of reaction rates to replicate the results in [Kuroda 2001]. Kuroda and collaborators have demonstrated that the dephosphorylation of PLA_2 regulates the LTD intermediate phase but does not affect its initial peak. A faster rate of PLA_2 dephosphorylation indeed restored the concentration levels of active PKC in the intermediate phase (Figure 5.9). This was the single modification necessary for the replication of [Kuroda 2001] after correcting the discrepancies in the original implementation.

In addition to the importance of PLA_2 to the LTD model, Kuroda et al have suggested that AA also mediates the feedback loop and, in turn, is responsible for the intermediate phase. Although [Kuroda 2001] showed that the PLA_2 inactivation evokes the disappearance of the intermediate phase, high calcium concentrations may also block the activity of the feedback loop (Figure 5.11). Levels of calcium much higher than the total PKC concentration may cause the saturation of PKC with calcium. Therefore, AA cannot activate the intermediate phase of PKC as all available forms of the kinase are bound to calcium.

Because most of the parameters in [Kuroda 2001] were assumed freely or adapted from kinetic simulations that are also based on incomplete information [Bhalla 1999], the modification of parameters to replicate the original study is a valid approach. Most importantly, the Pinto implementation with more realistic calcium levels qualitatively reproduces the signalling mechanisms in cerebellar LTD as in [Kuroda 2001].

To investigate the role of CaMKII in cerebellar plasticity, this kinase needs to be incorporated into the Kuroda model. First, a model for the activation of CaMKII is needed. A simple CaMKII activation model based on [Dupont 2003] is presented in the next chapter. Interesting findings arose during the development of the new CaMKII model and the study of [Dupont 2003]. The following chapter features the main contributions of this thesis to scientific knowledge.

Chapter 6

Study of CaMKII Frequency Sensitivity

Contents

For the study of calcium-calmodulin dependent protein kinase II (CaMKII) in cerebellar plasticity, I adopt the simplest and commonly used model of CaMKII activation developed by Dupont and collaborators [Dupont 2003]. This chapter proposes a rationalized version of the *Dupont model*. The original aim of this implementation was to include the CaMKII autophosphorylation pathway in the long-term depression model reimplemented in Chapter 5. However, interesting issues arose during the study of [Dupont 2003] which led to important findings. The greatest contributions of this thesis to knowledge are presented in this chapter.

Many studies have indicated that the CaMKII activation is sensitive to the frequency of calcium oscillations [Hanson 1992, Meyer 1992, Hanson 1994, Michelson 1994, Dosemeci 1996, De Koninck 1998, Eshete 2001, Dupont 2003] (see Section 3.3). The Dupont model of CaMKII activation by calcium-calmodulin replicates the experiments by De Koninck and Schulman [De Koninck 1998], as shown in Figure 3.4. Both theoretical and experimental studies have argued that the CaMKII phosphorylation depends on the calcium oscillation *frequency*.

The first section of this chapter presents a modified version of the CaMKII activation model in [Dupont 2003]. The following sections exhibit an investigation of the CaMKII frequency sensitivity studied in [De Koninck 1998, Dupont 2003]. This thesis demonstrates that my modified version of the model used by Dupont et al reproduces their results. However, my computer simulations unveil that the CaMKII phosphorylation is mostly determined by the *average calcium-calmodulin concentration*, and therefore depends only indirectly on the actual frequency of calcium oscillations. I show that the application of a constant level of calcium-calmodulin with the same average concentration as in the pulsed protocol results in identical levels of CaMKII phosphorylation.

To further investigate the behaviour of the model, a series of simulations were carried out. I compare the results of the deterministic simulations with those obtained using a stochastic model of CaMKII activation. The outcomes of stochastic simulations corroborate the findings obtained with the deterministic model.

6.1 CaMKII Activation Model

In the simple model for CaMKII activation by calcium-calmodulin ($\mathrm{Ca_4CaM}$) considered here, all CaMKII subunits are in one of four states. Following the terminology and notational convention used in [Dupont 2003], the four states are referred to as $\mathrm{W_i}$, $\mathrm{W_b}$, $\mathrm{W_p}$, and $\mathrm{W_a}$, where the subscripts i, b, p, and a stand for *inactive*, *bound*, *phosphorylated*, and *autonomous*, respectively. $\mathrm{W_i}$ and $\mathrm{W_b}$ are unphosphorylated, and $\mathrm{W_p}$ and $\mathrm{W_a}$ are phosphorylated states, whereas subunits in the $\mathrm{W_b}$ and $\mathrm{W_p}$ states have $\mathrm{Ca_4CaM}$ bound, and $\mathrm{W_i}$ and $\mathrm{W_a}$ have not. Figure 6.1A shows the interconversion routes between the different CaMKII subunit states.

Subunits in the $\mathrm{W_b}$, $\mathrm{W_p}$, and $\mathrm{W_a}$ states have kinase activity, and can, therefore, phosphorylate CaMKII's targets, including adjacent subunits in the CaMKII multimer. To be "ready" for phosphorylation, such adjacent subunits must be in the $\mathrm{W_b}$ state themselves. By way of example, Figure 6.1B shows a possible phosphorylation trajectory for a single 6-ring in the CaMKII dodecamer. The overall phosphorylation rate associated with this process is indicated as $\mathrm{V_a}$, which is calculated using a phenomenological non-linear function of kinase subunits in the $\mathrm{W_b}$, $\mathrm{W_p}$ and $\mathrm{W_a}$ forms as in [Dupont 2003]

$$\mathrm{V_a} = \mathrm{K_a}\left((\mathrm{c_b W_b})^2 + (\mathrm{c_b W_b})(\mathrm{c_p W_p}) + (\mathrm{c_b W_b})(\mathrm{c_a W_a})\right) , \qquad (6.1)$$

where $\mathrm{c_b}$, $\mathrm{c_p}$ and $\mathrm{c_a}$ are weighting factors proportional to the kinase activity of each active state. In the equations described in this chapter, $\mathrm{W_i}$, $\mathrm{W_b}$, $\mathrm{W_p}$, and $\mathrm{W_a}$ represent fractions of CaMKII subunits in each possible state as in [Dupont 2003]. For example, $\mathrm{W_b}$ is a shorthand for the fraction of kinase subunits that is in the bound state.

The earlier model [Dupont 2003] includes an empirical cubic function ($\mathrm{K_a}$) to model the neighbouring autophosphorylation, allowing the mathematical model to reproduce the experimental results in [De Koninck 1998]. The equation for $\mathrm{K_a}$ is

$$\mathrm{K_a} = \mathrm{K'_a}\left(\mathrm{a T_{ac}} + \mathrm{b T_{ac}^2} + \mathrm{c T_{ac}^3}\right) , \qquad (6.2)$$

where the phenomenological rate for CaMKII autophosphorylation is $\mathrm{K'_a}$, the total fraction of active subunits is $\mathrm{T_{ac}} = \mathrm{W_b} + \mathrm{W_p} + \mathrm{W_a}$, and a, b and c are parameters that Dupont et al adjusted to fit the experimental plots in [De Koninck 1998].

The CaMKII autophosphorylation is assumed as a unidirectional process in the model, that is, an active neighbour subunit can phosphorylate another subunit solely in the same direction within the CaMKII multimer. The direction of autophosphorylation of the simulations in [Dupont 2003] is not completely clear due to ambiguity or lack of information in the simulated protocols. However, as for the earlier model [Dupont 2003], the autophosphorylation direction is irrelevant, and identical results were obtained for the uni and bidirectional autophosphorylations by adjusting the fitting parameters: $\mathrm{K'_a}$, a, b and c (not shown).

The equation that represents the temporal evolution of $\mathrm{W_b}$ fractions is therefore

$$\frac{\mathrm{dW_b}}{\mathrm{dt}} = \mathrm{k_{ib}W_i\,[Ca_4CaM] - k_{bi}W_b - V_a} \ , \tag{6.3}$$

where $\mathrm{[Ca_4CaM]}$ denotes the concentration of $\mathrm{Ca_4CaM}$.

When the kinase subunit is phosphorylated, $\mathrm{W_p}$ can release the $\mathrm{Ca_4CaM}$ complex and switch to the $\mathrm{W_a}$ form. $\mathrm{W_p}$ is expressed as

$$\frac{\mathrm{dW_p}}{\mathrm{dt}} = \mathrm{V_a - k_{pa}W_p + k_{ap}W_a\,[Ca_4CaM]} \ , \tag{6.4}$$

and the amount of $\mathrm{W_a}$ can be calculated as

$$\frac{\mathrm{dW_a}}{\mathrm{dt}} = \mathrm{k_{pa}W_p - k_{ap}W_a\,[Ca_4CaM]} \ . \tag{6.5}$$

$\mathrm{W_i}$ fractions may be computed from the mass conservation relation

$$\mathrm{W_i = 1 - W_b - W_p - W_a} \ . \tag{6.6}$$

As for the experimental and computational studies in [De Koninck 1998, Dupont 2003], the cooperative binding of calcium and free CaM is considered to be in equilibrium and, therefore, is modelled as an instantaneous process. The concentration of CaM bound to four ions of calcium can be expressed as

$$\mathrm{[Ca_4CaM] = CaM_t \frac{Ca_t^4}{{K_d}^4 + Ca_t^4}} \tag{6.7}$$

as in [Dupont 2003], where $\mathrm{CaM_t}$ and $\mathrm{Ca_t}$ are total quantities of CaM and calcium, and $\mathrm{K_d}$ is the concentration of calcium required to achieve 50% $\mathrm{Ca_4CaM}$. In the model, $\mathrm{Ca_t}$ is given by an input table with oscillatory quantities of calcium over time at specific frequency, amplitude and duration. Furthermore, CaM is saturated with calcium for $\mathrm{Ca_t} = 500\ \mu\mathrm{M}$ in all stimulation protocols, as in [De Koninck 1998, Dupont 2003].

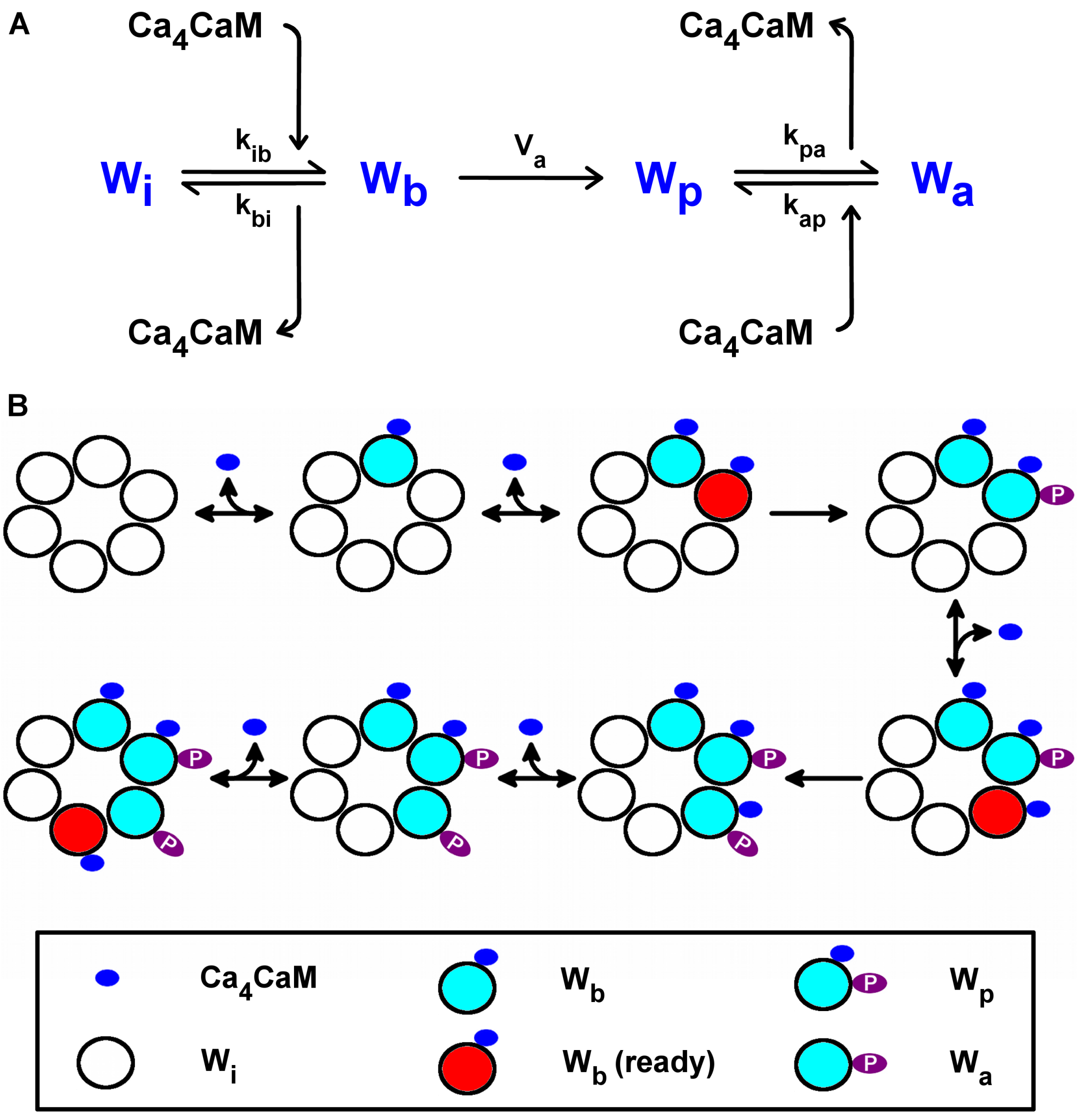

Figure 6.1: **Model of CaMKII activation by Ca_4CaM. A.** CaMKII subunit states are represented as W_i, W_b, W_p, and W_a, where the subscripts i, b, p, and a refer to the respective subunit states: inactive, bound to Ca_4CaM, phosphorylated and bound to Ca_4CaM, and autonomous: phosphorylated, but dissociated from Ca_4CaM. The kinetic constants of the reversible Ca_4CaM binding reactions are k_{ib}, k_{bi}, k_{pa} and k_{ap}, and the rate of the irreversible phosphorylation of W_b is V_a. **B.** A possible phosphorylation trajectory for a single 6-ring in the CaMKII dodecamer. The CaMKII activation initiates by the binding of Ca_4CaM to a kinase subunit. W_b is "ready" for phosphorylation (red) when its left neighbour within the CaMKII ring is an active subunit (cyan): W_b, W_p or W_a.

Meyer et al state that the affinity of CaM for CaMKII increases by a factor of about 1,000 upon phosphorylation [Meyer 1992]. However, there is no indication in their data that this "trapping" of CaM is, as the Dupont model [Dupont 2003] would suggest, solely due to an increased affinity of *apo-CaM* (CaM without any calcium ions bound) for phosphorylated CaMKII subunits. If equilibration of calcium and free CaM is modelled as an instantaneous process, as in both Dupont's and my models, it is reasonable to model equilibration of CaMKII-bound CaM as an instantaneous process as well. Therefore, unlike the model in [Dupont 2003], the model used here does not include a separate "trapped" state in which apo-CaM is bound to CaMKII. As a result, the values for the rate constants between the "trapped" CaM ($\mathrm{W_t}$) and $\mathrm{W_a}$ states in [Dupont 2003] were adopted here as $\mathrm{k_{ap}}$ and $\mathrm{k_{pa}}$.

The kinetic parameters used in all simulations were based on the Dupont model data (Appendix D). The value for $\mathrm{K'_a}$, which is considered as an unidirectional modelling parameter in this thesis, is identical to the value stated for the bidirectional autophosphorylation in [Dupont 2003]. This assumption does not influence the outcome of the simulations as $\mathrm{K'_a}$ is a hypothetical value. To replicate the results in [Dupont 2003], the fitting parameters a, b and c were then adjusted. Like the Dupont model, the model developed here solely considers phosphorylation, and omits any reverse CaMKII dephosphorylation reaction.

The simplified model was implemented in XPPAUT and the results were obtained by numerically integrating Equations 6.1-6.7, using the Euler method and a 1 ms time step size.

6.2 Model Validation

As described above, the model used here is a rationalized version of the model proposed in [Dupont 2003]. To examine whether the omission of $\mathrm{W_t}$ from the model has a significant effect on its behaviour, I carried out a series of simulations under the conditions used in [Dupont 2003] to explain key experimental observations of [De Koninck 1998].

The results show that the trajectories of fractions of phosphorylated CaMKII ($\mathrm{W_p + W_t}$ in the Dupont model; $\mathrm{W_p}$ in the rationalized version) overlap to a great extent (Figure 6.2). The differences in the trajectories are caused by the differences in kinase activity for the various phosphorylated species. In a model in which the relative kinase activity of $\mathrm{W_t}$ is the same as that of $\mathrm{W_p}$ rather than that of $\mathrm{W_a}$, these slight differences disappear almost completely (not shown). Thus, the behaviour of the original and rationalized versions of the model is to all intends and purposes the same, as also demonstrated in Figures 6.3-6.7. For that reason, I use the simpler version that does not explicitly specify "trapping" of apo-CaM in the investigations described in the following.

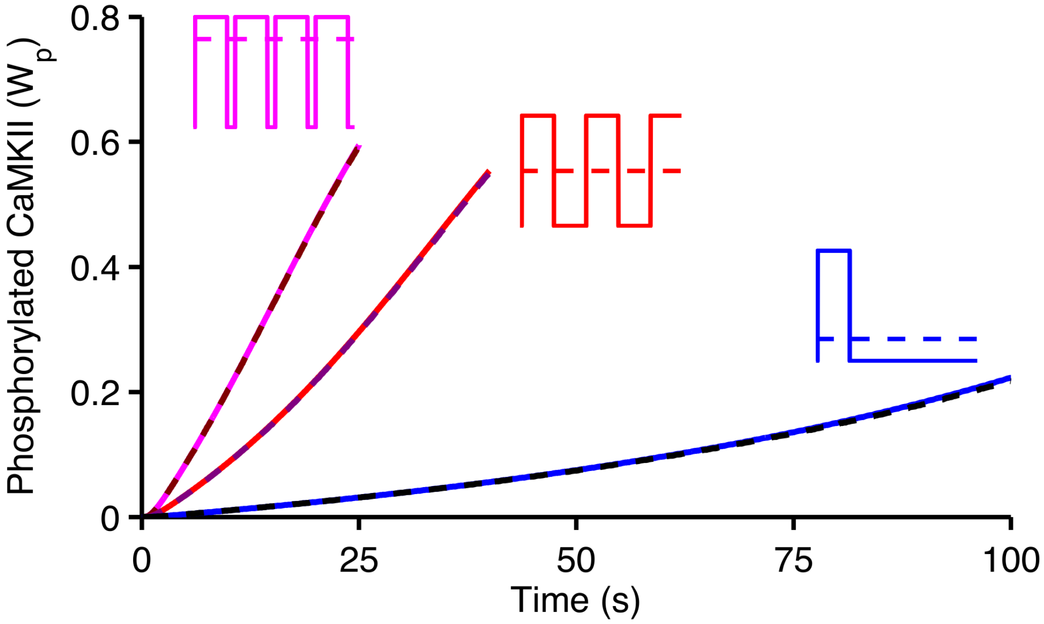

Figure 6.2: **CaMKII phosphorylation in response to repetitive square Ca_4CaM pulses with the same amplitude at varying frequencies.** Temporal evolution of fractions of phosphorylated CaMKII (W_p in the rationalized version - solid; $W_p + W_t$ in the Dupont model - dashed) in response to one hundred 200 ms square pulses of Ca_4CaM (100 nM) at frequencies of 1 (solid blue and dashed black), 2.5 (solid red and dashed purple) and 4 Hz (solid magenta and dashed brown). **Insets**. Representations of Ca_4CaM oscillations at these frequencies for 1 s (solid). The product of the amplitude, frequency and duration of Ca_4CaM pulses determines the average ("effective") Ca_4CaM concentration (dashed). This figure replicates the results of Figure 3.4.

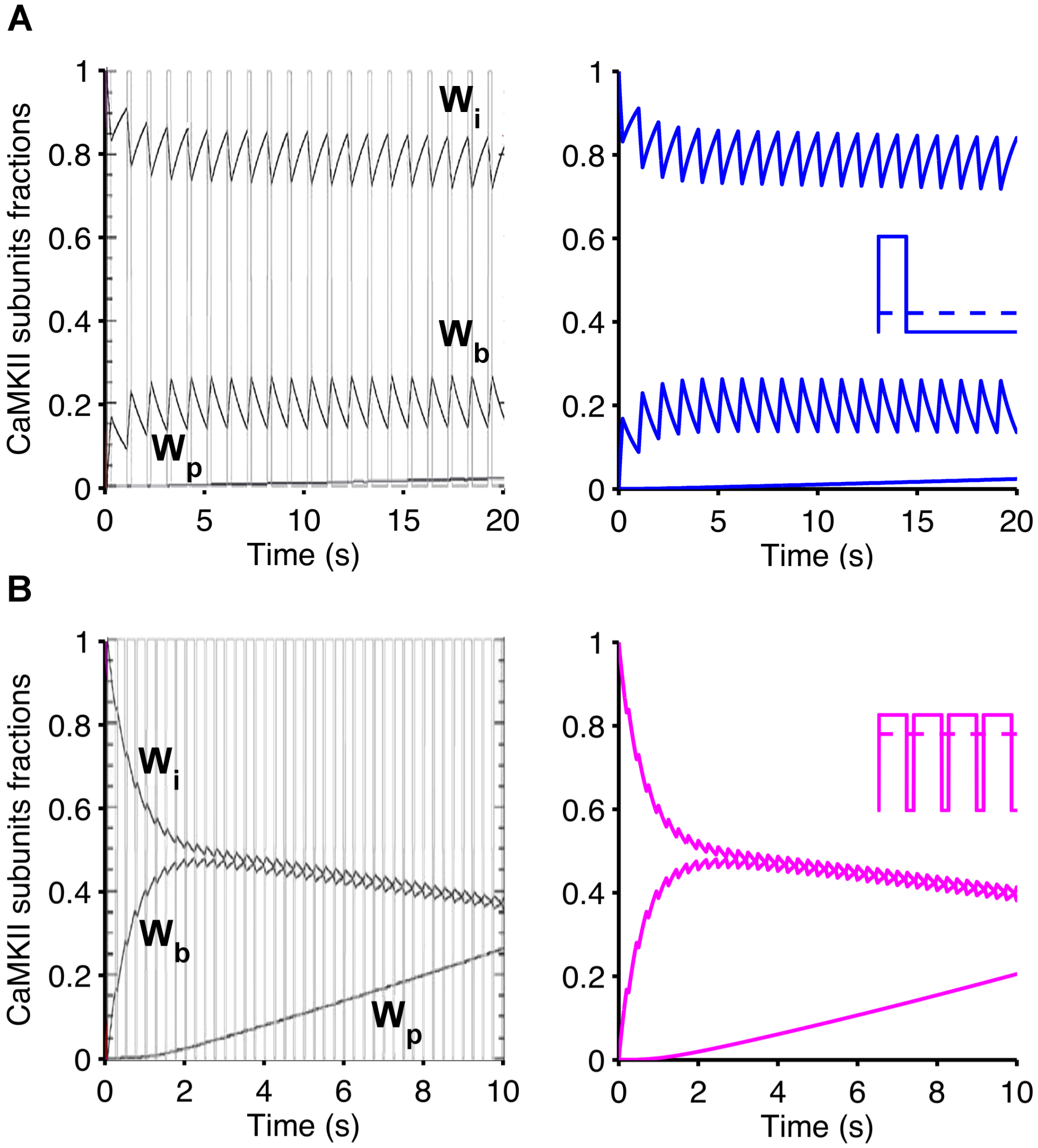

Figure 6.3: **Replication of Figure 4 in [Dupont 2003].** Trajectories of W_i, W_b and W_p fractions in response to the same protocol as in Figure 6.2 at frequencies of 1 (**A**, for 20 s) and 4 Hz (**B**, for 10 s). The results obtained from the simplified model replicate those in [Dupont 2003] (right and left panels, respectively). **Insets.** Ca_4CaM oscillations at 1 and 4 Hz for 1 s.

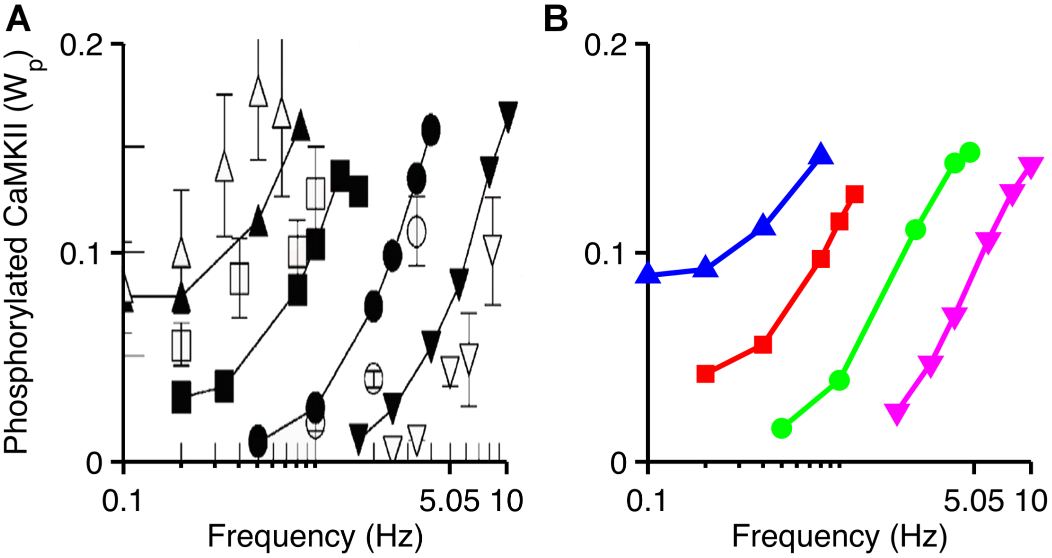

Figure 6.4: **Replication of Figure 3E in [Dupont 2003]. A.** Frequency sensitivity of phosphorylated CaMKII in response to varying *durations* of Ca$_4$CaM pulses (100 nM) in [Dupont 2003]. Each data point is the maximal level of W$_p$ after 6 s of stimulation. **B.** W$_p$ in the rationalized version of the Dupont model in response to the same protocol as in **A**. The durations of the Ca$_4$CaM pulses are 1,000 (blue ▲), 500 (red ■), 200 (green •) and 80 ms (magenta ▼).

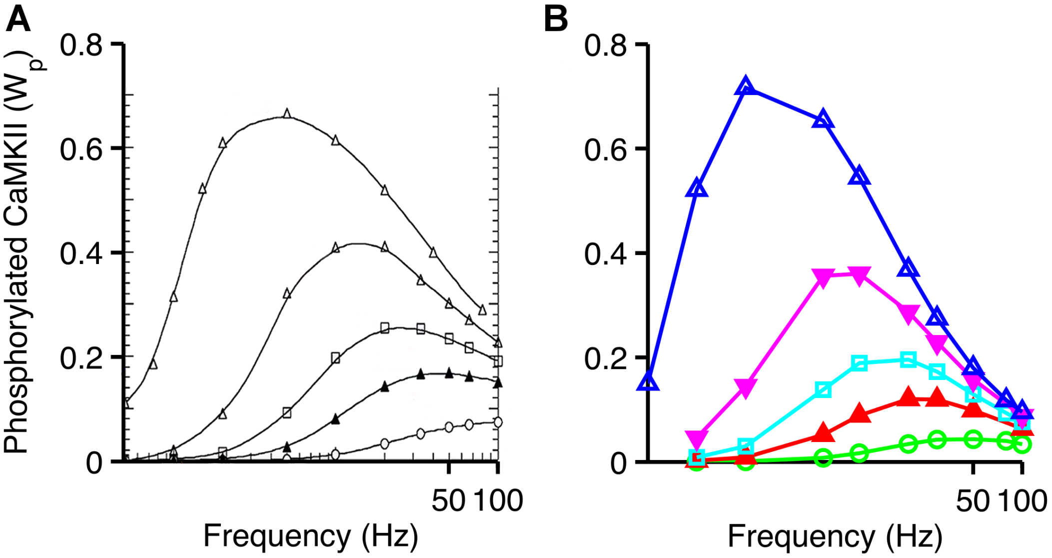

Figure 6.5: **Replication of Figure 6B in [Dupont 2003]. A.** CaMKII frequency sensitivity in response to Ca$_4$CaM pulses with high amplitude (2.5 μM) at varying *short durations* in [Dupont 2003]. Each data point represents the W$_p$ maximal level after 100 Ca$_4$CaM spikes at each frequency. **B.** W$_p$ in the simplified model in response to the same protocol. The durations of the Ca$_4$CaM pulses are 10 (blue △), 5 (magenta ▼), 3 (cyan □), 2 (red ▲) and 1 ms (green ○).

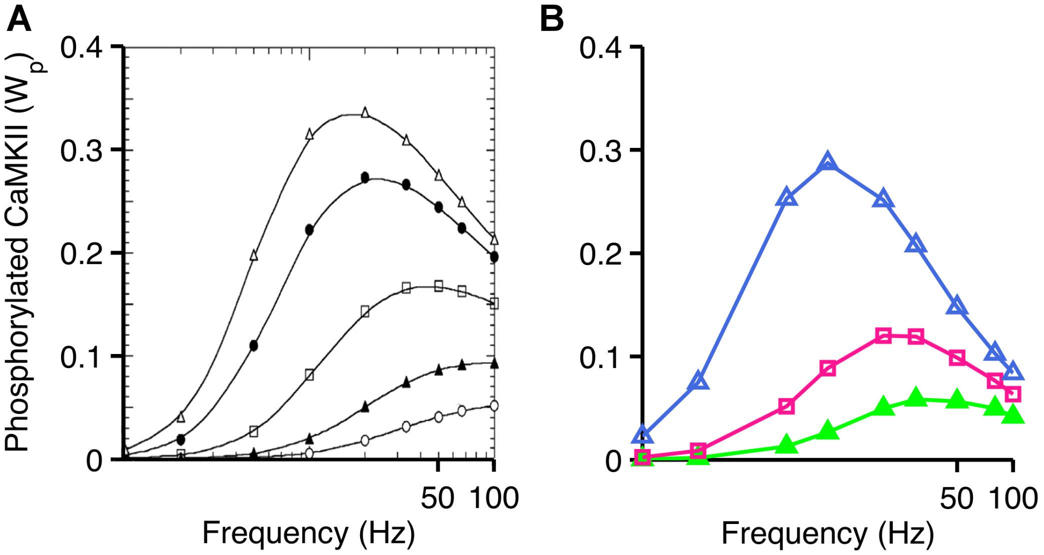

Figure 6.6: **Replication of Figure 6C in [Dupont 2003]. A.** CaMKII frequency sensitivity in response to Ca_4CaM spikes with short duration (2 ms) at varying *high amplitudes* in [Dupont 2003]. **B.** W_p in response to the same protocol in the simplified model. The amplitudes of the Ca_4CaM pulses are 5 (blue △), 4 (●), 2.5 (pink □), 1.5 (green ▲) and 1 μM (○).

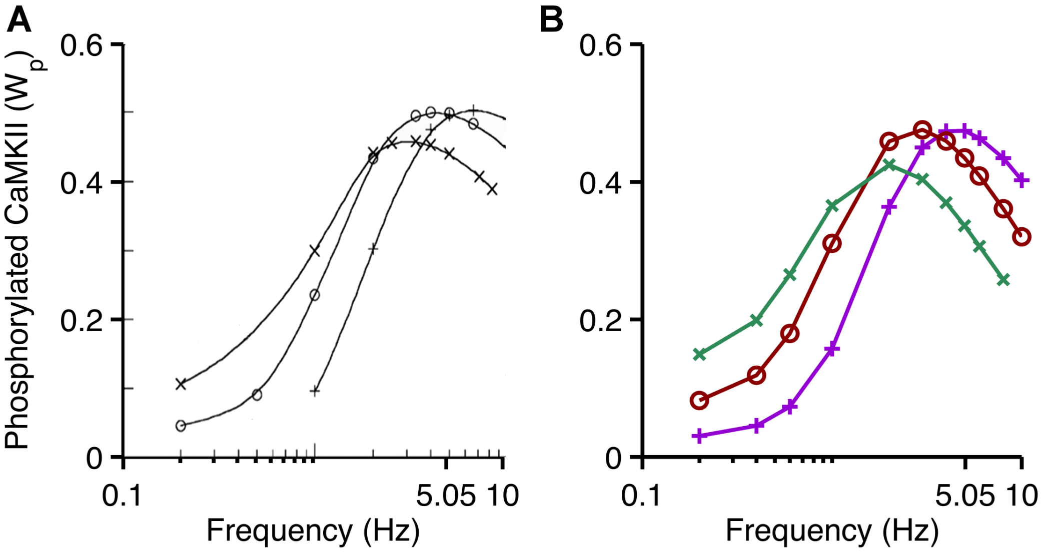

Figure 6.7: **Replication of Figure 7A in [Dupont 2003]. A.** Frequency sensitivity of phosphorylated CaMKII in response to varying *numbers* and *durations* of Ca_4CaM spikes (400 nM): 30 120 ms (green ×), 50 80 ms (red ○) and 80 50 ms (violet +). **B.** W_p in the rationalized version of the model in [Dupont 2003] in response to the same conditions as in **A**.

6.3 Effective Calcium-calmodulin Concentration Explains CaMKII Frequency Sensitivity

De Koninck and Schulman in [De Koninck 1998] and Dupont et al in [Dupont 2003] have presumed from experimental and computational observations that CaMKII may "decode" the calcium pulse frequencies. The kinase therefore may depend on the frequency of repetitive Ca_4CaM oscillations, as shown in Figure 6.2. In their protocols, CaMKII is subjected to repetitive square Ca_4CaM pulses at varying frequencies but with the same amplitude and duration. However, variations in the oscillation frequency accompany changes in the average, or "effective", Ca_4CaM concentration ($[Ca_4CaM]_{eff}$) which is calculated as

$$[Ca_4CaM]_{eff} = [Ca_4CaM]_{pulse}\, f\, L \ , \tag{6.8}$$

where $[Ca_4CaM]_{pulse}$ is the pulse amplitude, f is the pulse frequency, and L is the pulse duration. Because in those protocols the Ca_4CaM pulses contain the same amplitude and duration at varying frequencies, the kinase phosphorylation responds to different effective Ca_4CaM concentrations, which in turn affect the average amount of W_p (Figure 6.2). Hence, an affirmation that [De Koninck 1998] and [Dupont 2003] demonstrate the CaMKII sensitivity to the frequency of calcium spikes is a premature conclusion.

Is the CaMKII phosphorylation sensitive to the oscillation frequency or the effective concentration of Ca_4CaM? For this investigation, the pulse amplitude was rescaled to result in an equal effective Ca_4CaM concentration at varying frequencies, and the phosphorylation kinetics was then compared (Figure 6.8). Simulation of the model's behaviour showed that the levels of W_p at different frequencies are identical after rescaling the amplitude of Ca_4CaM pulses, i.e. stimuli with equal effective Ca_4CaM concentrations result in the same phosphorylation response. For the frequencies examined here, these results strongly indicate that the CaMKII autophosphorylation kinetics are dependent on the effective Ca_4CaM concentration, and therefore only indirectly on the actual pulse frequency.

6.4 Pulsed Application of Calcium-calmodulin is Not Required

As CaMKII does not depend on the actual frequency of Ca_4CaM pulses, the question arises: are the kinase phosphorylation levels the same under constant and pulsed concentrations of Ca_4CaM, while keeping the appropriate effective concentrations?

Simulation results indeed show a superposition of fractions of the various CaMKII subunit states in response to continuous and pulsed Ca_4CaM concentrations (Figure 6.9). This behaviour is also observed for a wider range of frequencies (Figure 6.10). Again, the outcome of the model demonstrates that the effective concentration of Ca_4CaM mediates the CaMKII phosphorylation, and not the actual pulse frequency.

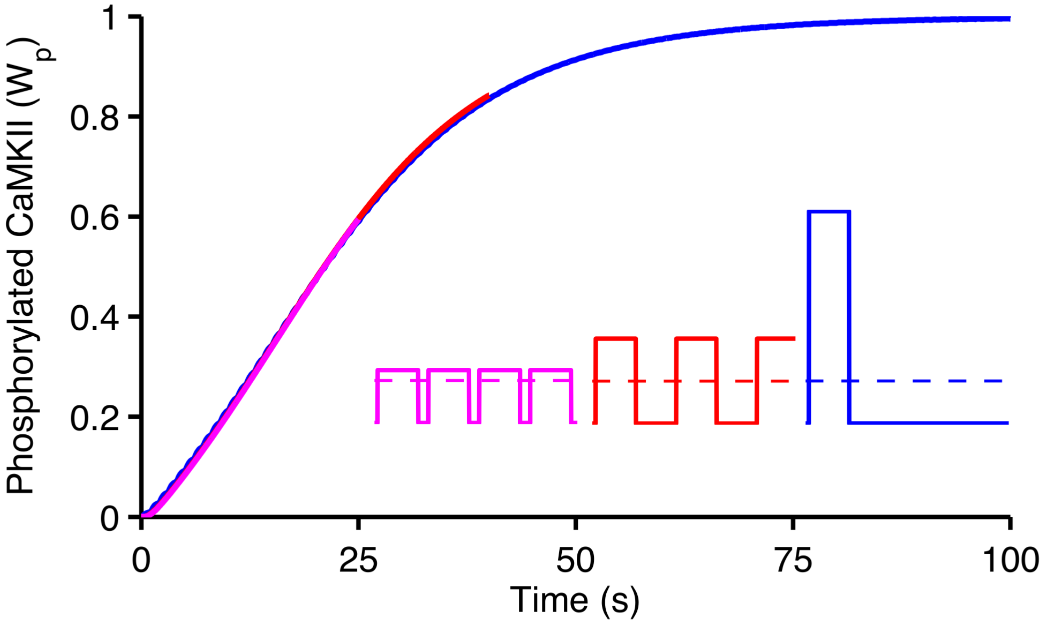

Figure 6.8: **Effective Ca_4CaM concentration determines the sensitivity of CaMKII to the frequency of Ca_4CaM oscillations.** CaMKII phosphorylation responds to one hundred 200 ms square pulses of Ca_4CaM at 1 (blue), 2.5 (red) and 4 Hz (magenta), but with scaled amplitudes to keep an equal effective Ca_4CaM concentration. **Insets**. Solid lines illustrate the rescaled amplitudes of Ca_4CaM pulses: 400 nM at 1 Hz (blue), 160 nM at 2.5 Hz (red) and 100 nM at 4 Hz (magenta). Thus, CaMKII is subjected to the same effective concentration of Ca_4CaM of 80 nM (dashed).

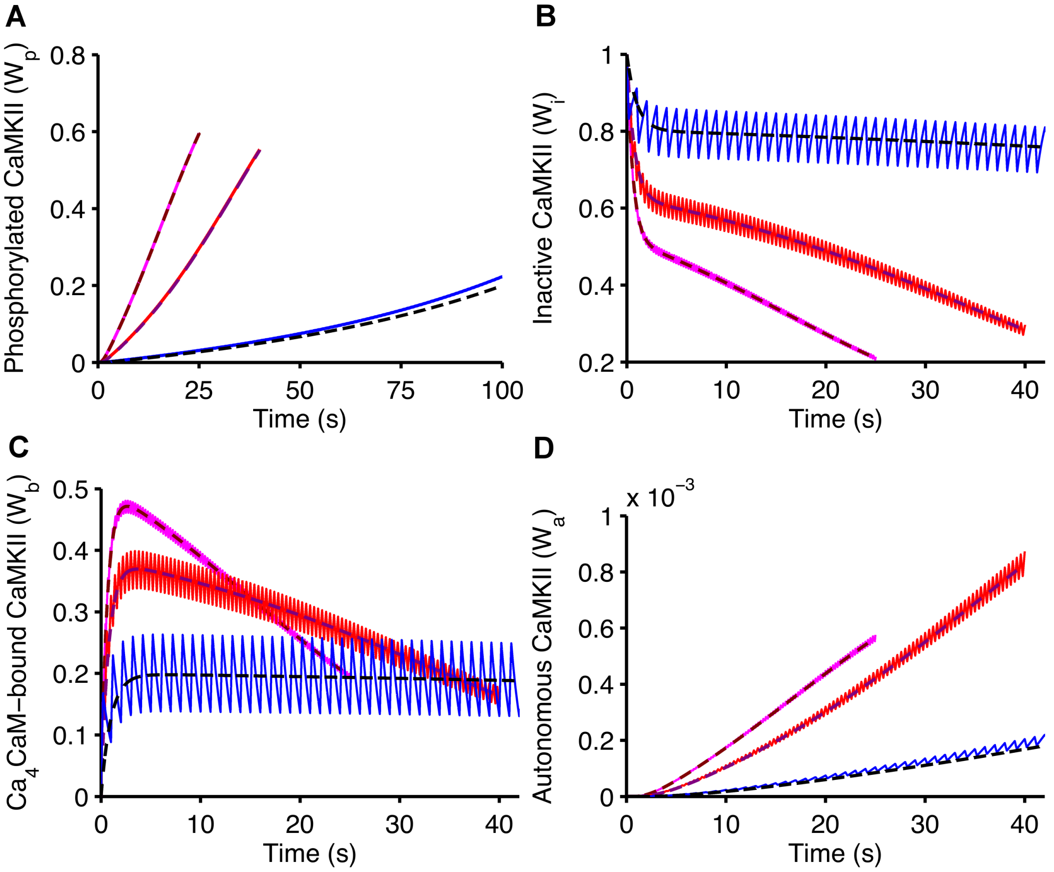

Figure 6.9: **Pulsed and continuous concentrations of Ca_4CaM produce identical CaMKII autophosphorylation kinetics.** Temporal evolution of the various forms of CaMKII subunits: phosphorylated (**A**), inactive (**B**), Ca_4CaM-bound (**C**) and autonomous (**D**). The solid lines indicate the CaMKII response to one hundred 200 ms pulses of Ca_4CaM (100 nM) at varying frequencies. These correspond to effective Ca_4CaM concentrations of 20 nM at 1Hz (blue), 50 nM at 2.5 Hz (red) and 80 nM at 4 Hz (magenta). The dashed lines represent the CaMKII trajectories in response to the application of continuous concentrations of Ca_4CaM at the same levels: 20 nM for 100 s (black), 50 nM for 40 s (purple) and 80 nM for 25 s (brown). In panels **B**, **C** and **D**, the stimulated Ca_4CaM pulses at 1 Hz (blue) and the continuous Ca_4CaM concentration of 20 nM (black) last 100 s.

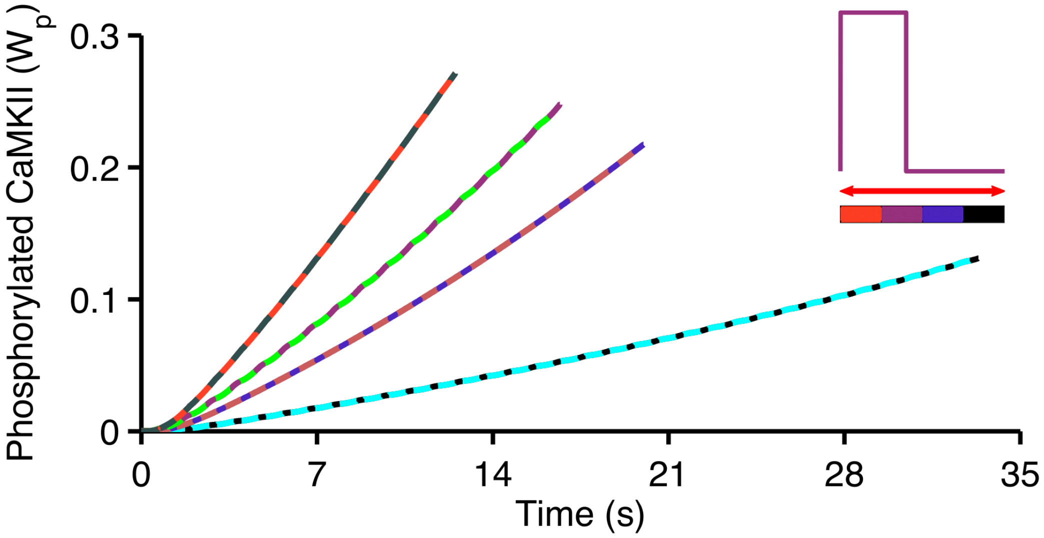

Figure 6.10: **Pulsed Ca_4CaM stimulation is irrelevant to CaMKII phosphorylation for a wide range of frequencies.** Trajectories of phosphorylated CaMKII in response to pulsed and continuous concentrations of Ca_4CaM at varying frequencies. The solid lines indicate the CaMKII response to one hundred 100 ms pulses of Ca_4CaM (100 nM) at varying frequencies: 3 (black), 5 (blue), 6 (purple) and 8 Hz (light red). The dashed lines represent the W_p levels in response to continuous concentrations of Ca_4CaM at the appropriate effective concentrations: 30 (cyan), 50 (dark red), 60 (green) and 80 nM (grey).

6.5 Stochastic Simulations Corroborate Findings with the Deterministic Model

In the deterministic model used here, the CaMKII autophosphorylation rate is expressed as a phenomenological function as in [Dupont 2003] (Equation 6.1). To examine whether this phenomenological process reflects the actual kinase autophosphorylation, the second supervisor of this thesis developed a stochastic model of CaMKII activation (Appendix C). This model stochastically simulates how the autophosphorylation process occurs within the CaMKII multimer, as illustrated in Figure 6.1B.

Results obtained from stochastic simulations are very similar to the outcomes of the deterministic model (Figure 6.11). The stochastic model corroborates all findings with the deterministic one, and also demonstrates the dependence of the overall autophosphorylation kinetics on the effective Ca_4CaM concentration.

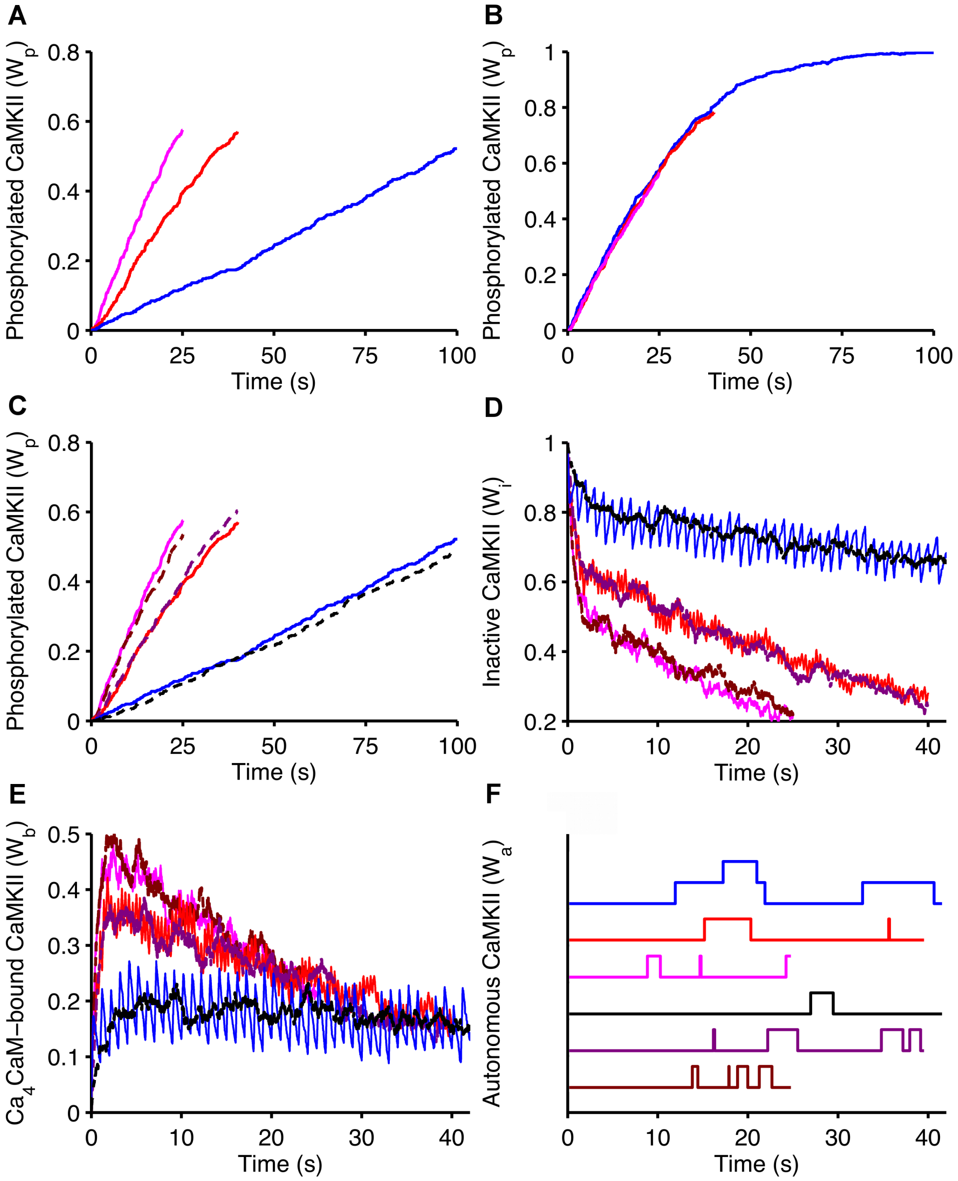

Figure 6.11: **Stochastic simulations corroborate findings with the deterministic model.** Results obtained from the stochastic model described in Appendix C reproduce the outcomes of the deterministic simulations. All curves in each panel result from a single stochastic simulation with 100 CaMKII rings of 6 subunits each. As for the deterministic results, W_i, W_b, W_p, and W_a represent fractions of CaMKII subunits in each possible state. **A**. Fractions of phosphorylated CaMKII (W_p) in response to Ca_4CaM pulses with identical amplitude at 1 (blue), 2.5 (red) and 4 Hz (magenta). This figure replicates Figure 6.2. **B**. CaMKII phosphorylation in response to the same protocol, but with scaled amplitudes of Ca_4CaM to keep the same effective concentration. This panel reproduces the results in Figure 6.8. **C**, **D**, **E** and **F**. The kinase autophosphorylation kinetics respond to pulsed and continuous concentrations of Ca_4CaM. These panels replicate Figures 6.9A, 6.9B, 6.9C and 6.9D, respectively. In panel **F**, each curve step corresponds to a single subunit in the autonomous form of CaMKII (W_a).

6.6 Variations in the Frequency, Amplitude and Duration of Calcium-calmodulin Oscillations

The effective concentration of Ca_4CaM depends on the amplitude, frequency and duration of Ca_4CaM pulses (Equation 6.8). So far, simulation results demonstrated that equal CaMKII phosphorylation levels are achieved at varying frequencies, while rescaling solely the amplitude of Ca_4CaM pulses and keeping the same effective concentration (Figure 6.8). For a thorough investigation, I also test the CaMKII phosphorylation in response to a wider range of frequencies, after rescaling the amplitude and duration of Ca_4CaM oscillations (Figure 6.12). As expected, the results reveal that indeed variations in the frequency, amplitude and duration of Ca_4CaM pulses at the same effective concentration produce similar levels of W_p. Very low frequencies produce distinct responses though. These differences mostly occur due to the almost complete dissociation of Ca_4CaM from CaMKII between low frequency pulses (Figures 6.12B and 6.12D). In a model in which solely the $W_i \rightleftharpoons W_b$ reaction is simulated and any type of CaMKII phosphorylation is then blocked, different responses for W_b fractions are yet observed (Figure 6.13).

6.7 Chapter Conclusions

Calcium is the major signalling substance in many cell types. The intracellular calcium concentration exhibits repetitive spikes that vary in their frequency, amplitude and duration. These oscillations regulate many cellular functions, but the intracellular mechanisms for responding to repetitive calcium spikes are not entirely understood. For instance, the phosphorylation of CaMKII has been suggested as a molecular mechanism for “decoding” the calcium pulse frequencies. For this reason, many studies aimed at investigating the sensitivity of CaMKII to the frequency of repetitive calcium signals. This chapter addressed the computer simulations in [Dupont 2003] that replicate the experiments with immobilized CaMKII in [De Koninck 1998]. Both studies have shown that the activation of CaMKII is sensitive to the calcium oscillation frequency. Using a simplified version of the model in [Dupont 2003], I have demonstrated that this assertion is misleading.

De Koninck and Schulman (1998) and Dupont et al (2003) delivered repetitive square Ca_4CaM pulses of equal amplitude at different frequencies. The variation of frequencies in those studies affected the average concentration of Ca_4CaM pulses which depends on their frequency, amplitude and width. Therefore, simulation with rescaled amplitudes of Ca_4CaM oscillations, keeping the same average concentration, produces identical levels of CaMKII phosphorylation. Furthermore, I have demonstrated that a pulsed application of Ca_4CaM is, in fact, not required at all. The same level of phosphorylated CaMKII is obtained in response to steady and pulsed stimulations of Ca_4CaM at identical average concentrations. These findings strongly indicate that CaMKII depends on the average Ca_4CaM concentration and not on the oscillation frequency per se as asserted in [De Koninck 1998, Dupont 2003].

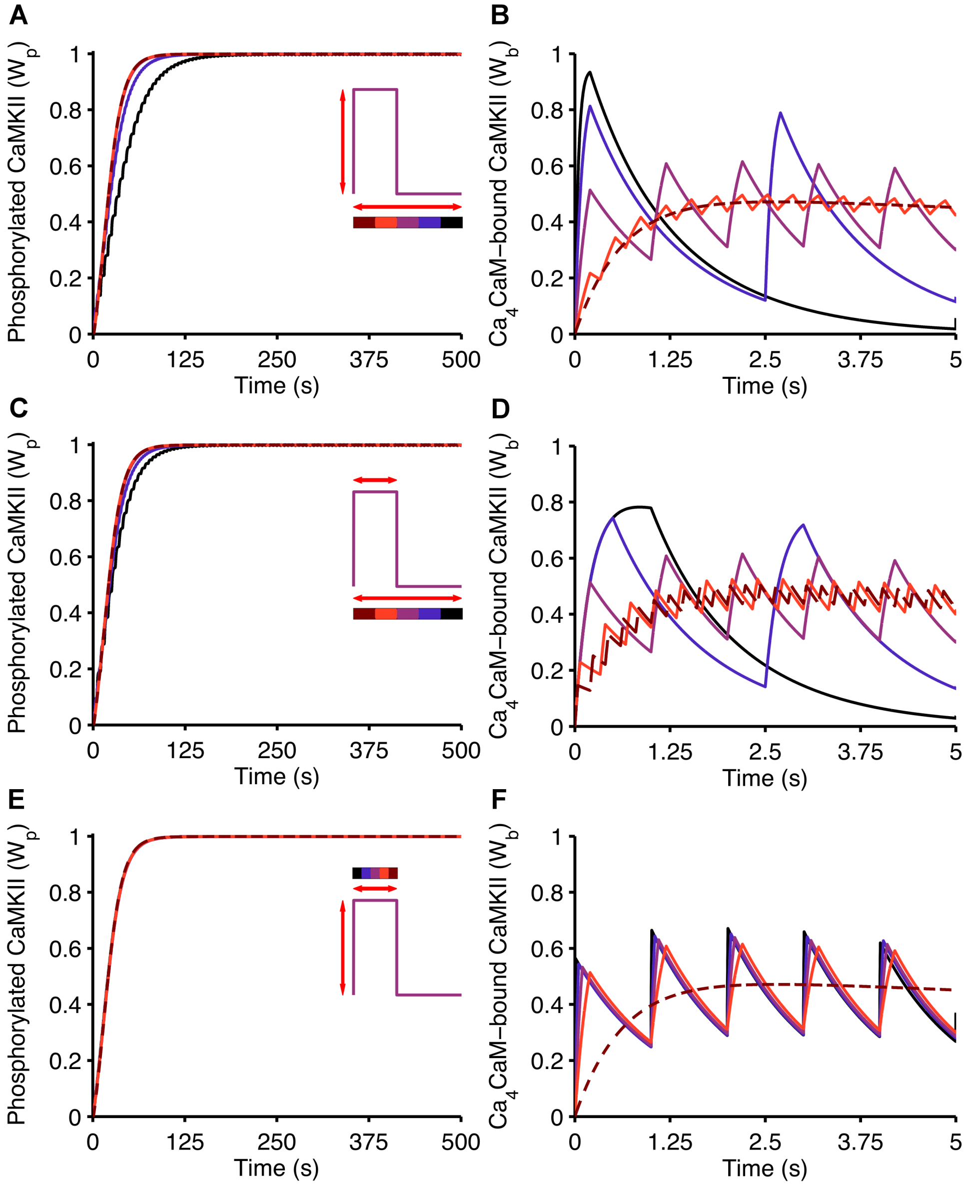

Figure 6.12: **Variations in the frequency, amplitude and duration of Ca_4CaM pulses produce the same CaMKII phosphorylation level.** Fractions of phosphorylated CaMKII (W_p) and Ca_4CaM-bound CaMKII (W_b) in response to Ca_4CaM stimuli with the same effective concentration of 80 nM for 500 s at varying frequencies, amplitudes and durations. **A** and **B**. CaMKII is subjected to a continuous Ca_4CaM concentration of 80 nM (brown), and to 200 ms Ca_4CaM pulses at varying amplitudes and frequencies: 133.33 nM at 3 Hz (red), 400 nM at 1 Hz (purple), 1 μM at 0.4 Hz (blue) and 2 μM at 0.2 Hz (black). **C** and **D**. Stimuli of oscillatory Ca_4CaM pulses with amplitude of 400 nM at varying durations and frequencies: 40 ms at 5 Hz (brown), 67 ms at 3 Hz (red), 200 ms at 1 Hz (purple), 500 ms at 0.4 Hz (blue) and 1 s at 0.2 Hz (black). **E** and **F**. CaMKII in reponse to a continuous Ca_4CaM concentration of 80 nM (brown), and to Ca_4CaM pulses at 1 Hz with varying amplitudes and durations: 8 μM and 10 ms (black), 1.6 μM and 50 ms (blue), 800 nM and 100 ms (purple) and 400 nM and 200 ms (red).

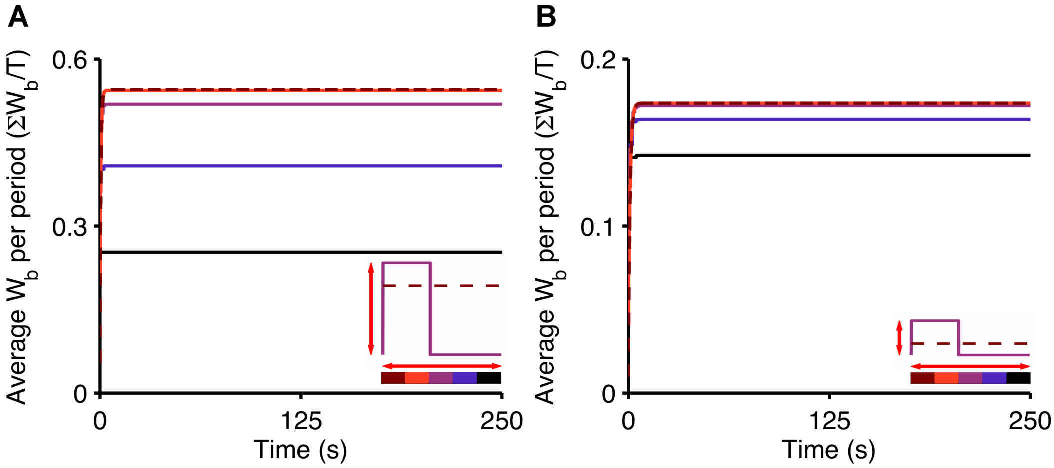

Figure 6.13: **CaMKII phosphorylation is sensitive to lower Ca_4CaM frequencies in the model.** Time-evolution of W_b in the absence of CaMKII phosphorylation ($V_a = 0$) in response to Ca_4CaM stimuli with high and low effective Ca_4CaM concentrations (**A** and **B**, respectively). Because $V_a = 0$, the model contains a single reaction: $W_i \rightleftharpoons W_b$. Results are shown as the average amount of W_b fractions per period (T). **A.** CaMKII is subjected to a continuous Ca_4CaM concentration of 96 nM (brown), and to 100 ms Ca_4CaM pulses at varying amplitudes and frequencies: 400 nM at 3 Hz (red), 1.2 μM at 1 Hz (purple), 3 μM at 0.4 Hz (blue) and 6 μM at 0.2 Hz (black). **B.** CaMKII responds to a continuous Ca_4CaM concentration of 16.8 nM (brown), and to 100 ms Ca_4CaM pulses at varying amplitudes and frequencies: 70 nM at 3 Hz (red), 210 nM at 1 Hz (purple), 525 nM at 0.4 Hz (blue) and 1.05 μM at 0.2 Hz (black).

The experimental observations by De Koninck and Schulman (1998) are widely cited. As a result, many theoretical studies also investigated the CaMKII sensitivity to the calcium oscillation frequency as [Dupont 2003] did. Most of these studies, however, mimic the misleading experimental protocols used in [De Koninck 1998] and also use square calcium pulses with equal amplitude [Hanson 1994, Kubota 2001, Dupont 2003]. Like my model, these models replicate the frequency sensitivity observed in [De Koninck 1998], and their stimulation protocols also present different average concentrations of Ca_4CaM to CaMKII which, not surprisingly, produce distinct levels of phosphorylated CaMKII at varying frequencies.

In contrast, a recent study proposed a model that simulates the frequency dependence at constant average calcium signals [Salazar 2008]. The input protocols developed by Salazar et al (2008) contain rescaled amplitudes of square calcium pulses that stimulate the model with equal average calcium signal [Salazar 2008]. Although their findings corroborate the idea raised in this chapter, this study cannot be compared to the investigation presented here because the authors simulate a different scenario from that described in this thesis and, consequently, do not directly address the studies in [De Koninck 1998, Dupont 2003]. They model the activation of a generic kinase, not the CaMKII activation modelled here, and also include the phosphorylation and dephosphorylation of a target protein, a process not considered in [De Koninck 1998, Dupont 2003] and in my study.

Interestingly, Li et al (2012) recently proposed a CaMKII activation model that indicates that the stimulation of a high amount of calcium at lower frequencies produces the same CaMKII phosphorylation level as a smaller amount at higher frequencies. However, the complex model in [Li 2012] includes calcineurin, the dephosphorylation of CaMKII by protein phosphatase 1 (PP1), and other biochemical compounds that differ from the model used in this thesis. Their study, therefore, models a different, more complex system from the one observed by De Koninck and Schulman (1998) and modelled in Dupont et al (2003) and here. Moreover, the model by Li et al (2012) simulates the actual dynamics of intracellular calcium concentration induced by action potentials, which differs from [De Koninck 1998, Dupont 2003], whose studies use square pulses. Furthermore, the stimulation protocols used in [Li 2012] comprise calcium signals modulated solely on frequencies with the same pulse amplitude. For instance, Figure 2b in [Li 2012] clearly demonstrates that stimulations of calcium with the same input size at higher frequencies raise the intracellular calcium concentration. As a result, CaMKII phosphorylation may again depend on concentrations of calcium rather than the pulse frequency itself, as in [De Koninck 1998, Dupont 2003]. Although Li et al state that a few stimulation protocols in their study were “modulated” to generate the same amount of calcium ions at varying frequencies, it is not clear how this has been done and in which simulations these protocols were used.

The simple model of CaMKII activation developed in this chapter can be easily used in models that simulate larger signalling cascades. For example, the CaMKII phosphorylation mechanism illustrated in Figure 6.1 may be incorporated into complex models that simulate plasticity in Purkinje cells as in Figure 5.1. The next chapter presents the inclusion of the CaMKII activation model presented in this chapter into a model of cerebellar long-term depression and long-term potentiation to investigate the role of CaMKII isoforms in bidirectional plasticity at parallel fibre-Purkinje cell synapses.

Chapter 7

Study of Bidirectional Plasticity in Purkinje Cells

Contents

Although it is known that calcium-calmodulin dependent protein kinase II (CaMKII) is essential for plasticity in the cerebellum, the role of this kinase in the mechanisms underlying cerebellar plasticity remains an enigma. Surprisingly, biochemical models that simulate the molecular machinery between parallel fibres (PF) and Purkinje cells (PCs) have never included CaMKII in their signalling pathways. Because experimental observations by themselves are not able to explain how CaMKII mediates plasticity in PCs, a new dynamic model of cerebellar long-term depression (LTD) and long-term potentiation (LTP) that includes CaMKII will contribute significantly to cerebellar research.

For this purpose, the initial aim of this thesis was to incorporate the CaMKII activation model discussed in Chapter 6 [Dupont 2003] into the cerebellar LTD model reimplemented in Chapter 5 [Kuroda 2001]. However, because this LTD framework accounts for a complex signalling network in which several biochemical reactions occur simultaneously (Figure 5.1), the understanding of the actual role of CaMKII in this model was limited by the complexity of its signalling pathways. For that reason, I adopt a new strategy: the development of a simple model of LTD and LTP induction to study the role of CaMKII in plasticity in cerebellar PCs. In particular, the simple model presented in this chapter aims at explaining the molecular mechanisms underlying the experimental observations in [van Woerden 2009] (Figure 3.6). Van Woerden et al have shown that βCaMKII mediates the bidirectional plasticity at PF-PC synapses (Section 3.4).

The beginning of this chapter briefly summarises the experimental findings in [van Woerden 2009]. The second section discusses the inclusion of CaMKII in the Kuroda model [Kuroda 2001]. The third section presents the simple dynamic model used to investigate the regulation of bidirectional plasticity in these experiments. Following on from this, simulation results first demonstrate that the model reproduces the mechanisms of plasticity at PF-PC synapses, in response to both constant and oscillatory calcium stimulations. The results obtained with the simple model replicate the experimental observations in [van Woerden 2009], and reveal that the filamentous actin (F-actin) binding may indeed enable βCaMKII to regulate the bidirectional plasticity in cerebellar PCs.

I also carried out a series of simulations following suggestions from the authors of [van Woerden 2009]. With new parameter values based on experimental observations, the model reproduces the observations of Van Woerden et al (2009) as well as the model with the original values does. Similar results were also obtained with a model that describes calcium-calmodulin binding to CaMKII in two steps rather than one. Thus, this chapter presents the first dynamic model that simulates the induction of LTD and LTP in cerebellar PCs mediated by CaMKII.

7.1 Results of the Study by Van Woerden and Collaborators

Experiments with *Camk2b* knockout mice that lack the β isoform of CaMKII have demonstrated that βCaMKII regulates the direction of plasticity at PF-PC synapses [van Woerden 2009] (Section 3.4). Figure 7.1 schematically illustrates the experimental results by Van Woerden et al. Calcium-dependent levels of *kinase* and *phosphatase* activities are represented for the *Camk2b* knockout mice and the wild-type mice, which contain both αCaMKII and βCaMKII. LTD is induced when the kinase concentration surpasses the phosphatase concentration, whereas the opposite case generates LTP. These experiments showed that protocols that induce LTD in wild-type mice lead to LTP in knockout mice that lack βCaMKII, and vice versa.

7.2 Including CaMKII in the Signalling Cascades of the Kuroda Model

To incorporate CaMKII into the signalling cascades proposed by Kuroda and collaborators [Kuroda 2001], I included the model of CaMKII activation presented in Chapter 6 in the Kuroda model reimplemented in Chapter 5. Because the Kuroda model simulates LTD in cerebellar PCs and not LTP, the adaptation of this model to simulate both LTD and LTP was unsuccessful, as discussed in the following.

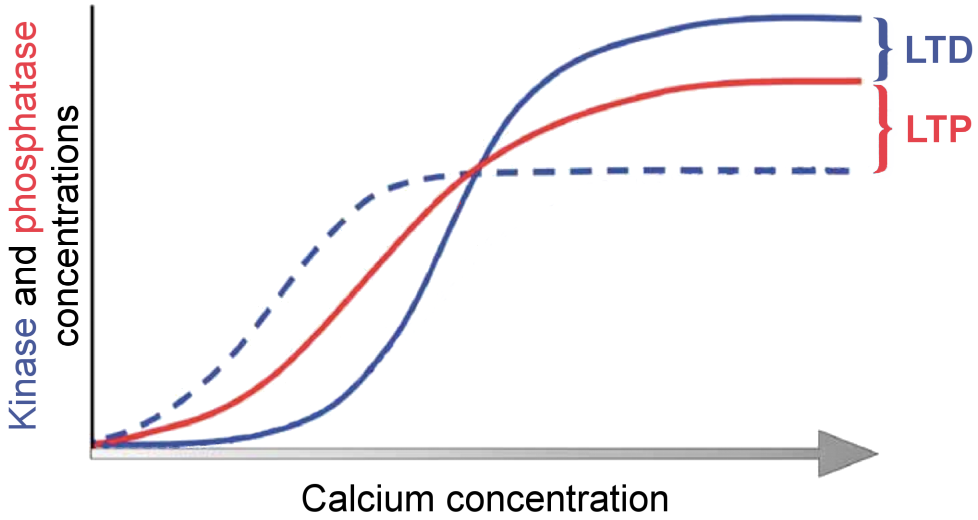

Figure 7.1: **Schematic representation of bidirectional plasticity at PF-PC synapses.** The experimental results obtained by Van Woerden et al (Figure 3.6) are schematically represented in this figure. The scheme illustrates how changes in the CaMKII-driven pathway evoke different concentration levels of calcium-dependent kinase (blue), resulting in the inversion of plasticity for wild-type and *Camk2b* knockout mice (solid and dashed, respectively). LTD is generated when the kinase concentration (blue) surpasses the phosphatase concentration (red), whereas the opposite case induces LTP. Adapted from [van Woerden 2009].

Kuroda et al (2001) simulated the inactivation of protein phosphatase 2A (PP2A) in their kinetic model. This contributes to the induction of LTD in [Kuroda 2001] as the concentration of protein kinase C surpasses the PP2A concentration. However, to simulate LTP in cerebellar PCs, it is necessary that PP2A keeps activated even when the calcium stimulation stops. The absence of the calcium stimulation after the initial phase of the AMPA receptor phosphorylation inhibited the activation of calcium-calmodulin dependent PP2A. This mechanism favours the LTD induction in all simulations. Due this fact and because many mechanisms occur simultaneously in the complex signalling network proposed by Kuroda and collaborators, I decided to propose a new model that simulates the phosphorylation of AMPA receptors in a simplified manner. Thus, to investigate the role of βCaMKII in the regulation of bidirectional plasticity at PF-PC synapses, I propose a kinetic model of AMPA receptor phosphorylation as follows.

7.3 Bidirectional Plasticity Model

A kinetic simulation of the phosphorylation and dephosphorylation of AMPA receptors by CaMKII and protein phosphatase 2B (PP2B) was developed here. This model is based on the CaMKII activation model presented in Section 6.1.

Because Van Woerden et al have suggested that the binding of F-actin to CaMKII could underlie the direction switch of plasticity [van Woerden 2009] (Section 3.4), the model then includes the binding of F-actin to CaMKII to simulate the plasticity induction in wild-type mice, whereas the F-actin binding was omitted in the knockout mice that lack βCaMKII.

The simple model for AMPA receptor phosphorylation consists of six reactions (Figure 7.2): calcium-calmodulin (Ca_4CaM)-dependent activation of CaMKII, CaMKII binding to F-actin, binding of calcium to CaM to form Ca_4CaM, PP2B activation by Ca_4CaM, and AMPA receptor phosphorylation and dephosphorylation by, respectively, CaMKII and PP2B.

CaMKII subunits in the model for AMPA receptor phosphorylation in *Camk2b* knockout mice are in one of four states: W_i, W_b, W_p, and W_a, as in the model developed in Section 6.1 (Figure 7.2A). The CaMKII subunits in the wild-type model can also be in states bound to F-actin (Ac): W_iAc, W_bAc, W_pAc, and W_aAc.

The formation of Ca_4CaM in Chapter 6 was modelled, effectively, as an instantaneous process (Equation 6.7). Here, the actual binding of four calcium ions to calmodulin (CaM) to form Ca_4CaM is included in the model (Figure 7.2B). Furthermore, the Ca_4CaM complex not only activates CaMKII, but is also responsible for the PP2B activation [Meyer 1992] (Figure 7.2C).

Because binding of βCaMKII to F-actin is thought to result in clustering of the kinase holoenzyme [Meyer 1992], W_bAc, W_pAc and W_aAc are unavailable for AMPA receptor phosphorylation. In the model presented here, phosphorylation of AMPA receptors is therefore mediated by the active CaMKII subunits that are not bound to F-actin ($\mathrm{CaMKII_{ac}} = W_b + W_p + W_a$). All active PP2B regulates the receptor dephosphorylation (Figure 7.2D).

The full kinetic model with its associated ordinary differential equations (ODEs) is detailed in Appendix E.1, and the parameter values adopted in all model simulations are given in Appendix E.3. All following results were obtained by numerically integrating Equations E.1-E.25 in XPPAUT, using the CVODE method with 10^{-10} relative and absolute error tolerances.

Before investigating the experimental results of bidirectional plasticity in [van Woerden 2009], it is necessary to validate the model developed here. For that reason, I first simulate the suggested mechanisms of plasticity at PF-PC synapses, as described in the following.

7.4 Plasticity in Purkinje Cells

The F-actin binding to CaMKII initially was not included in the model. The aim of the following simulations is to reproduce the processes of plasticity induction in PCs: low calcium concentrations mediate the induction of LTP, whereas LTD is generated by high calcium concentration increases. For this purpose, the kinase and phosphatase activations and the AMPA receptor phosphorylation were analysed in response to two types of calcium stimulations: constant and oscillatory.

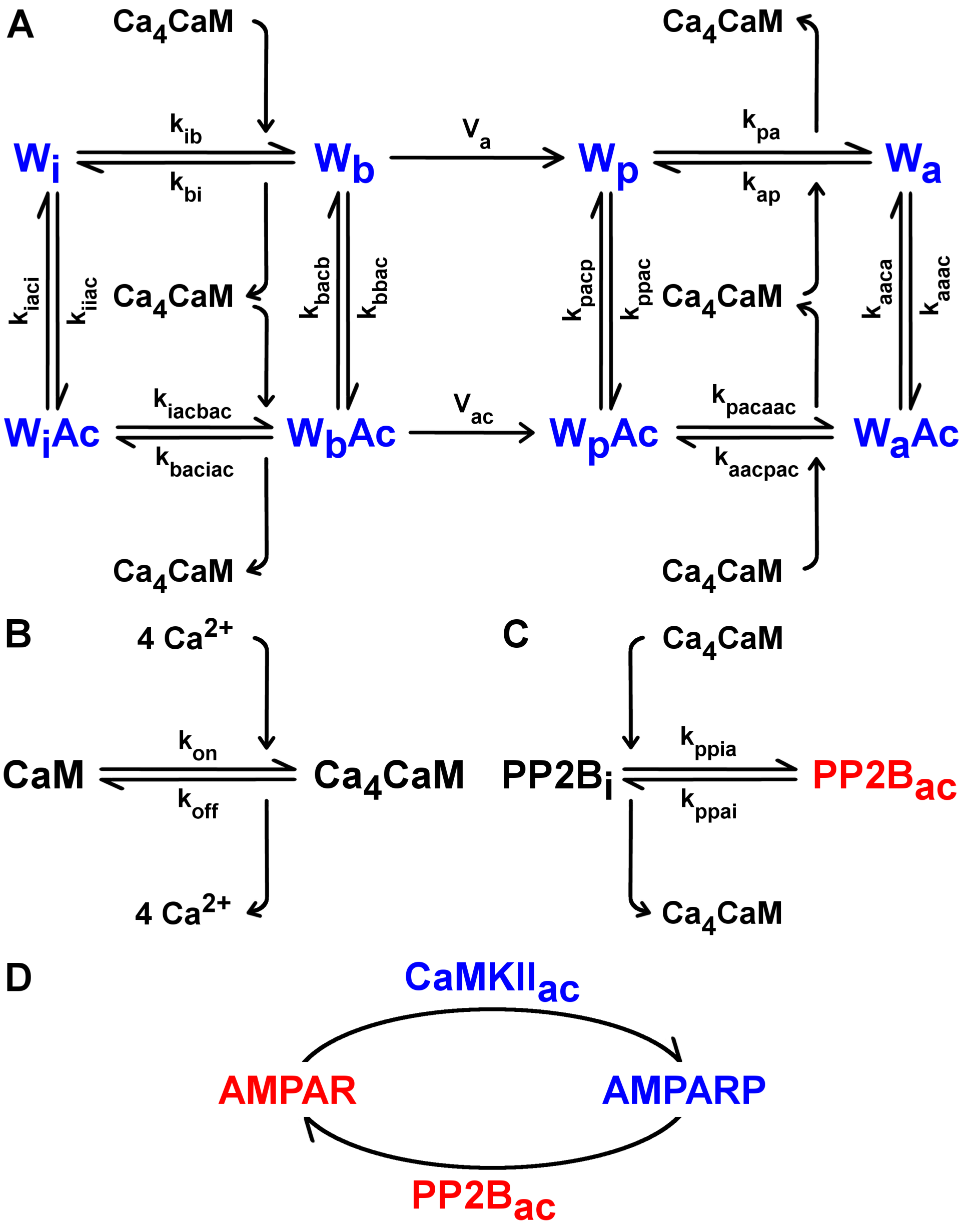

Figure 7.2: **Model of bidirectional plasticity at PF-PC synapses. A.** CaMKII activation by Ca_4CaM, and its binding to F-actin (Ac). As in Figure 6.1A, CaMKII subunits are in one of four states: W_i, W_b, W_p, and W_a for simulations of *Camk2b* knockout mice, whereas solely in simulations of wild-type mice, the kinase can also bind to Ac and be in the W_iAc, W_bAc, W_pAc, and W_aAc subunit states. The kinetic constants of the reversible Ca_4CaM binding reactions are k_{ib}, k_{bi}, k_{pa}, k_{ap}, k_{iacbac}, k_{baciac}, k_{pacaac} and k_{aacpac}, whereas k_{iiac}, k_{iaci}, k_{bbac}, k_{bacb}, k_{ppac}, k_{pacp}, k_{aaac} and k_{aaca} denote the speed of the reversible Ac binding reactions. The rates of the irreversible phosphorylation of W_b and W_bAc are V_a and V_{ac}, respectively. **B.** Binding of four calcium ions (4 Ca^{2+}) to CaM to form Ca_4CaM. k_{on} and k_{off} are the rate constants of the reversible 4 Ca^{2+} binding reaction. **C.** PP2B activation by Ca_4CaM. $PP2B_i$ and $PP2B_{ac}$ are the inactive and active forms of PP2B. The respective rates of PP2B activation and inactivation are k_{ppia} and k_{ppai}. **D.** AMPA receptor phosphorylation and dephosphorylation by active CaMKII ($CaMKII_{ac} = W_b + W_p + W_a$) and $PP2B_{ac}$.

7.4.1 Constant Calcium Stimulation

Constant calcium levels stimulate the induction of LTD and LTP in the model (Figures 7.3 and 7.4). For low calcium concentrations, the amount of active phosphatase (PP2B_{ac}) exceeds the active kinase levels ($\text{CaMKII}_{\text{ac}}$), resulting in LTP induction. LTD is generated in response to high concentrations of calcium, where $\text{CaMKII}_{\text{ac}}$ concentrations surpass PP2B_{ac} levels (Figure 7.3A). Moreover, the induction of LTP for low calcium concentrations results in higher levels of unphosphorylated AMPA receptors than phosphorylated. Because high concentrations of calcium generate LTD, the amount of phosphorylated AMPA receptors exceeds the unphosphorylated one for high constant calcium stimulations (Figure 7.3B).

Standard protocols of LTD and LTP induction normally involve repetitive calcium stimuli (e.g. 1 Hz for 300 s). In the next section, results obtained with a model that includes such pulsed calcium stimulation are described.

7.4.2 Pulsed Calcium Stimulation

To generate calcium pulses with concentrations that reflect experimental data [Wang 2000], the simple model of bidirectional plasticity uses a calcium dynamics model (Equation E.1):

$$\frac{d[\text{Ca}]}{dt} = -4\text{k}_{\text{on}}[\text{Ca}]^4[\text{CaM}] + 4\text{k}_{\text{off}}\,[\text{Ca}_4\text{CaM}] + \gamma(t) - \kappa\left([\text{Ca}] - [\text{Ca}_{\text{min}}]\right) \quad , \tag{7.1}$$

where $[x]$ denotes the concentration of substance x, e.g. [Ca] is the calcium concentration. The term $\gamma(t) - \kappa([\text{Ca}] - [\text{Ca}_{\text{min}}])$ describes the simple model of calcium dynamics I have adopted, where $\gamma(t)$ denotes calcium concentration increases at each time step which values originate from an input table, κ is a term that reflects the calcium removal through diffusion, pumps, exchanges, and $[\text{Ca}_{\text{min}}]$ is the basal calcium concentration.

Input with high calcium influx rates ($\gamma(t)$) was used to stimulate the model to generate realistic amplitudes of calcium in response to PF alone and PF + climbing fibre (CF) stimulations (Figure 7.5).

As in the simulation with a constant calcium concentration, low amplitudes of calcium spikes that represent PF stimulation alone generate LTP, whereas PF and CF stimulation, which is represented by high amplitudes of calcium pulses, induces LTD (Figures 7.6 and 7.7).

The adoption of oscillatory calcium concentrations requires modifications of kinetic parameters used for the constant stimulation protocol (Table E.1). Half the rate of Ca_4CaM dissociation from W_b and a hundred times faster Ca_4CaM formation rate are necessary to induce plasticity at PF-PC synapses in this case (Table E.2).

The simulation protocols used so far aimed at demonstrating that the simple model reproduces the suggested mechanisms of plasticity in PCs. To simulate the bidirectional plasticity at the PF-PC synapse and examine what may underlie the process observed by Van Woerden et al (2009), the F-actin binding was then incorporated into the model.

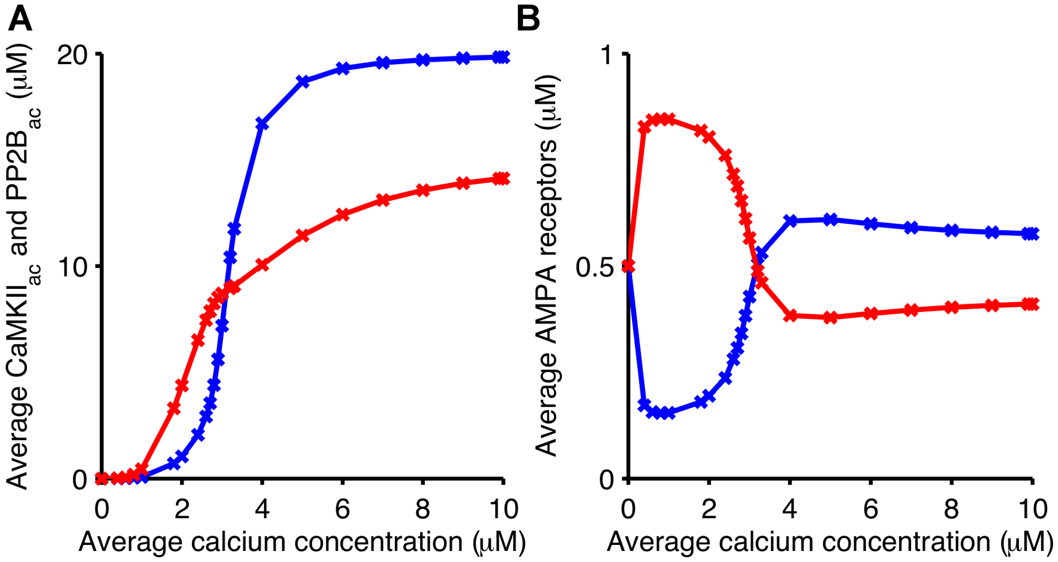

Figure 7.3: **Plasticity at PF-PC synapses in response to constant calcium stimulation.** The figure illustrates average concentrations of the compounds in Figure 7.2D as a function of constant calcium concentrations over a 300 s run. **A.** Average concentration levels of PP2B$_{ac}$ (red) surpass the CaMKII$_{ac}$ levels (blue) for low constant calcium concentrations, resulting in LTP induction, whereas the opposite case occurs for high calcium concentrations in which LTD is generated. **B.** The same mechanism is observed for average concentrations of unphosphorylated and phosphorylated AMPA receptors: AMPAR (red) and AMPARP (blue), respectively.

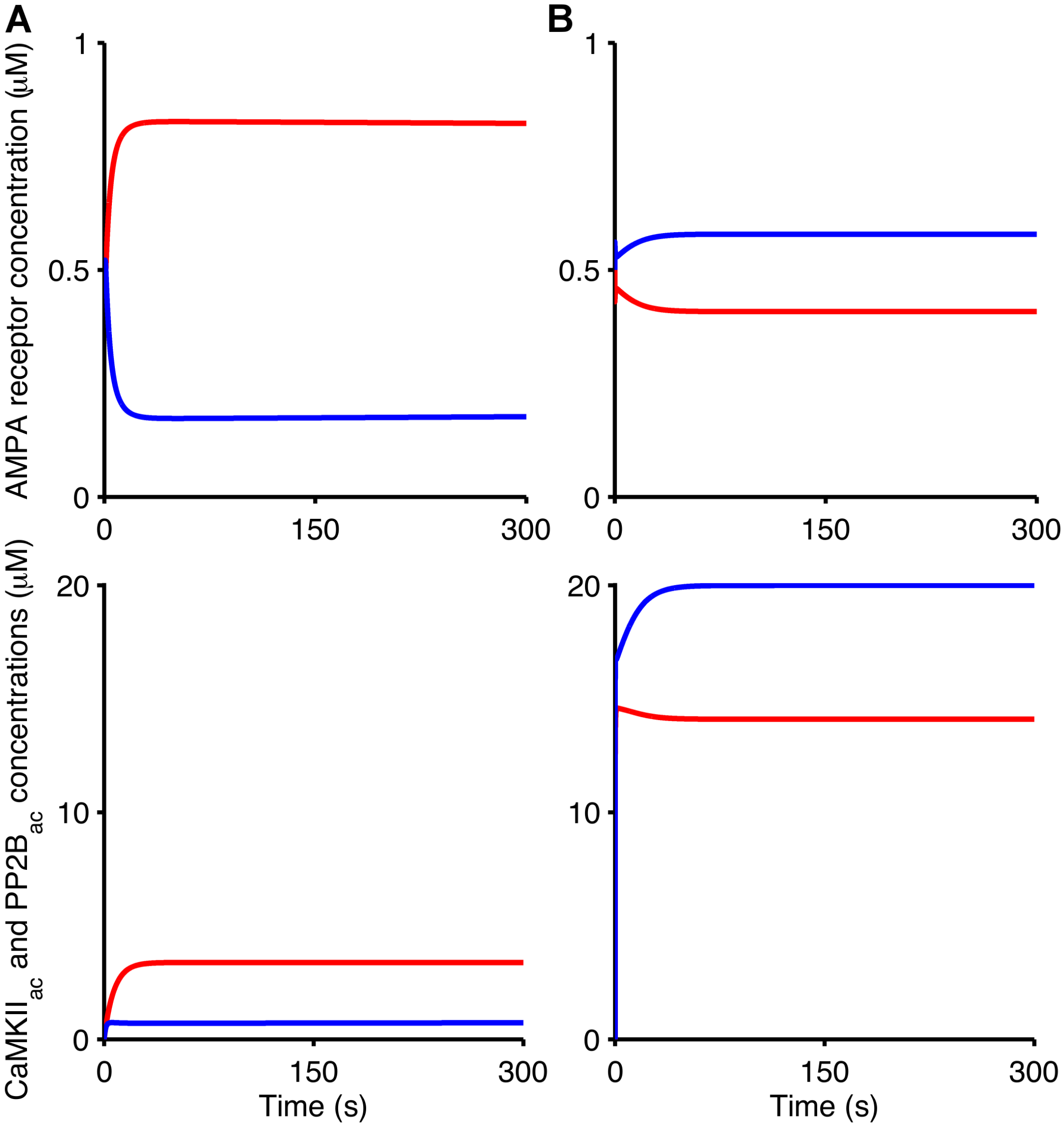

Figure 7.4: **Plasticity at PF-PC synapses in response to constant calcium stimulation.** Plasticity induction at this synapse is also observed while plotting the temporal evolution of the substances in Figure 7.3: unphosphorylated and phosphorylated AMPA receptors (top, red and blue), CaMKII$_{ac}$ and PP2B$_{ac}$ (bottom, blue and red). A low constant calcium concentration evokes LTP (**A**, 1.8 μM), while a high calcium concentration leads to LTD (**B**, 10 μM).

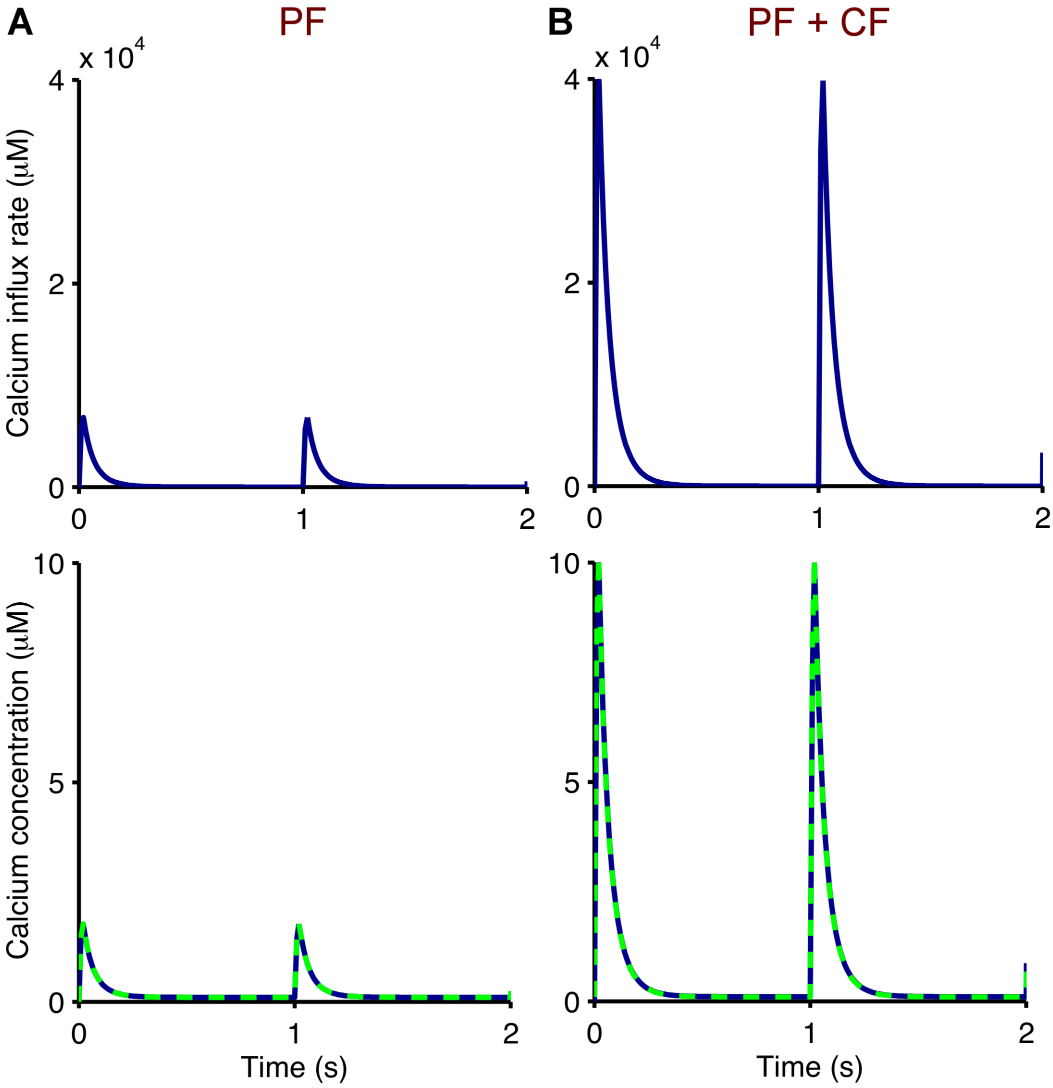

Figure 7.5: **Pulsed calcium stimulation for cerebellar PF-PC synapses.** Calcium influx rates (top, $\gamma(t)$ in Equation E.1) are used as input to the model developed in this chapter to generate the desired output of calcium spikes (bottom, [Ca] in Equation E.1). These match experimental data in [Wang 2000, Kuroda 2001] (dashed) which represent stimulations of PF alone (**A**, pulse amplitude of 1.8 μM) and paired PF and CF (**B**, pulse amplitude of 10 μM). Both calcium stimulations are applied at 1 Hz for 300 s.

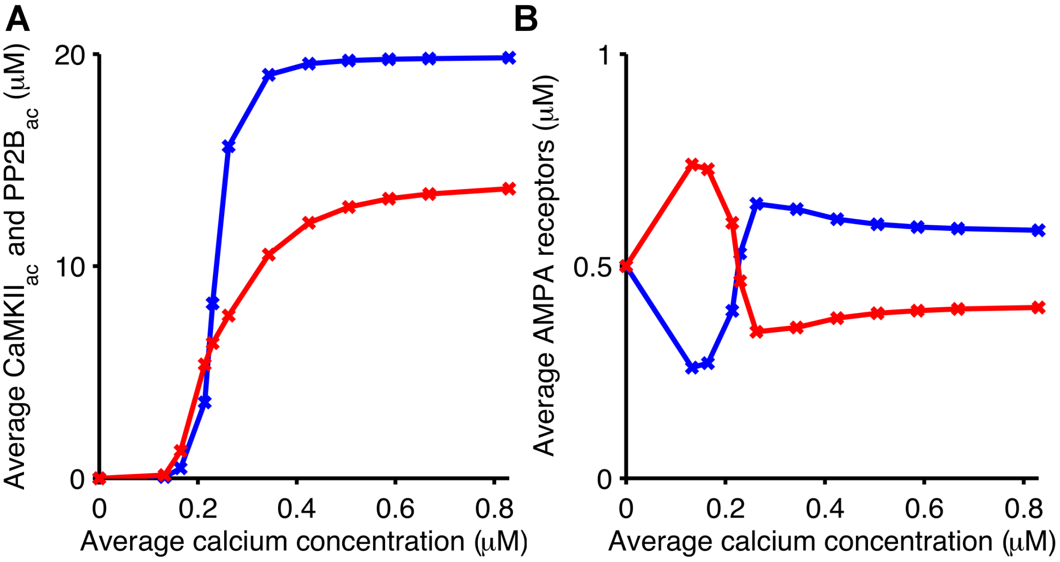

Figure 7.6: **Plasticity at PF-PC synapses in response to pulsed calcium stimulation.** The figure shows average concentrations of the substances in Figure 7.2D in response to different stimulations of pulsed calcium over 300 s. **A.** Concentration levels of PP2B$_{ac}$ (red) exceed the CaMKII$_{ac}$ levels (blue) for low concentrations of oscillatory calcium, generating LTP, whereas the opposite case is observed for high calcium concentrations in which LTD is induced. **B.** The same mechanism occurs for respective concentrations of unphosphorylated and phosphorylated AMPA receptors: AMPAR (red) and AMPARP (blue).

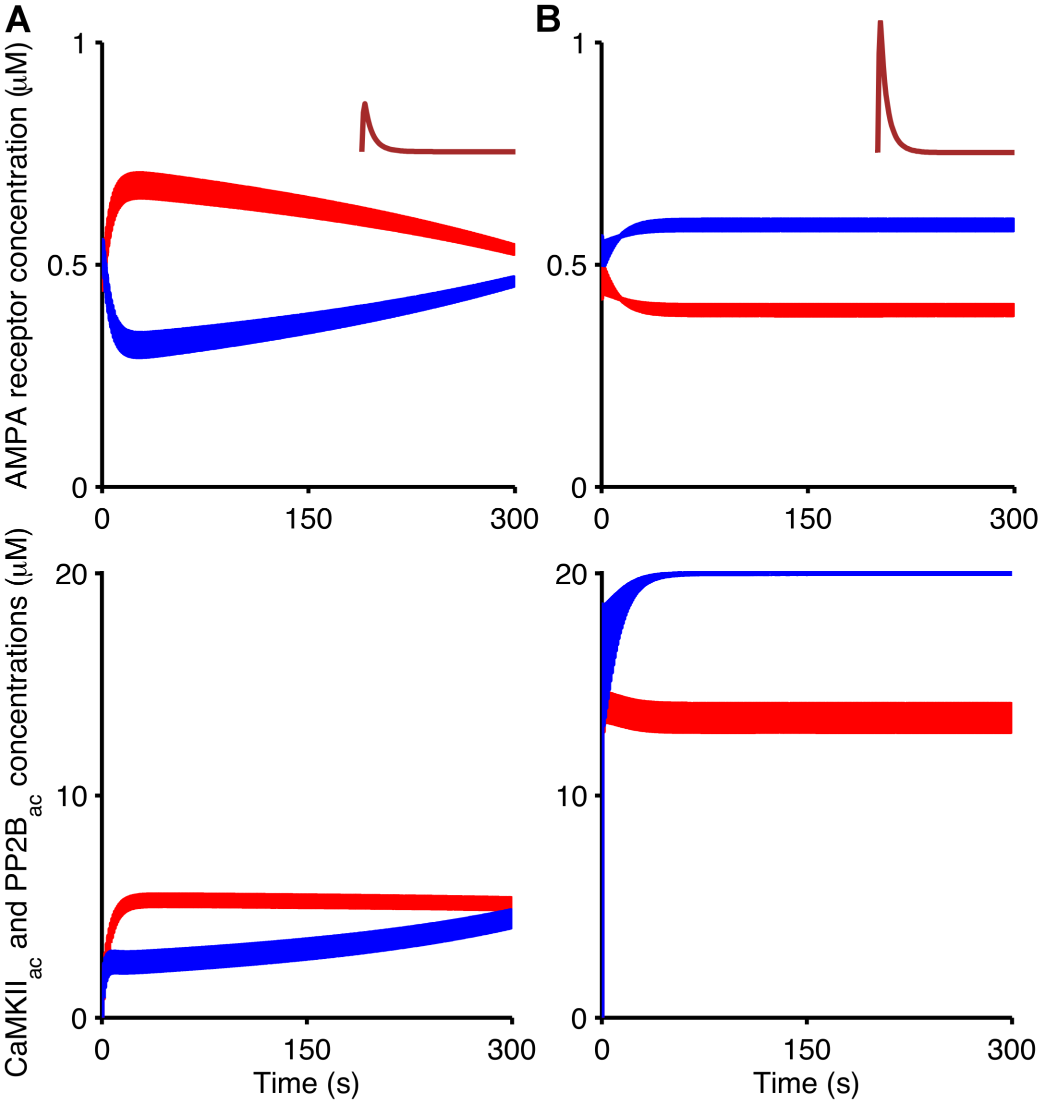

Figure 7.7: **Plasticity at PF-PC synapses in response to pulsed calcium stimulation.** Time-evolution of unphosphorylated and phosphorylated AMPA receptors (top, red and blue), CaMKII$_{ac}$ and PP2B$_{ac}$ (bottom, blue and red) in response to **A.** a low calcium concentration from the PF input alone (Figure 7.5A), and **B.** a high calcium concentration as a result of the paired PF and CF stimulation (Figure 7.5B).

7.5 Bidirectional Plasticity in Purkinje Cells

7.5.1 Replication of the Study by Van Woerden and Collaborators

To replicate the experimental findings in [van Woerden 2009], I simulate the AMPA receptor phosphorylation for wild-type and *Camk2b* knockout mice conditions. The F-actin binding to CaMKII was included to model the wild-type mice that contain both α and β kinase isoforms, while for the *Camk2b* knockout mice that lack βCaMKII the F-actin binding was omitted. Moreover, because the cerebellum contains four times as much βCaMKII as αCaMKII [Fink 2002], the total CaMKII concentration for the *Camk2b* knockout mice is five times lower.

The simple bidirectional plasticity model presented here replicates the experimental observations in [van Woerden 2009], suggesting that the binding of F-actin to βCaMKII may indeed contribute to the control of bidirectional plasticity at PF-PC synapses (Figures 7.8, 7.9 and 7.10).

The model predicts that the sign reversal of synaptic plasticity is based on a combination of three mechanisms operating at different calcium concentrations. At the low calcium concentrations that result from PF input alone, the loss of F-actin binding in the knockout mice leads to increased availability of active CaMKII compared to the wild-type mice, and to induction of LTD rather than LTP (Figure 7.8A). At the high calcium concentrations that are triggered by paired PF and CF input, the reduced CaMKII concentration in the knockout mice favours the dephosphorylation of AMPA receptors by PP2B, and the induction of LTP instead of LTD. This effect is exacerbated by the increased availability of Ca_4CaM that results from the decreased CaMKII levels, which further increases the activation of PP2B.

To reproduce the results in [van Woerden 2009], it was necessary to adjust a few rate constants previously adopted for the plasticity induction in response to pulsed calcium stimulation (Section 7.4.2): a higher CaMKII total concentration, more realistic kinetic constants for the phosphorylation and dephosphorylation of AMPA receptors, a faster Ca_4CaM formation, and a slower PP2B activation (Table E.3).

The next section gives simulation results of bidirectional plasticity with parameter values suggested by the authors of Van Woerden et al (2009).

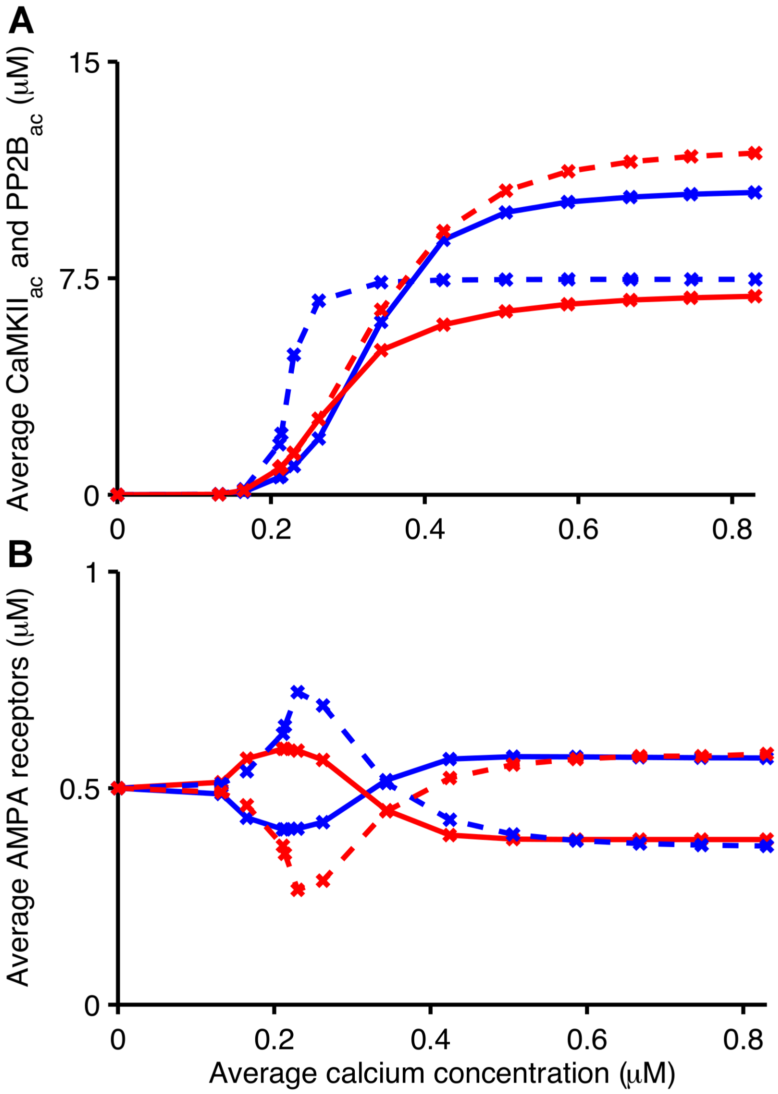

Figure 7.8: **Bidirectional plasticity at PF-PC synapses: replication of the experimental findings in [van Woerden 2009].** This figure reproduces the experimental observations illustrated in Figure 7.1 [van Woerden 2009]. Low calcium concentrations that induce LTP in wild-type mice (solid) lead to LTD in *Camk2b* knockout mice (dashed), and vice versa. In the model, the F-actin binding to CaMKII occurs in wild-type mice, whereas knockout mice that lack βCaMKII do not bind to F-actin. **A.** Average concentrations of CaMKII$_{ac}$ (blue) and PP2B$_{ac}$ (red) as a function of average concentrations of pulsed calcium. **B.** Average concentrations of unphosphorylated and phosphorylated AMPA receptors (red and blue, respectively) in response to the same stimulation protocols.

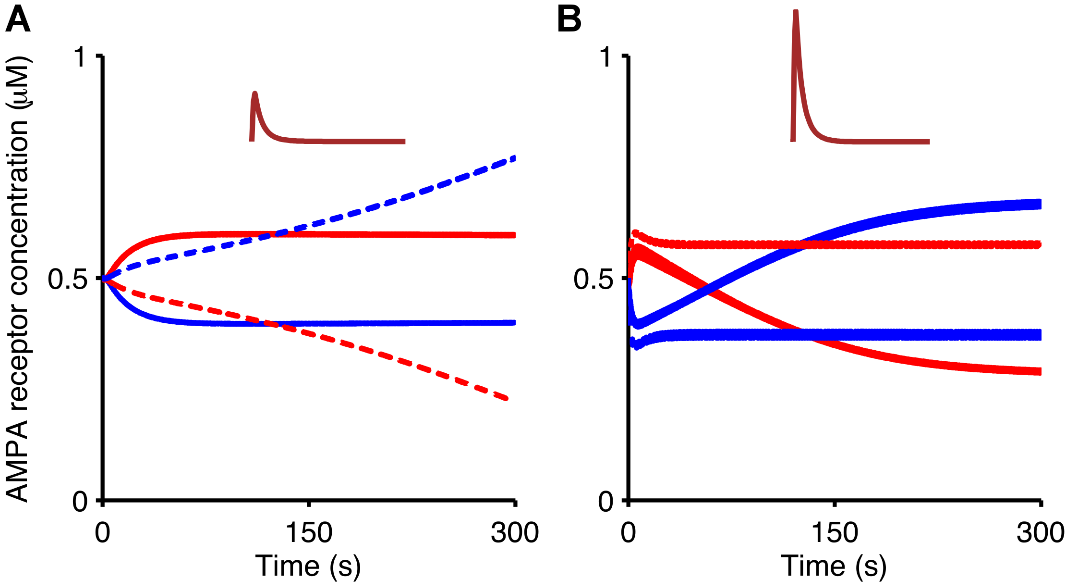

Figure 7.9: **Bidirectional plasticity at PF-PC synapses: replication of the experimental findings in [van Woerden 2009].** The mechanisms of bidirectional plasticity at this synapse are also observed while plotting the temporal evolution of unphosphorylated and phosphorylated AMPA receptors (red and blue, respectively) for wild-type and *Camk2b* knockout mice (solid and dashed, respectively) in response to a low calcium concentration from the PF input alone (**A**), and a high calcium concentration as a result of the paired PF and CF stimulation (**B**).

7.5.2 Parameter Values Based on Experimental Observations

Following suggestions from experimentalists of the Erasmus Medical Center Rotterdam, who are co-authors of [van Woerden 2009], new values for a few parameters used in the bidirectional plasticity model were included in the model (Table E.4). Although the cerebellum comprises four times as much βCaMKII as αCaMKII [Fink 2002], the actual α:β CaMKII ratio is 1:1 in PCs [Hansel 2006, van Woerden 2009]. Therefore, the CaMKII concentration for *Camk2b* knockout mice is now half the kinase concentration for wild-type mice, which was reduced as in [Lisman 2002]. Observations by [Brocke 1999] suggest that CaMKII isoforms have different affinities for Ca$_4$CaM, which is reflected in the new parameter values: βCaMKII has a greater affinity (0.02 μM) for Ca$_4$CaM than αCaMKII (0.04 μM). Moreover, the basal calcium concentration was reduced from 0.1 μM to 0.045 μM, based on observations described in [Airaksinen 1997, Schmidt 2003, Antunes 2012].

The experimentalists also pointed out that the calcium concentration levels triggered by PF input alone and PF + CF used in the model were higher than those observed by [Canepari 2008]. Thus, the maximum peak of calcium concentration in result to coincident PF and CF stimulation is now 1.8 μM [Canepari 2008] rather than 10 μM [Wang 2000], whereas PF input alone triggers a maximal calcium con-

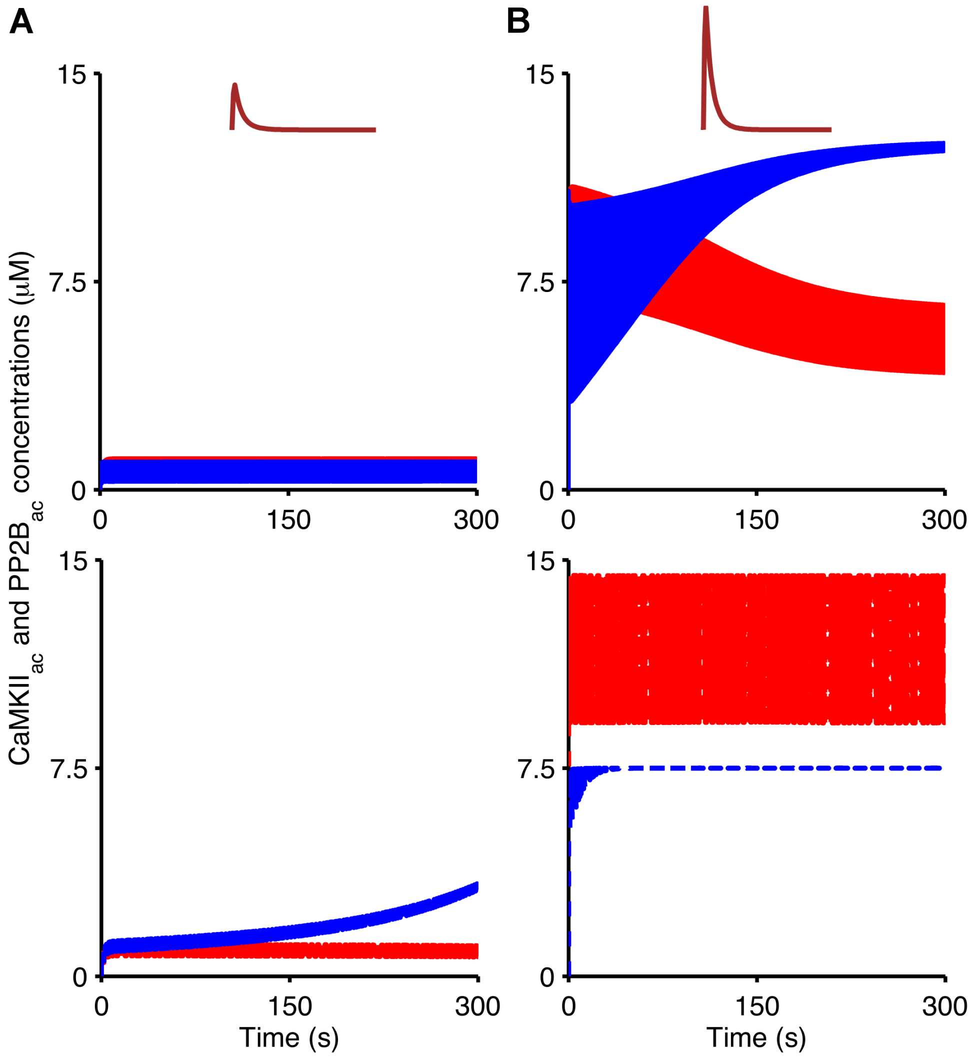

Figure 7.10: **Bidirectional plasticity at PF-PC synapses: replication of the experimental findings in [van Woerden 2009].** Time-evolution of CaMKII$_{ac}$ (blue) and PP2B$_{ac}$ (red) in wild-type mice (top, solid) and *Camk2b* knockout mice (bottom, dashed) in response to low calcium concentrations as a result of the PF input alone (**A**), and high calcium concentrations from the coincident PF and CF stimulation (**B**).

centration of 0.18 μM [Canepari 2008] instead of 1.8 μM [Wang 2000].

Simulations obtained with the simple model also replicate the experiments in [van Woerden 2009] when using new parameter values suggested by the authors of this paper (Figures 7.11, 7.12 and 7.13). As the new calcium concentration values are much lower than those reported in [Wang 2000], here Ca$_4$CaM formation is 25,000 times faster than in previous simulations. A slightly slower PP2B inactivation and the adjustment of a few parameters for F-actin dissociation from CaMKII were also necessary to simulate the bidirectional plasticity as in [van Woerden 2009]

(Table E.4).

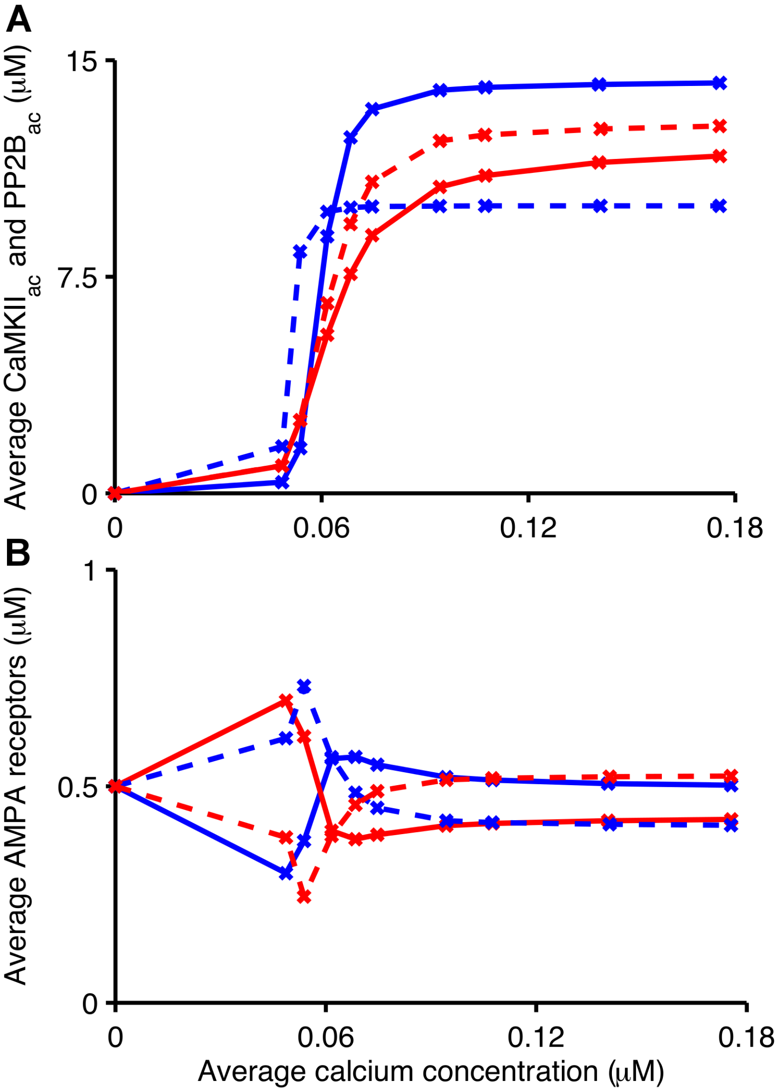

Figure 7.11: **Adoption of new experimental data still replicates the results in [van Woerden 2009]: lower calcium stimulation.** New values for a few parameters used to obtain the results in Figures 7.8, 7.9 and 7.10 were adopted here, following suggestions from the authors of [van Woerden 2009] (Table E.4). These include the adoption of lower amplitudes of calcium pulses that represent the PF input alone and the coincident PF and CF activation. **A.** Average concentrations of CaMKII$_{ac}$ (blue) and PP2B$_{ac}$ (red) as a function of average concentrations of pulsed calcium in wild-type mice (solid) and in *Camk2b* knockout mice (dashed). **B.** Average concentrations of unphosphorylated and phosphorylated AMPA receptors (red and blue, respectively) as a function of average concentrations of oscillatory calcium.

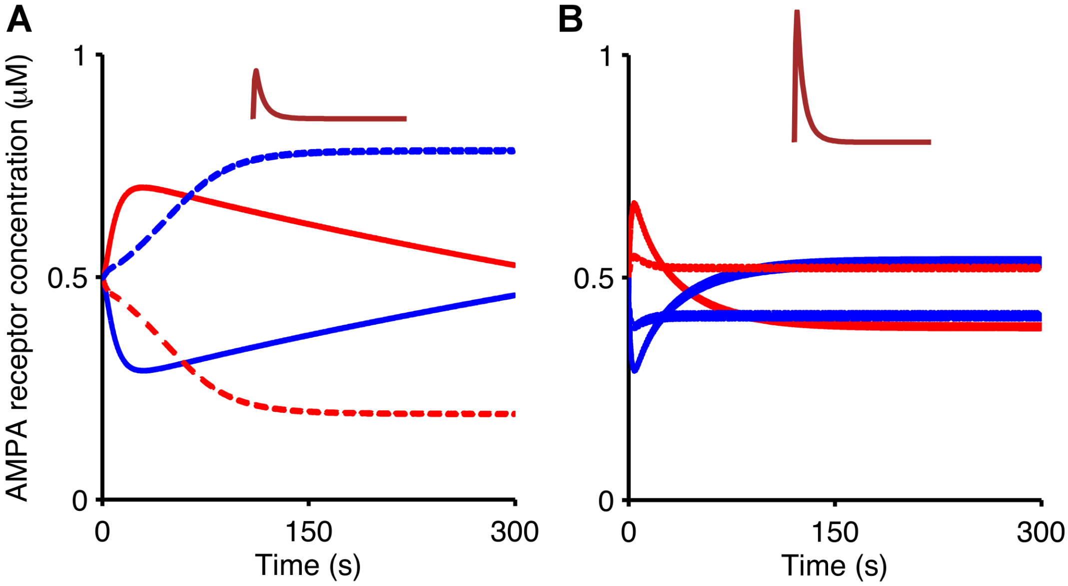

Figure 7.12: **Adoption of new experimental data still replicates the results in [van Woerden 2009]: lower calcium stimulation.** Temporal evolution of unphosphorylated and phosphorylated AMPA receptors (red and blue, respectively) in wild-type and *Camk2b* knockout mice (solid and dashed, respectively) in response to lower calcium concentrations from the PF input alone (**A**, pulse amplitude of 0.18 μM) and the paired PF and CF stimulation (**B**, pulse amplitude of 1.8 μM).

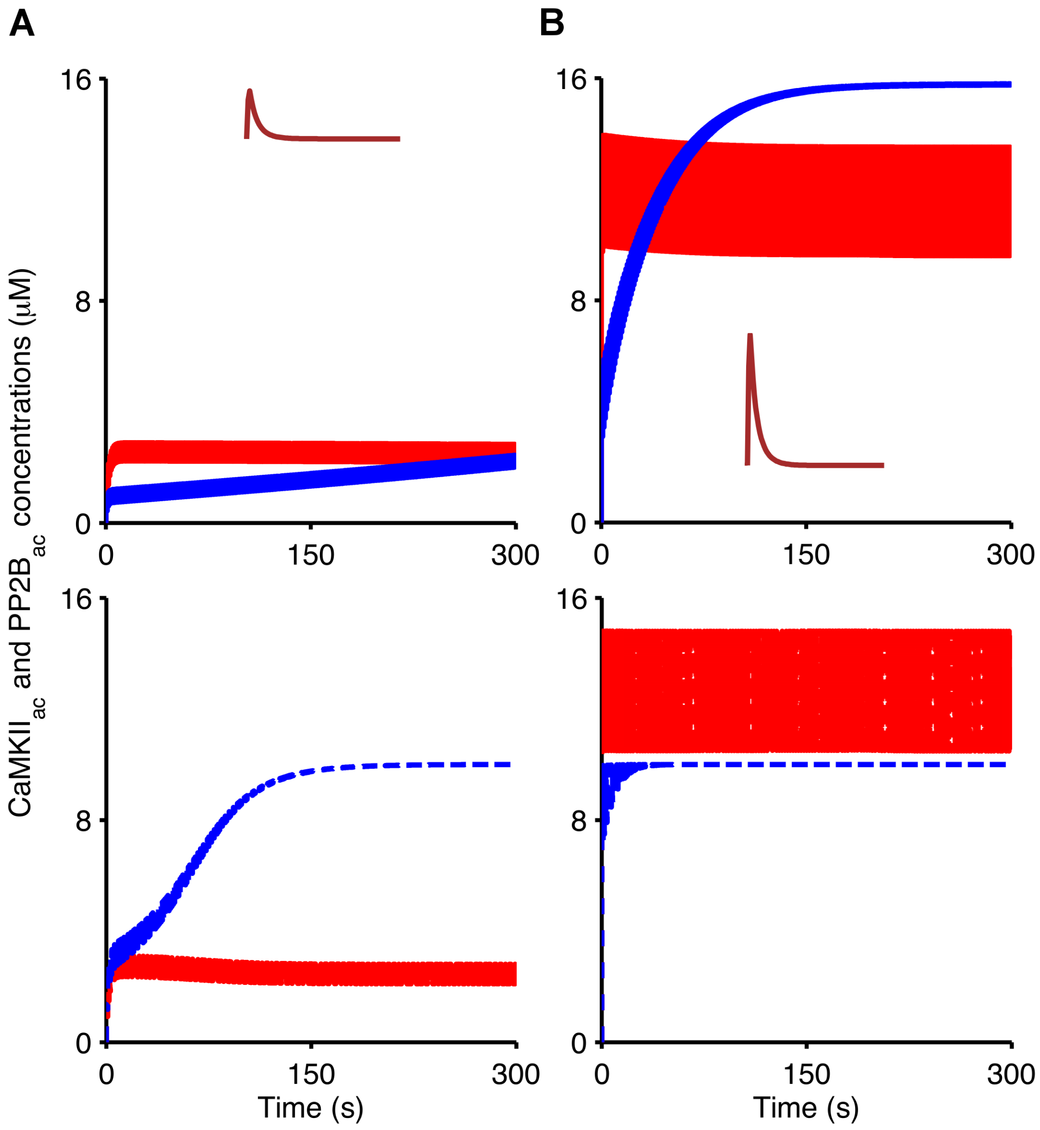

Figure 7.13: **Adoption of new experimental data still replicates the results in [van Woerden 2009]: lower calcium stimulation.** Time-evolution of CaMKII$_{ac}$ (blue) and PP2B$_{ac}$ (red) in wild-type mice (top, solid) and *Camk2b* knockout mice (bottom, dashed) in response to lower calcium concentrations from the PF input alone (**A**, pulse amplitude of 0.18 μM) and the paired PF and CF stimulation (**B**, pulse amplitude of 1.8 μM).

Although the new simulations reproduce the results in [van Woerden 2009], a much greater rate for Ca$_4$CaM formation and very low calcium concentrations may not represent real biological scenarios. For that reason, I readopt the original Ca$_4$CaM formation rate and the previous calcium concentrations as in Figure 7.5 (Table E.3). The adoption of these values still produces similar results as in [van Woerden 2009] (Figures 7.14, 7.15 and 7.16).

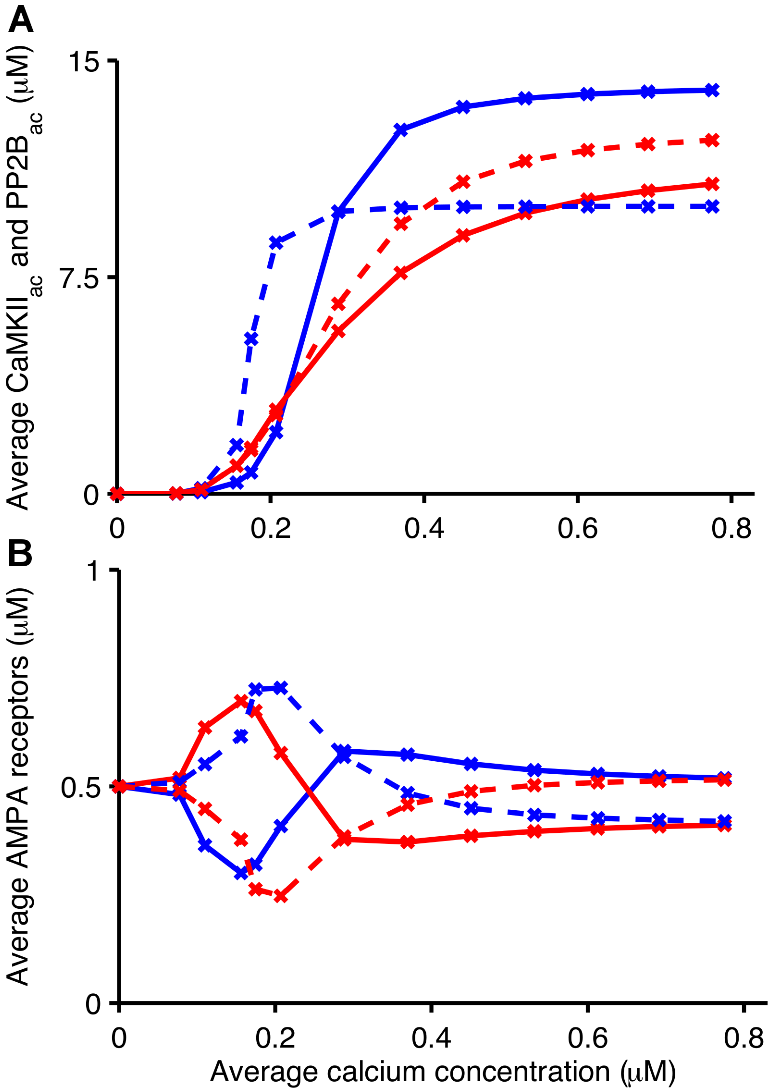

Figure 7.14: **Adoption of new experimental data still replicates the results in [van Woerden 2009]: original calcium stimulation.** The original calcium concentrations used in Figures 7.5-7.10 were readopted here. The figure demonstrates that the model again simulates the bidirectional plasticity at PF-PC synapses for higher calcium concentrations, while adopting the suggested experimental data in Table E.4. **A.** Average concentrations of CaMKII$_{ac}$ (blue) and PP2B$_{ac}$ (red) as a function of average concentrations of pulsed calcium in wild-type mice (solid) and in *Camk2b* knockout mice (dashed). **B.** Average concentrations of unphosphorylated and phosphorylated AMPA receptors (red and blue, respectively) as a function of average concentrations of oscillatory calcium.

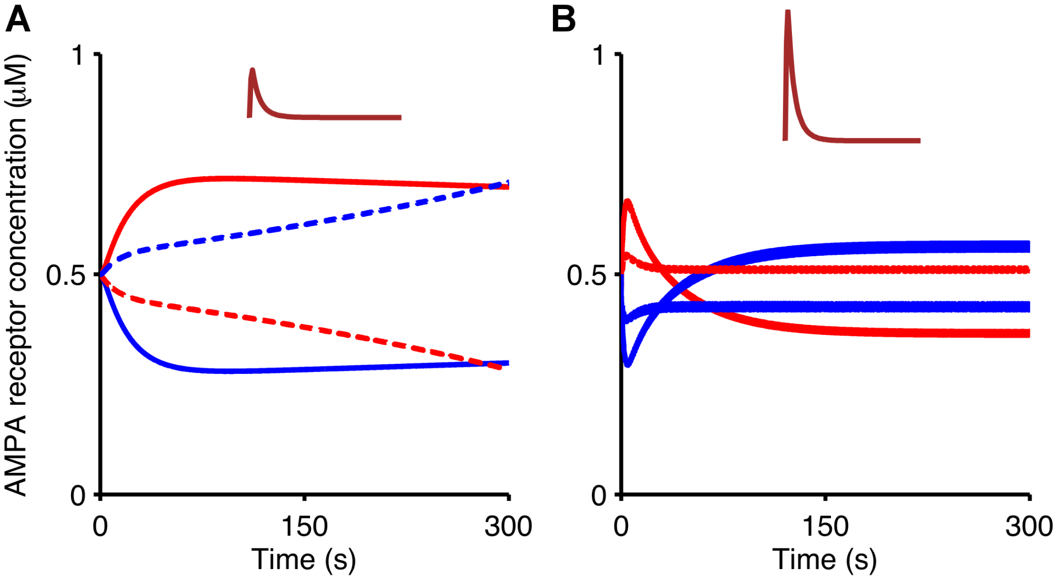

Figure 7.15: **Adoption of new experimental data still replicates the results in [van Woerden 2009]: original calcium stimulation.** Temporal evolution of unphosphorylated and phosphorylated AMPA receptors (red and blue, respectively) in wild-type and *Camk2b* knockout mice (solid and dashed, respectively) in response to low calcium concentrations from the PF input alone (**A**, pulse amplitude of 1.8 μM), and high calcium concentrations as a result of the paired PF and CF stimulation (**B**, pulse amplitude of 10 μM).

In the kinetic simulation developed here, CaM directly binds to four calcium ions in a single reaction, resulting in Ca_4CaM. However, the kinetics of calcium-induced CaM activation has not been resolved yet. The following section tests whether the bidirectional plasticity occurs at PF-PC synapses while modelling the CaM activation in two steps rather than one.

7.5.3 Two-step Calcium-calmodulin Binding

The bidirectional plasticity model was modified here to simulate the CaM binding to four calcium ions as follows: first two calcium ions bind to apo-CaM and form the Ca_2CaM complex, and then the complete saturation of CaM with two more calcium ions results in Ca_4CaM (Figure 7.17). Due to these modifications, apo-CaM and Ca_2CaM may bind to W_i and form the respective W_{b_0} (CaM-bound CaMKII without any calcium ion bound) and W_{b_2} (Ca_2CaM-bound CaMKII), or to W_iAc and result in $W_{b_0}Ac$ (Ac- and CaM-bound CaMKII without any calcium ion bound) and $W_{b_2}Ac$ (Ac- and Ca_2CaM-bound CaMKII), respectively. W_{b_0} and W_{b_2} then recruit two additional calcium ions to, respectively, form W_{b_2} and W_b (Ca_4CaM-bound CaMKII), whereas $W_{b_0}Ac$ and $W_{b_2}Ac$ can also bind to two calcium ions and result in $W_{b_2}Ac$ and W_bAc (Ac- and Ca_4CaM-bound CaMKII), respectively. The new W_{b_0} and W_{b_2} states may bind to Ac and switch to $W_{b_0}Ac$ and $W_{b_2}Ac$.

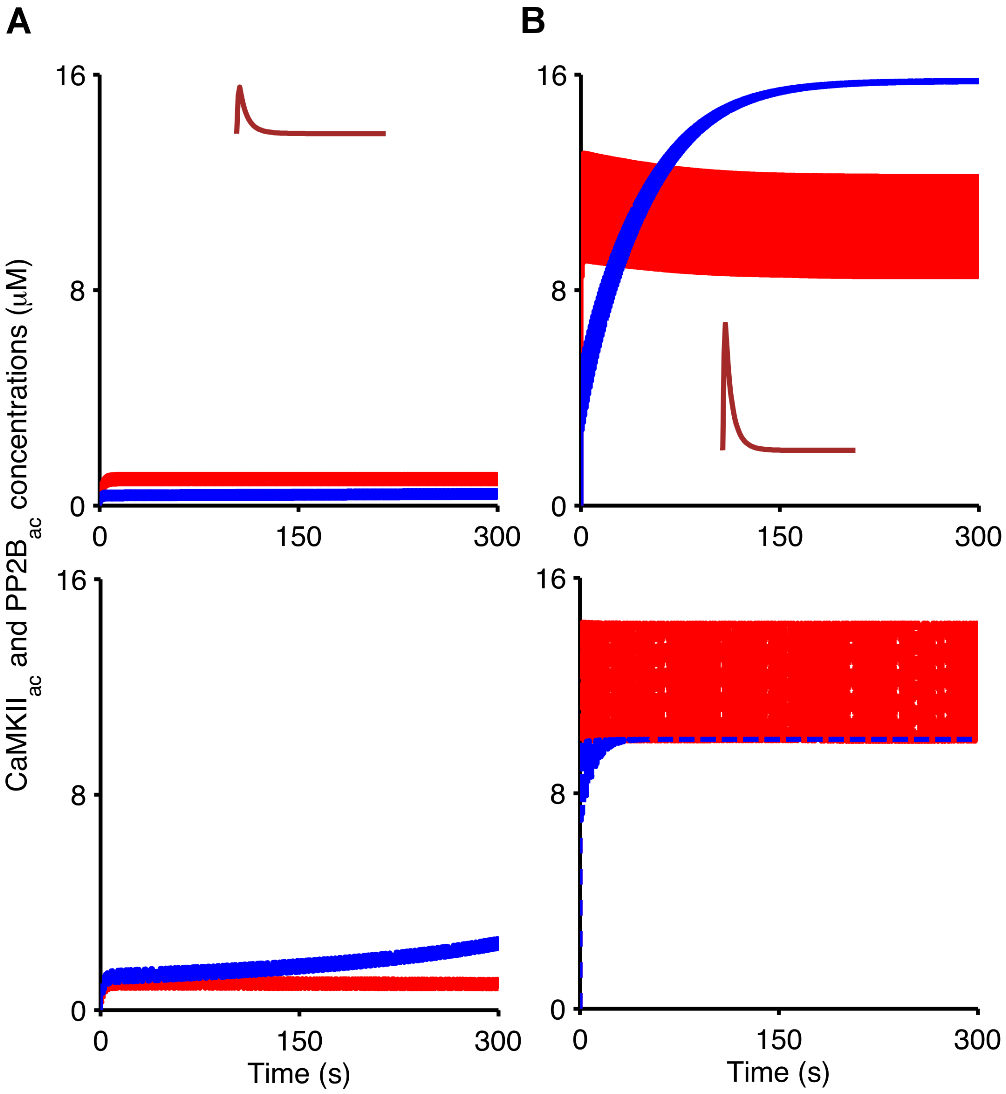

Figure 7.16: **Adoption of new experimental data still replicates the results in [van Woerden 2009]: original calcium stimulation.** Time-evolution of CaMKII$_{ac}$ (blue) and PP2B$_{ac}$ (red) in wild-type mice (top, solid) and *Camk2b* knockout mice (bottom, dashed) in response to low calcium concentrations from the PF input alone (**A**, pulse amplitude of 1.8 μM), and high calcium concentrations as a result of the paired PF and CF stimulation (**B**, pulse amplitude of 10 μM).

The new bidirectional plasticity model also replicates the results in [van Woerden 2009], while modelling the CaM activation by calcium in two steps instead of one (Figures 7.18, 7.19 and 7.20). The mathematical alterations of the model due to the new CaM binding modelling are described in Section E.2. Because new reactions have been added to the model, kinetic parameters were created. Their values were either assumed or calculated according to Hess's law presented in Section 4.1.3.2 (Table E.5).

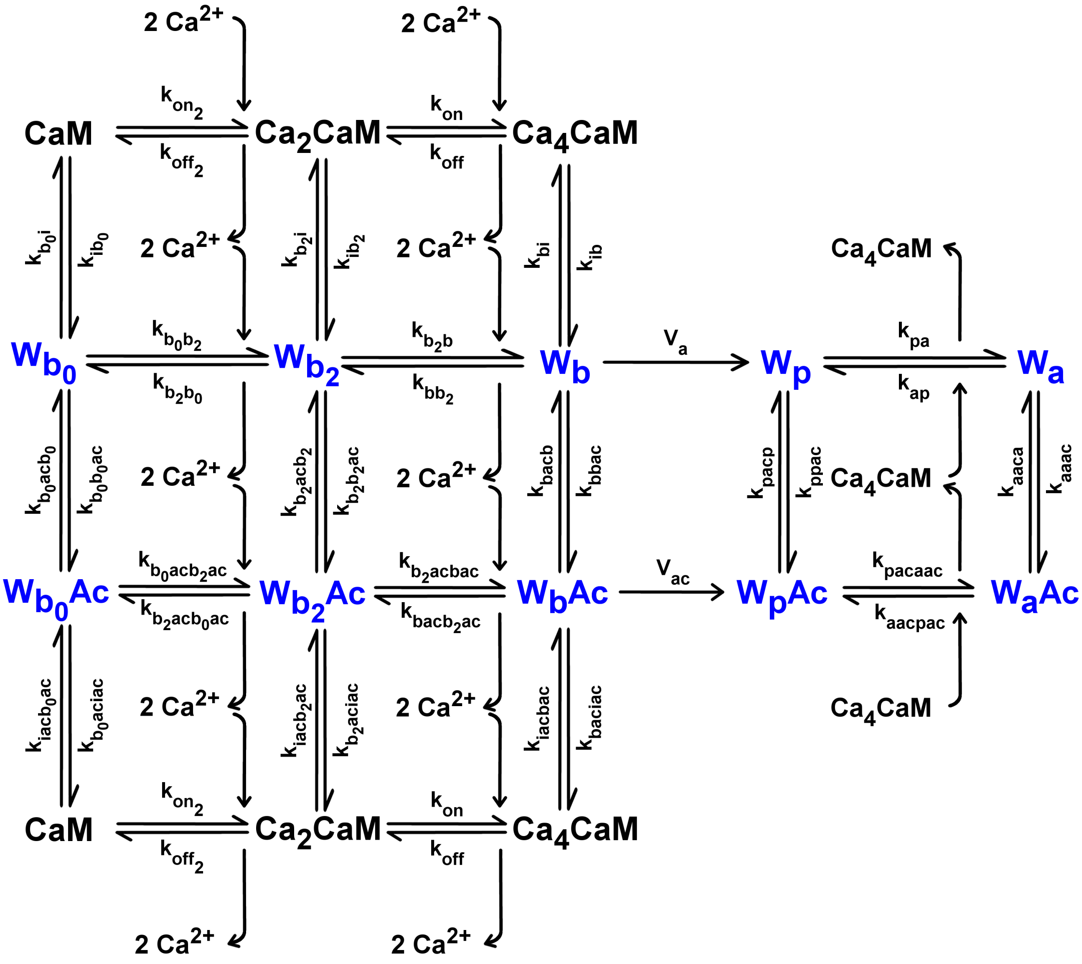

Figure 7.17: **Model of bidirectional plasticity including a two-step Ca_4CaM binding at PF-PC synapses.** The bidirectional plasticity model illustrated in Figure 7.2 was modified here to account for a two-step Ca_4CaM binding. Therefore, this figure substitutes Figures 7.2A and 7.2B. Ca_4CaM is formed in two steps: first two calcium ions (2 Ca^{2+}) bind to apo-CaM resulting in the Ca_2CaM complex, and then 2 Ca^{2+} bind to Ca_2CaM and complete the saturation of CaM. Due to these modifications, W_i and W_iAc can also bind to (i) apo-CaM and form the respective W_{b_0} and $W_{b_0}Ac$, or (ii) Ca_2CaM and form W_{b_2} and $W_{b_2}Ac$, respectively. As a result of the two-step Ca_4CaM binding, here activation of CaMKII by Ca_4CaM also occurs in two phases: W_{b_0} and $W_{b_0}Ac$ can bind to two calcium ions and form, respectively, W_{b_2} and $W_{b_2}Ac$, which may again bind to 2 Ca^{2+} and activate CaMKII, forming the respective W_b and W_bAc. The kinetic constants of the new model are described in Table E.5.

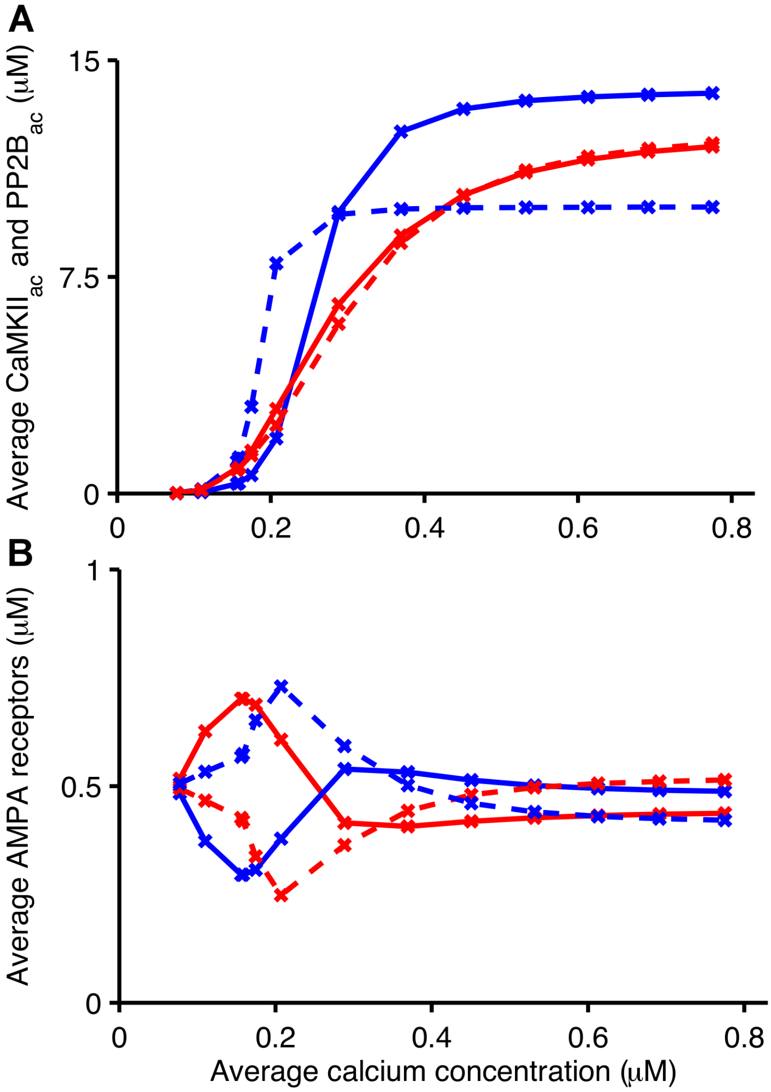

Figure 7.18: **Modelling a two-step Ca_4CaM binding still replicates the results in [van Woerden 2009].** The bidirectional plasticity model was modified to simulate the Ca_4CaM formation in two steps as illustrated in Figure 7.17. **A.** Average concentrations of $CaMKII_{ac}$ (blue) and $PP2B_{ac}$ (red) as a function of average concentrations of pulsed calcium in wild-type mice (solid) and in *Camk2b* knockout mice (dashed). **B.** Average concentrations of unphosphorylated and phosphorylated AMPA receptors (red and blue, respectively) as a function of average concentrations of oscillatory calcium.

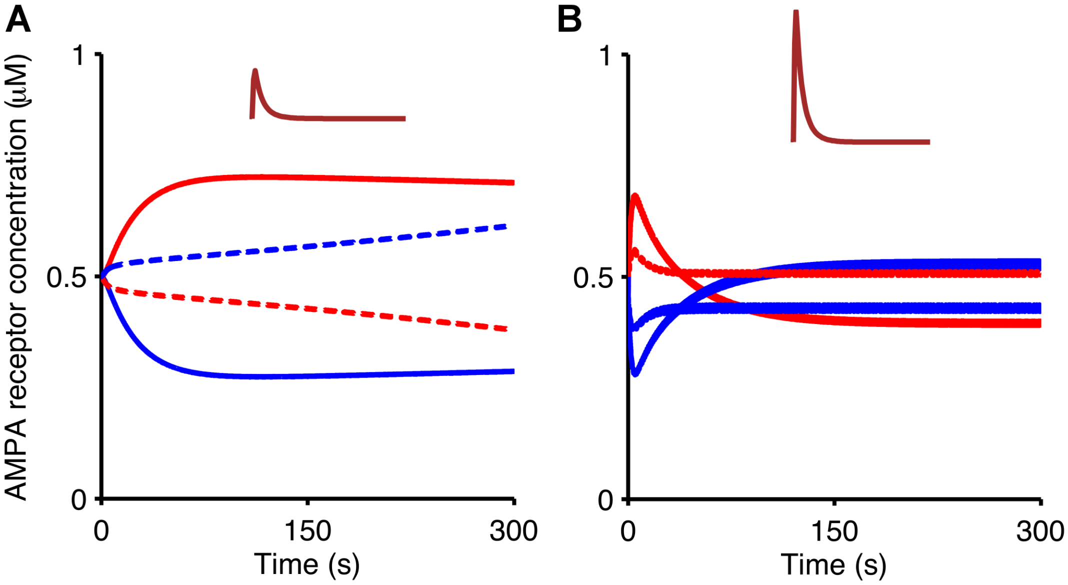

Figure 7.19: **Modelling a two-step Ca_4CaM binding still replicates the results in [van Woerden 2009].** Temporal evolution of unphosphorylated and phosphorylated AMPA receptors (red and blue, respectively) in wild-type and *Camk2b* knockout mice (solid and dashed, respectively) in response to low calcium concentrations from the PF input alone (**A**, pulse amplitude of 1.8 μM), and high calcium concentrations as a result of the paired PF and CF stimulation (**B**, pulse amplitude of 10 μM).

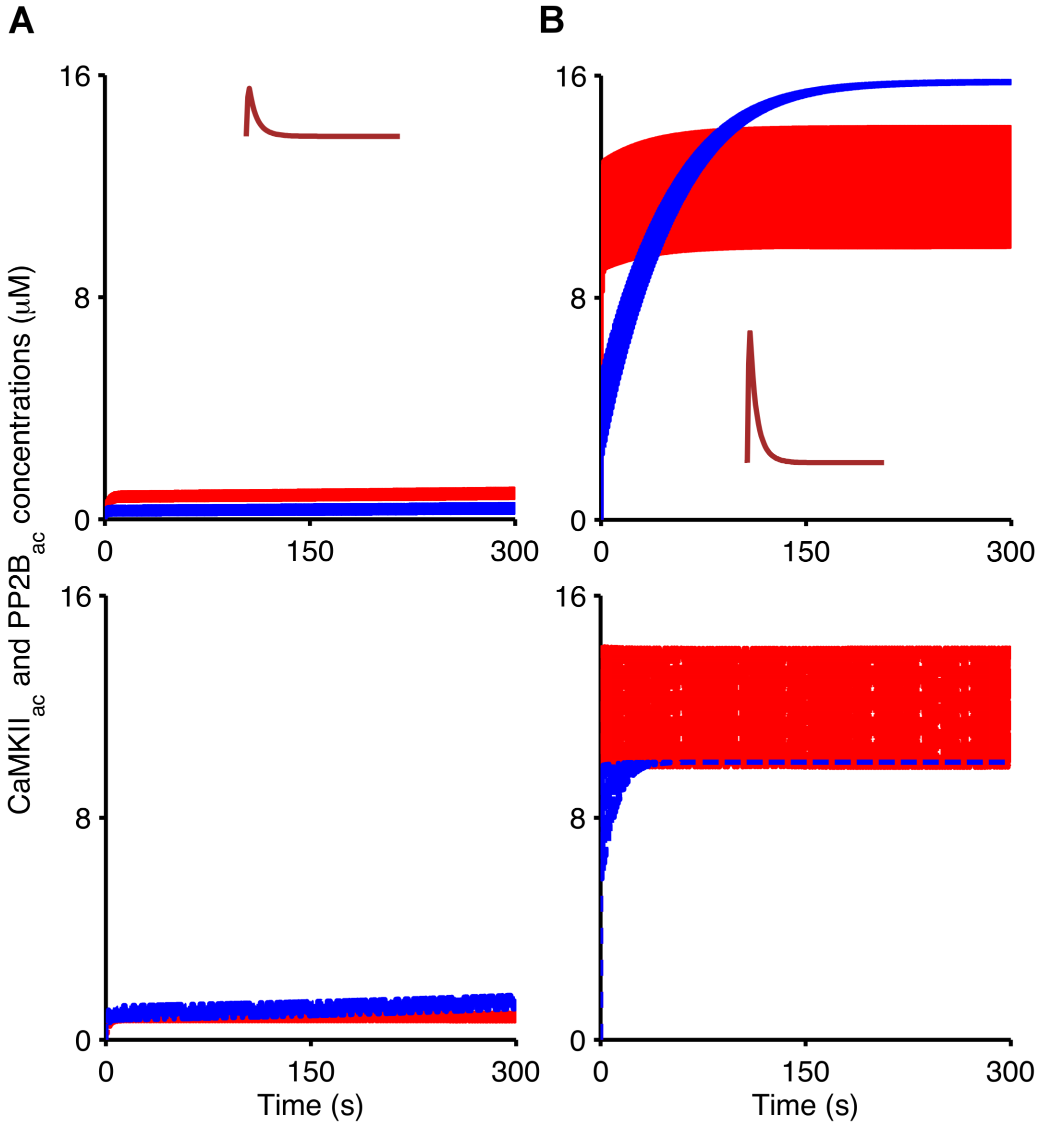

Figure 7.20: **Modelling a two-step Ca$_4$CaM binding still replicates the results in [van Woerden 2009].** Time-evolution of CaMKII$_{ac}$ (blue) and PP2B$_{ac}$ (red) in wild-type mice (top, solid) and *Camk2b* knockout mice (bottom, dashed) in response to low calcium concentrations from the PF input alone (**A**, pulse amplitude of 1.8 μM) and high calcium concentrations as a result of the paired PF and CF stimulation (**B**, pulse amplitude of 10 μM).

7.6 Chapter Conclusions

Long-term plasticity at PF-PC synapses is thought to mediate cerebellar motor learning. PF LTD can be induced by the paired activity of the PF and CF inputs to PCs, and PF LTP induction requires the PF activity alone. However, the β isoform of CaMKII was recently demonstrated to regulate the bidirectional inversion of PF-PC plasticity [van Woerden 2009]. Because the cellular events that underlie these experimental findings are still poorly understood, this chapter aimed at unravelling how βCaMKII controls the direction of plasticity at PF-PC synapses.

Belmeguenai and Hansel (2005) suggested that a kinase/phosphatase switch regulates the bidirectional plasticity in the cerebellum, and also showed that PP2B is involved in plasticity induction at PF-PC synapses [Belmeguenai 2005]. Moreover, it is known that LTD and LTP are mediated by AMPA receptor phosphorylation [Lee 2000, Kuroda 2001]. For those reasons, I proposed a simple model of phosphorylation and dephosphorylation of AMPA receptors by CaMKII and PP2B to investigate the experiments in [van Woerden 2009]. In the model, the F-actin binding was included to simulate wild-type mice that contain the α and β isoforms of CaMKII, and it was omitted in *Camk2b* knockout mice conditions that lack βCaMKII. This mechanism was implemented here because only βCaMKII is responsible for targeting the kinase to F-actin in neuronal cells [Shen 1998].

The bidirectional plasticity model presented in this chapter replicates the experimental observations in [van Woerden 2009]. For the first time, simulation results obtained from this model indicate the mechanisms that underlie the bidirectional inversion of cerebellar plasticity. As suggested by Van Woerden et al (2009), the F-actin binding indeed enables βCaMKII to regulate the bidirectional plasticity at PF-PC synapses. At low calcium concentrations that evoke LTP in wild-type mice, the induction of LTD in knockout mice is only possible due to the loss of F-actin that leads to the precocious activation of CaMKII even in low-calcium conditions. In contrast, different mechanisms are responsible for the induction of LTP at higher concentrations of calcium: the loss of βCaMKII in *Camk2b* knockout mice causes a significant reduction in the total concentration of CaMKII. This phenomenon contributes to a higher availability of Ca_4CaM for PP2B activation which, in turn, leads to LTP induction rather than LTD.

I also explored the bidirectional plasticity model developed here. This model was found to replicate the experimental observations in [van Woerden 2009] in response to different scenarios such as the adoption of parameter values suggested by the authors of [van Woerden 2009], and a two-step modelling of the Ca_4CaM binding. All simulation results demonstrated here reproduce the bidirectional inversion of PF-PC plasticity as in [van Woerden 2009]. These observations suggest that the model is relatively robust.

Although there are many models for PF LTD induction, none of these was set up to investigate the induction of LTP at PF-PC synapses. Indeed, the CaMKII pathway has, so far, not been included in the signalling cascades of existing PF-PC plasticity models. Therefore, this thesis presents the first model for induction of LTD and LTP at PF-PC synapses in which CaMKII plays a prominent role.

CHAPTER 8

Conclusions

Contents

THE aim of this thesis was to contribute to a better understanding of the molecular mechanisms that regulate the induction of synaptic plasticity in cerebellar Purkinje cells (PCs). The focus of the thesis was to investigate the role of the β isoform of calcium-calmodulin dependent protein kinase II (CaMKII) in the bidirectional modulation of plasticity induction at parallel fibre (PF)-PC synapses. The following four questions were addressed:

1. What are the mechanisms that determine the sensitivity of CaMKII to the frequency of calcium oscillations?
2. Does CaMKII decode the frequency of calcium oscillations?
3. How does the network of intracellular signalling molecules in cerebellar PCs implement the induction of long-term depression (LTD) and potentiation (LTP) at the PF-PC synapse?
4. In particular, how do different isoforms of CaMKII contribute to the bidirectional modulation of synaptic plasticity at this synapse?

To address these questions, computational models were constructed to simulate the CaMKII activation by calcium-calmodulin and the signalling network that mediates the plasticity induction at PF-PC synapses. Results of the computer simulations led to several contributions to knowledge in neuroscience that are summarised in the following section.

8.1 Main Contributions

The main contributions of this thesis to neuroscience are:

- **CaMKII is not sensitive to the actual frequency of calcium-calmodulin oscillations.** Simulations with a simplified version of the CaMKII activation model proposed in [Dupont 2003] demonstrated that CaMKII does not depend on the frequency of calcium-calmodulin pulses as stated in [De Koninck 1998, Dupont 2003].

- **The average calcium-calmodulin concentration determines the sensitivity of CaMKII to the frequency of calcium-calmodulin oscillations.** The application of calcium-calmodulin pulses with the same average concentration produces identical levels of phosphorylated CaMKII at varying frequencies. Therefore, the CaMKII phosphorylation is determined by the average concentration of calcium-calmodulin in the system, and not by its oscillation frequency.

- **Oscillatory applications of calcium-calmodulin are not required.** The same level of CaMKII phosphorylation is obtained in response to pulsed and constant applications of calcium-calmodulin with identical average concentrations. This indicates that the idea of CaMKII as a “decoder” of the calcium oscillation frequency is misleading [De Koninck 1998, Dupont 2003]. This thesis suggests new experimental tests with rescaled amplitudes of calcium-calmodulin pulses keeping the same mean concentration.

- **Proposing the first dynamic model of LTD and LTP at PF-PC synapses that includes CaMKII.** Existing theoretical studies of plasticity at these synapses have only focused on LTD induction. Moreover, CaMKII was never included in the signalling network proposed by these kinetic models. This thesis presents the first model of phosphorylation and dephosphorylation of AMPA receptors by CaMKII and protein phosphatase 2B (PP2B) that simulates the induction of LTD and LTP at the PF-PC synapse.

- **A CaMKII/PP2B switch mechanism underlies plasticity induction at PF-PC synapses.** The results of computer simulations of a simple mathematical model suggest that the balance of CaMKII-mediated phosphorylation and PP2B-mediated dephosphorylation of AMPA receptors determines whether LTD or LTP occurs at the PF-PC synapse. PF activity alone evokes PP2B concentration levels higher than CaMKII, leading to LTP induction. Instead, LTD occurs when the CaMKII concentration levels surpass the PP2B concentration in response to the paired activation of PF and climbing fibre (CF).

- **Filamentous actin binding enables βCaMKII to regulate bidirectional plasticity at PF-PC synapses.** The binding of filamentous actin (F-actin) to CaMKII was included into the model of AMPA receptor phosphorylation to simulate the induction of plasticity in wild-type mice, whereas in the knockout mice that lack βCaMKII, the F-actin binding was omitted. Simulation results replicate the experimental observations in [van Woerden 2009] and unravel how the βCaMKII isoform can control the sign reversal of plasticity at PF-PC synapses. This thesis demonstrates that the binding of F-actin to βCaMKII can indeed contribute to the control of bidirectional plasticity at these synapses, as suggested in [van Woerden 2009].

The computational model of intracellular signalling constructed in this thesis advances the understanding of the mechanisms of synaptic plasticity induction in the cerebellum. This simple model is a significant tool for future research by the scientific community.

8.2 Future Research

The following ideas are suggested as extensions to the study presented in this thesis:

- **Implementation of a more biologically realistic bidirectional plasticity model at PF-PC synapses.** The computer simulations that were described in this thesis predicted the underlying mechanisms regulating the bidirectional plasticity at these synapses. However, the biological realism of the simple bidirectional plasticity model can be incrementally extended by adding components of the existing model reimplemented in Chapter 5 [Kuroda 2001]. The comparison of results obtained from the simple bidirectional plasticity model with a more complex one should indicate the indirect contribution of other substances to regulating the sign reversal of plasticity at PF-PC synapses.

  Previous models of cerebellar LTD have measured synaptic plasticity by quantifying the concentration of phosphorylated AMPA receptors [Kuroda 2001, Tanaka 2007]. Indeed, this is the case for the simple dynamic model proposed in this thesis. However, Antunes and De Schutter have recently suggested that the extent of synaptic depression should be measured as a reduction in the number of synaptic AMPA receptors, rather than the concentration of phosphorylated receptors [Antunes 2012]. Thus, a next step of this research should be the inclusion of the AMPA receptor trafficking modelled by Antunes and De Schutter into the more complex model of plasticity induction at PF-PC synapses. Moreover, several concentrations of compounds and rate kinetic constants of biochemical reactions are free parameters in computational models due to the lack of experimental data in the literature. Additional experiments on PCs are necessary to provide realistic parameter values and to test the computational model at the PF-PC synapse. Experimental data will lead to an incremental improvement of the computational model, which in turn may suggest new experiments that need to be conducted.

- **Study of the involvement of calcium and CaMKII in the temporal integration of PF and CF inputs to PCs.** Synaptic plasticity in PCs is strongly dependent on the timing of PF and CF inputs to these cells [Kuroda 2001, van Woerden 2009]. The order as well as the timing of the PF and CF stimuli have been thought to play a significant role in the activation of protein kinase C (PKC) [Kotaleski 2002]. It is important to investigate the underlying mechanisms of the temporal requirements of PF and CF stimulation for the activation of CaMKII at the PF-PC synapse.

- **Study of the effects of diffusion and stochasticity in subcellular regions at the PF-PC synapse.** Most studies of intracellular signalling are based on the assumption that molecular concentrations are continuous. This type of analysis leads to deterministic solutions of systems of differential equations that describe mass-action kinetics. However, it is known that many signalling cascades involve very small numbers of molecules, and they should therefore be analysed using stochastic calculations [Bhalla 2004a, Bhalla 2004b, Rao 2002]. As a complement to the deterministic model of the PF-PC synapse, a stochastic model of bidirectional plasticity at this synapse, which accounts for spatial aspects of cellular signalling, should be developed. Results obtained from both deterministic and stochastic computational models should then be compared.

8.3 Publications and Conferences

In addition to this thesis, I have made scientific contributions to the discipline during the three years of my PhD. Seven international conferences were attended, at which two full conference papers and four abstracts were published. Two other abstracts were also accepted for publication at an international conference in July 2013. The work presented in this thesis was awarded with merit-based grants, and presented in contributed talks at two of these conferences and invited talks to prestigious research groups such as the Erasmus Medical Center Rotterdam whose experimentalists are co-authors in [van Woerden 2009]. One peer-reviewed journal paper is under review by the *Journal of Theoretical Biology*, and another journal paper about the work presented in Chapter 6 is nearly ready for submission to *PLoS Computational Biology*. The details of these contributions are listed below.

As a result of the work presented in Chapter 6, the following papers were published:

- TM Pinto, MJ Schilstra and V Steuber. *The Effective Calcium/calmodulin Concentration Determines the Sensitivity of CaMKII to the Frequency of Calcium Oscillations*. Lecture Notes in Computer Science, vol. 7223, pages 131-135, 2012 (Appendix F). This full conference paper was presented orally at the Ninth International Conference on Information Processing in Cells and Tissues (IPCAT 2012) in Cambridge, UK.

- TM Pinto, MJ Schilstra and V Steuber. *CaMKII activation by Ca_4-CaM does not depend on the actual frequency of oscillatory Ca^{2+} signals.* FENS Forum Abstr, vol. 75.29, 2012 (Appendix G). This abstract was presented as a poster at the Eighth FENS Forum of Neuroscience (FENS Forum 2012) in Barcelona, Spain.

- TM Pinto, MJ Schilstra and V Steuber. *Does CaMKII decode Ca^{2+} oscillations?* BMC Neuroscience, vol. 13, O15, 2012 (Appendix H). This is also an abstract presented orally at the Twentieth First Annual Computational Neuroscience Meeting (CNS 2012) in Atlanta/Decatur, USA. This work was awarded with travel grants.

- TM Pinto, MJ Schilstra and V Steuber. *The Average Calcium-calmodulin Concentration Regulates the CaMKII Dependence on the Frequency of Calcium-calmodulin Oscillations.* This peer-reviewed journal paper is nearly ready for submission to *PLoS Computational Biology.*

The following papers summarise some of the results presented in Chapter 7:

- TM Pinto, MJ Schilstra and V Steuber. *Modelling the role of βCaMKII in regulating bidirectional plasticity at parallel fibre-Purkinje cell synapses.* Frontiers in Computational Neuroscience, vol. 6, page 188, 2012 (Appendix I). This abstract was presented as a poster at the Bernstein Conference on Computational Neuroscience (BCCN 2012) in Munich, Germany. This conference was held consecutively with INCF Neuroinformatics 2012.

- TM Pinto, MJ Schilstra and V Steuber. *Filamentous actin binding enables βCaMKII to regulate bidirectional plasticity in cerebellar Purkinje cells.* BMC Neuroscience, 2013 (Appendix J). This abstract was accepted for publication in *BMC Neuroscience* and will be presented as a poster at the Twentieth Second Annual Computational Neuroscience Meeting (CNS 2013) in Paris, France.

The following publications were written during my PhD, however, these present results obtained from extensions to my Masters study. Although these papers are the outcome of my Masters rather than my PhD project, they portray my contribution to knowledge as an academic researcher:

- TM Pinto, RS Wedemann and CM Cortez. *A Comparison of the Electric Potential through the Membranes of Ganglion Neurons and Neuroblastoma Cells.* Lecture Notes in Computer Science, vol. 6792, pages 103-110, 2011 (Appendix K). This full conference paper was presented as a poster at the Twentieth First International Conference on Artificial Neural Networks (ICANN 2011) in Helsinki, Finland.

- TM Pinto, RS Wedemann and CM Cortez. *Computational modeling of the electric potential in biological membrane. A comparison between healthy and cancerous neurons.* BMC Neuroscience, vol. 12, P47, 2011 (Appendix L). Abstract presented as a poster at the Twentieth Annual Computational Neuroscience Meeting (CNS 2011) in Stockholm, Sweden.

- TM Pinto, RS Wedemann and CM Cortez. *The behavior of the electric potential across neuronal membranes of spinal ganglion and neuroblastoma cells.* BMC Neuroscience, 2013 (Appendix M). This abstract was accepted for publication in *BMC Neuroscience* and will also be presented as a poster at CNS 2013 in Paris, France.

- TM Pinto, RS Wedemann and CM Cortez. *Modeling the electric potential across neuronal membranes: The effect of fixed charges on spinal ganglion neurons and neuroblastoma cells* (Appendix N). This is a peer-reviewed journal paper that is under review by the *Journal of Theoretical Biology.*

Bibliography

[Airaksinen 1997] MS Airaksinen, J Eilers, O Garaschuk, H Thoenen, A Konnerth and M Meyer. *Ataxia and altered dendritic calcium signaling in mice carrying a targeted null mutation of the calbindin D28k gene.* Proc Natl Acad Sci USA, vol. 94, no. 4, pages 1488–1493, 1997. (Cited on page 90.)

[Antunes 2012] G Antunes and E De Schutter. *A stochastic signaling network mediates the probabilistic induction of cerebellar long-term depression.* J Neurosci, vol. 32, no. 27, pages 9288–9300, 2012. (Cited on pages 90, 107 and 154.)

[Atkins 2009] P Atkins and J de Paula. Physical chemistry. Oxford University Press, 2009. (Cited on pages 28 and 34.)

[Beaton 2010] A Beaton and P Mariën. *Language, cognition and the cerebellum: Grappling with an enigma.* Cortex, vol. 46, no. 7, pages 811–820, 2010. (Cited on page 1.)

[Belmeguenai 2005] A Belmeguenai and C Hansel. *A role for protein phosphatases 1, 2A, and 2B in cerebellar long-term potentiation.* J Neurosci, vol. 25, no. 46, pages 10768–10772, 2005. (Cited on pages 13 and 102.)

[Berg 2002] JM Berg, JL Tymoczko and L Stryer. Biochemistry. WH Freeman, 2002. (Cited on pages 31 and 32.)

[Bhalla 1999] US Bhalla and R Iyengar. *Emergent Properties of Networks of Biological Signaling Pathways.* Science, vol. 283, no. 381, pages 381–387, 1999. (Cited on pages 1 and 57.)

[Bhalla 2004a] US Bhalla. *Signaling in small subcellular volumes. I. Stochastic and diffusion effects on individual pathways.* Biophys J, vol. 87, no. 2, pages 733–744, 2004. (Cited on page 108.)

[Bhalla 2004b] US Bhalla. *Signaling in small subcellular volumes. II. Stochastic and diffusion effects on synaptic network properties.* Biophys J, vol. 87, no. 2, pages 745–753, 2004. (Cited on page 108.)

[Bower 2008] JM Bower and D Beeman. The book of GENESIS: exploring realistic neural models with the GEneral NEural SImulation System. Springer-Verlag New York, Inc New York, NY, USA, 2008. (Cited on pages 4 and 36.)

[Briggs 1925] GE Briggs and JB Haldane. *A note on the kinetics of enzyme action.* Biochem J, vol. 19, no. 2, pages 338–339, 1925. (Cited on pages 29 and 31.)

[Brocke 1999] L Brocke, LW Chiang, PD Wagner and H Schulman. *Functional implications of the subunit composition of neuronal CaM kinase II.* J Biol

Chem, vol. 274, no. 32, pages 22713–22722, 1999. (Cited on pages 20, 90 and 154.)

[Canepari 2008] M Canepari and KE Vogt. *Dendritic spike saturation of endogenous calcium buffer and induction of postsynaptic cerebellar LTP.* PLoS One, vol. 3, no. 12, page e4011, 2008. (Cited on pages 90 and 91.)

[Colbran 2004] RJ Colbran and AM Brown. *Calcium/calmodulin-dependent protein kinase II and synaptic plasticity.* Curr Opin Neurobiol, vol. 14, no. 3, pages 318–327, 2004. (Cited on page 20.)

[Cornish-Bowden 2004] A Cornish-Bowden. Fundamentals of enzyme kinetics. Portland Press, London, 2004. (Cited on pages 28 and 31.)

[D'Angelo 2012] E D'Angelo and S Casali. *Seeking a unified framework for cerebellar function and dysfunction: from circuit operations to cognition.* Front Neural Circuits, vol. 6, page 116, 2012. (Cited on page 9.)

[De Koninck 1998] P De Koninck and H Schulman. *Sensitivity of CaM Kinase II to the Frequency of Ca2+ Oscillations.* Science, vol. 279, no. 5348, pages 227–230, 1998. (Cited on pages 3, 5, 20, 21, 22, 25, 59, 60, 61, 63, 68, 73, 75, 76 and 106.)

[Din 2010] N Din, I Ahmad, I Ul Haq, S Elahi, DC Hoessli and AR Shakoori. *The function of GluR1 and GluR2 in cerebellar and hippocampal LTP and LTD is regulated by interplay of phosphorylation and O-GlcNAc modification.* J Cell Biochem, vol. 109, no. 3, pages 585–597, Feb 2010. (Cited on page 42.)

[Doi 2005] T Doi, S Kuroda, T Michikawa and M Kawato. *Inositol 1,4,5-trisphosphate-dependent Ca2+ threshold dynamics detect spike timing in cerebellar Purkinje cells.* J Neurosci, vol. 25, no. 4, pages 950–961, 2005. (Cited on pages 2 and 13.)

[Doi 2006] T Doi. *Neuroinformatics: Exploration of Signal Transduction Pathways in Cerebellar Long-Term Depression by Kinetic Simulation [Simulation Demo in GENESIS/kinetikit].* http://www.cns.atr.jp/neuroinfo/kuroda/, 2006. (Cited on pages 54 and 56.)

[Dosemeci 1996] A Dosemeci and RW Albers. *A mechanism for synaptic frequency detection through autophosphorylation of CaM kinase II.* Biophys J, vol. 70, no. 6, pages 2493–2501, 1996. (Cited on pages 20 and 59.)

[Dupont 2003] G Dupont, G Houart and P De Koninck. *Sensitivity of CaM kinase II to the frequency of Ca2+ oscillations: a simple model.* Cell Calcium, vol. 34, no. 6, pages 485–497, 2003. (Cited on pages 3, 5, 21, 22, 25, 58, 59, 60, 61, 63, 65, 66, 67, 68, 71, 73, 75, 76, 77, 106, 145, 153 and 154.)

[Eccles 1967] JC Eccles. *Circuits in the cerebellar control of movement.* Proc Natl Acad Sci USA, vol. 58, no. 1, pages 336–343, 1967. (Cited on page 8.)

[Ermentrout 2002] B Ermentrout. *XPPAUT (X-Windows Phase Plane plus Auto)*, 2002. (Cited on pages 4 and 36.)

[Eshete 2001] F Eshete and RD Fields. *Spike Frequency Decoding and Autonomous Activation of Ca2+–Calmodulin-Dependent Protein Kinase II in Dorsal Root Ganglion Neurons.* J Neurosci, vol. 21, no. 17, pages 6694–6705, 2001. (Cited on page 59.)

[Fiala 1996] JC Fiala, S Grossberg and D Bullock. *Metabotropic glutamate receptor activation in cerebellar Purkinje cells as substrate for adaptive timing of the classically conditioned eye-blink response.* J Neurosci, vol. 16, no. 11, pages 3760–3774, 1996. (Cited on pages 2 and 13.)

[Fink 2002] CC Fink and T Meyer. *Molecular mechanisms of CaMKII activation in neuronal plasticity.* Curr Opin Neurobiol, vol. 12, no. 3, pages 293–299, 2002. (Cited on pages 18, 19, 20, 88, 90 and 154.)

[Gillespie 1977] DT Gillespie. *Exact stochastic simulation of coupled chemical reactions.* J Phys Chem, vol. 81, no. 25, pages 2340–2361, 1977. (Cited on page 144.)

[Glickstein 2009] M Glickstein, P Strata and J Voogd. *Cerebellum: history.* Neuroscience, vol. 162, no. 3, pages 549–559, 2009. (Cited on page 1.)

[Hansel 2006] C Hansel, M de Jeu, A Belmeguenai, SH Houtman, GHS Buitendijk, D Andreev, CI De Zeeuw and Y Elgersma. *alphaCaMKII is essential for cerebellar LTD and motor learning.* Neuron, vol. 51, no. 6, pages 835–843, 2006. (Cited on pages 2, 22, 23 and 90.)

[Hanson 1992] PI Hanson and H Schulman. *Neuronal Ca2+/Calmodulin-Dependent Protein Kinases.* Annu Rev Biochem, vol. 61, no. 1, pages 559–601, 1992. (Cited on page 59.)

[Hanson 1994] PI Hanson, T Meyer, L Stryer and H Schulman. *Dual role of calmodulin in autophosphorylation of multifunctional CaM kinase may underlie decoding of calcium signals.* Neuron, vol. 12, no. 5, pages 943–956, 1994. (Cited on pages 20, 59 and 75.)

[Haynie 2001] DT Haynie. Biological thermodynamics. Cambridge University Press, 2001. (Cited on page 34.)

[Henley 2011] JM Henley, EA Barker and OO Glebov. *Routes, destinations and delays: recent advances in AMPA receptor trafficking.* Trends Neurosci, vol. 34, no. 5, pages 258–268, 2011. (Cited on page 42.)

[Hess 1840] GH Hess. *Bulletin scientifique.* Academie imperiale des sciences de Saint-Pétersbourg, vol. 8, pages 257–272, 1840. (Cited on page 35.)

[Hudmon 2002] A Hudmon and H Schulman. *Structure-function of the multifunctional Ca2+/calmodulin-dependent protein kinase II.* Biochem. J., vol. 364, no. 3, pages 593–611, 2002. (Cited on page 20.)

[Ito 1982] M Ito and M Kano. *Long-lasting depression of parallel fiber-Purkinje cell transmission induced by conjunctive stimulation of parallel fibers and climbing fibers in the cerebellar cortex.* Neurosci Lett, vol. 33, no. 3, pages 253–258, 1982. (Cited on page 12.)

[Ito 1989] M Ito. *Long-Term Depression.* Annu Rev Neurosci, vol. 12, no. 1, pages 85–102, 1989. (Cited on page 12.)

[Ito 2002] M Ito. *The molecular organization of cerebellar long-term depression.* Nat Rev Neurosci, vol. 3, no. 11, pages 896–902, 2002. (Cited on pages 1, 2, 10 and 12.)

[Ito 2006] M Ito. *Cerebellar circuitry as a neuronal machine.* Prog Neurobiol, vol. 78, no. 3-5, pages 272–303, 2006. (Cited on page 8.)

[Kandel 1991] ER Kandel, JH Schwartz and TM Jessel. Principles of neural science. Elsevier Science Publishing, New York, 1991. (Cited on pages 8, 9, 11 and 12.)

[Kawaguchi 2011] S Kawaguchi, N Nagasaki and T Hirano. *Dynamic impact of temporal context of Ca2+ signals on inhibitory synaptic plasticity.* Sci Rep, vol. 1, page 143, 2011. (Cited on page 2.)

[Kier 2005] LB Kier, D Bonchev and GA Buck. *Modeling biochemical networks: a cellular-automata approach.* Chem Biodivers, vol. 2, no. 2, pages 2–4, 2005. (Cited on page 2.)

[Kotaleski 2002] JH Kotaleski, D Lester and KT Blackwell. *Subcellular interactions between parallel fibre and climbing fibre signals in Purkinje cells predict sensitivity of classical conditioning to interstimulus interval.* Integr Physiol Behav Sci, vol. 37, no. 4, pages 265–292, 2002. (Cited on page 108.)

[Kotaleski 2010] JH Kotaleski and KT Blackwell. *Modelling the molecular mechanisms of synaptic plasticity using systems biology approaches.* Nat Rev Neurosci, vol. 11, no. 4, pages 239–251, 2010. (Cited on pages 1 and 13.)

[Kubota 2001] Y Kubota and JM Bower. *Transient versus asymptotic dynamics of CaM kinase II: possible roles of phosphatase.* J Comput Neurosci, vol. 11, no. 3, pages 263–279, 2001. (Cited on page 75.)

[Kuroda 2001] S Kuroda, N Schweighofer and M Kawato. *Exploration of Signal Transduction Pathways in Cerebellar Long-Term Depression by Kinetic Simulation.* J Neurosci, vol. 21, no. 15, pages 5693–5702, 2001. (Cited on pages v, 2, 3, 4, 13, 15, 36, 39, 41, 42, 43, 44, 45, 46, 47, 48, 49, 50, 51, 52, 53, 54, 55, 56, 57, 77, 78, 79, 85, 102, 107, 108, 139, 140, 141, 153 and 154.)

[Lee 2000] HK Lee, M Barbarosie, K Kameyama, MF Bear and RL Huganir. *Regulation of distinct AMPA receptor phosphorylation sites during bidirectional synaptic plasticity.* Nature, vol. 405, no. 6789, pages 955–959, 2000. (Cited on page 102.)

[Lent 2005] Roberto Lent. Cem bilhões de neurônios: conceitos fundamentais de neurociência (In Portuguese). Atheneu, 2005. (Cited on page 9.)

[Li 2012] L Li, MI Stefan and N Le Novère. *Calcium Input Frequency, Duration and Amplitude Differentially Modulate the Relative Activation of Calcineurin and CaMKII.* PLoS ONE, vol. 7, no. 9, page e43810, 2012. (Cited on page 76.)

[Lisman 2002] JE Lisman, H Schulman and H Cline. *The molecular basis of CaMKII function in synaptic and behavioural memory.* Nat Rev Neurosci, vol. 3, pages 175–190, 2002. (Cited on pages 18, 19, 90, 153 and 154.)

[Manninen 2010] T Manninen, K Hituri, JH Kotaleski, KT Blackwell and M Linne. *Postsynaptic signal transduction models for long-term potentiation and depression.* Front Comput Neurosci, vol. 4, page 152, 2010. (Cited on page 12.)

[Marino 2012] Eliseo Carrascal Marino. *Histología*, 2012. (Cited on page 7.)

[Meyer 1992] T Meyer, PI Hanson, L Stryer and H Schulman. *Calmodulin Trapping by Calcium-Calmodulin-Dependent Protein Kinase.* Science, vol. 256, pages 1199–1201, 1992. (Cited on pages 20, 59, 63, 80, 153 and 154.)

[Michaelis 1913] L Michaelis and M Menten. *Die Kinetik der Invertinwirkung.* Biochemistry Zeitung, vol. 49, pages 333–369, 1913. (Cited on pages 29 and 31.)

[Michelson 1994] S Michelson and H Schulman. *CaM Kinase: A Model for its Activation and Dynamics.* J Theor Biol, vol. 171, pages 281–290, 1994. (Cited on pages 20 and 59.)

[Nelson 2005] DL Nelson and MM Cox. Lehninger Principles of Biochemistry. WH Freeman and Company, 2005. (Cited on page 34.)

[Nephron 2012] Nephron. *GeneWiki: Cerebellum*, 2012. (Cited on page 11.)

[Rao 2002] CV Rao, DM Wolf and AP Arkin. *Control, exploitation and tolerance of intracellular noise.* Nature, vol. 420, no. 6912, pages 231–237, 2002. (Cited on page 108.)

[Salazar 2008] C Salazar, AZ Politi and T Hofer. *Decoding of calcium oscillations by phosphorylation cycles: analytic results.* Biophys J, vol. 94, no. 4, pages 1203–1215, 2008. (Cited on page 75.)

[Sanabria 2009] H Sanabria, MT Swulius, SJ Kolodziej, J Liu and MN Waxham. *[beta]CaMKII Regulates Actin Assembly and Structure.* Journal of Biological Chemistry, vol. 284, no. 15, pages 9770–9780, 2009. (Cited on page 154.)

[Schilstra 2008] MJ Schilstra, SR Martin and SM Keating. *Methods for simulating the dynamics of complex biological processes.* Methods Cell Biol, vol. 84, pages 807–842, 2008. (Cited on page 2.)

[Schmidt 2003] H Schmidt, KM Stiefel, P Racay, B Schwaller and J Eilers. *Mutational analysis of dendritic Ca2+ kinetics in rodent Purkinje cells: role of parvalbumin and calbindin D28k.* J Physiol, vol. 551, no. Pt 1, pages 13–32, 2003. (Cited on page 90.)

[Shen 1998] K Shen, MN Teruel, K Subramanian and T Meyer. *CaMKII[beta] Functions As an F-Actin Targeting Module that Localizes CaMKII[alpha]/[beta] Heterooligomers to Dendritic Spines.* Neuron, vol. 21, no. 3, pages 593–606, 1998. (Cited on pages 22 and 102.)

[Spitalnik 2012] Patrice Spitalnik. *Central Nervous System: Brain*, 2012. (Cited on page 8.)

[Steuber 2004] V Steuber and D Willshaw. *A biophysical model of synaptic delay learning and temporal pattern recognition in a cerebellar Purkinje cell.* J Comput Neurosci, vol. 17, no. 2, pages 149–164, 2004. (Cited on page 1.)

[Steuber 2007] V Steuber, W Mittmann, FE Hoebeek, RA Silver, CI De Zeeuw, M Häusser and E De Schutter. *Cerebellar LTD and Pattern Recognition by Purkinje Cells.* Neuron, vol. 54, no. 1, pages 121–136, 2007. (Cited on page 1.)

[Tanaka 2007] K Tanaka, L Khiroug, F Santamaria, T Doi, H Ogasawara, G Ellis-Davies, M Kawato and G Augustine. *Ca2+ requirements for cerebellar long-term synaptic depression: role for a postsynaptic leaky integrator.* Neuron, vol. 54, no. 5, pages 787–800, 2007. (Cited on page 107.)

[van Woerden 2009] GM van Woerden, FE Hoebeek, Z Gao, RY Nagaraja, C Hoogenraad, SA Kushner, C Hansel, CI De Zeeuw and Y Elgersma. *[beta]CaMKII controls the direction of plasticity at parallel fiber-Purkinje cell synapses.* Nat Neurosci, vol. 12, no. 7, pages 823–825, 2009. (Cited on pages 2, 4, 5, 23, 24, 25, 78, 79, 80, 88, 89, 90, 91, 92, 93, 94, 95, 96, 97, 99, 100, 101, 102, 107, 108 and 154.)

[Vayttaden 2004] SJ Vayttaden and US Bhalla. *Developing complex signaling models using GENESIS/Kinetikit.* Sci STKE, vol. 2004, no. 219, page pl4, 2004. (Cited on page 36.)

[Waage 1864] P Waage and CM Guldberg. Studies concerning affinity, volume 35. Forhandlinger: Videnskabs-Selskabet i Christiana, 1864. (Cited on page 28.)

[Wang 2000] SS Wang, W Denk and M Häusser. *Coincidence detection in single dendritic spines mediated by calcium release.* Nat Neurosci, vol. 12, pages

1266–1273, 2000. (Cited on pages 2, 13, 14, 15, 51, 53, 82, 85, 90, 91, 147 and 153.)

Appendices

Appendix A

Reimplementation of Kuroda Model

A.1 Biochemical Reactions

A.1.1 mGluR/G_q/PLC Pathway

$$\mathrm{mGluR} + \mathrm{G}_{\alpha\beta\gamma} \underset{\mathrm{k}_{\mathrm{b}_1}}{\overset{\mathrm{k}_{\mathrm{f}_1}}{\rightleftharpoons}} \mathrm{mGluR\_G_q} \tag{A.1}$$

$$\mathrm{mGluR\_G_q} + \mathrm{Glu} \underset{\mathrm{k}_{\mathrm{b}_2}}{\overset{\mathrm{k}_{\mathrm{f}_2}}{\rightleftharpoons}} \mathrm{Glu\_mGluR\_G_q} \tag{A.2}$$

$$\mathrm{Glu\_mGluR\_G_q} \xrightarrow{\mathrm{k}_{\mathrm{f}_3}} \mathrm{Glu\_mGluR} + \mathrm{G}_{\beta\gamma} + \mathrm{GTP\_G}_{\alpha} \tag{A.3}$$

$$\mathrm{Glu\_mGluR} \xrightarrow{\mathrm{k}_{\mathrm{f}_4}} \mathrm{mGluR} + \mathrm{Glu_{dec}} \tag{A.4}$$

$$\mathrm{GTP\_G}_{\alpha} \xrightarrow{\mathrm{k}_{\mathrm{f}_5}} \mathrm{GDP\_G}_{\alpha} \tag{A.5}$$

$$\mathrm{GTP\_G}_{\alpha} + \mathrm{PLC} \underset{\mathrm{k}_{\mathrm{b}_6}}{\overset{\mathrm{k}_{\mathrm{f}_6}}{\rightleftharpoons}} \mathrm{GTP\_G}_{\alpha}\mathrm{\_PLC} \tag{A.6}$$

$$\mathrm{GTP\_G}_{\alpha}\mathrm{\_PLC} \xrightarrow{\mathrm{k}_{\mathrm{f}_7}} \mathrm{GDP\_G}_{\alpha} + \mathrm{PLC} \tag{A.7}$$

$$\begin{aligned}\mathrm{GTP\_G}_{\alpha}\mathrm{\_PLC} + \mathrm{PIP_2} \quad & \underset{\mathrm{k}_{\mathrm{b}_8}}{\overset{\mathrm{k}_{\mathrm{f}_8}}{\rightleftharpoons}} \mathrm{GTP\_G}_{\alpha}\mathrm{\_PLC\_PIP_2} \\ & \xrightarrow{\mathrm{k}_{\mathrm{cat}_8}} \mathrm{GTP\_G}_{\alpha}\mathrm{\_PLC} + \mathrm{IP_3} + \mathrm{DAG}\end{aligned} \tag{A.8}$$

$$\mathrm{IP_3} \xrightarrow{\mathrm{k}_{\mathrm{f}_9}} \mathrm{IP}_{3_{\mathrm{dec}}} \tag{A.9}$$

$$3\,\mathrm{IP_3} + \mathrm{IP_3R} \xrightarrow{\mathrm{k}_{\mathrm{f}_{10}}} \mathrm{IP_3\_IP_3R} \tag{A.10}$$

$$\mathrm{IP_3\_IP_3R} \xrightarrow{\mathrm{k}_{\mathrm{f}_{11}}} \mathrm{IP_3\_IP_3R_{dec}} \tag{A.11}$$

$$\mathrm{DAG} \xrightarrow{\mathrm{k}_{\mathrm{f}_{12}}} \mathrm{DAG_{dec}} \tag{A.12}$$

$$\mathrm{GDP\_G}_{\alpha} + \mathrm{G}_{\beta\gamma} \xrightarrow{\mathrm{k}_{\mathrm{f}_{13}}} \mathrm{G}_{\alpha\beta\gamma} \tag{A.13}$$

A.1.2 PLA$_2$ Pathway

$$\mathrm{PLA_2 + Ca \underset{k_{b_{14}}}{\overset{k_{f_{14}}}{\rightleftharpoons}} PLA_2\_Ca} \tag{A.14}$$

$$\mathrm{PLA_2\_Ca + APC \underset{k_{b_{15}}}{\overset{k_{f_{15}}}{\rightleftharpoons}} PLA_2\_Ca\_APC \xrightarrow{k_{cat_{15}}} PLA_2\_Ca + AA} \tag{A.15}$$

$$\mathrm{PLA_2\_Ca + DAG \underset{k_{b_{16}}}{\overset{k_{f_{16}}}{\rightleftharpoons}} PLA_2\_Ca\_DAG} \tag{A.16}$$

$$\begin{aligned}\mathrm{PLA_2\_Ca\_DAG + APC} &\mathrm{\underset{k_{b_{17}}}{\overset{k_{f_{17}}}{\rightleftharpoons}} PLA_2\_Ca\_DAG\_APC} \\ &\mathrm{\xrightarrow{k_{cat_{17}}} PLA_2\_Ca\_DAG + AA}\end{aligned} \tag{A.17}$$

$$\mathrm{PLA_2 + PIP_2 \underset{k_{b_{18}}}{\overset{k_{f_{18}}}{\rightleftharpoons}} PLA_2\_PIP_2} \tag{A.18}$$

$$\mathrm{PLA_2\_PIP_2 + APC \underset{k_{b_{19}}}{\overset{k_{f_{19}}}{\rightleftharpoons}} PLA_2\_PIP_2\_APC \xrightarrow{k_{cat_{19}}} PLA_2\_PIP_2 + AA} \tag{A.19}$$

$$\mathrm{AA \xrightarrow{k_{f_{20}}} APC} \tag{A.20}$$

$$\mathrm{PIP_2 + PLA_2\_Ca \underset{k_{b_{21}}}{\overset{k_{f_{21}}}{\rightleftharpoons}} PLA_2\_Ca\_PIP_2} \tag{A.21}$$

$$\begin{aligned}\mathrm{PLA_2\_Ca\_PIP_2 + APC} &\mathrm{\underset{k_{b_{22}}}{\overset{k_{f_{22}}}{\rightleftharpoons}} PLA_2\_Ca\_PIP_2\_APC} \\ &\mathrm{\xrightarrow{k_{cat_{22}}} PLA_2\_Ca\_PIP_2 + AA}\end{aligned} \tag{A.22}$$

$$\begin{aligned}\mathrm{MAPK\_PP + PLA_2} &\mathrm{\underset{k_{b_{23}}}{\overset{k_{f_{23}}}{\rightleftharpoons}} MAPK\_PP\_PLA_2} \\ &\mathrm{\xrightarrow{k_{cat_{23}}} MAPK\_PP + PLA_2\_P}\end{aligned} \tag{A.23}$$

$$\mathrm{PLA_2\_P \xrightarrow{k_{f_{24}}} PLA_2} \tag{A.24}$$

$$\mathrm{2\,PLA_2\_P + APC \underset{k_{b_{25}}}{\overset{k_{f_{25}}}{\rightleftharpoons}} PLA_2\_P\_APC \xrightarrow{k_{cat_{25}}} PLA_2\_P + AA} \tag{A.25}$$

A.1.3 PKC Pathway

$$\mathrm{PKC + Ca} \underset{\mathrm{k_{b_{26}}}}{\overset{\mathrm{k_{f_{26}}}}{\rightleftharpoons}} \mathrm{PKC\_Ca} \tag{A.26}$$

$$\mathrm{PKC\_Ca + DAG} \underset{\mathrm{k_{b_{27}}}}{\overset{\mathrm{k_{f_{27}}}}{\rightleftharpoons}} \mathrm{PKC\_Ca\_DAG} \tag{A.27}$$

$$\mathrm{PKC + DAG} \underset{\mathrm{k_{b_{28}}}}{\overset{\mathrm{k_{f_{28}}}}{\rightleftharpoons}} \mathrm{PKC\_DAG} \tag{A.28}$$

$$\mathrm{PKC\_DAG + AA} \underset{\mathrm{k_{b_{29}}}}{\overset{\mathrm{k_{f_{29}}}}{\rightleftharpoons}} \mathrm{PKC\_DAG\_AA} \tag{A.29}$$

$$\mathrm{PKC + AA} \underset{\mathrm{k_{b_{30}}}}{\overset{\mathrm{k_{f_{30}}}}{\rightleftharpoons}} \mathrm{PKC\_AA} \tag{A.30}$$

$$\mathrm{PKC\_Ca + AA} \underset{\mathrm{k_{b_{31}}}}{\overset{\mathrm{k_{f_{31}}}}{\rightleftharpoons}} \mathrm{PKC\_Ca\_AA} \tag{A.31}$$

$$\mathrm{PKC\_Ca} \xrightarrow{\mathrm{k_{f_{32}}}} \mathrm{PKC\_Ca\_mem} \tag{A.32}$$

$$\mathrm{PKC\_Ca\_DAG} \xrightarrow{\mathrm{k_{f_{33}}}} \mathrm{PKC\_Ca\_DAG\_mem} \tag{A.33}$$

$$\mathrm{PKC\_DAG} \xrightarrow{\mathrm{k_{f_{34}}}} \mathrm{PKC\_DAG\_mem} \tag{A.34}$$

$$\mathrm{PKC\_DAG\_AA} \xrightarrow{\mathrm{k_{f_{35}}}} \mathrm{PKC\_DAG\_AA\_mem} \tag{A.35}$$

$$\begin{gathered}\mathrm{PKC\_Ca\_mem + PKC\_Ca\_DAG\_mem + PKC\_DAG\_mem +}\\ \mathrm{PKC\_DAG\_AA\_mem + PKC\_AA + PKC\_Ca\_AA +}\\ \mathrm{PKC_{active}} \xrightarrow{\mathrm{k_{f_{36}}}} \mathrm{PKC_{active_{dec}}}\end{gathered} \tag{A.36}$$

A.1.4 NO/cGMP Pathway

$$\mathrm{NO + GC} \underset{\mathrm{k_{b_{37}}}}{\overset{\mathrm{k_{f_{37}}}}{\rightleftharpoons}} \mathrm{NO\_GC} \tag{A.37}$$

$$\mathrm{NO\_GC} \xrightarrow{\mathrm{k_{f_{38}}}} \mathrm{NO_{dec} + GC} \tag{A.38}$$

$$\mathrm{NO\_GC + GTP} \underset{\mathrm{k_{b_{39}}}}{\overset{\mathrm{k_{f_{39}}}}{\rightleftharpoons}} \mathrm{NO\_GC\_GTP} \xrightarrow{\mathrm{k_{cat_{39}}}} \mathrm{NO\_GC + cGMP} \tag{A.39}$$

$$\mathrm{PDE + cGMP} \underset{\mathrm{k_{b_{40}}}}{\overset{\mathrm{k_{f_{40}}}}{\rightleftharpoons}} \mathrm{PDE\_cGMP} \xrightarrow{\mathrm{k_{cat_{40}}}} \mathrm{PDE + 5'\,GMP} \tag{A.40}$$

$$\mathrm{cGMP + PKG} \underset{\mathrm{k_{b_{41}}}}{\overset{\mathrm{k_{f_{41}}}}{\rightleftharpoons}} \mathrm{cGMP\_PKG} \tag{A.41}$$

$$\begin{aligned}\mathrm{G_{sub}} + \mathrm{cGMP\_PKG} \quad &\underset{\mathrm{k_{b_{42}}}}{\overset{\mathrm{k_{f_{42}}}}{\rightleftharpoons}} \mathrm{G_{sub}\_cGMP\_PKG} \\ &\xrightarrow{\mathrm{k_{cat_{42}}}} \mathrm{cGMP\_PKG} + \mathrm{G_{sub}\_P}\end{aligned} \tag{A.42}$$

$$\mathrm{G_{sub}\_P} \xrightarrow{\mathrm{k_{f_{43}}}} \mathrm{G_{sub}} \tag{A.43}$$

$$\mathrm{PP2A} + \mathrm{G_{sub}\_P} \underset{\mathrm{k_{b_{44}}}}{\overset{\mathrm{k_{f_{44}}}}{\rightleftharpoons}} \mathrm{PP2A\_G_{sub}\_P} \tag{A.44}$$

A.1.5 AMPA Receptor and PKC

$$\begin{aligned}\mathrm{PKC_{active}} + \mathrm{AMPAR} \quad &\underset{\mathrm{k_{b_{45}}}}{\overset{\mathrm{k_{f_{45}}}}{\rightleftharpoons}} \mathrm{PKC_{active}\_AMPAR} \\ &\xrightarrow{\mathrm{k_{cat_{45}}}} \mathrm{PKC_{active}} + \mathrm{AMPAR\_P}\end{aligned} \tag{A.45}$$

$$\mathrm{PP2A} + \mathrm{AMPAR\_P} \underset{\mathrm{k_{b_{46}}}}{\overset{\mathrm{k_{f_{46}}}}{\rightleftharpoons}} \mathrm{PP2A\_AMPAR\_P} \xrightarrow{\mathrm{k_{cat_{46}}}} \mathrm{PP2A} + \mathrm{AMPAR} \tag{A.46}$$

$$\mathrm{PKC_{active}} + \mathrm{Raf} \underset{\mathrm{k_{b_{47}}}}{\overset{\mathrm{k_{f_{47}}}}{\rightleftharpoons}} \mathrm{PKC_{active}\_Raf} \xrightarrow{\mathrm{k_{cat_{47}}}} \mathrm{PKC_{active}} + \mathrm{Raf\_P} \tag{A.47}$$

A.1.6 CRHR Pathway

$$\mathrm{CRHR} + \mathrm{CRF} \underset{\mathrm{k_{b_{48}}}}{\overset{\mathrm{k_{f_{48}}}}{\rightleftharpoons}} \mathrm{CRHR\_CRF} \tag{A.48}$$

$$\mathrm{CRHR\_CRF} \xrightarrow{\mathrm{k_{f_{49}}}} \mathrm{CRF_{dec}} + \mathrm{CRHR} \tag{A.49}$$

$$\begin{aligned}\mathrm{CRHR\_CRF} + \mathrm{Raf} \quad &\underset{\mathrm{k_{b_{50}}}}{\overset{\mathrm{k_{f_{50}}}}{\rightleftharpoons}} \mathrm{CRHR\_CRF\_Raf} \\ &\xrightarrow{\mathrm{k_{cat50}}} \mathrm{CRHR\_CRF} + \mathrm{Raf\_P}\end{aligned} \tag{A.50}$$

A.1.7 Lyn Pathway

$$\mathrm{Lyn_{active}} + \mathrm{Raf} \underset{\mathrm{k_{b_{51}}}}{\overset{\mathrm{k_{f_{51}}}}{\rightleftharpoons}} \mathrm{Lyn_{active}\_Raf} \xrightarrow{\mathrm{k_{cat_{51}}}} \mathrm{Lyn_{active}} + \mathrm{Raf\_P} \tag{A.51}$$

$$\mathrm{Lyn_{active}} \xrightarrow{\mathrm{k_{f_{52}}}} \mathrm{Lyn_{active_{dec}}} \tag{A.52}$$

A.1.8 Raf/MEK/MAPK Pathway

$$\mathrm{PP2A + Raf\_P} \underset{k_{b_{53}}}{\overset{k_{f_{53}}}{\rightleftharpoons}} \mathrm{PP2A\_Raf\_P} \xrightarrow{k_{cat_{53}}} \mathrm{PP2A + Raf} \tag{A.53}$$

$$\mathrm{Raf\_P + MEK} \underset{k_{b_{54}}}{\overset{k_{f_{54}}}{\rightleftharpoons}} \mathrm{Raf\_P\_MEK} \xrightarrow{k_{cat_{54}}} \mathrm{Raf\_P + MEK\_P} \tag{A.54}$$

$$\mathrm{Raf\_P + MEK\_P} \underset{k_{b_{55}}}{\overset{k_{f_{55}}}{\rightleftharpoons}} \mathrm{Raf\_P\_MEK\_P} \xrightarrow{k_{cat_{55}}} \mathrm{Raf\_P + MEK\_PP} \tag{A.55}$$

$$\mathrm{PP2A + MEK\_PP} \underset{k_{b_{56}}}{\overset{k_{f_{56}}}{\rightleftharpoons}} \mathrm{PP2A\_MEK\_PP} \xrightarrow{k_{cat_{56}}} \mathrm{PP2A + MEK\_P} \tag{A.56}$$

$$\mathrm{PP2A + MEK\_P} \underset{k_{b_{57}}}{\overset{k_{f_{57}}}{\rightleftharpoons}} \mathrm{PP2A\_MEK\_P} \xrightarrow{k_{cat_{57}}} \mathrm{PP2A + MEK} \tag{A.57}$$

$$\begin{aligned} \mathrm{MEK\_PP + MAPK} \quad & \underset{k_{b_{58}}}{\overset{k_{f_{58}}}{\rightleftharpoons}} \mathrm{MEK\_PP\_MAPK} \\ & \xrightarrow{k_{cat_{58}}} \mathrm{MEK\_PP + MAPK\_P} \end{aligned} \tag{A.58}$$

$$\begin{aligned} \mathrm{MEK\_PP + MAPK\_P} \quad & \underset{k_{b_{59}}}{\overset{k_{f_{59}}}{\rightleftharpoons}} \mathrm{MEK\_PP\_MAPK\_P} \\ & \xrightarrow{k_{cat_{59}}} \mathrm{MEK\_PP + MAPK\_PP} \end{aligned} \tag{A.59}$$

$$\mathrm{MKP_1 + MAPK\_P} \underset{k_{b_{60}}}{\overset{k_{f_{60}}}{\rightleftharpoons}} \mathrm{MKP_1\_MAPK\_P} \xrightarrow{k_{cat_{60}}} \mathrm{MKP_1 + MAPK} \tag{A.60}$$

$$\begin{aligned} \mathrm{MKP_1 + MAPK\_PP} \quad & \underset{k_{b_{61}}}{\overset{k_{f_{61}}}{\rightleftharpoons}} \mathrm{MKP_1\_MAPK\_PP} \\ & \xrightarrow{k_{cat_{61}}} \mathrm{MKP_1 + MAPK\_P} \end{aligned} \tag{A.61}$$

A.2 Ordinary Differential Equations

$$\begin{aligned}\frac{d\text{NO\_GC}}{dt} &= k_{f_{37}} \times \text{GC} \times \text{NO} - k_{b_{37}} \times \text{NO\_GC} - \\ &\quad k_{f_{38}} \times \text{NO\_GC} - k_{f_{39}} \times \text{GTP} \times \text{NO\_GC} + \\ &\quad (k_{b_{39}} + k_{cat_{39}}) \times \text{NO\_GC\_GTP} \qquad \text{(A.62)}\end{aligned}$$

$$\frac{d\text{GC}}{dt} = -k_{f_{37}} \times \text{GC} \times \text{NO} + k_{b_{37}} \times \text{NO\_GC} + k_{f_{38}} \times \text{NO\_GC} \qquad \text{(A.63)}$$

$$\begin{aligned}\frac{d\text{NO\_GC\_GTP}}{dt} &= k_{f_{39}} \times \text{GTP} \times \text{NO\_GC} - \\ &\quad (k_{b_{39}} + k_{cat_{39}}) \times \text{NO\_GC\_GTP} \qquad \text{(A.64)}\end{aligned}$$

$$\begin{aligned}\frac{d\text{cGMP}}{dt} &= k_{cat_{39}} \times \text{NO\_GC\_GTP} - k_{f_{40}} \times \text{PDE} \times \text{cGMP} + \\ &\quad k_{b_{40}} \times \text{PDE\_cGMP} - k_{f_{41}} \times \text{cGMP} \times \text{PKG} + \\ &\quad k_{b_{41}} \times \text{cGMP\_PKG} \qquad \text{(A.65)}\end{aligned}$$

$$\frac{d\text{PDE}}{dt} = -k_{f_{40}} \times \text{PDE} \times \text{cGMP} + (k_{b_{40}} + k_{cat_{40}}) \times \text{PDE\_cGMP} \qquad \text{(A.66)}$$

$$\begin{aligned}\frac{d\text{PDE\_cGMP}}{dt} &= k_{f_{40}} \times \text{PDE} \times \text{cGMP} - \\ &\quad (k_{b_{40}} + k_{cat_{40}}) \times \text{PDE\_cGMP} \qquad \text{(A.67)}\end{aligned}$$

$$\begin{aligned}\frac{d\text{cGMP\_PKG}}{dt} &= k_{f_{41}} \times \text{cGMP} \times \text{PKG} - k_{b_{41}} \times \text{cGMP\_PKG} - \\ &\quad k_{f_{42}} \times \text{G\_Sub} \times \text{cGMP\_PKG} + \\ &\quad (k_{b_{42}} + k_{cat_{42}}) \times \text{G}_{\text{sub}}\text{\_cGMP\_PKG} \qquad \text{(A.68)}\end{aligned}$$

$$\frac{d\text{PKG}}{dt} = -k_{f_{41}} \times \text{cGMP} \times \text{PKG} + k_{b_{41}} \times \text{cGMP\_PKG} \qquad \text{(A.69)}$$

$$\begin{aligned}\frac{d\text{G}_{\text{sub}}\text{\_cGMP\_PKG}}{dt} &= k_{f_{42}} \times \text{G\_Sub} \times \text{cGMP\_PKG} - \\ &\quad (k_{b_{42}} + k_{cat_{42}}) \times \text{G}_{\text{sub}}\text{\_cGMP\_PKG} \qquad \text{(A.70)}\end{aligned}$$

$$\begin{aligned}\frac{d\text{G}_{\text{sub}}}{dt} &= -k_{f_{42}} \times \text{G\_Sub} \times \text{cGMP\_PKG} + \\ &\quad k_{b_{42}} \times \text{G}_{\text{sub}}\text{\_cGMP\_PKG} + k_{f_{43}} \times \text{G}_{\text{sub}}\text{\_P} \qquad \text{(A.71)}\end{aligned}$$

$$\begin{aligned}\frac{d\mathrm{G_{sub}\_P}}{dt} = {} & k_{cat_{42}} \times \mathrm{G_{sub}\_cGMP\_PKG} - \\ & k_{f_{44}} \times \mathrm{G_{sub}\_P} \times \mathrm{PP2A} + \\ & k_{b_{44}} \times \mathrm{PP2A\_G_{sub}\_P} - k_{f_{43}} \times \mathrm{G_{sub}\_P}\end{aligned} \tag{A.72}$$

$$\begin{aligned}\frac{d\mathrm{PP2A\_G_{sub}\_P}}{dt} = {} & k_{f_{44}} \times \mathrm{G_{sub}\_P} \times \mathrm{PP2A} - \\ & k_{b_{44}} \times \mathrm{PP2A\_G_{sub}\_P}\end{aligned} \tag{A.73}$$

$$\begin{aligned}\frac{d\mathrm{PP2A}}{dt} = {} & -k_{f_{44}} \times \mathrm{G_{sub}\_P} \times \mathrm{PP2A} + k_{b_{44}} \times \mathrm{PP2A\_G_{sub}\_P} - \\ & -k_{f_{57}} \times \mathrm{PP2A} \times \mathrm{MEK\_P} + (k_{b_{57}} + k_{cat_{57}}) \times \mathrm{PP2A\_MEK\_P} - \\ & -k_{f_{53}} \times \mathrm{PP2A} \times \mathrm{Raf\_P} + (k_{b_{53}} + k_{cat_{53}}) \times \mathrm{PP2A\_Raf\_P} - \\ & -k_{f_{56}} \times \mathrm{PP2A} \times \mathrm{MEK\_PP} + (k_{b_{56}} + k_{cat_{56}}) \times \mathrm{PP2A\_MEK\_PP} - \\ & -k_{f_{46}} \times \mathrm{PP2A} \times \mathrm{AMPAR\_P} + \\ & (k_{b_{46}} + k_{cat_{46}}) \times \mathrm{PP2A\_AMPAR\_P}\end{aligned} \tag{A.74}$$

$$\begin{aligned}\frac{d\mathrm{CRHR}}{dt} = {} & -k_{f_{48}} \times \mathrm{CRHR} \times \mathrm{CRF} + k_{b_{48}} \times \mathrm{CRHR\_CRF} + \\ & k_{f_{49}} \times \mathrm{CRHR\_CRF}\end{aligned} \tag{A.75}$$

$$\begin{aligned}\frac{d\mathrm{CRHR\_CRF}}{dt} = {} & k_{f_{48}} \times \mathrm{CRHR} \times \mathrm{CRF} - k_{b_{48}} \times \mathrm{CRHR\_CRF} - \\ & k_{f_{49}} \times \mathrm{CRHR\_CRF} - k_{f_{50}} \times \mathrm{CRHR\_CRF} \times \mathrm{Raf} + \\ & (k_{b_{50}} + k_{cat_{50}}) \times \mathrm{CRHR\_CRF\_Raf}\end{aligned} \tag{A.76}$$

$$\begin{aligned}\frac{d\mathrm{mGluR\_Gq}}{dt} = {} & -k_{f_2} \times \mathrm{mGluR\_Gq} \times \mathrm{Glu} + k_{b_2} \times \mathrm{Glu\_mGluR\_Gq} + \\ & k_{f_1} \times \mathrm{mGluR} \times \mathrm{G}_{\alpha\beta\gamma} - k_{b_1} \times \mathrm{mGluR\_Gq}\end{aligned} \tag{A.77}$$

$$\begin{aligned}\frac{d\mathrm{Glu\_mGluR\_Gq}}{dt} = {} & k_{f_2} \times \mathrm{mGluR\_Gq} \times \mathrm{Glu} - k_{b_2} \times \mathrm{Glu\_mGluR\_Gq} - \\ & k_{f_3} \times \mathrm{Glu\_mGluR\_Gq}\end{aligned} \tag{A.78}$$

$$\begin{aligned}\frac{d\mathrm{mGluR}}{dt} = {} & -k_{f_1} \times \mathrm{mGluR} \times \mathrm{G}_{\alpha\beta\gamma} + k_{b_1} \times \mathrm{mGluR\_G_q} + \\ & k_{f_4} \times \mathrm{Glu\_mGluR}\end{aligned} \tag{A.79}$$

$$\begin{aligned}\frac{d\mathrm{G}_{\alpha\beta\gamma}}{dt} = {} & k_{f_{13}} \times \mathrm{GDP\_G_\alpha} \times \mathrm{G}_{\beta\gamma} - k_{f_1} \times \mathrm{mGluR} \times \mathrm{G}_{\alpha\beta\gamma} + \\ & k_{b_1} \times \mathrm{mGluR\_G_q}\end{aligned} \tag{A.80}$$

$$\frac{d\text{Glu\_mGluR}}{dt} = -k_{f_4} \times \text{Glu\_mGluR} + k_{f_3} \times \text{Glu\_mGluR\_Gq} \tag{A.81}$$

$$\frac{d\text{G}_{\beta\gamma}}{dt} = -k_{f_{13}} \times \text{GDP\_G}_{\alpha} \times \text{G}_{\beta\gamma} + k_{f_3} \times \text{Glu\_mGluR\_Gq} \tag{A.82}$$

$$\begin{aligned}\frac{d\text{GDP\_G}_{\alpha}}{dt} = {} & k_{f_5} \times \text{GTP\_G}_{\alpha} - k_{f_{13}} \times \text{GDP\_G}_{\alpha} \times \text{G}_{\beta\gamma} + \\ & k_{f_7} \times \text{GTP\_G}_{\alpha}\text{\_PLC}\end{aligned} \tag{A.83}$$

$$\begin{aligned}\frac{d\text{GTP\_G}_{\alpha}}{dt} = {} & -k_{f_5} \times \text{GTP\_G}_{\alpha} - k_{f_6} \times \text{GTP\_G}_{\alpha} \times \text{PLC} + \\ & k_{b_6} \times \text{GTP\_G}_{\alpha}\text{\_PLC} + k_{f_3} \times \text{Glu\_mGluR\_Gq}\end{aligned} \tag{A.84}$$

$$\begin{aligned}\frac{d\text{PLC}}{dt} = {} & -k_{f_6} \times \text{GTP\_G}_{\alpha} \times \text{PLC} + k_{b_6} \times \text{GTP\_G}_{\alpha}\text{\_PLC} + \\ & k_{f_7} \times \text{GTP\_G}_{\alpha}\text{\_PLC}\end{aligned} \tag{A.85}$$

$$\begin{aligned}\frac{d\text{GTP\_G}_{\alpha}\text{\_PLC}}{dt} = {} & k_{f_6} \times \text{GTP\_G}_{\alpha} \times \text{PLC} - k_{b_6} \times \text{GTP\_G}_{\alpha}\text{\_PLC} - \\ & k_{f_7} \times \text{GTP\_G}_{\alpha}\text{\_PLC} - k_{f_8} \times \text{GTP\_G}_{\alpha}\text{\_PLC} \times \text{PIP}_2 + \\ & (k_{b_8} + k_{cat_8}) \times \text{GTP\_G}_{\alpha}\text{\_PLC\_PIP}_2\end{aligned} \tag{A.86}$$

$$\begin{aligned}\frac{d\text{GTP\_G}_{\alpha}\text{\_PLC\_PIP}_2}{dt} = {} & k_{f_8} \times \text{GTP\_G}_{\alpha}\text{\_PLC} \times \text{PIP}_2 - \\ & (k_{b_8} + k_{cat_8}) \times \text{GTP\_G}_{\alpha}\text{\_PLC\_PIP}_2\end{aligned} \tag{A.87}$$

$$\begin{aligned}\frac{d\text{IP}_3}{dt} = {} & k_{cat_8} \times \text{GTP\_G}_{\alpha}\text{\_PLC\_PIP}_2 - \\ & k_{f_9} \times \text{IP}_3 - k_{f_{10}} \times {\text{IP}_3}^3 \times \text{IP}_3\text{R}\end{aligned} \tag{A.88}$$

$$\begin{aligned}\frac{d\text{DAG}}{dt} = {} & k_{cat_8} \times \text{GTP\_G}_{\alpha}\text{\_PLC\_PIP}_2 - k_{f_{12}} \times \text{DAG} - \\ & k_{f_{27}} \times \text{PKC\_Ca} \times \text{DAG} + k_{b_{27}} \times \text{PKC\_Ca\_DAG} - \\ & k_{f_{28}} \times \text{PKC} \times \text{DAG} + k_{b_{28}} \times \text{PKC\_DAG} - \\ & k_{f_{16}} \times \text{PLA}_2\text{\_Ca} \times \text{DAG} + k_{b_{16}} \times \text{PLA}_2\text{\_Ca\_DAG}\end{aligned} \tag{A.89}$$

$$\frac{d\text{IP}_3\text{R}}{dt} = -k_{f_{10}} \times {\text{IP}_3}^3 \times \text{IP}_3\text{R} \tag{A.90}$$

$$\frac{d\text{IP}_3\text{\_IP}_3\text{R}}{dt} = k_{f_{10}} \times {\text{IP}_3}^3 \times \text{IP}_3\text{R} - k_{f_{11}} \times \text{IP}_3\text{\_IP}_3\text{R} \tag{A.91}$$

$$\begin{aligned}\frac{d\mathrm{Lyn}_{\mathrm{active}}}{dt} &= -k_{f_{52}} \times \mathrm{Lyn}_{\mathrm{active}} - k_{f_{51}} \times \mathrm{Lyn}_{\mathrm{active}} \times \mathrm{Raf} + \\ &\quad (k_{b_{51}} + k_{cat_{51}}) \times \mathrm{Lyn}_{\mathrm{active\_}}\mathrm{Raf}\end{aligned} \tag{A.92}$$

$$\begin{aligned}\frac{d\mathrm{Raf}}{dt} &= -k_{f_{51}} \times \mathrm{Lyn}_{\mathrm{active}} \times \mathrm{Raf} + k_{b_{51}} \times \mathrm{Lyn}_{\mathrm{active\_}}\mathrm{Raf} - \\ &\quad k_{f_{47}} \times \mathrm{PKC}_{\mathrm{active}} \times \mathrm{Raf} + k_{b_{47}} \times \mathrm{PKC}_{\mathrm{active\_}}\mathrm{Raf} - \\ &\quad k_{f_{50}} \times \mathrm{CRHR\_CRF} \times \mathrm{Raf} + k_{b_{50}} \times \mathrm{CRHR\_CRF\_Raf} + \\ &\quad k_{cat_{53}} \times \mathrm{PP2A\_Raf\_P}\end{aligned} \tag{A.93}$$

$$\begin{aligned}\frac{d\mathrm{Lyn}_{\mathrm{active\_}}\mathrm{Raf}}{dt} &= k_{f_{51}} \times \mathrm{Lyn}_{\mathrm{active}} \times \mathrm{Raf} - \\ &\quad (k_{b_{51}} + k_{cat_{51}}) \times \mathrm{Lyn}_{\mathrm{active\_}}\mathrm{Raf}\end{aligned} \tag{A.94}$$

$$\begin{aligned}\frac{d\mathrm{RafP}}{dt} &= (k_{cat_{51}} \times \mathrm{Lyn}_{\mathrm{active\_}}\mathrm{Raf} + k_{cat_{47}} \times \mathrm{PKC}_{\mathrm{active\_}}\mathrm{Raf} + \\ &\quad k_{cat_{50}} \times \mathrm{CRHR\_CRF\_Raf} - k_{f_{54}} \times \mathrm{Raf\_P} \times \mathrm{MEK} + \\ &\quad (k_{b_{54}} + k_{cat_{54}}) \times \mathrm{Raf\_P\_MEK} - k_{f_{55}} \times \mathrm{Raf\_P} \times \mathrm{MEK\_P} + \\ &\quad (k_{b_{55}} + k_{cat_{55}}) \times \mathrm{Raf\_P\_MEK\_P} - k_{f_{53}} \times \mathrm{PP2A} \times \mathrm{Raf\_P} + \\ &\quad k_{b_{53}} \times \mathrm{PP2A\_Raf\_P}) \times 2.5\end{aligned} \tag{A.95}$$

$$\mathrm{Raf\_P} = \mathrm{RafP} \times 0.4 \tag{A.96}$$

$$\begin{aligned}\frac{d\mathrm{PKC}_{\mathrm{active\_}}\mathrm{Raf}}{dt} &= k_{f_{47}} \times \mathrm{PKC}_{\mathrm{active}} \times \mathrm{Raf} - \\ &\quad (k_{b_{47}} + k_{cat_{47}}) \times \mathrm{PKC}_{\mathrm{active\_}}\mathrm{Raf}\end{aligned} \tag{A.97}$$

$$\begin{aligned}\frac{d\mathrm{CRHR\_CRF\_Raf}}{dt} &= k_{f_{50}} \times \mathrm{CRHR\_CRF} \times \mathrm{Raf} - \\ &\quad (k_{b_{50}} + k_{cat_{50}}) \times \mathrm{CRHR\_CRF\_Raf}\end{aligned} \tag{A.98}$$

$$\begin{aligned}\frac{d\mathrm{MEK}}{dt} &= -k_{f_{54}} \times \mathrm{Raf\_P} \times \mathrm{MEK} + k_{b_{54}} \times \mathrm{Raf\_P\_MEK} + \\ &\quad k_{cat_{57}} \times \mathrm{PP2A\_MEK\_P}\end{aligned} \tag{A.99}$$

$$\begin{aligned}\frac{d\mathrm{Raf\_P\_MEK}}{dt} &= k_{f_{54}} \times \mathrm{Raf\_P} \times \mathrm{MEK} - \\ &\quad (k_{b_{54}} + k_{cat_{54}}) \times \mathrm{Raf\_P\_MEK}\end{aligned} \tag{A.100}$$

$$\begin{aligned}\frac{d\mathrm{MEK\_P}}{dt} &= k_{cat_{54}} \times \mathrm{Raf\_P\_MEK} - k_{f_{55}} \times \mathrm{Raf\_P} \times \mathrm{MEK\_P} + \\ &\quad k_{b_{55}} \times \mathrm{Raf\_P\_MEK\_P} - k_{f_{57}} \times \mathrm{PP2A} \times \mathrm{MEK\_P} + \\ &\quad k_{b_{57}} \times \mathrm{PP2A\_MEK\_P} + k_{cat_{56}} \times \mathrm{PP2A\_MEK\_PP}\end{aligned} \tag{A.101}$$

$$\begin{aligned}\frac{d\text{Raf\_P\_MEK\_P}}{dt} &= k_{f_{55}} \times \text{Raf\_P} \times \text{MEK\_P} - \\ &\quad (k_{b_{55}} + k_{cat_{55}}) \times \text{Raf\_P\_MEK\_P}\end{aligned} \tag{A.102}$$

$$\begin{aligned}\frac{d\text{MEK\_PP}}{dt} &= k_{cat_{55}} \times \text{Raf\_P\_MEK\_P} - k_{f_{56}} \times \text{PP2A} \times \text{MEK\_PP} + \\ &\quad k_{b_{56}} \times \text{PP2A\_MEK\_PP} - k_{f_{58}} \times \text{MEK\_PP} \times \text{MAPK} + \\ &\quad (k_{b_{58}} + k_{cat_{58}}) \times \text{MEK\_PP\_MAPK} - \\ &\quad k_{f_{59}} \times \text{MEK\_PP} \times \text{MAPK\_P} + \\ &\quad (k_{b_{59}} + k_{cat_{59}}) \times \text{MEK\_PP\_MAPK\_P}\end{aligned} \tag{A.103}$$

$$\begin{aligned}\frac{d\text{PP2A\_MEK\_P}}{dt} &= k_{f_{57}} \times \text{PP2A} \times \text{MEK\_P} - \\ &\quad (k_{b_{57}} + k_{cat_{57}}) \times \text{PP2A\_MEK\_P}\end{aligned} \tag{A.104}$$

$$\begin{aligned}\frac{d\text{PP2A\_Raf\_P}}{dt} &= k_{f_{53}} \times \text{PP2A} \times \text{Raf\_P} - \\ &\quad (k_{b_{53}} + k_{cat_{53}}) \times \text{PP2A\_Raf\_P})\end{aligned} \tag{A.105}$$

$$\begin{aligned}\frac{d\text{PP2A\_MEK\_PP}}{dt} &= k_{f_{56}} \times \text{PP2A} \times \text{MEK\_PP} - \\ &\quad (k_{b_{56}} + k_{cat_{56}}) \times \text{PP2A\_MEK\_PP}\end{aligned} \tag{A.106}$$

$$\begin{aligned}\frac{d\text{AMPAR\_P}}{dt} &= -k_{f_{46}} \times \text{PP2A} \times \text{AMPAR\_P} + k_{b_{46}} \times \text{PP2A\_AMPAR\_P} + \\ &\quad k_{cat_{45}} \times \text{PKC}_{\text{active\_}}\text{AMPAR}\end{aligned} \tag{A.107}$$

$$\begin{aligned}\frac{d\text{AMPAR}}{dt} &= k_{cat_{46}} \times \text{PP2A\_AMPAR\_P} - k_{f_{45}} \times \text{PKC}_{\text{active}} \times \text{AMPAR} + \\ &\quad k_{b_{45}} \times \text{PKC}_{\text{active\_}}\text{AMPAR}\end{aligned} \tag{A.108}$$

$$\begin{aligned}\frac{d\text{PP2A\_AMPAR\_P}}{dt} &= k_{f_{46}} \times \text{PP2A} \times \text{AMPAR\_P} - \\ &\quad (k_{b_{46}} + k_{cat_{46}}) \times \text{PP2A\_AMPAR\_P}\end{aligned} \tag{A.109}$$

$$\begin{aligned}\frac{d\text{PKC}_{\text{active\_}}\text{AMPAR}}{dt} &= k_{f_{45}} \times \text{PKC}_{\text{active}} \times \text{AMPAR} - \\ &\quad (k_{b_{45}} + k_{cat_{45}}) \times \text{PKC}_{\text{active\_}}\text{AMPAR}\end{aligned} \tag{A.110}$$

$$\begin{aligned}\frac{d\text{MAPK}_2}{dt} &= (-k_{f_{58}} \times \text{MEK\_PP} \times \text{MAPK} + k_{b_{58}} \times \text{MEK\_PP\_MAPK} + \\ &\quad k_{cat_{60}} \times \text{MKP}_1\text{\_MAPK\_P}) \times 2.5\end{aligned} \tag{A.111}$$

$$\mathrm{MAPK} = \mathrm{MAPK}_2 \times 0.4 \tag{A.112}$$

$$\begin{aligned}\frac{d\mathrm{MEK\_PP\_MAPK}}{dt} &= k_{f_{58}} \times \mathrm{MEK\_PP} \times \mathrm{MAPK} - \\ &\quad (k_{b_{58}} + k_{cat_{58}}) \times \mathrm{MEK\_PP\_MAPK}\end{aligned} \tag{A.113}$$

$$\begin{aligned}\frac{d\mathrm{MAPK\_P}}{dt} &= k_{cat_{58}} \times \mathrm{MEK\_PP\_MAPK} - k_{f_{59}} \times \mathrm{MEK\_PP} \times \mathrm{MAPK\_P} + \\ &\quad k_{b_{59}} \times \mathrm{MEK\_PP\_MAPK\_P} - k_{f_{60}} \times \mathrm{MKP}_1 \times \mathrm{MAPK\_P} + \\ &\quad k_{b_{60}} \times \mathrm{MKP}_1\mathrm{\_MAPK\_P} + \\ &\quad k_{cat_{61}} \times \mathrm{MKP}_1\mathrm{\_MAPK\_PP}\end{aligned} \tag{A.114}$$

$$\begin{aligned}\frac{d\mathrm{MEK\_PP\_MAPK\_P}}{dt} &= k_{f_{59}} \times \mathrm{MEK\_PP} \times \mathrm{MAPK\_P} - (k_{b_{59}} + \\ &\quad k_{cat_{59}}) \times \mathrm{MEK\_PP\_MAPK\_P}\end{aligned} \tag{A.115}$$

$$\begin{aligned}\frac{d\mathrm{MAPK\_PP}}{dt} &= k_{cat_{59}} \times \mathrm{MEK\_PP\_MAPK\_P} - k_{f_{61}} \times \mathrm{MKP}_1 \times \mathrm{MAPK\_PP} + \\ &\quad k_{b_{61}} \times \mathrm{MKP}_1\mathrm{\_MAPK\_PP} - k_{f_{23}} \times \mathrm{MAPK\_PP} \times \mathrm{PLA}_2 + \\ &\quad (k_{b_{23}} + k_{cat_{23}}) \times \mathrm{MAPK\_PP\_PLA}_2\end{aligned} \tag{A.116}$$

$$\begin{aligned}\frac{d\mathrm{MKP1}}{dt} &= (-k_{f_{60}} \times \mathrm{MKP}_1 \times \mathrm{MAPK\_P} + (k_{b_{60}} + k_{cat_{60}}) \times \\ &\quad \mathrm{MKP}_1\mathrm{\_MAPK\_P} - k_{f_{61}} \times \mathrm{MKP}_1 \times \mathrm{MAPK\_PP} + \\ &\quad (k_{b_{61}} + k_{cat_{61}}) \times \mathrm{MKP}_1\mathrm{\_MAPK\_PP}) \times 2.5\end{aligned} \tag{A.117}$$

$$\mathrm{MKP}_1 = \mathrm{MKP1} \times 0.4 \tag{A.118}$$

$$\begin{aligned}\frac{d\mathrm{MKP}_1\mathrm{\_MAPK\_P}}{dt} &= k_{f_{60}} \times \mathrm{MKP}_1 \times \mathrm{MAPK\_P} - \\ &\quad (k_{b_{60}} + k_{cat_{60}}) \times \mathrm{MKP}_1\mathrm{\_MAPK\_P}\end{aligned} \tag{A.119}$$

$$\begin{aligned}\frac{d\mathrm{MKP}_1\mathrm{\_MAPK\_PP}}{dt} &= k_{f_{61}} \times \mathrm{MKP}_1 \times \mathrm{MAPK\_PP} - \\ &\quad (k_{b_{61}} + k_{cat_{61}}) \times \mathrm{MKP}_1\mathrm{\_MAPK\_PP}\end{aligned} \tag{A.120}$$

$$\begin{aligned}\frac{d\mathrm{PLA}_2}{dt} &= -k_{f_{23}} \times \mathrm{MAPK\_PP} \times \mathrm{PLA}_2 + \\ &\quad k_{b_{23}} \times \mathrm{MAPK\_PP\_PLA}_2 + k_{f_{24}} \times \mathrm{PLA}_2\mathrm{\_P} - \\ &\quad k_{f_{14}} \times \mathrm{PLA}_2 \times \mathrm{Ca} + k_{b_{14}} \times \mathrm{PLA}_2\mathrm{\_Ca} - \\ &\quad k_{f_{18}} \times \mathrm{PLA}_2 \times \mathrm{PIP}_2 + k_{b_{18}} \times \mathrm{PLA}_2\mathrm{\_PIP}_2\end{aligned} \tag{A.121}$$

$$\begin{aligned}\frac{d\text{MAPK\_PP\_PLA}_2}{dt} &= k_{f_{23}} \times \text{MAPK\_PP} \times \text{PLA}_2 - \\ &\quad (k_{b_{23}} + k_{cat_{23}}) \times \text{MAPK\_PP\_PLA}_2\end{aligned} \tag{A.122}$$

$$\begin{aligned}\frac{d\text{PLA}_2\text{\_P}}{dt} &= k_{cat_{23}} \times \text{MAPK\_PP\_PLA}_2 - k_{f_{25}} \times (\text{PLA}_2\text{\_P})^2 \times \text{APC} + \\ &\quad (k_{b_{25}} + k_{cat_{25}}) \times \text{PLA}_2\text{\_P\_APC} - k_{f_{24}} \times \text{PLA}_2\text{\_P}\end{aligned} \tag{A.123}$$

$$\begin{aligned}\frac{d\text{PLA}_2\text{\_Ca}}{dt} &= k_{f_{14}} \times \text{PLA}_2 \times \text{Ca} - k_{b_{14}} \times \text{PLA}_2\text{\_Ca} - \\ &\quad k_{f_{16}} \times \text{PLA}_2\text{\_Ca} \times \text{DAG} + k_{b_{16}} \times \text{PLA}_2\text{\_Ca\_DAG} - \\ &\quad k_{f_{21}} \times \text{PIP}_2 \times \text{PLA}_2\text{\_Ca} + k_{b_{21}} \times \text{PLA}_2\text{\_Ca\_PIP}_2 - \\ &\quad k_{f_{15}} \times \text{PLA}_2\text{\_Ca} \times \text{APC} + \\ &\quad (k_{b_{15}} + k_{cat_{15}}) \times \text{PLA}_2\text{\_Ca\_APC}\end{aligned} \tag{A.124}$$

$$\begin{aligned}\frac{d\text{PLA}_2\text{\_PIP}_2}{dt} &= k_{f_{18}} \times \text{PLA}_2 \times \text{PIP}_2 - k_{b_{18}} \times \text{PLA}_2\text{\_PIP}_2 - \\ &\quad k_{f_{19}} \times \text{PLA}_2\text{\_PIP}_2 \times \text{APC} + \\ &\quad (k_{b_{19}} + k_{cat_{19}}) \times \text{PLA}_2\text{\_PIP}_2\text{\_APC}\end{aligned} \tag{A.125}$$

$$\begin{aligned}\frac{d\text{PKC\_Ca}}{dt} &= -k_{f_{27}} \times \text{PKC\_Ca} \times \text{DAG} + k_{b_{27}} \times \text{PKC\_Ca\_DAG} - \\ &\quad k_{f_{31}} \times \text{PKC\_Ca} \times \text{AA} + k_{b_{31}} \times \text{PKC\_Ca\_AA} + \\ &\quad k_{f_{26}} \times \text{PKC} \times \text{Ca} - k_{b_{26}} \times \text{PKC\_Ca} - \\ &\quad k_{f_{32}} \times \text{PKC\_Ca} + k_{b_{32}} \times \text{PKC\_Ca\_mem}\end{aligned} \tag{A.126}$$

$$\begin{aligned}\frac{d\text{PKC\_Ca\_DAG}}{dt} &= k_{f_{27}} \times \text{PKC\_Ca} \times \text{DAG} - k_{b_{27}} \times \text{PKC\_Ca\_DAG} - \\ &\quad k_{f_{33}} \times \text{PKC\_Ca\_DAG} + \\ &\quad k_{b_{33}} \times \text{PKC\_Ca\_DAG\_mem}\end{aligned} \tag{A.127}$$

$$\begin{aligned}\frac{d\text{PKC}}{dt} &= -k_{f_{28}} \times \text{PKC} \times \text{DAG} + k_{b_{28}} \times \text{PKC\_DAG} - \\ &\quad -k_{f_{30}} \times \text{PKC} \times \text{AA} + k_{b_{30}} \times \text{PKC\_AA} - \\ &\quad k_{f_{26}} \times \text{PKC} \times \text{Ca} + k_{b_{26}} \times \text{PKC\_Ca}\end{aligned} \tag{A.128}$$

$$\begin{aligned}\frac{d\text{PKC\_DAG}}{dt} &= k_{f_{28}} \times \text{PKC} \times \text{DAG} - k_{b_{28}} \times \text{PKC\_DAG} - \\ &\quad k_{f_{29}} \times \text{PKC\_DAG} \times \text{AA} + k_{b_{29}} \times \text{PKC\_DAG\_AA} - \\ &\quad k_{f_{34}} \times \text{PKC\_DAG} + k_{b_{34}} \times \text{PKC\_DAG\_mem}\end{aligned} \tag{A.129}$$

$$\begin{aligned}\frac{d\mathrm{PLA_2\_Ca\_DAG}}{dt} &= k_{f_{16}} \times \mathrm{PLA_2\_Ca} \times \mathrm{DAG} - k_{b_{16}} \times \mathrm{PLA_2\_Ca\_DAG} - \\ &\quad k_{f_{17}} \times \mathrm{PLA_2\_Ca\_DAG} \times \mathrm{APC} + \\ &\quad (k_{b_{17}} + k_{cat_{17}}) \times \mathrm{PLA_2\_Ca\_DAG\_APC} \qquad \text{(A.130)}\end{aligned}$$

$$\begin{aligned}\frac{d\mathrm{PLA_2\_Ca\_PIP_2}}{dt} &= k_{f_{21}} \times \mathrm{PIP_2} \times \mathrm{PLA_2\_Ca} - k_{b_{21}} \times \mathrm{PLA_2\_Ca\_PIP_2} - \\ &\quad k_{f_{22}} \times \mathrm{PLA_2\_Ca\_PIP_2} \times \mathrm{APC} + \\ &\quad (k_{b_{22}} + k_{cat_{22}}) \times \mathrm{PLA_2\_Ca\_PIP_2\_APC} \qquad \text{(A.131)}\end{aligned}$$

$$\begin{aligned}\frac{d\mathrm{AA}}{dt} &= -k_{f_{20}} \times \mathrm{AA} - k_{f_{30}} \times \mathrm{PKC} \times \mathrm{AA} + \\ &\quad k_{b_{30}} \times \mathrm{PKC\_AA} - k_{f_{31}} \times \mathrm{PKC\_Ca} \times \mathrm{AA} + \\ &\quad k_{b_{31}} \times \mathrm{PKC\_Ca\_AA} - k_{f_{29}} \times \mathrm{PKC\_DAG} \times \mathrm{AA} + \\ &\quad k_{b_{29}} \times \mathrm{PKC\_DAG\_AA} + k_{cat_{17}} \times \mathrm{PLA_2\_Ca\_DAG\_APC} + \\ &\quad k_{cat_{15}} \times \mathrm{PLA_2\_Ca\_APC} + k_{cat_{19}} \times \mathrm{PLA_2\_PIP_2\_APC} + \\ &\quad k_{cat_{22}} \times \mathrm{PLA_2\_Ca\_PIP_2\_APC} + k_{cat_{25}} \times \mathrm{PLA_2\_P\_APC} \qquad \text{(A.132)}\end{aligned}$$

$$\begin{aligned}\frac{d\mathrm{PKC\_AA}}{dt} &= k_{f_{30}} \times \mathrm{PKC} \times \mathrm{AA} - k_{b_{30}} \times \mathrm{PKC\_AA} - \\ &\quad k_{f_{36}} \times \mathrm{PKC\_AA} \qquad \text{(A.133)}\end{aligned}$$

$$\begin{aligned}\frac{d\mathrm{PKC\_Ca\_AA}}{dt} &= k_{f_{31}} \times \mathrm{PKC\_Ca} \times \mathrm{AA} - k_{b_{31}} \times \mathrm{PKC\_Ca\_AA} - \\ &\quad k_{f_{36}} \times \mathrm{PKC\_Ca\_AA} \qquad \text{(A.134)}\end{aligned}$$

$$\begin{aligned}\frac{d\mathrm{PKC\_DAG\_AA}}{dt} &= k_{f_{29}} \times \mathrm{PKC\_DAG} \times \mathrm{AA} - k_{b_{29}} \times \mathrm{PKC\_DAG\_AA} - \\ &\quad k_{f_{35}} \times \mathrm{PKC\_DAG\_AA} + \\ &\quad k_{b_{35}} \times \mathrm{PKC\_DAG\_AA\_mem} \qquad \text{(A.135)}\end{aligned}$$

$$\begin{aligned}\frac{d\mathrm{PLA_2\_Ca\_DAG\_APC}}{dt} &= k_{f_{17}} \times \mathrm{PLA_2\_Ca\_DAG} \times \mathrm{APC} - \\ &\quad (k_{b_{17}} + k_{cat_{17}}) \times \\ &\quad \mathrm{PLA_2\_Ca\_DAG\_APC} \qquad \text{(A.136)}\end{aligned}$$

$$\begin{aligned}\frac{d\mathrm{PLA_2\_Ca\_APC}}{dt} &= k_{f_{15}} \times \mathrm{PLA_2\_Ca} \times \mathrm{APC} - \\ &\quad (k_{b_{15}} + k_{cat_{15}}) \times \mathrm{PLA_2\_Ca\_APC} \qquad \text{(A.137)}\end{aligned}$$

$$\begin{aligned}\frac{d\mathrm{PLA_2\_PIP_2\_APC}}{dt} &= k_{f_{19}} \times \mathrm{PLA_2\_PIP_2} \times \mathrm{APC} - \\ &\quad (k_{b_{19}} + k_{cat_{19}}) \times \mathrm{PLA_2\_PIP_2\_APC} \qquad \text{(A.138)}\end{aligned}$$

$$\begin{aligned}\frac{d\mathrm{PLA_2\_Ca\_PIP_2\_APC}}{dt} &= k_{f_{22}} \times \mathrm{PLA_2\_Ca\_PIP_2} \times \mathrm{APC} - \\ &\quad (k_{b_{22}} + k_{cat_{22}}) \times \\ &\quad \mathrm{PLA_2\_Ca\_PIP_2\_APC} \end{aligned} \tag{A.139}$$

$$\begin{aligned}\frac{d\mathrm{PLA_2\_P\_APC}}{dt} &= k_{f_{25}} \times (\mathrm{PLA_2\_P})^2 \times \mathrm{APC} - \\ &\quad (k_{b_{25}} + k_{cat_{25}}) \times \mathrm{PLA_2\_P\_APC} \end{aligned} \tag{A.140}$$

$$\begin{aligned}\frac{d\mathrm{PKC\_DAG\_mem}}{dt} &= k_{f_{34}} \times \mathrm{PKC\_DAG} - k_{b_{34}} \times \mathrm{PKC\_DAG\_mem} - \\ &\quad k_{f_{36}} \times \mathrm{PKC\_DAG\_mem} \end{aligned} \tag{A.141}$$

$$\begin{aligned}\frac{d\mathrm{PKC\_Ca\_mem}}{dt} &= k_{f_{32}} \times \mathrm{PKC\_Ca} - k_{b_{32}} \times \mathrm{PKC\_Ca\_mem} - \\ &\quad k_{f_{36}} \times \mathrm{PKC\_Ca\_mem} \end{aligned} \tag{A.142}$$

$$\begin{aligned}\frac{d\mathrm{PKC\_Ca\_DAG\_mem}}{dt} &= k_{f_{33}} \times \mathrm{PKC\_Ca\_DAG} - \\ &\quad k_{b_{33}} \times \mathrm{PKC\_Ca\_DAG\_mem} - \\ &\quad k_{f_{36}} \times \mathrm{PKC\_Ca\_DAG\_mem} \end{aligned} \tag{A.143}$$

$$\begin{aligned}\frac{d\mathrm{PKC\_DAG\_AA\_mem}}{dt} &= k_{f_{35}} \times \mathrm{PKC\_DAG\_AA} - \\ &\quad k_{b_{35}} \times \mathrm{PKC\_DAG\_AA\_mem} - \\ &\quad k_{f_{36}} \times \mathrm{PKC\_DAG\_AA\_mem} \end{aligned} \tag{A.144}$$

$$\begin{aligned}\mathrm{PKC_{act}} &= \mathrm{PKC\_DAG\_mem} + \mathrm{PKC\_Ca\_DAG\_mem} + \\ &\quad \mathrm{PKC\_DAG\_AA\_mem} + \mathrm{PKC\_AA} + \mathrm{PKC\_Ca\_AA} + \\ &\quad \mathrm{PKC\_Ca\_mem} + \mathrm{PKC_{active}} \end{aligned} \tag{A.145}$$

$$\begin{aligned}\frac{d\mathrm{PKC_{active}}}{dt} &= -k_{f_{47}} \times \mathrm{PKC_{act}} \times \mathrm{Raf} + (k_{b_{47}} + k_{cat_{47}}) \times \mathrm{PKC_{active\_}Raf} - \\ &\quad k_{f_{45}} \times \mathrm{PKC_{act}} \times \mathrm{AMPAR} + \\ &\quad (k_{b_{45}} + k_{cat_{45}}) \times \mathrm{PKC_{active\_}AMPAR} \end{aligned} \tag{A.146}$$

A.3 Kinetic Parameters

Reaction	k_{f_i} (μM^{-1}s^{-1})	k_{b_i} (s^{-1})	k_{cat_i} (s^{-1})
A.1	0.5988	1	
A.2	16.667	0.1	
A.3	0.1		
A.4	0.1		
A.5	0.1		
A.6	2.5189	0.1	
A.7	10		
A.8	25	77	48
A.9	10		
A.10	50		
A.11	5		
A.12	10		
A.13	1		
A.14	0.01	0.1	
A.15	30	546	54
A.16	0.05	0.1	
A.17	30	540	60
A.18	2×10^{-10}	0.5	
A.19	10	188.96	11.04
A.20	0.001		
A.21	2×10^{-10}	0.5	
A.22	10	164	36
A.23	10	236	20
A.24	0.17		
A.25	10	80	120
A.26	0.013	0.13	
A.27	0.03	0.015	
A.28	0.03	0.015	
A.29	0.2	10	
A.30	0.2	10	
A.31	0.2	10	
A.32	2×10^{5}	1	
A.33	1×10^{6}	1	
A.34	1×10^{6}	1	
A.35	1×10^{6}	1	
A.36	0.004		
A.37	0.01	0.0025	
A.38	0.673		
A.39	50	517.65	7.35
A.40	50	96.13	3.87

Reaction	k_{f_i} (μM^{-1}s^{-1})	k_{b_i} (s^{-1})	k_{cat_i} (s^{-1})
A.41	2	0.1	
A.42	5	0.28	0.72
A.43	0.0001		
A.44	1	0.27	
A.45	5	16.5	1.5
A.46	5	72.283	6
A.47	5	57.466	0.0335
A.48	1	0.0001	
A.49	0.02		
A.50	5	87.497	0.0025
A.51	5	125	0.001
A.52	0.001		
A.53	5	72.283	6
A.54	10	1.486	0.105
A.55	10	1.486	0.105
A.56	5	72.283	6
A.57	5	72.283	6
A.58	10	0.313	0.15
A.59	10	0.313	0.15
A.60	20	0.3334	1
A.61	20	0.3334	1

A.4 Initial Concentrations

Compound	Initial concentration (μM)
AMPAR	0.5
APC	0.5
CRHR	0.5
$G_{\alpha\beta\gamma}$	0.89513
GC	3
Glu_mGluR_G_q	0.10465
G_{sub}	10.8
GTP	10
IP_3R	0.016643
$MAPK_2$	1
MEK	0.5
mGluR	0.19524
MKP1	0.0032
PDE	2
PIP_2	10
PKC	1
PKC_Ca_DAG	8.4632×10^{-23}
PKC_DAG	1.161×10^{-16}
PKC_DAG_AA	2.5188×10^{-19}
PKG	2.445
PLA_2	0.4
PLC	0.8
PP2A	2.7
Raf	0.5

Appendix B

Alterations in the Reimplementation of Kuroda Model

B.1 Modifications in the Pinto Implementation

The alterations needed in the Pinto implementation to replicate the original results in [Kuroda 2001] are summarised as follows (Figure 5.8)

1. $k_{cat_{40}} = 0$ in Equation A.66;
2. $k_{cat_{55}} = 0$ in Equation A.95;
3. $k_{f_{24}} = 0$ and $k_{cat_{25}} = 0$ in Equation A.123;
4. $k_{cat_{19}} = 0$ in Equation A.125;
5. squaring phosphorylated PLA_2 in Equations A.123 and A.140;
6. rescaling the concentrations of MAP kinase, MKP_1 and phosphorylated Raf whose modifications follow: adding Equations A.96, A.112 and A.118 to the LTD model, and multiplying Equations A.95, A.111 and A.117 by 2.5;
7. deleting Equation A.146 that models the enzymatic reactions between PKC and two different species: Raf and AMPA receptor. Therefore, $\mathrm{PKC}_{\mathrm{active}} = 0$ in Equation A.145.

B.2 Alterations in the Kuroda Implementation

The modifications performed in the Kuroda implementation to obtain the results illustrated in Figure 5.8 are following described

1. setting the linear interpolation in the calcium, NO and glutamate input tables;
2. deleting the arrow from glutamate (mGlu in Kuroda's code) to Lyn;
3. deleting the following compounds: CRH_pkc, PKC_CRH_mem, Ca_basal, Ca_pump, Ca_ext, Cachannel, and Ca_store that are useless in the model;
4. changing the time step size from 5×10^{-4} s to 5×10^{-5} s.

B.3 Inconsistencies in [Kuroda 2001]

Various inconsistencies were also detected in the supplementary information (SI) of the paper by Kuroda and co-authors [Kuroda 2001]:

- Reactions A.7, A.10 and A.11 need to be included in SI 9;
- Reaction A.20 is missing from the PLA_2 kinase pathway in SI 7;
- Reactions A.32-A.35 are also not included in SI 8.

Some reactions listed in the SI of [Kuroda 2001] were not modelled in the Kuroda implementation and need to be modified in their documentation, as follows

- Reaction A.38 replaces $NO \longrightarrow NO_{dec}$ in SI 5;
- Reaction A.49 substitutes $CRF \longrightarrow CRF_{dec}$ in SI 2;
- $PKC_{active} \longrightarrow PKC_{active_{dec}}$ in SI 1 is modelled as in Reaction A.36 instead;
- Reaction A.23 is a correction from Reaction 9 in SI 7;
- Reaction A.47 corrects Reaction 1 in SI 6.

Moreover, the correct PDE concentration in Table 1 of [Kuroda 2001] is 2 μM rather than 5 μM, and K_m from enzymatic reaction 3 is 10.5 μM rather than 45 μM.

B.4 Correction of Errors from the Kuroda Implementation

The correction of the errors adopted in the XPPAUT code due to inconsistencies in the Kuroda implementation is following demonstrated (Figure 5.9)

1. $k_{cat_{40}} = 3.87\ \mu M^{-1} s^{-1}$ in Equation A.66;
2. $k_{cat_{55}} = 0.105\ s^{-1}$ in Equation A.95;
3. $k_{f_{24}} = 0.39\ s^{-1}$ and $k_{cat_{25}} = 120\ s^{-1}$ in Equation A.123;
4. $k_{cat_{19}} = 11.04\ s^{-1}$ in Equation A.125;
5. Reaction A.25 was corrected by introducing a single phosphorylated PLA_2 instance instead of two. Therefore, phosphorylated PLA_2 is not squared in Equations A.123 and A.140;
6. the same volume was used to all compounds in the model. The equations for MAP kinase, MKP_1 and phosphorylated Raf were then altered. Equations A.96, A.112 and A.118 were deleted, and Equations A.95, A.111 and A.117 are not multiplied by 2.5;

7. Equation A.146 was included to model changes in $\mathrm{PKC}_{\mathrm{active}}$ which, in turn, also influences Equation A.145 in which the $\mathrm{PKC}_{\mathrm{active}}$ concentration is not zero;

8. $k_{f_{24}} = 0.39\,\mathrm{s}^{-1}$ to compensate the loss of the double instance of phosphorylated PLA_2 and to restore the LTD intermediate phase.

B.5 Modifications After Adopting New Calcium Levels

Parameter	Previous Value	New Value
$k_{f_{15}}$	30 $\mu\mathrm{M}^{-1}\mathrm{s}^{-1}$	0.1 $\mu\mathrm{M}^{-1}\mathrm{s}^{-1}$
$k_{f_{24}}$	0.39 s^{-1}	0.013 s^{-1}
$k_{f_{26}}$	0.13 $\mu\mathrm{M}^{-1}\mathrm{s}^{-1}$	0.013 $\mu\mathrm{M}^{-1}\mathrm{s}^{-1}$
$k_{f_{32}}$	2×10^5 s^{-1}	50 s^{-1}

Table B.1: **Modified kinetic constants to reproduce the results in [Kuroda 2001] after adopting new calcium levels** (Figure 5.12).

Appendix C

Stochastic Model of CaMKII Activation

This section was written by Dr Maria Schilstra.

For the purpose of the stochastic simulations, calcium-calmodulin (Ca_4CaM) dependent protein kinase II (CaMKII) molecules are assumed to be organised in 6-membered rings. As it is necessary to keep track of individual CaMKII subunits, each subunit has a ring coordinate c_r, with $0 \leq c_r < 6$, and a ring number n_r, with $0 \leq n_r < N_R$, where N_R is the total number of rings used in the simulation. Subunits are numbered consecutively, so that the subunits directly to the "left" and "right" of a subunit have ring coordinates $(c_r - 1)$ *modulo* 6, and $(c_r + 1)$ *modulo* 6, respectively. Thus, subunit 3 is to the "left" of subunit 4, and subunit 0 is to the "right" of subunit 5, and so on.

Each CaMKII subunit is either unphosphorylated (indicated as *Kin0*) or phosphorylated (*KinP*), and may be bound to one Ca_4CaM complex (*Cm*). Association and dissociation of the *Cm-Kin0* and *Cm-KinP* complexes are described by the kinetic and thermodynamic constants specified for the deterministic model. Phosphorylation is irreversible, and can only happen to a subunit that is "ready" to be phosphorylated. A subunit with a ring coordinate c is ready only when it is unphosphorylated (*Cm-Kin0*), and the subunit on its left (with ring coordinate $(c-1)$ *modulo* 6) has kinase activity, i.e. is in the *Cm-Kin0*, *KinP*, or *Cm-KinP* state. Asterisks are used to indicate that a particular subunit is ready. To keep the model as simple as possible, subunits that are ready for phosphorylation (*Kin0** and *Cm-Kin**) have the same probability to become phosphorylated, independent of the state of their left neighbours.

Thus, there are a total of six different CaMKII states: *Kin0* (1), *Kin0** (2), *Cm-Kin0* (3), *Cm-Kin0** (4), *KinP* (5), and *Cm-KinP* (6), which are involved in a total of eight different reactions: *Kin0* + *Cm* → *Cm-Kin0* (1), *Kin0** + *Cm* → *Cm-Kin0** (2), *Cm-Kin0* → *Kin0* + *Cm* (3), *Cm-Kin0** → *Kin0** + *Cm* (4), *KinP* + *Cm* → *Cm-KinP* (5), *Cm-KinP* → *KinP* + *Cm* (6), *Kin0** → *KinP* (7), and *Cm-Kin0** → *Cm-KinP* (8). Reactions 1, 2, 5, and 6 are second order reactions that involve binding of Ca_4CaM. However, the model assumes that the total concentration of Ca_4CaM, Cm_{tot}, is much larger than that of CaMKII, so that none of these reactions is capable of depleting the concentration of unbound Ca_4CaM. As a result, all reactions in the system will exhibit first order kinetics, and it is not necessary to specify a reaction volume.

At any time t, the instantaneous rate (flux), J_i, for each reaction i is computed as $J_i = kEff_i \times nR_i$. Here, the effective rate constant $kEff_i$ is equal to the actual first-order rate constant k_i for reactions 3, 4, 6, 7, and 8, and equal to $k_i \times Cm_{tot}$ for the remaining pseudo-first order reactions (1, 2, 5, 6). Furthermore, nR_i is the number of reactant CaMKII subunits for each reaction i present at time t.

Simulations were performed using a variant of Gillespie's next reaction algorithm [Gillespie 1977], implemented in Python with extensive use of Python's numerical library *numpy*. In short, simulations are started with all $6 \times N_R$ individual subunits in state *Kin0*, and during the simulation a tally is kept of the state of each subunit. In each simulation step, a random number, rnd_i, between 0 (included) and 1 (excluded) is drawn for each reaction i with finite (i.e. non-zero) flux J_i, and a provisional time interval, Δt_i, between the current simulated time, t, and the next event is computed as $\Delta t_i = ln(1 - rnd_i)/J_i$. The reaction r_i that generates the shortest time interval, Δt_{min}, is then selected as the next reaction, r_{next}, to occur at $t + \Delta t_{min}$. The actual subunit that will undergo this transition is then randomly chosen out of the nR_{next} subunits that are present at time t in the reactant pool for r_{next}. Once the time for the next event, the transition, and the actual subunit have been established, the simulated time is increased to $t + \Delta t_{min}$, and the state of the selected subunit and, where necessary, that of its left neighbour is updated. The process is then repeated until $t + \Delta t_{min}$ exceeds a pre-set maximum simulation time.

Appendix D

Parameters for CaMKII Activation Models

Table D.1: **Values of kinetic parameters for deterministic and stochastic simulations of CaMKII activation.**

Parameter description	**Symbol**	**Value**	**Reference**
Rate of association of Ca_4CaM to a W_i subunit	k_{ib}	$0.01\ nM^{-1}s^{-1}$	[Dupont 2003]
Rate of dissociation of Ca_4CaM from a W_b subunit	k_{bi}	$0.8\ s^{-1}$	[Dupont 2003]
Rate of association of Ca_4CaM to a W_a subunit	k_{ap}	$0.01\ nM^{-1}s^{-1}$	[Dupont 2003]
Rate of dissociation of Ca_4CaM from a W_p subunit	k_{pa}	$0.0008\ s^{-1}$	[Dupont 2003]
Ca_4CaM binding half maximal concentration	K_d	1×10^3 nM	[Dupont 2003]
Amplitude of calcium pulses	Ca_t	500×10^3 nM	[Dupont 2003]
Phenomenological rate of kinase autophosphorylation	K'_a	$0.29\ s^{-1}$	[Dupont 2003]
Rate of autophosphorylation for stochastic simulations	kPhos	$0.12\ s^{-1}$	
Coefficient of the kinase activity at W_b subunit	c_b	75 %	[Dupont 2003]
Coefficient of the kinase activity at W_p subunit	c_p	100 %	[Dupont 2003]
Coefficient of the kinase activity at W_a subunit	c_a	80 %	[Dupont 2003]
Fitting parameter a	a	0.5	
Fitting parameter b	b	1.956	
Fitting parameter c	c	-1.8	

The parameters K_d, Ca_t, K'_a, c_b, c_p, c_a, a, b and c are exclusive for the deterministic model, while kPhos is used in the stochastic model. The other parameter values are adopted in both the deterministic and stochastic simulations.

Appendix E

Bidirectional Plasticity Model

E.1 Model Description

In the simple model that simulates the bidirectional plasticity in Purkinje cells (Figure 7.2), changes in calcium concentration are expressed as

$$\frac{d[\mathrm{Ca}]}{dt} = -4\mathrm{k_{on}}[\mathrm{Ca}]^4[\mathrm{CaM}] + 4\mathrm{k_{off}}\,[\mathrm{Ca_4CaM}] + \gamma(t) - \kappa\left([\mathrm{Ca}] - [\mathrm{Ca_{min}}]\right) \quad , \tag{E.1}$$

where $[x]$ denotes the concentration of substance x, e.g. [Ca] is the calcium concentration. The term $\gamma(t) - \kappa([\mathrm{Ca}] - [\mathrm{Ca_{min}}])$ describes the simple model of calcium dynamics adopted here to obtain calcium pulses with concentrations that reflect experimental data [Wang 2000]. Calcium concentration increases at each time step are denoted by $\gamma(t)$ which values originate from an input table (Figure 7.5A), κ is a term that reflects the calcium removal through diffusion, pumps, exchanges, and $[\mathrm{Ca_{min}}]$ is the basal calcium concentration.

The temporal evolution of CaM is written as

$$\frac{d[\mathrm{CaM}]}{dt} = -\mathrm{k_{on}}[\mathrm{Ca}]^4[\mathrm{CaM}] + \mathrm{k_{off}}\,[\mathrm{Ca_4CaM}] \quad . \tag{E.2}$$

$\mathrm{Ca_4CaM}$ results from the binding of four calcium ions to CaM, and activates PP2B, $\mathrm{W_b}$, $\mathrm{W_p}$, $\mathrm{W_bAc}$ and $\mathrm{W_pAc}$. The equation that represents the evolution of $\mathrm{Ca_4CaM}$ concentration is

$$\begin{aligned}\frac{d[\mathrm{Ca_4CaM}]}{dt} \quad = \quad & \mathrm{k_{on}}[\mathrm{Ca}]^4[\mathrm{CaM}] - \mathrm{k_{off}}\,[\mathrm{Ca_4CaM}] - \\ & \mathrm{k_{ppia}}[\mathrm{PP2B_i}]\,[\mathrm{Ca_4CaM}] + \mathrm{k_{ppai}}[\mathrm{PP2B_{ac}}] - \\ & \mathrm{k_{ib}}[\mathrm{W_i}]\,[\mathrm{Ca_4CaM}] + \mathrm{k_{bi}}[\mathrm{W_b}] + \\ & \mathrm{k_{pa}}[\mathrm{W_p}] - \mathrm{k_{ap}}[\mathrm{W_a}]\,[\mathrm{Ca_4CaM}] - \\ & \mathrm{k_{iacbac}}\,[\mathrm{W_iAc}]\,[\mathrm{Ca_4CaM}] + \mathrm{k_{baciac}}\,[\mathrm{W_bAc}] + \\ & \mathrm{k_{pacaac}}\,[\mathrm{W_pAc}] - \mathrm{k_{aacpac}}\,[\mathrm{W_aAc}]\,[\mathrm{Ca_4CaM}] \quad . \end{aligned} \tag{E.3}$$

The CaMKII activation model described in Section 6.1 was adapted here to include the CaMKII subunit states bound to Ac (Figure 7.2), and also to express all kinase states in concentrations rather than fractions. Therefore, Equation 6.6 was modified to express the $\mathrm{W_i}$ concentration as

$$[\mathrm{W_i}] = [\mathrm{W_{tot}}] - [\mathrm{W_b}] - [\mathrm{W_p}] - [\mathrm{W_a}] - [\mathrm{W_iAc}] - [\mathrm{W_bAc}] - [\mathrm{W_pAc}] - [\mathrm{W_aAc}] \quad , \tag{E.4}$$

where $[\mathrm{W_{tot}}]$ is the total concentration of CaMKII. The phenomenological model to calculate the CaMKII autophosphorylation is again adopted here. Equations 6.1 and 6.2 were slightly modified to account for $\mathrm{W_{tot}}$, as follows

$$\mathrm{V_a} = \frac{\mathrm{K_a}\left(\left(c_b[\mathrm{W_b}]\right)^2 + \left(c_b[\mathrm{W_b}]\right)\left(c_p[\mathrm{W_p}]\right) + \left(c_b[\mathrm{W_b}]\right)\left(c_a[\mathrm{W_a}]\right)\right)}{[\mathrm{W_{tot}}]^2} \quad , \tag{E.5}$$

$$\mathrm{K_a} = \mathrm{K'_a}\left(\mathrm{aT_{ac}} + \mathrm{bT_{ac}^2} + \mathrm{cT_{ac}^3}\right) \quad , \tag{E.6}$$

and here

$$\mathrm{T_{ac}} = \frac{[\mathrm{W_b}] + [\mathrm{W_p}] + [\mathrm{W_a}]}{[\mathrm{W_{tot}}]} \quad . \tag{E.7}$$

Once $\mathrm{Ca_4CaM}$ binds to $\mathrm{W_i}$, the resulting $\mathrm{W_b}$ form can either be phosphorylated, release $\mathrm{Ca_4CaM}$, or bind to Ac. $\mathrm{W_b}$ is an active CaMKII subunit that can also phosphorylate AMPA receptors (AMPARs). The equation for $\mathrm{W_b}$ is therefore

$$\begin{aligned}\frac{d[\mathrm{W_b}]}{dt} \;=\;& -\mathrm{V_a}[\mathrm{W_{tot}}] + \mathrm{k_{ib}}[\mathrm{W_i}]\,[\mathrm{Ca_4CaM}] - \mathrm{k_{bi}}[\mathrm{W_b}] - \\ & \mathrm{k_{bbac}}[\mathrm{W_b}]\,[\mathrm{Ac}] + \mathrm{k_{bacb}}\,[\mathrm{W_bAc}] - \\ & \mathrm{k_{f_{phos}}}[\mathrm{W_b}]\,[\mathrm{AMPAR}] + \left(\mathrm{k_{b_{phos}}} + \mathrm{k_{cat_{phos}}}\right)[\mathrm{W_bAMPAR}] \quad ,\end{aligned} \tag{E.8}$$

where $[\mathrm{W_bAMPAR}]$ is the concentration of $\mathrm{W_b}$ bound to AMPARs. The $\mathrm{W_p}$ subunit can release $\mathrm{Ca_4CaM}$, switching to the $\mathrm{W_a}$ state, or bind to Ac and form $\mathrm{W_pAc}$. As for $\mathrm{W_b}$, $\mathrm{W_p}$ also phosphorylates AMPARs. The amount of $\mathrm{W_p}$ is calculated as

$$\begin{aligned}\frac{d[\mathrm{W_p}]}{dt} \;=\;& \mathrm{V_a}[\mathrm{W_{tot}}] - \mathrm{k_{pa}}[\mathrm{W_p}] + \mathrm{k_{ap}}[\mathrm{W_a}]\,[\mathrm{Ca_4CaM}] - \\ & \mathrm{k_{ppac}}[\mathrm{W_p}]\,[\mathrm{Ac}] + \mathrm{k_{pacp}}\,[\mathrm{W_pAc}] - \\ & \mathrm{k_{f_{phos}}}[\mathrm{W_p}]\,[\mathrm{AMPAR}] + \left(\mathrm{k_{b_{phos}}} + \mathrm{k_{cat_{phos}}}\right)[\mathrm{W_pAMPAR}] \quad ,\end{aligned} \tag{E.9}$$

where $[\mathrm{W_pAMPAR}]$ is the concentration of the complex of $\mathrm{W_p}$ bound to AMPARs. $\mathrm{W_a}$ can bind to either $\mathrm{Ca_4CaM}$ or Ac, and phosphorylate AMPARs as well. Thus

$$\begin{aligned}\frac{d[\mathrm{W_a}]}{dt} \;=\;& \mathrm{k_{pa}}[\mathrm{W_p}] - \mathrm{k_{ap}}[\mathrm{W_a}]\,[\mathrm{Ca_4CaM}] - \\ & \mathrm{k_{aaac}}[\mathrm{W_a}]\,[\mathrm{Ac}] + \mathrm{k_{aaca}}\,[\mathrm{W_aAc}] - \\ & \mathrm{k_{f_{phos}}}[\mathrm{W_a}]\,[\mathrm{AMPAR}] + \left(\mathrm{k_{b_{phos}}} + \mathrm{k_{cat_{phos}}}\right)[\mathrm{W_aAMPAR}] \quad ,\end{aligned} \tag{E.10}$$

and $[\mathrm{W_aAMPAR}]$ is the amount of $\mathrm{W_a}$ trapped to AMPARs.

$\mathrm{W_iAc}$ binds to $\mathrm{Ca_4CaM}$ and changes to the active $\mathrm{W_bAc}$ form, or dissociates from Ac and switches to the $\mathrm{W_i}$ state. Changes in $\mathrm{W_iAc}$ concentration are

$$\begin{aligned}\frac{d[\mathrm{W_iAc}]}{dt} \;=\;& \mathrm{k_{iiac}}[\mathrm{W_i}]\,[\mathrm{Ac}] - \mathrm{k_{iaci}}\,[\mathrm{W_iAc}] - \\ & \mathrm{k_{iacbac}}\,[\mathrm{W_iAc}]\,[\mathrm{Ca_4CaM}] + \mathrm{k_{baciac}}\,[\mathrm{W_bAc}] \quad .\end{aligned} \tag{E.11}$$

$\mathrm{W_bAc}$ can be phosphorylated by neighbouring active Ac-bound subunits: $\mathrm{W_bAc}$ itself, $\mathrm{W_pAc}$ or $\mathrm{W_aAc}$. The autophosphorylation process for Ac-bound CaMKII is analogous to the mechanism of autophosphorylation of the kinase unbound to Ac (Equations E.5, E.6 and E.7). The autophosphorylation rate for Ac-bound CaMKII subunits ($\mathrm{V_{ac}}$) is therefore

$$\mathrm{V_{ac}} = \frac{\mathrm{K_{ac}}\Big(\left(c_b\,[\mathrm{W_bAc}]\right)^2 + \left(c_b\,[\mathrm{W_bAc}]\right)\left(c_p\,[\mathrm{W_pAc}]\right) + \left(c_b\,[\mathrm{W_bAc}]\right)\left(c_a\,[\mathrm{W_aAc}]\right)\Big)}{[\mathrm{W_{tot}}]^2} \; , \tag{E.12}$$

where

$$\mathrm{K_{ac}} = \mathrm{K'_a}\left(\mathrm{aT_{Ac}} + \mathrm{bT_{Ac}^2} + \mathrm{cT_{Ac}^3}\right) \; , \tag{E.13}$$

and

$$\mathrm{T_{Ac}} = \frac{[\mathrm{W_bAc}] + [\mathrm{W_pAc}] + [\mathrm{W_aAc}]}{[\mathrm{W_{tot}}]} \; . \tag{E.14}$$

$\mathrm{W_bAc}$ can also switch to $\mathrm{W_iAc}$ once $\mathrm{Ca_4CaM}$ dissociates from this kinase subunit, or dissociate from Ac and change to $\mathrm{W_b}$. Thus

$$\begin{aligned}\frac{d[\mathrm{W_bAc}]}{dt} \;=\;& -\mathrm{V_{ac}}[\mathrm{W_{tot}}] + \mathrm{k_{iacbac}}\,[\mathrm{W_iAc}]\,[\mathrm{Ca_4CaM}] - \mathrm{k_{baciac}}\,[\mathrm{W_bAc}] + \\ & \mathrm{k_{bbac}}[\mathrm{W_b}]\,[\mathrm{Ac}] - \mathrm{k_{bacb}}\,[\mathrm{W_bAc}] \; . \end{aligned} \tag{E.15}$$

The phosphorylated Ac- and $\mathrm{Ca_4CaM}$-bound form of CaMKII can release $\mathrm{Ca_4CaM}$ and switch to the $\mathrm{W_aAc}$ form, or dissociate from Ac and swap to the $\mathrm{W_p}$ state. The concentration of $\mathrm{W_pAc}$ at each time step is expressed as

$$\begin{aligned}\frac{d[\mathrm{W_pAc}]}{dt} \;=\;& \mathrm{V_{ac}}[\mathrm{W_{tot}}] - \mathrm{k_{pacaac}}\,[\mathrm{W_pAc}] + \mathrm{k_{aacpac}}\,[\mathrm{W_aAc}]\,[\mathrm{Ca_4CaM}] + \\ & \mathrm{k_{ppac}}[\mathrm{W_p}]\,[\mathrm{Ac}] - \mathrm{k_{pacp}}\,[\mathrm{W_pAc}] \; , \end{aligned} \tag{E.16}$$

whereas $\mathrm{W_aAc}$ can bind to $\mathrm{Ca_4CaM}$ and switch to $\mathrm{W_pAc}$, or dissociate from Ac and turn into $\mathrm{W_a}$. The equation for $\mathrm{W_aAc}$ is

$$\begin{aligned}\frac{d[\mathrm{W_aAc}]}{dt} \;=\;& \mathrm{k_{pacaac}}\,[\mathrm{W_pAc}] - \mathrm{k_{aacpac}}[\mathrm{W_aAc}]\,[\mathrm{Ca_4CaM}] + \\ & \mathrm{k_{aaac}}[\mathrm{W_a}]\,[\mathrm{Ac}] - \mathrm{k_{aaca}}\,[\mathrm{W_aAc}] \; . \end{aligned} \tag{E.17}$$

$\mathrm{Ca_4CaM}$ not only activates CaMKII, but can also bind to the inactive form of PP2B ($\mathrm{PP2B_i}$). The phosphatase then gets activated and switches to the $\mathrm{PP2B_{ac}}$ form. $\mathrm{PP2B_{ac}}$ mediates the dephosphorylation of AMPA receptors. The temporal evolution of $\mathrm{PP2B_i}$ concentration is

$$\frac{d[\mathrm{PP2B_i}]}{dt} = -\mathrm{k_{ppia}}[\mathrm{PP2B_i}]\,[\mathrm{Ca_4CaM}] + \mathrm{k_{ppai}}[\mathrm{PP2B_{ac}}] \; , \tag{E.18}$$

whereas $\mathrm{PP2B_{ac}}$ concentration changes are expressed as

$$\begin{aligned}\frac{d[\mathrm{PP2B_{ac}}]}{dt} \;=\;& \mathrm{k_{ppia}}[\mathrm{PP2B_i}]\,[\mathrm{Ca_4CaM}] - \mathrm{k_{ppai}}[\mathrm{PP2B_{ac}}] - \\ & \mathrm{k_{f_{dephos}}}[\mathrm{PP2B_{ac}}]\,[\mathrm{AMPARP}] + \\ & \left(\mathrm{k_{b_{dephos}}} + \mathrm{k_{cat_{dephos}}}\right)[\mathrm{PP2B_{ac}AMPARP}] \; , \end{aligned} \tag{E.19}$$

where [PP2B$_{\mathrm{ac}}$AMPARP] expresses the concentration of PP2B$_{\mathrm{ac}}$ bound to phosphorylated AMPA receptors (AMPARPs). Moreover, the evolution of unphosphorylated AMPA receptors at each time step is

$$\begin{aligned}\frac{d[\mathrm{AMPAR}]}{dt} = \; & -\mathrm{k}_{\mathrm{f_{phos}}}[\mathrm{W_b}]\,[\mathrm{AMPAR}] + \mathrm{k}_{\mathrm{b_{phos}}}\,[\mathrm{W_bAMPAR}] - \\ & \mathrm{k}_{\mathrm{f_{phos}}}[\mathrm{W_p}]\,[\mathrm{AMPAR}] + \mathrm{k}_{\mathrm{b_{phos}}}\,[\mathrm{W_pAMPAR}] - \\ & \mathrm{k}_{\mathrm{f_{phos}}}[\mathrm{W_a}]\,[\mathrm{AMPAR}] + \mathrm{k}_{\mathrm{b_{phos}}}\,[\mathrm{W_aAMPAR}] + \\ & \mathrm{k}_{\mathrm{cat_{dephos}}}\,[\mathrm{PP2B_{ac}AMPARP}] \quad , \end{aligned} \tag{E.20}$$

where

$$\frac{d[\mathrm{W_bAMPAR}]}{dt} = \mathrm{k}_{\mathrm{f_{phos}}}[\mathrm{W_b}]\,[\mathrm{AMPAR}] - \left(\mathrm{k}_{\mathrm{b_{phos}}} + \mathrm{k}_{\mathrm{cat_{phos}}}\right)[\mathrm{W_bAMPAR}] \quad , \tag{E.21}$$

$$\frac{d[\mathrm{W_pAMPAR}]}{dt} = \mathrm{k}_{\mathrm{f_{phos}}}[\mathrm{W_p}]\,[\mathrm{AMPAR}] - \left(\mathrm{k}_{\mathrm{b_{phos}}} + \mathrm{k}_{\mathrm{cat_{phos}}}\right)[\mathrm{W_pAMPAR}] \quad , \tag{E.22}$$

$$\frac{d[\mathrm{W_aAMPAR}]}{dt} = \mathrm{k}_{\mathrm{f_{phos}}}[\mathrm{W_a}]\,[\mathrm{AMPAR}] - \left(\mathrm{k}_{\mathrm{b_{phos}}} + \mathrm{k}_{\mathrm{cat_{phos}}}\right)[\mathrm{W_aAMPAR}] \quad , \tag{E.23}$$

and

$$\begin{aligned}\frac{d[\mathrm{PP2B_{ac}AMPARP}]}{dt} = \; & \mathrm{k}_{\mathrm{f_{dephos}}}[\mathrm{PP2B_{ac}}]\,[\mathrm{AMPARP}] - \\ & \left(\mathrm{k}_{\mathrm{b_{dephos}}} + \mathrm{k}_{\mathrm{cat_{dephos}}}\right)[\mathrm{PP2B_{ac}AMPARP}] \quad . \end{aligned} \tag{E.24}$$

At last, the equation that represents the evolution of AMPARPs is

$$\begin{aligned}\frac{d[\mathrm{AMPARP}]}{dt} = \; & \mathrm{k}_{\mathrm{cat_{phos}}}\,[\mathrm{W_bAMPAR}] + \mathrm{k}_{\mathrm{cat_{phos}}}\,[\mathrm{W_pAMPAR}] + \\ & \mathrm{k}_{\mathrm{cat_{phos}}}\,[\mathrm{W_aAMPAR}] - \mathrm{k}_{\mathrm{f_{dephos}}}[\mathrm{PP2B_{ac}}]\,[\mathrm{AMPARP}] + \\ & \mathrm{k}_{\mathrm{b_{dephos}}}\,[\mathrm{PP2B_{ac}AMPARP}] \quad . \end{aligned} \tag{E.25}$$

E.2 Modelling Two-step Calcium-calmodulin Binding

The bidirectional plasticity model described above was modified to simulate the calcium-dependent CaM activation in two steps rather than one (Section 7.5.3). These modifications led to the creation of new ODEs and to the amendment of a few equations, as follows:

$$\begin{aligned}\frac{d[\mathrm{Ca}]}{dt} = \; & -2\mathrm{k}_{\mathrm{on_2}}[\mathrm{Ca}]^2[\mathrm{CaM}] + 2\mathrm{k}_{\mathrm{off_2}}\,[\mathrm{Ca_2CaM}] - \\ & 2\mathrm{k}_{\mathrm{on}}[\mathrm{Ca}]^2[\mathrm{Ca_2CaM}] + 2\mathrm{k}_{\mathrm{off}}\,[\mathrm{Ca_4CaM}] - \\ & \mathrm{k}_{\mathrm{b_2b}}[\mathrm{W_{b_2}}][\mathrm{Ca}]^2 + \mathrm{k}_{\mathrm{bb_2}}[\mathrm{W_b}] - \\ & \mathrm{k}_{\mathrm{b_0b_2}}[\mathrm{W_{b_0}}][\mathrm{Ca}]^2 + \mathrm{k}_{\mathrm{b_2b_0}}[\mathrm{W_{b_2}}] - \\ & \mathrm{k}_{\mathrm{b_0acb_2ac}}[\mathrm{W_{b_0}Ac}][\mathrm{Ca}]^2 + \mathrm{k}_{\mathrm{b_2acb_0ac}}[\mathrm{W_{b_2}Ac}] - \\ & \mathrm{k}_{\mathrm{b_2acbac}}[\mathrm{W_{b_2}Ac}][\mathrm{Ca}]^2 + \mathrm{k}_{\mathrm{bacb_2ac}}[\mathrm{W_bAc}] + \\ & \gamma(t) - \kappa\left([\mathrm{Ca}] - [\mathrm{Ca_{min}}]\right) \quad , \end{aligned} \tag{E.26}$$

$$\begin{aligned}\frac{d[\mathrm{CaM}]}{dt} = {} & -\mathrm{k_{on_2}}[\mathrm{Ca}]^2[\mathrm{CaM}] + \mathrm{k_{off_2}}\,[\mathrm{Ca_2CaM}] - \\ & \mathrm{k_{ib_0}}[\mathrm{W_i}][\mathrm{CaM}] + \mathrm{k_{b_0i}}[\mathrm{W_{b_0}}] - \\ & \mathrm{k_{iacb_0ac}}[\mathrm{W_iAc}][\mathrm{CaM}] + \mathrm{k_{b_0aciac}}[\mathrm{W_{b_0}Ac}]\ ,\end{aligned} \tag{E.27}$$

$$\begin{aligned}\frac{d[\mathrm{Ca_2CaM}]}{dt} = {} & \mathrm{k_{on_2}}[\mathrm{Ca}]^2[\mathrm{CaM}] - \mathrm{k_{off_2}}\,[\mathrm{Ca_2CaM}] - \\ & \mathrm{k_{on}}[\mathrm{Ca}]^2[\mathrm{Ca_2CaM}] + \mathrm{k_{off}}\,[\mathrm{Ca_4CaM}] - \\ & \mathrm{k_{ib_2}}[\mathrm{W_i}]\,[\mathrm{Ca_2CaM}] + \mathrm{k_{b_2i}}[\mathrm{W_{b_2}}] - \\ & \mathrm{k_{iacb_2ac}}\,[\mathrm{W_iAc}]\,[\mathrm{Ca_2CaM}] + \mathrm{k_{b_2aciac}}\,[\mathrm{W_{b_2}Ac}]\ ,\end{aligned} \tag{E.28}$$

$$\begin{aligned}\frac{d[\mathrm{Ca_4CaM}]}{dt} = {} & \mathrm{k_{on}}[\mathrm{Ca}]^2[\mathrm{Ca_2CaM}] - \mathrm{k_{off}}\,[\mathrm{Ca_4CaM}] - \\ & \mathrm{k_{ppia}}[\mathrm{PP2B_i}]\,[\mathrm{Ca_4CaM}] + \mathrm{k_{ppai}}[\mathrm{PP2B_{ac}}] - \\ & \mathrm{k_{ib}}[\mathrm{W_i}]\,[\mathrm{Ca_4CaM}] + \mathrm{k_{bi}}[\mathrm{W_b}] + \\ & \mathrm{k_{pa}}[\mathrm{W_p}] - \mathrm{k_{ap}}[\mathrm{W_a}]\,[\mathrm{Ca_4CaM}] - \\ & \mathrm{k_{iacbac}}\,[\mathrm{W_iAc}]\,[\mathrm{Ca_4CaM}] + \mathrm{k_{baciac}}\,[\mathrm{W_bAc}] + \\ & \mathrm{k_{pacaac}}\,[\mathrm{W_pAc}] - \mathrm{k_{aacpac}}\,[\mathrm{W_aAc}]\,[\mathrm{Ca_4CaM}]\ ,\end{aligned} \tag{E.29}$$

$$\begin{aligned}[\mathrm{W_i}] = {} & [\mathrm{W_{tot}}] - [\mathrm{W_{b_0}}] - [\mathrm{W_{b_2}}] - [\mathrm{W_b}] - \\ & [\mathrm{W_p}] - [\mathrm{W_a}] - [\mathrm{W_iAc}] - [\mathrm{W_{b_0}Ac}] - \\ & [\mathrm{W_{b_2}Ac}] - [\mathrm{W_bAc}] - [\mathrm{W_pAc}] - [\mathrm{W_aAc}]\ ,\end{aligned} \tag{E.30}$$

$$\begin{aligned}\frac{d[\mathrm{W_{b_0}}]}{dt} = {} & \mathrm{k_{ib_0}}[\mathrm{W_i}]\,[\mathrm{CaM}] - \mathrm{k_{b_0i}}[\mathrm{W_{b_0}}] - \\ & \mathrm{k_{b_0b_2}}[\mathrm{W_{b_0}}][\mathrm{Ca}]^2 + \mathrm{k_{b_2b_0}}[\mathrm{W_{b_2}}] - \\ & \mathrm{k_{b_0b_0ac}}[\mathrm{W_{b_0}}][\mathrm{Ac}] + \mathrm{k_{b_0acb_0}}[\mathrm{W_{b_0}Ac}]\ ,\end{aligned} \tag{E.31}$$

$$\begin{aligned}\frac{d[\mathrm{W_{b_2}}]}{dt} = {} & \mathrm{k_{ib_2}}[\mathrm{W_i}]\,[\mathrm{Ca_2CaM}] - \mathrm{k_{b_2i}}[\mathrm{W_{b_2}}] - \\ & \mathrm{k_{b_2b}}[\mathrm{W_{b_2}}][\mathrm{Ca}]^2 + \mathrm{k_{bb_2}}[\mathrm{W_b}] + \\ & \mathrm{k_{b_0b_2}}[\mathrm{W_{b_0}}][\mathrm{Ca}]^2 - \mathrm{k_{b_2b_0}}[\mathrm{W_{b_2}}] - \\ & \mathrm{k_{b_2b_2ac}}[\mathrm{W_{b_2}}][\mathrm{Ac}] + \mathrm{k_{b_2acb_2}}[\mathrm{W_{b_2}Ac}]\ ,\end{aligned} \tag{E.32}$$

$$\begin{aligned}\frac{d[\mathrm{W_b}]}{dt} &= -\mathrm{V_a}[\mathrm{W_{tot}}] + \mathrm{k_{ib}}[\mathrm{W_i}]\,[\mathrm{Ca_4CaM}] - \mathrm{k_{bi}}[\mathrm{W_b}] + \\ &\quad \mathrm{k_{b_2b}}[\mathrm{W_{b_2}}]\,[\mathrm{Ca}]^2 - \mathrm{k_{bb_2}}[\mathrm{W_b}] - \\ &\quad \mathrm{k_{bbac}}[\mathrm{W_b}]\,[\mathrm{Ac}] + \mathrm{k_{bacb}}\,[\mathrm{W_bAc}] - \\ &\quad \mathrm{k_{f_{phos}}}[\mathrm{W_b}]\,[\mathrm{AMPAR}] + \left(\mathrm{k_{b_{phos}}} + \mathrm{k_{cat_{phos}}}\right)[\mathrm{W_bAMPAR}] \quad , \end{aligned} \tag{E.33}$$

$$\begin{aligned}\frac{d[\mathrm{W_iAc}]}{dt} &= \mathrm{k_{iiac}}[\mathrm{W_i}]\,[\mathrm{Ac}] - \mathrm{k_{iaci}}\,[\mathrm{W_iAc}] - \\ &\quad \mathrm{k_{iacbac}}\,[\mathrm{W_iAc}]\,[\mathrm{Ca_4CaM}] + \mathrm{k_{baciac}}\,[\mathrm{W_bAc}] - \\ &\quad \mathrm{k_{iacb_0ac}}[\mathrm{W_iAc}]\,[\mathrm{CaM}] + \mathrm{k_{b_0aciac}}\,[\mathrm{W_{b_0}Ac}] - \\ &\quad \mathrm{k_{iacb_2ac}}[\mathrm{W_iAc}]\,[\mathrm{Ca_2CaM}] + \mathrm{k_{b_2aciac}}\,[\mathrm{W_{b_2}Ac}] \quad , \end{aligned} \tag{E.34}$$

$$\begin{aligned}\frac{d[\mathrm{W_{b_0}Ac}]}{dt} &= \mathrm{k_{iacb_0ac}}[\mathrm{W_iAc}]\,[\mathrm{CaM}] - \mathrm{k_{b_0aciac}}\,[\mathrm{W_{b_0}Ac}] + \\ &\quad \mathrm{k_{b_0b_0ac}}\,[\mathrm{W_{b_0}}]\,[\mathrm{Ac}] - \mathrm{k_{b_0acb_0}}\,[\mathrm{W_{b_0}Ac}] - \\ &\quad \mathrm{k_{b_0acb_2ac}}[\mathrm{W_{b_0}Ac}]\,[\mathrm{Ca}]^2 + \mathrm{k_{b_2acb_0ac}}\,[\mathrm{W_bAc}] \quad , \end{aligned} \tag{E.35}$$

$$\begin{aligned}\frac{d[\mathrm{W_{b_2}Ac}]}{dt} &= \mathrm{k_{iacb_2ac}}[\mathrm{W_iAc}]\,[\mathrm{Ca_2CaM}] - \mathrm{k_{b_2aciac}}\,[\mathrm{W_{b_2}Ac}] + \\ &\quad \mathrm{k_{b_2b_2ac}}\,[\mathrm{W_{b_2}}]\,[\mathrm{Ac}] - \mathrm{k_{b_2acb_2}}\,[\mathrm{W_{b_2}Ac}] + \\ &\quad \mathrm{k_{b_0acb_2ac}}[\mathrm{W_{b_0}Ac}]\,[\mathrm{Ca}]^2 - \mathrm{k_{b_2acb_0ac}}\,[\mathrm{W_{b_2}Ac}] - \\ &\quad \mathrm{k_{b_2acbac}}[\mathrm{W_{b_2}Ac}]\,[\mathrm{Ca}]^2 + \mathrm{k_{bacb_2ac}}\,[\mathrm{W_bAc}] \quad , \end{aligned} \tag{E.36}$$

$$\begin{aligned}\frac{d[\mathrm{W_bAc}]}{dt} &= -\mathrm{V_{ac}}[\mathrm{W_{tot}}] + \mathrm{k_{iacbac}}\,[\mathrm{W_iAc}]\,[\mathrm{Ca_4CaM}] - \\ &\quad \mathrm{k_{baciac}}\,[\mathrm{W_bAc}] + \mathrm{k_{bbac}}[\mathrm{W_b}]\,[\mathrm{Ac}] - \mathrm{k_{bacb}}\,[\mathrm{W_bAc}] + \\ &\quad \mathrm{k_{b_2acbac}}[\mathrm{W_{b_2}Ac}]\,[\mathrm{Ca}]^2 - \mathrm{k_{bacb_2ac}}\,[\mathrm{W_bAc}] \quad . \end{aligned} \tag{E.37}$$

E.3 Model Parameters

E.3.1 Plasticity in Purkinje Cells

E.3.1.1 Constant Calcium Stimulation

Parameter description	**Symbol**	**Value**	**Reference**
CaMKII total concentration	W_{tot}	20 μM	[Lisman 2002]
Unphosphorylated AMPA receptor initial concentration	AMPAR	0.5 μM	[Kuroda 2001]
Phosphorylated AMPA receptor initial concentration	AMPARP	0.5 μM	[Kuroda 2001]
Basal calcium concentration	Ca_{min}	0.1 μM	[Wang 2000]
CaM initial concentration	CaM	36 μM	
Inactive PP2B initial concentration	$PP2B_i$	15 μM	
Rate of association of Ca_4CaM to a W_i subunit	k_{ib}	10 $\mu M^{-1}s^{-1}$	[Dupont 2003]
Rate of dissociation of Ca_4CaM from a W_b subunit	k_{bi}	0.8 s^{-1}	[Dupont 2003]
Rate of association of Ca_4CaM to a W_a subunit	k_{ap}	10 $\mu M^{-1}s^{-1}$	[Dupont 2003]
Rate of dissociation of Ca_4CaM from a W_p subunit	k_{pa}	0.008 s^{-1}	[Meyer 1992]
Rate of association of Ca_4CaM to $PP2B_i$	k_{ppia}	10 $\mu M^{-1}s^{-1}$	
Rate of dissociation of Ca_4CaM from $PP2B_{ac}$	k_{ppai}	0.1 s^{-1}	
Rate of association of calcium to CaM	k_{on}	2×10^2 $\mu M^{-4}s^{-1}$	
Rate of dissociation of calcium from Ca_4CaM	k_{off}	2.3×10^7 s^{-1}	
Rates of AMPA receptor phosphorylation by CaMKII	$k_{f_{phos}}$	5 $\mu M^{-1}s^{-1}$	[Kuroda 2001]
	$k_{b_{phos}}$	72.283 s^{-1}	[Kuroda 2001]
	$k_{cat_{phos}}$	6,000 s^{-1}	
Rates of AMPA receptor dephosphorylation by PP2B	$k_{f_{dephos}}$	5 $\mu M^{-1}s^{-1}$	[Kuroda 2001]
	$k_{b_{dephos}}$	72.283 s^{-1}	[Kuroda 2001]
	$k_{cat_{dephos}}$	6,000 s^{-1}	
Phenomenological rate of CaMKII autophosphorylation	K'_a	0.29 s^{-1}	[Dupont 2003]
Coefficient of CaMKII activity at W_b subunit	c_b	75 %	[Dupont 2003]
Coefficient of CaMKII activity at W_p subunit	c_p	100 %	[Dupont 2003]
Coefficient of CaMKII activity at W_a subunit	c_a	80 %	[Dupont 2003]
Fitting parameter a	a	0.500	
Fitting parameter b	b	1.956	
Fitting parameter c	c	−1.800	

Table E.1: **Values of kinetic parameters for the constant calcium stimulation protocol** (Figures 7.3 and 7.4).

E.3.1.2 Pulsed Calcium Stimulation

Parameter description	**Symbol**	**Value**
Rate of dissociation of Ca_4CaM from a W_b subunit	k_{bi}	0.4 s^{-1}
Rate of association of calcium to CaM	k_{on}	2×10^4 $\mu M^{-4}s^{-1}$
Parameter that reflects calcium removal	κ	4×10^3

Table E.2: **Modified values of rate constants for the pulsed calcium stimulation protocol** (Figures 7.6 and 7.7).

E.3.2 Bidirectional Plasticity in Purkinje Cells

E.3.2.1 Replication of the Study by Van Woerden and Collaborators

Parameter description	**Symbol**	**Value**	**Reference**
CaMKII total concentration for wild-type mice	W_{tot}	$30\ \mu M$	
CaMKII total concentration for *Camk2b* knockout mice	W_{tot}	$7.5\ \mu M$	[Fink 2002]
F-actin total concentration	Ac	$40\ \mu M$	[Sanabria 2009]
Rate of association of Ca_4CaM to a W_iAc subunit	k_{iacbac}	$10\ \mu M^{-1}s^{-1}$	[Dupont 2003]
Rate of dissociation of Ca_4CaM from a W_bAc subunit	k_{baciac}	$2\ s^{-1}$	
Rate of association of Ca_4CaM to a W_aAc subunit	k_{aacpac}	$10\ \mu M^{-1}s^{-1}$	[Dupont 2003]
Rate of dissociation of Ca_4CaM from a W_pAc subunit	k_{pacaac}	$0.04\ s^{-1}$	[Meyer 1992]
Rate of association of F-actin to a W_i subunit	k_{iiac}	$10\ \mu M^{-1}s^{-1}$	
Rate of dissociation of F-actin from a W_iAc subunit	k_{iaci}	$60.2\ s^{-1}$	
Rate of association of F-actin to a W_b subunit	k_{bbac}	$10\ \mu M^{-1}s^{-1}$	
Rate of dissociation of F-actin from a W_bAc subunit	k_{bacb}	$301\ s^{-1}$	
Rate of association of F-actin to a W_p subunit	k_{ppac}	$10\ \mu M^{-1}s^{-1}$	
Rate of dissociation of F-actin from a W_pAc subunit	k_{pacp}	$301\ s^{-1}$	
Rate of association of F-actin to a W_a subunit	k_{aaac}	$10\ \mu M^{-1}s^{-1}$	
Rate of dissociation of F-actin from a W_aAc subunit	k_{aaca}	$60.2\ s^{-1}$	
Rate of association of Ca_4CaM to $PP2B_i$	k_{ppia}	$5\ \mu M^{-1}s^{-1}$	
Rate of dissociation of Ca_4CaM from $PP2B_{ac}$	k_{ppai}	$0.5\ s^{-1}$	
Rate of association of calcium to CaM	k_{on}	$2 \times 10^3\ \mu M^{-4}s^{-1}$	
Rate of dissociation of calcium from Ca_4CaM	k_{off}	$2.3 \times 10^6\ s^{-1}$	
Rates of AMPA receptor phosphorylation by CaMKII	$k_{f_{phos}}$	$0.5\ \mu M^{-1}s^{-1}$	
	$k_{cat_{phos}}$	$6\ s^{-1}$	[Kuroda 2001]
Rates of AMPA receptor dephosphorylation by PP2B	$k_{f_{dephos}}$	$0.5\ \mu M^{-1}s^{-1}$	
	$k_{cat_{dephos}}$	$6\ s^{-1}$	[Kuroda 2001]

Table E.3: **Modified values of kinetic parameters for the replication of [van Woerden 2009]** (Figures 7.8, 7.9 and 7.10).

E.3.2.2 Parameter Values Based on Experimental Observations

Parameter description	**Symbol**	**Value**	**Reference**
Basal calcium concentration	Ca_{min}	$0.045\ \mu M$	[Antunes 2012]
CaMKII total concentration for wild-type mice	W_{tot}	$20\ \mu M$	[Lisman 2002]
CaMKII total concentration for *Camk2b* knockout mice	W_{tot}	$10\ \mu M$	[van Woerden 2009]
Rate of dissociation of Ca_4CaM from W_b for wild-type mice	k_{bi}	$0.2\ s^{-1}$	[Brocke 1999]
Rate of dissociation of Ca_4CaM from W_p for wild-type mice	k_{pa}	$0.004\ s^{-1}$	[Meyer 1992]
Rate of dissociation of Ca_4CaM from W_bAc	k_{baciac}	$1\ s^{-1}$	
Rate of dissociation of Ca_4CaM from W_pAc	k_{pacaac}	$0.02\ s^{-1}$	[Meyer 1992]
Rate of dissociation of F-actin from W_iAc	k_{iaci}	$30.1\ s^{-1}$	
Rate of dissociation of F-actin from W_bAc	k_{bacb}	$150.5\ s^{-1}$	
Rate of dissociation of F-actin from a W_pAc	k_{pacp}	$1{,}505\ s^{-1}$	
Rate of dissociation of F-actin from W_aAc	k_{aaca}	$301\ s^{-1}$	
Rate of dissociation of Ca_4CaM from $PP2B_{ac}$	k_{ppai}	$0.4\ s^{-1}$	
Rate of association of calcium to CaM	k_{on}	$5 \times 10^7\ \mu M^{-4}s^{-1}$	

Table E.4: **Modified values of kinetic parameters following suggestions from the authors of [van Woerden 2009]** (Figures 7.11-7.16).

E.3.2.3 Two-step Calcium-calmodulin Binding

Parameter description	Symbol	Value
Rate of association of two calcium ions to Ca_2CaM	k_{on}	2×10^2 $\mu M^{-2}s^{-1}$
Rate of dissociation of two calcium ions from Ca_4CaM	k_{off}	2.3×10^3 s^{-1}
Rate of association of two calcium ions to apo-CaM	k_{on_2}	20 $\mu M^{-2}s^{-1}$
Rate of dissociation of two calcium ions from Ca_2CaM	k_{off_2}	2.3×10^3 s^{-1}
Rate of association of apo-CaM to W_i	k_{ib_0}	10 $\mu M^{-1}s^{-1}$
Rate of dissociation of apo-CaM from W_{b_0} for wild-type mice	k_{b_0i}	2×10^3 s^{-1}
Rate of dissociation of apo-CaM from W_{b_0} for *Camk2b* knockout mice	k_{b_0i}	4×10^3 s^{-1}
Rate of association of Ca_2CaM to W_i	k_{ib_2}	10 $\mu M^{-1}s^{-1}$
Rate of dissociation of Ca_2CaM from W_{b_2} for wild-type mice	k_{b_2i}	2×10^3 s^{-1}
Rate of dissociation of Ca_2CaM from W_{b_2} for *Camk2b* knockout mice	k_{b_2i}	4×10^3 s^{-1}
Rate of association of two calcium ions to W_{b_0}	$k_{b_0b_2}$	20 $\mu M^{-2}s^{-1}$
Rate of dissociation of two calcium ions from W_{b_2}	$k_{b_2b_0}$	2.3×10^3 s^{-1}
Rate of association of two calcium ions to W_{b_2}	k_{b_2b}	2×10^2 $\mu M^{-2}s^{-1}$
Rate of dissociation of two calcium ions from W_b	k_{bb_2}	2.3×10^{-1} s^{-1}
Rate of association of two calcium ions to $W_{b_0}Ac$	$k_{b_0acb_2ac}$	2×10^2 $\mu M^{-2}s^{-1}$
Rate of dissociation of two calcium ions from $W_{b_2}Ac$	$k_{b_2acb_0ac}$	2.3×10^{-2} s^{-1}
Rate of association of two calcium ions to $W_{b_2}Ac$	k_{b_2acbac}	2×10^2 $\mu M^{-2}s^{-1}$
Rate of dissociation of two calcium ions from W_bAc	k_{bacb_2ac}	2.3×10^{-1} s^{-1}
Rate of association of apo-CaM to W_iAc	k_{iacb_0ac}	10 $\mu M^{-1}s^{-1}$
Rate of dissociation of apo-CaM from $W_{b_0}Ac$	k_{b_0aciac}	1×10^{10} s^{-1}
Rate of association of Ca_2CaM to W_iAc	k_{iacb_2ac}	10 $\mu M^{-1}s^{-1}$
Rate of dissociation of Ca_2CaM from $W_{b_2}Ac$	k_{b_2aciac}	1×10^4 s^{-1}
Rate of association of F-actin to W_{b_0}	$k_{b_0b_0ac}$	10 $\mu M^{-1}s^{-1}$
Rate of dissociation of F-actin from $W_{b_0}Ac$	$k_{b_0acb_0}$	1.505×10^8 s^{-1}
Rate of association of F-actin to W_{b_2}	$k_{b_2b_2ac}$	10 $\mu M^{-1}s^{-1}$
Rate of dissociation of F-actin from $W_{b_2}Ac$	$k_{b_2acb_2}$	1.505×10^2 s^{-1}

Table E.5: **Modified values of kinetic parameters while modelling a two-step Ca_4CaM binding** (Figures 7.18, 7.19 and 7.20).

Appendix F

The Effective Calcium/Calmodulin Concentration Determines the Sensitivity of CaMKII to the Frequency of Calcium Oscillations

The Effective Calcium/Calmodulin Concentration Determines the Sensitivity of CaMKII to the Frequency of Calcium Oscillations

Thiago M. Pinto, Maria J. Schilstra, and Volker Steuber

Science and Technology Research Institute,
University of Hertfordshire, Hatfield, Herts, AL10 9AB, UK
{t.pinto,m.j.1.schilstra,v.steuber}@herts.ac.uk

Abstract. Calcium/calmodulin-dependent protein kinase II (CaMKII) is involved in the induction of many forms of synaptic plasticity in the brain. Experimental and computational studies have shown that CaMKII is sensitive to the frequency of oscillatory Ca^{2+} signals. Here we demonstrate that in a simple, commonly used kinetic model of CaMKII phosphorylation, the overall phosphorylation rate under sustained application of $Ca_4 - CaM$ pulses ultimately depends on the average ('effective') concentration of $Ca_4 - CaM$ in the system, rather than on the pulse frequency itself. As a corollary, equal phosphorylation levels are achieved in response to pulsed and constant applications of equal effective concentrations of $Ca_4 - CaM$.

Keywords: CaMKII, calmodulin, Ca^{2+} oscillations.

1 Introduction

Calcium/calmodulin-dependent protein kinase II (CaMKII), which is present in high concentrations in the brain, is a multifunctional protein kinase involved in Ca^{2+} signalling systems that underlie the induction of synaptic plasticity. Brief Ca^{2+} signals can activate CaMKII, and stimulate an autophosphorylation reaction that allows the kinase to maintain its activation level [1].

Earlier computer simulations based on a widely used CaMKII autophosphorylation model indicated that CaMKII activation is sensitive to the frequency of Ca^{2+} oscillations [2–5], and *in vitro* experiments have demonstrated that the kinase does indeed respond differently to different frequencies of Ca^{2+} spikes [6].

Here, we present a somewhat simplified version of the CaMKII activation model developed by Dupont et al. [5], and show that this model reproduces the results of the more complex one. Further, we demonstrate that CaMKII activation by Ca^{2+} and calmodulin (CaM) in the model is mostly determined by the effective $Ca_4 - CaM$ concentration, which varies with the frequency of $Ca_4 - CaM$ pulses, but does not depend on the actual frequency of Ca^{2+} oscillations. Moreover, we show that the application of a constant level of $Ca_4 - CaM$ with the same mean concentration as in the pulsed protocol results in the same level of CaMKII phosphorylation.

M.A. Lones et al. (Eds.): IPCAT 2012, LNCS 7223, pp. 131–135, 2012.

2 CaMKII Activation Model

In the simplified CaMKII activation model (Fig. 1), CaMKII can be in four different states: inactive (W_i), bound to $Ca_4 - CaM$ (W_b), phosphorylated and bound to $Ca_4 - CaM$ (W_p), and autonomous (W_a): phosphorylated, but dissociated from $Ca_4 - CaM$. As in the earlier model [5], we assume that $Ca_4 - CaM$ formation is rapid and complete. Binding of $Ca_4 - CaM$ to a CaMKII subunit results in the activation of the subunit's kinase function, allowing it to phosphorylate its substrates. These substrates include the subunit's nearest neighbours in the CaMKII multimer. The autophosphorylation rate associated with this process is indicated as V_a, and is described using the phenomenological nonlinear function of the concentrations of W_b, W_p and W_a as in [5]. Dissociation of $Ca_4 - CaM$ from the phosphorylated form yields the so-called autonomous form of CaMKII, which retains some or all of its kinase activity.

Different from the Dupont model [5], we do not model a "trapped" state [7], mainly because dissociation of Ca^{2+} and CaM cannot be distinguished experimentally (nor described thermodynamically) as two distinct processes.

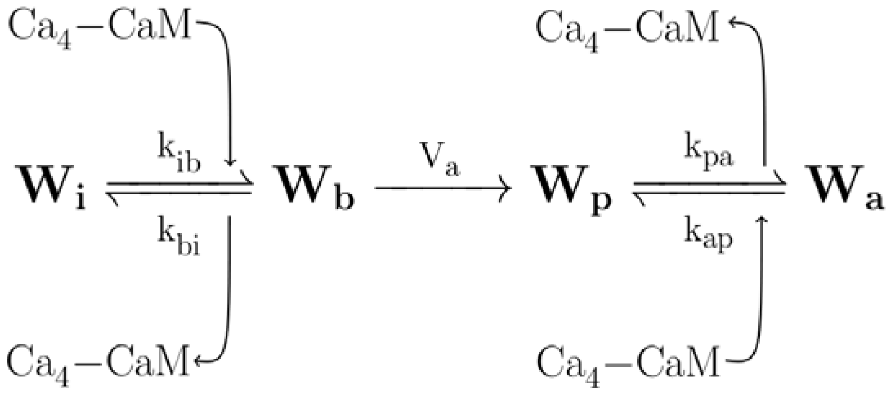

Fig. 1. Model of the activation of CaMKII by $Ca_4 - CaM$. k_{ib}, k_{bi}, k_{pa} and k_{ap} are the rate constants of the reversible $Ca_4 - CaM$ binding reactions, and V_a is the rate of the irreversible phosphorylation of W_b

The model was implemented as a set of 4 coupled ordinary differential equations (ODEs), which were solved numerically using the XPPAUT software (X-Windows Phase Plane plus Auto).

3 Results

To examine whether the omission of trapped state had any significant effect, and to investigate the dependence of the overall autophosphorylation kinetics on the frequency of $Ca_4 - CaM$ oscillations, we replicated the simulations presented in [5] with our simplified model. Figure 2b shows the simulated response to 100

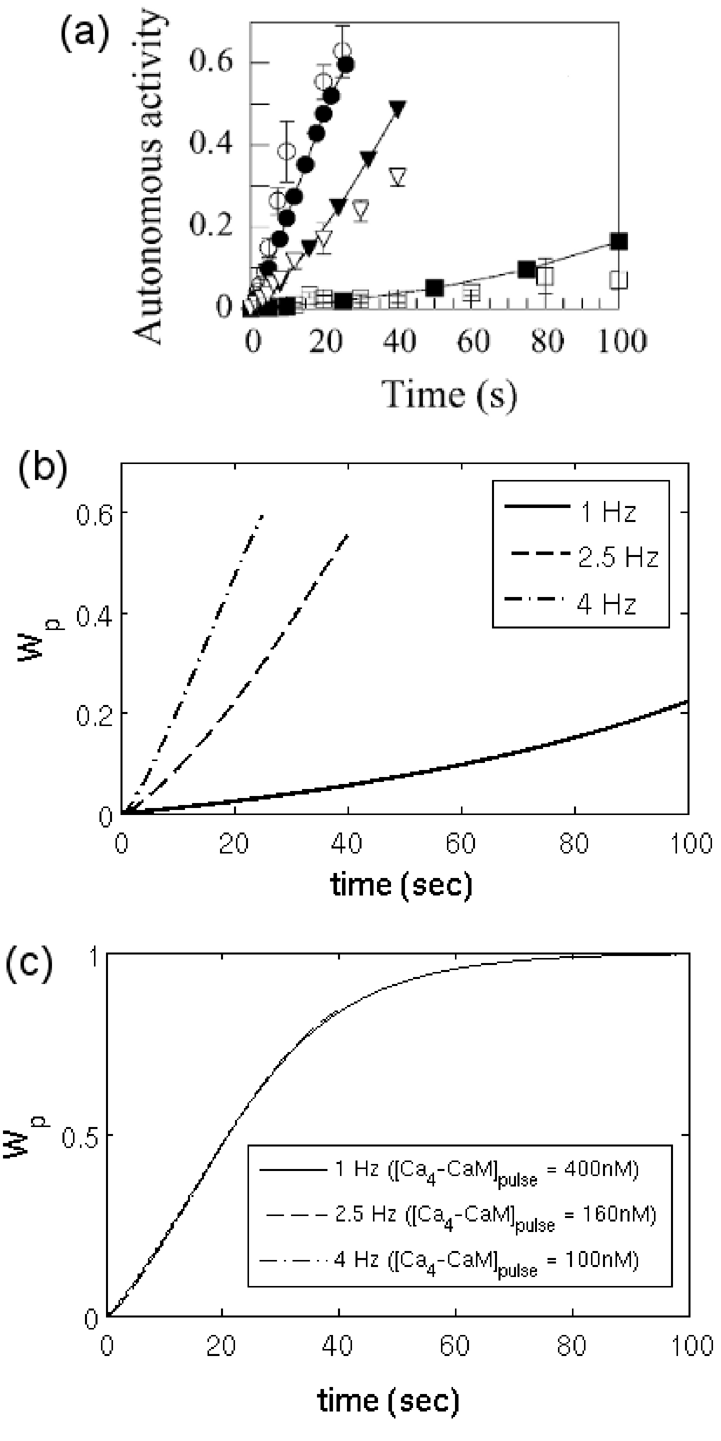

Fig. 2. CaMKII phosphorylation and its dependence on the effective $Ca_4 - CaM$ concentration. **(a)** Temporal evolution of the phosphorylated form of CaMKII (W_p) in response to 100 200 ms square pulses of $Ca_4 - CaM$ (100 nM) at frequencies of 1 Hz (solid squares), 2.5 Hz (solid triangles) and 4 Hz (solid circles) in the Dupont model [5]. **(b)** W_p in response to the same protocol in our simplified model. **(c)** W_p in response to 100 200 ms square pulses of $Ca_4 - CaM$ at 1, 2.5 and 4 Hz, but with scaled pulse amplitudes so that the effective concentration of $Ca_4 - CaM$ is 80 nM. The amplitudes of $Ca_4 - CaM$ pulses are 400 nM at 1 Hz (solid), 160 nM at 2.5 Hz (dashed) and 100 nM at 4 Hz (dashed-dotted).

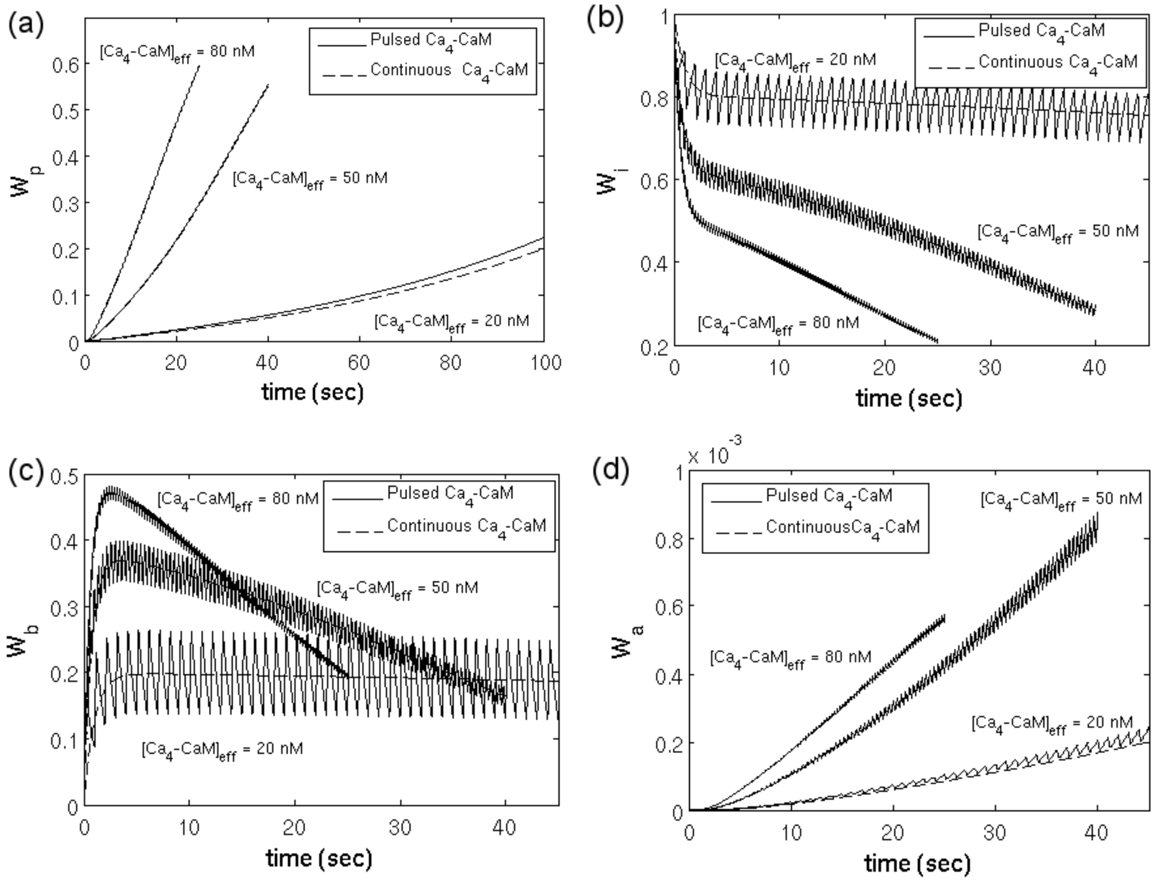

Fig. 3. Temporal evolution of W_p **(a)**, W_i **(b)**, W_b **(c)** and W_a **(d)** in response to pulsed and continuous applications of $Ca_4 - CaM$. In all panels, the solid lines represent the CaMKII responses to 100 200 ms pulses of $Ca_4 - CaM$ (100 nM) at 1, 2.5 and 4 Hz, corresponding to the effective $Ca_4 - CaM$ concentrations of 20 nM, 50 nM and 80 nM, respectively. The dashed lines indicate the CaMKII response to the application of continuous $Ca_4 - CaM$ concentrations at the same levels.

square $Ca_4 - CaM$ pulses with amplitude of 100 nM and duration of 200 ms each, applied at 1, 2.5 and 4 Hz. The results are very similar to those presented in [5] (cf Fig. 2a).

Dupont et al. [5] argue that CaMKII autophosphorylation is dependent on the frequency of Ca^{2+} oscillations, and that, therefore, CaMKII may act as a decoder of Ca^{2+} spike frequencies. A change in pulse frequency is accompanied by a change in average, or 'effective' $Ca_4 - CaM$ concentration, $[Ca_4 - CaM]_{eff}$, which is computed as $[Ca_4 - CaM]_{eff} = [Ca_4 - CaM]_{pulse} \times f \times L$ (where $[Ca_4 - CaM]_{pulse}$ is the pulse amplitude, f is the pulse frequency, and L the pulse duration). Thus, CaMKII is subjected to different effective $Ca_4 - CaM$ concentrations, which in turn affects the average concentration of W_b and W_p, and the autophosphorylation kinetics. To investigate whether the autophosphorylation kinetics are primarily determined by the pulse frequency, or by the accompanying variation in $[Ca_4 - CaM]_{eff}$, we rescaled the $Ca_4 - CaM$ concentrations to an equal effective concentration of 80 nM, and compared the phosphorylation kinetics.

Figure 2c shows that the phosphorylation kinetics at 1, 2.5 and 4 Hz pulses are identical after rescaling the $Ca_4 - CaM$ concentration. This strongly indicates that, at least for the frequency range examined here, the CaMKII autophosphorylation kinetics are independent of the pulse frequency itself.

We also investigated whether the autophosphorylation kinetics are the same under constant and pulsed $Ca_4 - CaM$ concentrations at the appropriate effective concentrations. Figure 3 shows a superposition of concentrations of the various species under pulsed and continuous $Ca_4 - CaM$ concentration conditions. Again, these results indicate that the CaMKII autophosphorylation kinetics in this model are determined by the effective $Ca_4 - CaM$ concentration, not by the actual pulse frequency.

References

1. Hanson, P., Schulman, H.: Neuronal Ca2+/calmodulin-dependent protein kinases. Annual Review of Biochemistry 61(1), 559–601 (1992)
2. Hanson, P., Meyer, T., Stryer, L., Schulman, H.: Dual role of calmodulin in autophosphorylation of multifunctional CaM kinase may underlie decoding of calcium signals. Neuron 12(5), 943–956 (1994)
3. Michelson, S., Schulman, H.: CaM kinase: A model for its activation and dynamics. Journal of Theoretical Biology 171, 281–290 (1994)
4. Dosemeci, A., Albers, R.: A mechanism for synaptic frequency detection through autophosphorylation of CaM kinase II. Biophysical Journal 70(6), 2493–2501 (1996)
5. Dupont, G., Houart, G., De Koninck, P.: Sensitivity of CaM kinase II to the frequency of Ca2+ oscillations: a simple model. Cell Calcium 34(6), 485–497 (2003)
6. De Koninck, P., Schulman, H.: Sensitivity of CaM kinase II to the frequency of Ca2+ oscillations. Science 279(5348), 227–230 (1998)
7. Waxham, M., Putkey, J., Tsai, A.: A mechanism for calmodulin (CaM) trapping by CaM-kinase II defined by a family of CaM-binding peptides. Journal of Biological Chemistry 273(28), 17579–17584 (1998)

Appendix G

CaMKII Activation by Ca_4-CaM Does Not Depend on the Actual Frequency of Oscillatory Ca^{2+} Signals

CaMKII activation by Ca_4-CaM does not depend on the actual frequency of oscillatory Ca^{2+} signals

Thiago M. Pinto, Maria J. Schilstra and Volker Steuber

Science and Technology Research Institute, University of Hertfordshire, Hatfield, Herts, AL10 9AB, UK
E-mail: {t.pinto, m.j.1.schilstra, v.steuber}@herts.ac.uk

Ca^{2+}/calmodulin-dependent protein kinase II (CaMKII) plays an important role in the induction of synaptic plasticity, by linking neuronal Ca^{2+} signals with the phosphorylation of neurotransmitter receptors. A crucial step in this biochemical cascade is the Ca^{2+} / calmodulin (Ca_4-CaM) dependent autophosphorylation of CaMKII. Previous experimental (De Koninck and Schulman, 1998) and computational (Dupont et al., 2003) studies have demonstrated that the extent of autophosphorylation of CaMKII is determined by the frequency of repetitive Ca^{2+} signals. In the present study, we use a simplified version of the CaMKII activation model by Dupont and collaborators to unravel the mechanism that underlies this observed frequency dependence. In the simulations by Dupont et al., CaMKII was subjected to different average, or 'effective', Ca_4-CaM concentrations, which in turn affected the average concentration of the CaMKII subunits, and the autophosphorylation kinetics. After demonstrating that our model reproduces the results of the Dupont model, we therefore rescale the Ca_4-CaM concentration to an equal effective concentration, and demonstrate that the CaMKII autophosphorylation kinetics in the model are determined by this effective Ca_4-CaM concentration and not by the actual pulse frequency. We also show that the application of a constant level of Ca_4-CaM with the same mean concentration as in the pulsed protocol results in the same level of CaMKII phosphorylation. Our simulation results indicate that the notion of CaMKII as a decoder of Ca^{2+} oscillations is misleading and suggest experimental tests with rescaled Ca^{2+} concentrations.

De Koninck, P., Schulman, H. Science 279, 227-230 (1998).
Dupont, G., Houart, G., De Koninck, P. Cell Calcium 34, 485–497 (2003).

Appendix H

Does CaMKII decode Ca^{2+} oscillations?

Pinto *et al. BMC Neuroscience* 2012, **13**(Suppl 1):O15
http://www.biomedcentral.com/1471-2202/13/S1/O15

BMC Neuroscience

ORAL PRESENTATION | Open Access

Does CaMKII decode Ca^{2+} oscillations?

Thiago M Pinto*, Maria J Schilstra, Volker Steuber

From Twenty First Annual Computational Neuroscience Meeting: CNS*2012
Decatur, GA, USA. 21-26 July 2012

Ca^{2+}/calmodulin-dependent protein kinase II (CaMKII), which is present in high concentrations in the brain, contributes to many forms of synaptic plasticity. The induction of synaptic plasticity by CaMKII involves an intracellular signalling cascade that links neuronal Ca^{2+} signals with the phosphorylation of neurotransmitter receptors; an important step in this biochemical cascade is the autophosphorylation of CaMKII after binding of Ca^{2+}/calmodulin (Ca_4-CaM).

The dependence of this autophosphorylation reaction on the temporal structure of Ca_4-CaM signals has been investigated in previous experiments [1] and computer simulations [2]. These experimental and theoretical studies have indicated that the autophosphorylation of CaMKII is sensitive to the frequency of repetitive Ca^{2+} pulses, and it has been concluded that CaMKII can decode oscillatory Ca^{2+} signals [1,2].

Here, we apply a simplified version of the commonly used CaMKII activation model by Dupont and collaborators [2] to investigate the mechanism that underlies the dependence of the overall autophosphorylation kinetics on the frequency of Ca^{2+} oscillations. In the simulations by Dupont et al., CaMKII was subjected to different average, or 'effective', Ca_4-CaM concentrations, which in turn affected the average concentration of the CaMKII subunits, and the autophosphorylation kinetics.

We first replicate the simulation results presented in [2] with our simplified model (Figure 1A). To identify the mechanism that underlies the observed frequency dependence, we then rescale the Ca_4-CaM concentrations to an equal effective concentration, and compare the phosphorylation kinetics (Figure 1B). We demonstrate that in our model the overall phosphorylation rate under sustained application of Ca_4-CaM pulses depends

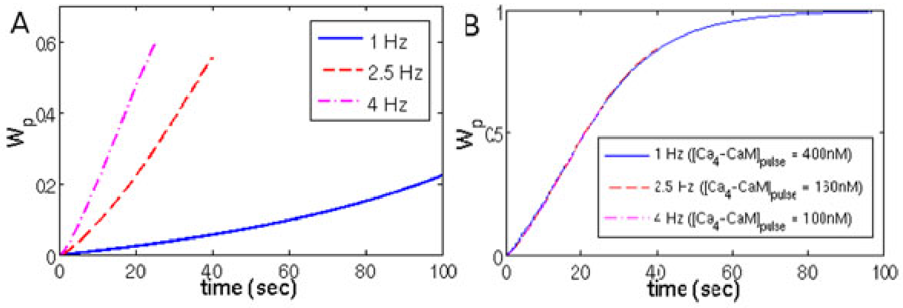

Figure 1 CaMKII phosphorylation and its dependence on the effective Ca_4-CaM concentration. **(A)** Temporal evolution of the phosphorylated form of CaMKII (Wp) in response to one hundred 200 ms square pulses of Ca_4-CaM (100 nM) at frequencies of 1 Hz (solid blue), 2.5 Hz (dashed red) and 4 Hz (dashed-dotted magenta) in our simplified model. **(B)** Wp in response to one hundred 200 ms square pulses of Ca_4-CaM at 1, 2.5 and 4 Hz, but with scaled pulse amplitudes so that the effective concentration of Ca_4-CaM is 80 nM. The amplitudes of Ca_4-CaM pulses are 400 nM at 1 Hz (solid blue), 160 nM at 2.5 Hz (dashed red) and 100 nM at 4 Hz (dashed-dotted magenta).

---

* Correspondence: t.pinto@herts.ac.uk
Science and Technology Research Institute, University of Hertfordshire, Hatfield, Herts, AL10 9AB, UK

on the average (‘effective’) concentration of Ca_4-CaM in the system, rather than on the pulse frequency itself. Moreover, we show that the application of a constant level of Ca_4-CaM with the same mean concentration as in the pulsed protocol results in the same level of CaMKII phosphorylation.

Our simulation results indicate that the notion of CaMKII as a decoder of Ca^{2+} oscillations is misleading and suggest experimental tests with rescaled Ca_4-CaM concentrations.

Published: 16 July 2012

References

1. De Koninck P, Schulman H: **Sensitivity of CaM kinase II to the frequency of Ca2+ oscillations.** *Science* 1998, **279(5348)**:227-230.
2. Dupont G, Houart G, De Koninck P: **Sensitivity of CaM kinase II to the frequency of Ca2+ oscillations: a simple model.** *Cell Calcium* 2003, **34(6)**:485-497.

doi:10.1186/1471-2202-13-S1-O15
Cite this article as: Pinto *et al.*: Does CaMKII decode Ca^{2+} oscillations? *BMC Neuroscience* 2012 **13**(Suppl 1):O15.

APPENDIX I

Modelling the Role of βCaMKII in Regulating Bidirectional Plasticity at Parallel Fibre-Purkinje Cell Synapses

Modelling the role of βCaMKII in regulating bidirectional plasticity at parallel fibre–Purkinje cell synapses

Thiago M. Pinto*, Maria J. Schilstra and Volker Steuber
Science and Technology Research Institute, University of Hertfordshire, Hatfield, Herts, AL10 9AB, UK
E-mail: {t.pinto, m.j.1.schilstra, v.steuber}@herts.ac.uk

Synaptic plasticity, the strengthening and weakening of connections between neurons, is crucial for learning and memory in neuronal circuits. However, a better comprehension of the mechanisms of many forms of synaptic plasticity is limited by the complexity of the underlying intracellular signalling pathways.

Cerebellar long-term depression (LTD) and potentiation (LTP) are calcium-dependent forms of synaptic plasticity that weaken and strengthen synapses between parallel fibres (PF) and Purkinje cells (PCs). While LTD is induced by large increases in intracellular calcium concentrations in response to paired PF and climbing fibre (CF) input, smaller calcium concentration increases that result from PF input alone lead to LTP. The induction of LTD and LTP is mediated by enzymes such as calcium/calmodulin-dependent kinase type II (CaMKII) and protein phosphatase 2B (PP2B) that regulate the phosphorylation and dephosphorylation of postsynaptic AMPA receptors.

The CaMKII holoenzyme is composed of αCaMKII and βCaMKII isoforms. Recent experiments with *Camk2b* knockout mice have revealed that βCaMKII, which is the predominant CaMKII isoform in the cerebellum, controls the direction of plasticity at the PF–PC synapse (van Woerden et al., 2009). More specifically, protocols that induce LTD in wild-type mice result in LTP in knockout mice that lack βCaMKII, and vice versa.

Here, we use a simple model of the phosphorylation and dephosphorylation of AMPA receptors by CaMKII and PP2B to investigate the mechanisms that underlie the regulation of bidirectional plasticity at the PF–PC synapse. The model is based on our recent model of CaMKII activation (Pinto et al., 2012). In the model, the binding of calcium to calmodulin (CaM), the activation of CaMKII and PP2B by calcium/calmodulin (Ca_4–CaM), and the AMPA receptor phosphorylation and dephosphorylation are represented by coupled ordinary differential equations.

Van Woerden et al. (2009) suggested that the sign reversal of synaptic plasticity in the *Camk2b* knockout mice is due to a biochemical difference between the α and βCaMKII isoforms. The βCaMKII, but not αCaMKII, subunits can bind to filamentous actin (F-actin), which could result in clustering of the CaMKII holoenzyme to F-actin, making it unavailable for AMPA receptor phosphorylation. We included the binding of CaMKII to F-actin in our simulations of synaptic plasticity induction in wild-type mice, whilst omitting it when modelling plasticity induction in *Camk2b* knockout mice. Moreover, Purkinje cells contain about four times as much βCaMKII as αCaMKII, and the loss of βCaMKII did not result in up-regulation of αCaMKII in the knockout mice. Thus, we also included the corresponding reduction in CaMKII concentration in our simulations of knockout mice.

We simulate the induction of synaptic plasticity in response to PF stimulation with and without paired CF stimulation in our model by applying calcium pulses with concentrations that reflect experimental data, and we record the resulting phosphorylation and dephosphorylation of AMPA receptors. Our simulations replicate the experimental findings by van Woerden et al. (2009), suggesting that the binding of βCaMKII to F-actin can indeed contribute to the control of bidirectional plasticity at PF–PC synapses. Our model predicts that the sign reversal of synaptic plasticity is based on a combination of three mechanisms operating at different calcium concentrations. At the low calcium concentrations that result from PF input alone, the loss of F-actin binding in the knockout mice leads to increased availability of active CaMKII compared to the wild-type mice, and to induction of LTD rather than LTP. At the high calcium concentrations that are triggered by paired PF and CF input, the reduced CaMKII concentration in the knockout mice favours the dephosphorylation of AMPA receptors by PP2B, and the induction of LTP instead of LTD. This effect is exacerbated by the increased availability of Ca_4–CaM that results from the decreased CaMKII levels, which further increases the activation of PP2B.

References

Van Woerden, G.M., Hoebeek, F.E., Gao, Z., Nagaraja, R.Y., Hoogenraad, C.C., Kushner, S.A., Hansel, C., De Zeeuw, C.I., Elgersma, Y.: [beta]CaMKII controls the direction of plasticity at parallel fiber–Purkinje cell synapses. Nature Neuroscience 12, 823–825 (2009).

Pinto, T.M., Schilstra, M.J., Steuber, V.: The Effective Calcium/Calmodulin Concentration Determines the Sensitivity of CaMKII to the Frequency of Calcium Oscillations. Lecture Notes in Computer Science 7223, 131-135 (2012).

Appendix J

Filamentous Actin Binding Enables βCaMKII to Regulate Bidirectional Plasticity in Cerebellar Purkinje Cells

Filamentous actin binding enables βCaMKII to regulate bidirectional plasticity in cerebellar Purkinje cells

Thiago M Pinto, Maria J Schilstra, Volker Steuber
Science and Technology Research Institute, University of Hertfordshire, Hatfield, Herts, AL10 9AB, UK
E-mail: {t.pinto, m.j.1.schilstra, v.steuber}@herts.ac.uk

Synaptic plasticity is an activity-dependent alteration in the strength of synaptic connections between pre and postsynaptic neurons. The long-term strengthening and weakening of synapses are known as long-term potentiation (LTP) and long-term depression (LTD), respectively. Long-lasting changes in synaptic strength are thought to be the basis of learning and the formation of memories. In particular, these calcium-dependent forms of plasticity are involved in learning and pattern recognition by cerebellar Purkinje cells (PCs). Different levels of intracellular calcium mediate the induction of LTD and LTP between parallel fibres (PF) and PCs. The coincident activation of PF and climbing fibre (CF) input evokes large concentrations of intracellular calcium, which in turn lead to LTD. In contrast, the induction of LTP is induced by small increases in intracellular calcium concentration in response to PF input alone.

Research has pointed out that complex interactions between many intracellular signalling components underlie cerebellar plasticity. In particular, calcium/calmodulin-dependent protein kinase II (CaMKII) and protein phosphatase 2B (PP2B) mediate the phosphorylation and dephosphorylation of AMPA receptors, regulating LTD and LTP in cerebellar PCs. The CaMKII holoenzyme comprises different isoforms such as αCaMKII and βCaMKII. Although βCaMKII is the predominant isoform of CaMKII in the cerebellum, its role in cerebellar learning and memory has yet to be established.

Recent experiments with Camk2b knockout mice, which lack the β isoform of CaMKII, have addressed the role of βCaMKII in plasticity in cerebellar PCs. These studies have revealed that βCaMKII regulates the direction of plasticity at PF-PC synapses [1]. Experimental protocols that induce LTP in wild-type mice, which contain both α and βCaMKII isoforms, result in LTP in knockout mice that lack βCaMKII, and vice versa. However, the underlying mechanism that may explain these experimental findings is not clear. Van Woerden et al. [1] have suggested that the binding of CaMKII to F-actin could underlie the switch of direction of synaptic plasticity. The βCaMKII, but not αCaMKII, isoform can bind to F-actin, which could result in clustering of the CaMKII holoenzyme to F-actin, making it unavailable for phosphorylation of AMPA receptors.

To investigate the role of βCaMKII in the regulation of bidirectional plasticity at PF-PC synapses, we developed a simple kinetic model of the phosphorylation and dephosphorylation of AMPA receptors by CaMKII and PP2B. The model is based on our recent model of CaMKII activation by calcium/calmodulin [2,3]. We then included the binding of F-actin to CaMKII to simulate the induction of plasticity in wild-type mice, while in the knockout mice that lack βCaMKII F-actin binding was omitted.

Our simulation results replicate the experimental observations by van Woerden et al. [1] and unravel how the βCaMKII isoform can control the sign reversal of plasticity at PF-PC synapses. We demonstrate that the binding of F-actin to βCaMKII can indeed contribute to the control of bidirectional plasticity at these synapses. At low concentrations of calcium in response to PF stimulation alone, the loss of F-actin binding in the knockout mice enhances the availability of active CaMKII when compared to the wild-type mice. This mechanism leads to the induction of LTD instead of LTP. However, for the large increases of calcium concentrations that result from coincident activation of PF and CF, the reduction in the CaMKII concentration in the knockout mice leads to AMPA receptor dephosphorylation by PP2B, favouring the induction of LTP rather than LTD.

References

1. Van Woerden GM, Hoebeek FE, Gao Z, Nagaraja RY, Hoogenraad CC, Kushner SA, Hansel C, De Zeeuw CI, Elgersma Y: **[beta]CaMKII controls the direction of plasticity at parallel fiber-Purkinje cell synapses.** *Nature Neuroscience* 2009, **12:**823–825.
2. Pinto TM, Schilstra MJ, Steuber V: **The effective calcium/calmodulin concentration determines the sensitivity of CaMKII to the frequency of calcium oscillations.** *Lecture Notes in Computer Science* 2012, **7223:**131–135.
2. Pinto TM, Schilstra MJ, Steuber V: **Does CaMKII decode Ca^{2+} oscillations?** *BMC Neuroscience* 2012, **13(Suppl 1):**O15.

Appendix K

A Comparison of the Electric Potential through the Membranes of Ganglion Neurons and Neuroblastoma Cells

A Comparison of the Electric Potential through the Membranes of Ganglion Neurons and Neuroblastoma Cells

Thiago M. Pinto, Roseli S. Wedemann, and Célia Cortez

Instituto de Matemática e Estatística, Universidade do Estado do Rio de Janeiro,
Rua São Francisco Xavier 524, 20550 − 900, Rio de Janeiro, Brazil
{thiagomatos,roseli,ccortezs}@ime.uerj.br

Abstract. We have modeled the electric potential profile, across the membranes of the ganglion neuron and neuroblastoma cells. We considered the resting and action potential states, and analyzed the influence of fixed charges of the membrane on the electric potential of the surface of the membranes of these cells, based on experimental values of membrane properties. The ganglion neuron portrays a healthy neuron, and the neuroblastoma cell, which is tumorous, represents a pathologic neuron. We numerically solved the non-linear Poisson-Boltzmann equation, by considering the densities of charges dissolved in an electrolytic solution and fixed on both glycocalyx and cytoplasmic proteins. We found important differences among the potential profiles of the two cells.

Keywords: Membrane model, electric potential, electrophoresis, neuroblastoma.

1 Introduction

We study the influence of surface electric charges on the stability of the neural cell membrane, by modeling the electric potential profile. This profile describes the behavior of the potential along the axis perpendicular to the cell membrane, from the outer bulk region to the inner one [1,2,3]. It has been shown that the electrophoretic behavior of neuroblastoma cells provides information about its surface charge, in different phases of the cellular cycle [4,5]. This evidence shows that membrane anionic groups are mainly responsible for the surface charges of murine neuroblastoma cells. These groups are distributed in a 0.2 e/nm^3 density, in a layer that covers the cell's outer surface, with a 10 nm thickness.

We compare the effects of fixed charges in the glycocalyx and those associated with cytoplasmic proteins, on the electric potential on the surfaces of the membranes of the lipid bilayer of the ganglion neuron and the neuroblastoma cells, considering both natural states of neuronal cells, *i.e.* the resting and the action potential (AP) states. The AP state refers to the state in which the neuron has been stimulated enough and is firing. We also calculated the potential profile across the membrane, including data from electrophoretic experiments

T. Honkela et al. (Eds.): ICANN 2011, Part II, LNCS 6792, pp. 103–110, 2011.

in our model. We have thus applied a model devoloped in [1,2,3] to the ganglion neuron, which is a healthy neuron, and to the neuroblastoma cell, which is a tumorous pathologic neuron. Although there are models for studying morphological and mechanical properties of cell membranes, we know of no other models for predicting the electric potential along an axis perpendicular to the membrane.

2 The Membrane Model

In the neuron membrane model we have adopted [2] shown in Fig. 1, four different regions are represented: extracellular, glycocalyx, bilayer and cytoplasm. The bilayer thickness is h and the width of the glycocalyx is h_g. Surface potentials are represented as $\phi_{-\infty e}$ for the potential in $-\infty$ in the electrolytic extracellular phase, $\phi_{S_{eg}}$ for the potential on the surface between the extracellular and glycocalyx regions, $\phi_{S_{gb}}$ is the potential on the surface between the glycocalyx and the bilayer, $\phi_{S_{bc}}$ is the potential on the surface between the bilayer and cytoplasm, and $\phi_{c+\infty}$ is the potential in $+\infty$, *i.e.* in the bulk cytoplasmic region.

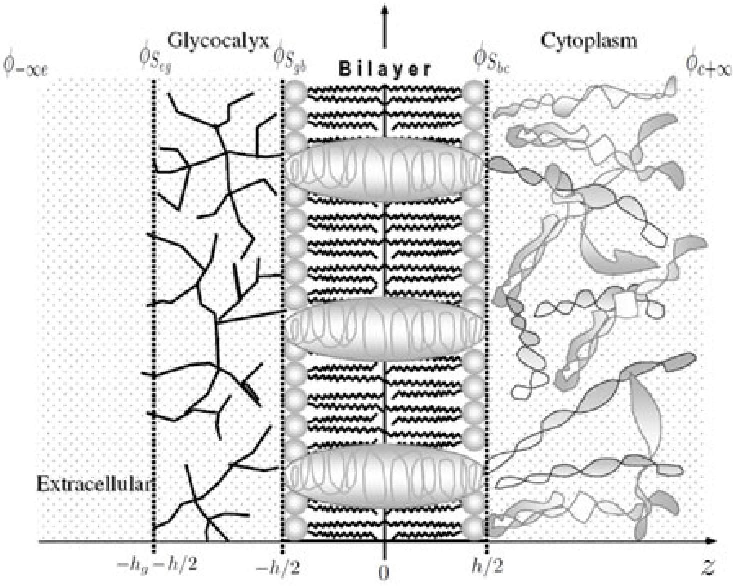

Fig. 1. Model for a neuron membrane. Different regions are represented, with the corresponding symbols for the potentials in the regions and on surfaces dividing regions. Symbols are explained in the text.

2.1 The Electric Potential in the Membrane Regions

In order to determine the potential profile across the membrane, we first considered as in [2] the Poisson equation, including the fixed charges on the surfaces

$$\nabla^2 \phi_i(x,y,z) = \frac{-4\pi(\rho_i + \rho_{fi})}{\epsilon_i} \text{ for } i = ext, g, b, c \ , \tag{1}$$

where $\phi_i(x,y,z)$ is the electric potential in any region i; $i = ext$ for the outer electrolytic region; $i = g$ for the glycocalyx; $i = b$ for the bilayer; $i = c$ for the cytoplasm. The volumetric charge density due to the electrolytes in solution of area i is ρ_i, and ρ_{fi} is the density of charges fixed onto proteins of area i.

In a situation where the Boltzmann condition for equilibrium of the electrochemical potential for ionic solutes in a diluted solution holds, it is possible to use the Boltzmann distribution with the above Poisson equation Eq. (1) [2]. Considering a homogeneous charge distribution in directions x and y, Boltzmann equilibrium and Eq. (1), we obtain [2,6]

$$\frac{\partial}{\partial z}\phi_i(z) = \sqrt{\frac{Q_{m_i}\cosh\beta\left(\phi_i - \phi_{S_i}\right)}{\beta} + \frac{Q_{d_i}\cosh^2\beta\left(\phi_i - \phi_{S_i}\right)}{\beta} + g_i\phi_i + W_i} \ , \tag{2}$$

where

$$Q_{m_i} = \left[\frac{8\pi e\eta_{1,S_i}}{\epsilon_i}\right], \ Q_{d_i} = \left[\frac{16\pi e\eta_{2,S_i}}{\epsilon_i}\right], \ \beta = \frac{e}{KT}, \text{ and } g_i = -\frac{4\pi\rho_{fi}}{\epsilon_i} \ , \tag{3}$$

and ϕ_i is the electric potential at any point within region i; ϕ_{S_i} is the limiting electric potential at surface S_i; e is the electron charge; K is Boltzmann's constant; T is the temperature; ϵ_i is the dielectric constant in region i; W_i is an integration constant for region i; the monovalent ionic concentration is η_{1,S_i} and the divalent ionic concentration is η_{2,S_i}, both on surface S_i. Eq. (2) is the Poisson-Boltzmann equation for the electric potential in region i [2,6].

2.2 Surface Potentials

Considering the discontinuity of the displacement of the electric field vector on the surface S_{gb} and considering the solution of the Poisson-Boltzmann equation in the cytoplasmic and electrolytic regions, we have obtained [2,6]

$$\phi_{S_{bc}} = \phi_{S_{gb}} - \frac{4\pi Q_{S_{gb}} h}{\epsilon_b} + \frac{\epsilon_g h}{\epsilon_b}\sqrt{\alpha} \ , \tag{4}$$

where,

$$\begin{aligned}\alpha = 2\frac{Q_{m_g}\sinh^2(\frac{\beta}{2}\left(\phi_g - \phi_{S_{eg}}\right))}{\beta} + \frac{Q_{d_g}\sinh^2(\beta\left(\phi_g - \phi_{S_{eg}}\right))}{\beta} + \\ g_g\left(\phi_g - \phi_{S_{eg}}\right) + \left(\frac{4\pi Q_{S_{eg}} - \epsilon_{ext}\nabla\phi_{ext}|_{S_{eg}}}{\epsilon_g}\right)^2 \ ,\end{aligned} \tag{5}$$

and $Q_{S_{gb}}$ and $Q_{S_{eg}}$ stand for the charge density on the surfaces between the regions, glycocalyx and the bilayer, and electrolytic and glycocalyx, respectively. Applying the same procedure for the S_{bc} surface,

$$\phi_{S_{gb}} = \phi_{S_{bc}} - \frac{4\pi Q_{S_{bc}} h}{\epsilon_b} + \frac{\epsilon_c h}{\epsilon_b} \times$$
$$\sqrt{2\frac{Q_{m_c} \sinh^2 \frac{\beta}{2} \left(\phi_c - \phi_{c+\infty}\right)}{\beta} + \frac{Q_{d_c} \sinh^2 \beta \left(\phi_c - \phi_{c+\infty}\right)}{\beta} + g_c \left(\phi_c - \phi_{c+\infty}\right)} \quad (6)$$

We have used data obtained from experimental results [5,7] for values of parameters, in order to solve the first order ordinary differential equations, obtained from the Poisson-Boltzmann Eq. (2), for the different regions of the membrane. Some experimental values were obtained from electrophoresis experiments. Since each kind of cell presents a specific electrophoretic mobility, the values of some parameters are different for the ganglion neuron and the neuroblastoma, in our calculations. Due to space limitations, we refer the reader to [6] for a table with all experimental values of the paramenters used to solve the equations. We have thus examined the influence of parameters representing electric properties of the membrane, over resting and AP states, analyzing the differences between the healthy ganglion neuron and a neuroblastoma cell.

We implemented an algorithm for finding roots of functions, to calculate $\phi_{S_{gb}}$ and $\phi_{S_{bc}}$ from Eqs. (4) and (6), in C. The potential $\phi_{S_{eg}}$ was calculated from data obtained from electrophoretic experiments. We numerically calculated values of the potential profiles with Eq. (2), using the Runge-Kutta method, also in C.

3 Results

We examined the bilayer surface potentials as a function of ρ_{fc}/ρ_{fg} (ρ_{fc} and ρ_{fg} are the fixed charge densities in the cytoplasm and in the glycocalyx, respectively). Figs. 2 and 3 present the behavior of $\phi_{S_{gb}}$ and $\phi_{S_{bc}}$ with the variation of ρ_{fc}/ρ_{fg}, considering the same $Q_{S_{bc}}$ value, for both cells. During the resting potential state, results in Fig. 2 show that, while $\phi_{S_{gb}}$ remains constant while increasing ρ_{fc}/ρ_{fg}, by making the fixed charges in the cytoplasm more negative (decreasing negative values of ρ_{fc}), $\phi_{S_{bc}}$ decreases expressively, for both $Q_{S_{gb}} = 0$ (Fig. 2(a)) and $Q_{S_{gb}} \neq 0$ (Fig. 2(b)). However, comparing Figs. 2(a) and 2(b), we see that the increase of negativity of $Q_{S_{gb}}$ visibly decreases the value of $\phi_{S_{gb}}$, for the ganglion neuron. The same behavior is observed, when comparing Figs. 3(a) and 3(b). During the AP state (Fig. 3), the potential $\phi_{S_{bc}}$ of both cells shows a quick drop, when $\rho_{fc}/\rho_{fg} < 20$, becoming almost constant for $\rho_{fc}/\rho_{fg} > 20$. However, $\phi_{S_{gb}}$ remains constant for all values of ρ_{fc}/ρ_{fg}.

In Fig. 4, we compared the electric potential profile across the membranes of both cells. We verify that the gradual decrease of the potential along the z axis, up to the surface of the glycocalyx ($z < -h_g - h/2$) is higher for the ganglion neuron than for the neuroblastoma cell, and both curve shapes are similar. Through the glycocalyx ($-h_g - h/2 < z < -h/2$) we can see that the fall continues for the ganglion neuron, but is negligible for the cancerous cell. During the resting potential state, the value of the intracellular potential increases exponentially, from the bilayer surface to the bulk cytoplasmic region.

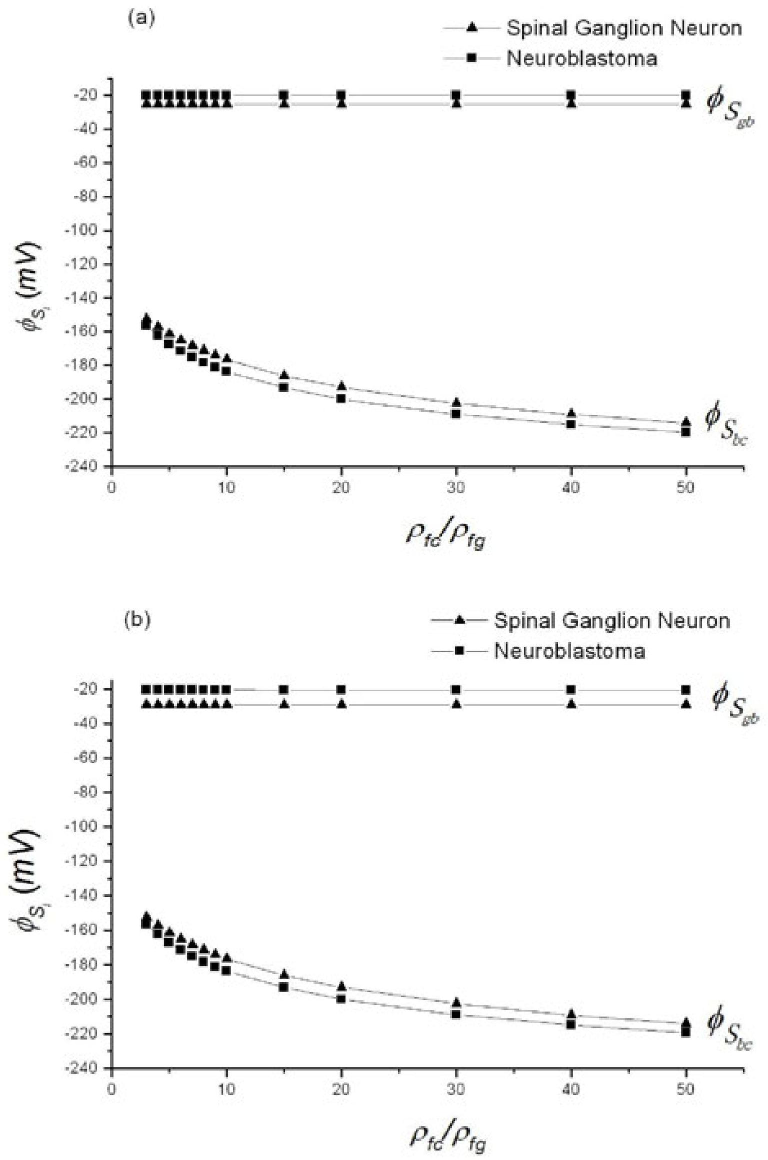

Fig. 2. $\phi_{S_{bc}}$ and $\phi_{S_{gb}}$ as a function of ρ_{fc}/ρ_{fg}, during resting state, on the ganglion neuron and neuroblastoma membranes. In both figures, $Q_{S_{bc}} = -5.4\times10^{-2}$ C/m^2. $Q_{S_{eg}} = -0.012$ e/nm^2 and $\phi_R = -69$ mV for the ganglion neuron. $Q_{S_{eg}} = -0.02$ e/nm^2 and $\phi_R = -64$ mV for the neuroblastoma. (a) $Q_{S_{gb}} = 0$. (b) $Q_{S_{gb}} = -3.20 \times 10^{-3}$ C/m^2, for the neuroblastoma; and $Q_{S_{gb}} = -1.92 \times 10^{-3}$ C/m^2, for the ganglion neuron. The resting transmembrane potential is ϕ_R.

4 Conclusions

Simulation experiments maintaining constant values of $Q_{S_{bc}}$ and $Q_{S_{eg}}$, resulted in no detectable changes in $\phi_{S_{gb}}$, but $\phi_{S_{bc}}$ of both neurons decreases gradually with the increase of ρ_{fc}/ρ_{fg}, by making the fixed charges in the cytoplasm more negative (decreasing negative values of ρ_{fc}), during the resting potential state (Fig. 2) and also during the AP state (Fig. 3). For the AP state, the drop in the values of $\phi_{S_{bc}}$ occurred mainly for the small values of ρ_{fc}/ρ_{fg}, tending to

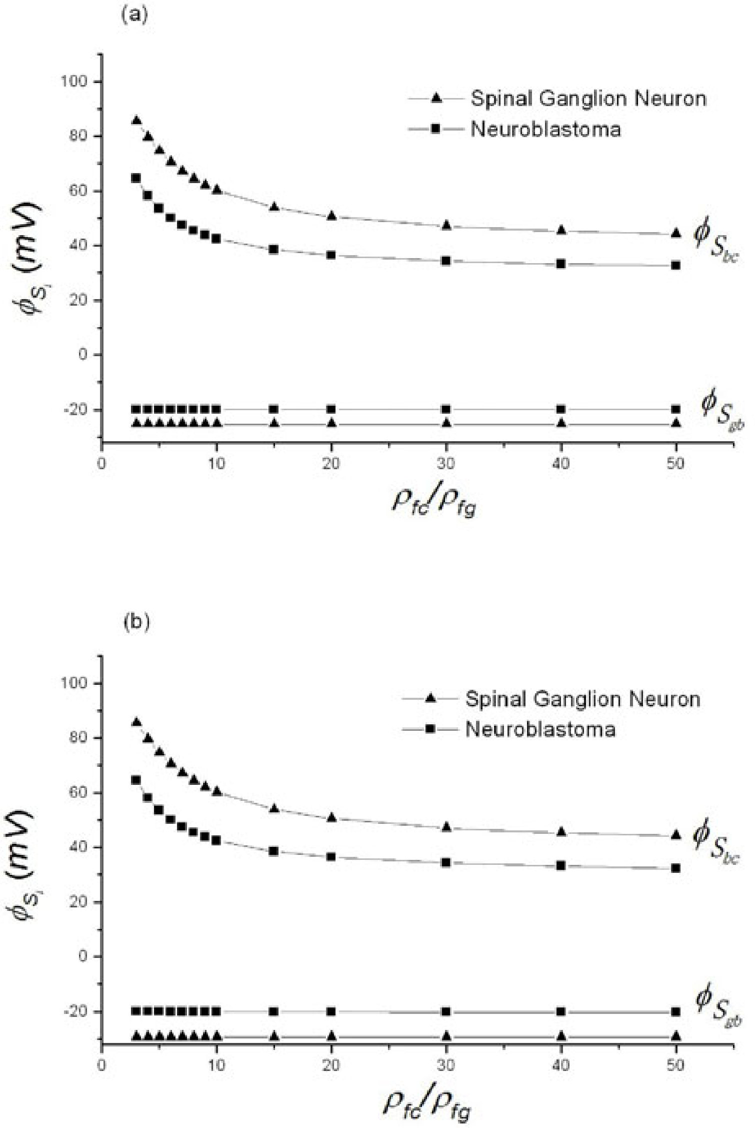

Fig. 3. $\phi_{S_{bc}}$ and $\phi_{S_{gb}}$ as a function of ρ_{fc}/ρ_{fg}, during action state, on ganglion neuron and neuroblastoma membranes. In all curves, $Q_{S_{bc}} = -5.4 \times 10^{-2}$ C/m^2. $Q_{S_{eg}} = -0.012$ e/nm^2 and $\phi_R = -69$ mV for the ganglion neuron. $Q_{S_{eg}} = -0.02$ e/nm^2 and $\phi_R = -64$ mV for the neuroblastoma. (a) $Q_{S_{gb}} = 0$. (b) $Q_{S_{gb}} = -3.20 \times 10^{-3}$ C/m^2, for the neuroblastoma; and $Q_{S_{gb}} = -1.92 \times 10^{-3}$ C/m^2, for the ganglion neuron.

become constant for higher values. Comparing Figs. 2(a) and 2(b), we verify, for $Q_{S_{gb}} \neq 0$, that $\phi_{S_{gb}}$ for the ganglion neuron is more negative than when $Q_{S_{gb}} = 0$, which was the only detectable alteration with this change in charge value. The results obtained for the ganglion neuron match those for the squid axon membrane found by Cortez et al. [2]. Using a model with similar equations as we used in this study, the authors observed variations of the surface potentials with a change in surface charge $Q_{S_{gb}}$ compatible with those observed here.

During the resting potential state, the net value of the protein charge in the cytoplasm is predominantly negative [2]. However, in our simulation experiments,

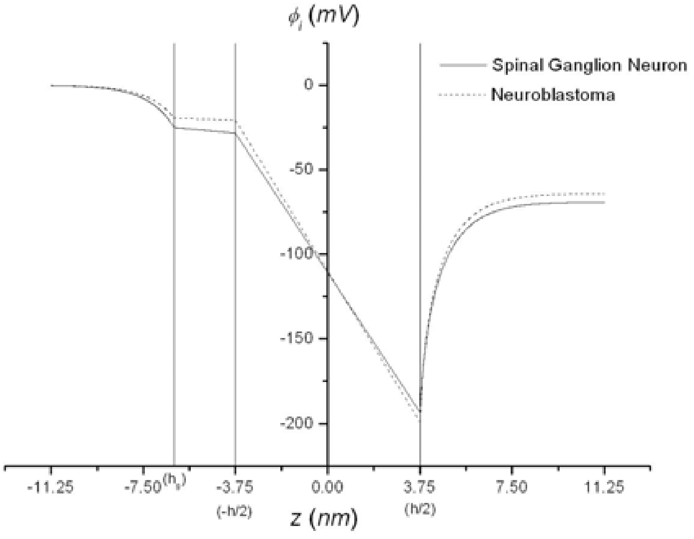

Fig. 4. Electric potential profile, during the resting state, across the ganglion neuron membrane, for $\phi_{S_{bc}} = -193.39\text{mV}$, $\phi_{S_{gb}} = -28.42\text{mV}$, $\phi_{S_{eg}} = -25.10\text{mV}$, $Q_{S_{gb}} = -1.92 \times 10^{-3}\text{C/m}^2$ and $\phi_R = -69\text{mV}$. Same profile for the neuroblastoma membrane, for $\phi_{S_{bc}} = -199.08\text{mV}$, $\phi_{S_{gb}} = -20.65\text{mV}$, $\phi_{S_{eg}} = -19.52\text{mV}$, $Q_{S_{gb}} = -3.20 \times 10^{-3}\text{C/m}^2$, $\phi_R = -64\text{mV}$. In both curves, $Q_{S_{bc}} = 30 \times Q_{S_{gb}}$ and $\rho_{fc} = 20\rho_{fg}$.

the contribution of these charges to the inner potential profile was smaller than the effect of the fixed charges in the inner surface of the bilayer, due to the curvature of the potential in this region, whereas the calculated value of $\phi_{S_{bc}}$ was smaller than the bulk region $\phi_{S_{bc}}$. It is known that the neuroblastoma cells, like all other cancerous cells, multiply themselves quickly. Alterations of the dynamics of cellular multiplication implicate changes in the synthesis, structure and degradation of the membrane components [8], which result in deformations in structure and composition of the plasma membrane surface [9]. These deformations implicate changes in the electric charge of the membrane.

Our results indicate that the alteration of the fixed electric charges of the membrane influences the behavior of its surface electric potential. Although we used the same model and equations for both types of cells, contrary to what was observed for the ganglion neuron, using the parameters of the neuroblastoma cells led to solutions of the equation for the electric potential, where a change of values of $Q_{S_{gb}}$ and ρ_{fc} charges practically didn't affect the surface potentials. It corroborates results of experimental observations, that the resting potential and the generation of action potentials in human neuroblastoma cells depend on the degree of the morphologic differentiation of the cell. Some of these cells are relatively non-excitable [10,11]. These properties should affect the transmission of signals through networks of these neurons and the functions of storage and communication of information.

The different values of the potential in the glycocalyx for the neuroblastoma and the spinal ganglion neuron must represent important alterations in the transport function of the membrane, due to the outer electric field, which is responsible for the orientation of the charged particles which are closer to the membrane. Also, the potential at the outer surface of the membrane is determinant for many cell processes, such as the beginning of the process of triggering of the action potential, which depends on the opening of specific Na^+ channels.

References

1. Cortez, C., Bisch, P.: The effect of ionic strength and outer surface charge on the membrane electric potential profile: a simple model for the erythrocyte membrane. Bioelectrochemistry and Bioenergetics 32, 305–315 (1993)
2. Cortez, C., Cruz, F., Silva, D., Costa, L.: Influence of fixed electric charges on potential profile across the squid axon membrane. Physica B 403, 644–652 (2008)
3. Cruz, F., Vilhena, F., Cortez, C.: Solution of non-linear Poisson-Boltzmann equation for erythrocyte membrane. Brazilian Journal of Physics 3, 403–409 (2000)
4. Belan, P., Dolgaya, E., Mironov, S., Tepikin, A.: Relation between the surface potential of mouse neuroblastoma clone c1300 cells and the phase of the cell cycle. Neurophysiology 19(1), 130–133 (1987)
5. Dolgaya, E., Mironov, S., Pogorelaya, N.: Changes in surface charge of mouse neuroblastoma cells during growth and morphological differentiation of the cell population. Neurophysiology 17(2), 168–174 (1985)
6. Pinto, T.M.: Modelagem do Potencial Elétrico através da Membrana do Neurônio Ganglionar e Células de Neuroblastoma: Efeitos das Cargas Superficiais. Masters Dissertation, Universidade do Estado do Rio de Janeiro, Rio de Janeiro (2010)
7. Mironov, S., Dolgaya, E.: Surface charge of mammalian neurones as revealed by microelectrophoresis. J. Membrane Biol. 86, 197–202 (1985)
8. Dehlinger, P., Schimke, R.: Size distribution of membrane proteins of rat liver and their relative rates of degradation. J. Biol. Chem. 246(8), 2574–2583 (1971)
9. Schubert, D., Humphreys, S., Jacob, F.: Induced differentiation of a neuroblastoma. Dev. Biol. 25(4), 514–546 (1971)
10. Gèrard, V., Rouzaire-Dubois, B., Dilda, P.: Alterations of ionic membrane permeabilities in multidrug-resistant neuroblastoma x glioma hybrid cells. J. Exp. Biol. 201, 21–31 (1998)
11. Kuramoto, T., Perez-Polo, J., Haber, B.: Membrane properties of a human neuroblastoma II: Effects of differentiation. J. Neurosci. Res. 6(4), 441–449 (1981)

Appendix L

Computational Modeling of the Electric Potential in Biological Membrane. A Comparison between Healthy and Cancerous Neurons

Pinto *et al. BMC Neuroscience* 2011, **12**(Suppl 1):P47
http://www.biomedcentral.com/1471-2202/12/S1/P47

BMC Neuroscience

POSTER PRESENTATION **Open Access**

Computational modeling of the electric potential in biological membrane. A comparison between healthy and cancerous neurons

Thiago M Pinto*, Roseli S Wedemann, Célia M Cortez

From Twentieth Annual Computational Neuroscience Meeting: CNS*2011
Stockholm, Sweden. 23-28 July 2011

We have studied the behavior of the electric potential profile across the membrane of the ganglion neuron and the neuroblastoma cell. We considered the physico-chemical conditions during the resting and action potential (AP) states of the neuronal cells, and analyzed the influence of the fixed charges of the membrane on the surface electric potential of these cells, based on values of electric parameters obtained from experimental results. The ganglion neuron portrays a healthy neuron and the neuroblastoma cell, which is a tumorous cell, represents a pathologic neuron. We solved the non-linear Poisson-Boltzmann equation, by considering the volumetric charge densities due to charges dissolved in an electrolytic solution, and also charges fixed on both glycocalyx and cytoplasmic proteins.

Data obtained from experimental results [1,2] have been used to solve the first order ordinary differential Poisson-Boltzmann equations [3,4], which have been obtained for the regions of the membrane model we have adopted. Therefore, we have examined the influence of the electric parameters during resting and AP states, analyzing the differences between the healthy ganglion neuron and a neuroblastoma cell.

We implemented an algorithm for finding roots of functions with a program in C language, to calculate the surface potentials between the glycocalyx and the bilayer, and between the bilayer and the cytoplasm, regions of the membrane. The surface potential between the electrolytic region and the glycocalyx has been calculated from electrophoretic experimental data. We have calculated the potential profiles using the Runge-Kutta method, also implemented in C language.

We analyzed the electric potential profile across the membranes. Comparing both neuronal types, we verified that the gradual potential fall from the electrolytic region to the surface of glycocalyx is higher for the ganglion neuron than for the neuroblastoma cell, and both curve shapes are similar. Through the glycocalyx we could see that the fall continues for the ganglion neuron, but this fall is negligible for the cancerous cell. The intracellular potential, during the resting state, increases exponentially from the bilayer surface to the bulk cytoplasmic region.

During the resting state, the net value of the protein charge in the cytoplasm is predominantly negative [4]. However, in our neuron model the contribution of these charges to the inner potential profile was smaller than the effect of the fixed charges in the inner surface of the bilayer, due to the curvature of the potential in this region, whereas the calculated potential on the surface between the bilayer and the cytoplasm was smaller than the potential in the bulk region. It is known that the neuroblastoma cells, like all the other cancerous cells, multiply themselves quickly. Alterations of the dynamics of the cellular multiplication cause changes in the synthesis, structure and promotes degradation of the membrane components [5], which results in deformations in structure and composition of the plasma membrane.

Conclusions

Our results may also contribute to the understanding of the neuroblastoma resistance to certain chemotherapeutic treatments. The small change of the surface potential as a response to changes in the culture (pH, for instance) and in the fixed electric charges, due to alterations in the composition and structure of the

Instituto de Matemática e Estatística, Universidade do Estado do Rio de Janeiro, Rio de Janeiro, RJ, 20550-900, Brazil

membrane, may be the electric property responsible for the low pharmacological response.

Published: 18 July 2011

References

1. Dolgaya E, Mironov S, Pogorelaya N: Changes in surface charge of mouse neuroblastoma cells during growth and morphological differentiation of the cell population. *Neirofiziologiia* 1985, **17**:168-174.
2. Mironov S, Dolgaya E: Surface charge of mammalian neurones as revealed by microelectrophoresis. *J. Membr. Biol* 1985, **86**:197-202.
3. Cortez CM, Cruz FAO, Silva D, Costa L: Influence of fixed electric charges on potential profile across the squid axon membrane. *Physica B* 2008, **403**:644-652.
4. Cruz FAO, Vilhena F, Cortez CM: Solution of non-linear Poisson-Boltzmann equation for erythrocyte membrane. *Braz. J. Physics* 2000, **30**:403-409.
5. Dehlinger PJ, Schimke RT: Size distribution of membrane proteins of rat liver and their relative rates of degradation. *J. Biol. Chem* 1971, **246**:2574-2583.

doi:10.1186/1471-2202-12-S1-P47
Cite this article as: Pinto *et al*.: Computational modeling of the electric potential in biological membrane. A comparison between healthy and cancerous neurons. *BMC Neuroscience* 2011 **12**(Suppl 1):P47.

Appendix M

The Behavior of the Electric Potential across Neuronal Membranes of Spinal Ganglion and Neuroblastoma Cells

The behavior of the electric potential across neuronal membranes of spinal ganglion and neuroblastoma cells

Thiago M Pinto[1,2], Roseli S Wedemann[1], Célia M Cortez[1]
[1] Instituto de Matemática e Estatística, Universidade do Estado do Rio de Janeiro, Rio de Janeiro, RJ, 20550-900, Brazil
[2] Science and Technology Research Institute, University of Hertfordshire, Hatfield, Herts, AL10 9AB, UK
E-mail: {thiagomatos, roseli, ccortezs}@ime.uerj.br

Electrical signals underlie the propagation of information in the nervous system. It is known that neuronal cells can generate electric potentials by diffusing ions across the neuronal membrane. We have previously studied the effects of electric charges fixed onto the inner surface of the membrane, on the potential of the membrane surfaces of healthy and cancerous neuronal cells [1,2]. Based on this work, we have developed a computational model that simulates the electric potential profile across neuronal membranes. This profile shows the behavior of the electric potential along the axis (*z*), perpendicular to the membrane, from the extracellular region to the inner cytoplasmic region. In particular, we compared the electric potential profile of the membranes of spinal ganglion and neuroblastoma cells, during the resting and action potential (AP) states. The spinal ganglion neurons represent healthy cells, while neuroblastomas denote tumorous neurons.

To analyze the electric potential profile of neuronal membranes, we numerically solved the Poisson-Boltzmann equation [1,3]. The model considers the following electric charges: (i) fixed on surfaces of the glycocalyx and the lypidic bilayer, (ii) dissolved in the electrolytic solutions for regions of the membrane model we have adopted, and (iii) fixed on the cytoplasmic proteins. All parameter values are based on measurements collected from experimental observations [4,5].

For the resting and AP states of spinal ganglion neurons and neuroblastoma cells, simulation results indicate that the electric potential significantly decreases along the *z* axis from the extracellular region to the surface of the glycocalyx. The decay of the potential is more expressive for the neuroblastoma than for the ganglion neuron. An interesting observation is that the electric potential continues to decrease across the glycocalyx region of the spinal ganglion neuron. This however does not occur for the neuroblastoma cells, whose potential does not change in this region of the membrane.

Because there is no electric charge within the lypidic bilayer, our results demonstrate linear variations of the potential across the bilayer of neuronal membranes. Furthermore, the intracellular potential of both spinal ganglion neurons and neuroblastoma cells exponentially increases from the inner membrane surface to the bulk cytoplasmic region during the resting state. However, during the AP state, the electric potential remains unchanged in the cytoplasm.

Our simulation results match those obtained for the membrane of the squid axon [3], whose mathematical model is based on similar ordinary differential equations to those of this study. Moreover, the different behavior of the electric potential observed in the spinal ganglion when compared to the neuroblastoma cells, in the glycocalyx region, may explain the difference in the electrophoretic behavior of these cells, as observed in experiments [4,5].

References

1. Pinto TM, Wedemann RS, Cortez C: **A Comparison of the Electric Potential through the Membranes of Ganglion Neurons and Neuroblastoma Cells**. *Lecture Notes in Computer Science* 2011, **6792:** 103-110.
2. Pinto TM, Wedemann RS, Cortez C: **Computational modeling of the electric potential in biological membrane. A comparison between healthy and cancerous neurons**. *BMC Neuroscience* 2011, **12(Suppl 1):** P47.
3. Cortez CM, Cruz FAO, Silva D, Costa L: **Influence of fixed electric charges on potential profile across the squid axon membrane**. *Physica B* 2008, **403:** 644-652.
4. Dolgaya E, Mironov S, Pogorelaya N: **Changes in surface charge of mouse neuroblastoma cells during growth and morphological differentiation of the cell population**. *Neirofiziologiia* 1985, **17:** 168-174.
5. Mironov S, Dolgaya E: **Surface charge of mammalian neurones as revealed by microelectrophoresis**. *Journal of Membrane Biology* 1985, **86:** 197-202.

APPENDIX N

Modeling the Electric Potential across Neuronal Membranes: The Effect of Fixed Charges on Spinal Ganglion Neurons and Neuroblastoma Cells

Modeling the electric potential across neuronal membranes: The effect of fixed charges on spinal ganglion neurons and neuroblastoma cells

Thiago M. Pinto[a,b,**], Roseli S. Wedemann[a,*], Célia M. Cortez[a,*]

[a] *Instituto de Matemática e Estatística, Universidade do Estado do Rio de Janeiro, Rua São Francisco Xavier* 524, 20550 − 900*, Rio de Janeiro, Brazil*
[b] *Science and Technology Research Institute, University of Hertfordshire, Hatfield, Herts, AL10 9AB, UK*

Abstract

We present a model for the electric potential profile across the membranes of neuronal cells. We considered the resting and action potential states, and analyzed the influence of fixed charges of the membrane on its electric potential, based on experimental values of membrane properties of the spinal ganglion neuron and the neuroblastoma cell. The spinal ganglion neuron represents a healthy neuron, and the neuroblastoma cell, which is tumorous, represents a pathological neuron. We numerically solved the non-linear Poisson-Boltzmann equation for the regions of the membrane model we have adopted, by considering the densities of charges dissolved in an electrolytic solution and fixed on both glycocalyx and cytoplasmic proteins. Our model predicts that there is a difference in the behavior of the electric potential profiles of the two types of cells, in response to changes in charge concentrations in the membrane. Our results also describe an insensitivity of the neuroblastoma cell membrane, as observed in some biological experiments. This electrical property may be responsible for the low pharmacological response of the neuroblastoma to certain chemotherapeutic treatments.

Keywords: neuronal membrane model, electric potential, electrophoresis, neuroblastoma

---

1. Introduction

Electrostatic forces affect the passive and active transport of charged particles through biological membranes. The flow rate of ions through the membrane depends on the strength of the intramembranous electric field. These forces also affect the robustness of some ligands of the membrane (Iglic et al., 1997).

We study the influence of surface electric charges on the stability of the cell membrane, by modeling the electric potential profile. The profile describes the behavior of the potential along the axis perpendicular to the cell membrane, from the outer bulk region to the inner cytoplasmic region (Heinrich et al., 1982; Cortez and Bisch, 1993; Cortez et al., 2008; Cruz et al., 2000). We did not yet consider time variations of the electric potential, and treat only the electrostatic case in this work.

The electric potential on a cell surface is determined as the difference of potential between the membrane-solution interface and the bulk region (Iglic et al., 1997). It has been shown that the electrophoretic behavior of neuroblastoma cells provides information about their surface charges, in different phases of the cellular cycle (Belan et al., 1987; Dolgaya et al., 1985; Hernandez et al., 1996). These experiments show that membrane anionic groups are mainly responsible for the surface charges of murine neuroblastoma cells (Hernandez et al., 1996). It is known that neuroblastoma cells, like all other cancerous cells, multiply quickly. Alterations of the dynamics of cellular multiplication compromise the synthesis and structure of components of the membrane, with possible degradation of these components, promoting deformations of the structure and composition of the plasma membrane (Dehlinger and Schimke, 1971).

---

[*] Corresponding author
[**] Principal corresponding author

Email addresses: `thiagomatos@ime.uerj.br` (Thiago M. Pinto), `roseli@ime.uerj.br` (Roseli S. Wedemann), `ccortezs@ime.uerj.br` (Célia M. Cortez)

We have applied a model developed by Cortez and collaborators (Cortez and Bisch, 1993; Cortez et al., 2008; Cruz et al., 2000) to the spinal ganglion neuron, which is a healthy neuron, and to the neuroblastoma cell, which is a tumorous neuron. With simulations of this model, we compare the effects of charges fixed onto the inner surface of the membrane and those associated with cytoplasmic proteins, on the electric potential on the surfaces of the membranes of both types of cells, considering both natural states of neurons, the resting and the action potential (AP) states. The AP state refers to the state in which the neuron has been stimulated enough and is firing. We also calculated the potential profile across the membrane, including data from electrophoretic experiments in our model.

2. The Membrane Model

In the neuronal membrane model we have adopted, shown in Fig. (1), four different regions are presented: extracellular, glycocalyx, bilayer and cytoplasm. The bilayer thickness is h and the width of the glycocalyx is h_g. Surface potentials are represented as $\phi_{S_{eg}}$ for the potential on the surface S_{eg}, between the extracellular and glycocalyx regions, $\phi_{S_{gb}}$ is the potential on the surface S_{gb}, between the glycocalyx and the bilayer, and $\phi_{S_{bc}}$ is the potential on the surface S_{bc}, between the bilayer and cytoplasm. We denote by $\phi_{-\infty}$ and $\phi_{+\infty}$ the potentials at $-\infty$, in the electrolytic extracellular phase, and at $+\infty$, in the bulk cytoplasmic region, respectively.

2.1. The Electric Potential in the Membrane Regions

To determine the potential profile across the membrane, we first consider the Poisson equation (Cortez and Bisch, 1993; Verwey and Overbeek, 1948),

$$\nabla^2\phi_i(x,y,z) = \frac{-4\pi\rho_i(z)}{\epsilon_i} \, , \quad \text{for } i \in \{ext, g, b, c\} \, , \qquad (1)$$

where $\phi_i(x,y,z)$ is the electric potential in any region i; $i = ext$ for the outer electrolytic region; $i = g$ for the glycocalyx; $i = b$ for the bilayer; and $i = c$ for the cytoplasm. The volumetric charge density due to the electrolytes in solution of area i is $\rho_i(z)$, and ϵ_i is the dielectric constant in region i. There is no charge in the bilayer ($i = b$), due to its hydrophobic property, and thus $\rho_b(z) = 0$.

We consider the further boundary conditions to calculate the constants of integration:

1. When z tends to an extreme value, $z \to -\infty$ (in region ext) or $z \to +\infty$ (in the cytoplasm), the electric potential tends to limiting values represented by $\phi_{-\infty}$ and $\phi_{+\infty}$, respectively. Ionic concentrations assume values $\eta_{\gamma,ext}(z)$ and $\eta_{\gamma,c}(z)$, where γ represents an ion, such as Na^+, K^+, or Cl^-.
2. When $z = -h_g - h/2$ and $z = \pm h/2$, we consider the continuity of the electric potentials, $\phi_{S_{eg}}$, $\phi_{S_{gb}}$ and $\phi_{S_{bc}}$, respectively.
3. There is a discontinuity of the electric field vector on the surfaces between regions.

2.1.1. The Effect of Fixed Charges

When we include the effect of fixed charges in the solution, Poisson Eq. (1) becomes

$$\nabla^2\phi_i(x,y,z) = \frac{-4\pi(\rho_i(z) + \rho_{fi})}{\epsilon_i} \, , \qquad (2)$$

where, as in (Cortez et al., 2008), ρ_{fi} is the density of charges fixed onto proteins of area i ($\rho_{fext} = 0$, for the outer electrolytic region, ρ_{fg} for the glycocalyx, and ρ_{fc} for the cytoplasm).

The volumetric charge density $\rho_i(z)$ is the sum of the charge densities of positive and negative ions in the solution (Cortez and Bisch, 1993)

$$\rho_i(z) = \sum_{\gamma^+} eV_{\gamma^+}\eta_{\gamma^+,i}(z) + \sum_{\gamma^-} eV_{\gamma^-}\eta_{\gamma^-,i}(z) \, , \qquad (3)$$

where γ^+ represents a positive ion, and γ^-, a negative ion. The molar density for an ion γ in region i is $\eta_{\gamma,i}(z)$, and V_γ is the valency of ion γ. For example, $V_{Ca^{2+}} = 2$ and $V_{Cl^-} = -1$. The absolute value of the electron charge is e. Due to the electroneutrality condition (Cortez and Bisch, 1993; Cortez et al., 2008), we can write

$$\sum_{\gamma^+} eV_{\gamma^+}\eta_{\gamma^+,i}(z) = -\sum_{\gamma^-} eV_{\gamma^-}\eta_{\gamma^-,i}(z) \, . \qquad (4)$$

In our model, we suppose that the dimensions of the membrane tend to infinity, in the x and y directions, perpendicular to z, and that the distribution of charges in these directions is homogeneous

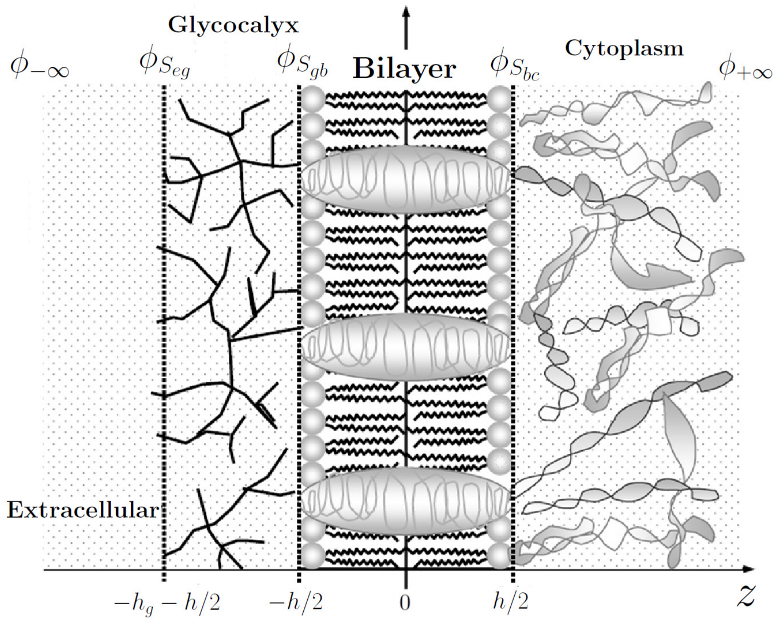

Figure 1: Model for a neuronal membrane. Different regions are presented, with the corresponding symbols for the potentials on the surfaces dividing regions. Symbols are explained in the text.

(Cortez and Bisch, 1993; Cortez et al., 2008). Considering this and substituting Eq. (3) in Eq. (2), we obtain

$$\frac{d^2\phi_i(z)}{dz^2} = -\frac{4\pi}{\epsilon_i}\left(\sum_{\gamma^+} eV_{\gamma^+}\eta_{\gamma^+,i}(z) + \sum_{\gamma^-} eV_{\gamma^-}\eta_{\gamma^-,i}(z)\right) + a_i \quad , \tag{5}$$

where

$$a_i = -\frac{4\pi\rho_{fi}}{\epsilon_i} \quad . \tag{6}$$

To determine $\eta_{\gamma,i}(z)$, we use the equation for the electrochemical potential, due to an ionic solute in a diluted solution (Cortez and Bisch, 1993; Cortez et al., 2008)

$$\mu_{\gamma,i}(z) = \mu^0_{\gamma,i}(P,T) + KTln(\eta_{\gamma,i}(z)) + eV_\gamma\phi_i(z) \quad , \tag{7}$$

where K is Boltzmann's constant, T is the temperature, $\mu^0_{\gamma,i}(P,T)$ is the standard chemical potential, dependent on pressure and temperature, $KTln(\eta_{\gamma,i}(z))$ is a term that expresses the influence of the ionic concentration $\eta_{\gamma,i}(z)$, and $eV_\gamma\phi_i(z)$ is the contribution of the electric potential.

Applying the $\vec{\nabla}$ operator in Eq. (7) (Cortez et al., 2008) and again considering the homogeneous distribution of charges in the directions perpendicular to z, we verify that

$$\frac{d\mu_{\gamma,i}(z)}{dz} = \frac{d\mu^0_{\gamma,i}(P,T)}{dz} + KT\frac{d}{dz}ln(\eta_{\gamma,i}(z)) + eV_\gamma\frac{d\phi_i(z)}{dz} \quad . \tag{8}$$

In a situation where the Boltzmann condition for equilibrium of the electrochemical potential for ionic solutes in a diluted solution holds, $\frac{d\mu_{\gamma,i}(z)}{dz} = 0$ and $\frac{d\mu^0_{\gamma,i}(P,T)}{dz} = 0$ (Cortez et al., 2008), and Eq. (8) becomes

$$0 = KT\frac{d}{dz}ln(\eta_{\gamma,i}(z)) + eV_\gamma\frac{d\phi_i(z)}{dz} \quad . \tag{9}$$

The integration of Eq. (9) from z in one of the three regions, extracellular, glycocalyx and cytoplasm, to the closest surface in the direction of the bilayer, such as z in $-h_g - h/2 < z < -h/2$ to $-h/2$, or z in $h/2 < z < +\infty$ to $h/2$, considering the electrolytes distributed over the adjacency of the bilayer gives

$$\int_{\eta_{\gamma,i}(z)}^{\eta_{\gamma,S_{ij}}} KT\frac{d}{d\eta_{\gamma,i}} ln(\eta_{\gamma,i}(z))d\eta_{\gamma,i} = -\int_{\phi_i(z)}^{\phi_{S_{ij}}} eV_\gamma \frac{d\phi_i(z)}{d\phi_i}d\phi_i \ , \tag{10}$$

where $\phi_{S_{ij}}$ is the electric potential on surface S_{ij} between regions i and j, and $\eta_{\gamma,S_{ij}}$ is the ionic concentration of γ on surface S_{ij}. The solution of Eq. (10) results in

$$\eta_{\gamma,i}(z) = \exp^{\left(\frac{-eV_\gamma \Delta\phi_i(z)}{KT}\right)} \eta_{\gamma,S_{ij}} \ , \tag{11}$$

where

$$\Delta\phi_i(z) = \phi_i(z) - \phi_{S_{ij}} \ . \tag{12}$$

The molar density for a positive γ ion is thus given by

$$\eta_{\gamma^+,i}(z) = \exp^{\left(\frac{-eZ_{\gamma^+}\Delta\phi_i(z)}{KT}\right)} \eta_{\gamma^+,S_{ij}} \ , \tag{13}$$

and for a negative γ ion

$$\eta_{\gamma^-,i}(z) = \exp^{\left(\frac{eZ_{\gamma^-}\Delta\phi_i(z)}{KT}\right)} \eta_{\gamma^-,S_{ij}} \ , \tag{14}$$

where

$$Z_\gamma = |V_\gamma| \ . \tag{15}$$

Equations (13) and (14) are the Boltzmann distribution of charges due to the presence of positive and negative γ ions (Verwey and Overbeek, 1948), respectively, in the phases adjacent to the bilayer. Substituting Eqs. (13) and (14) in Eq. (5), we obtain

$$\frac{d^2\phi_i(z)}{dz^2} = -\frac{4\pi}{\epsilon_i} \times \left(\sum_{\gamma^+} eZ_{\gamma^+} \exp^{\left(\frac{-eZ_{\gamma^+}\Delta\phi_i(z)}{KT}\right)} \eta_{\gamma^+,S_{ij}} - \sum_{\gamma^-} eZ_{\gamma^-} \exp^{\left(\frac{eZ_{\gamma^-}\Delta\phi_i(z)}{KT}\right)} \eta_{\gamma^-,S_{ij}}\right) + a_i \ . \tag{16}$$

We can rewrite Eq. (16), considering Eq. (4), as

$$\frac{d^2\phi_i(z)}{dz^2} = -\sum_\gamma \frac{4\pi eZ_\gamma \eta_{\gamma,S_{ij}}}{\epsilon_i} \times \left(\exp^{\left(\frac{-eZ_\gamma\Delta\phi_i(z)}{KT}\right)} - \exp^{\left(\frac{eZ_\gamma\Delta\phi_i(z)}{KT}\right)}\right) + a_i \ . \tag{17}$$

If we consider that

$$\exp^{\left(\frac{-eZ_\gamma\Delta\phi_i(z)}{KT}\right)} - \exp^{\left(\frac{eZ_\gamma\Delta\phi_i(z)}{KT}\right)} = -2\sinh\left(\frac{eZ_\gamma\Delta\phi_i(z)}{KT}\right) \ , \tag{18}$$

we can write Eq. (17) as

$$\frac{d^2\phi_i(z)}{dz^2} = \sum_\gamma \left(\frac{8\pi eZ_\gamma\eta_{\gamma,S_{ij}}}{\epsilon_i}\sinh\left[\frac{eZ_\gamma\Delta\phi_i(z)}{KT}\right]\right) + a_i \ . \tag{19}$$

Our model only considers mono ($Z_1 = 1$) and divalent ($Z_2 = 2$) ions, as in (Cortez et al., 2008). We thus limit the γ sum to

$$\frac{d^2\phi_i(z)}{dz^2} = \left[\frac{8\pi e\eta_{1,S_{ij}}}{\epsilon_i}\right]\sinh\left(\frac{e\Delta\phi_i(z)}{KT}\right) + \left[\frac{16\pi e\eta_{2,S_{ij}}}{\epsilon_i}\right]\sinh\left(\frac{2e\Delta\phi_i(z)}{KT}\right) + a_i \ . \tag{20}$$

To simplify further calculations, we denote

$$A_i = \frac{8\pi e\eta_{1,S_{ij}}}{\epsilon_i} \ , \ B_i = \frac{16\pi e\eta_{2,S_{ij}}}{\epsilon_i} \ , \ \beta = \frac{e}{KT} \ , \tag{21}$$

and Eq. (20) may be expressed as

$$\frac{d^2\phi_i(z)}{dz^2} = A_i\sinh(\beta\Delta\phi_i(z)) + B_i\sinh(2\beta\Delta\phi_i(z)) + a_i \ . \tag{22}$$

Considering that

$$\sinh(2\beta\Delta\phi_i(z)) = 2\sinh(\beta\Delta\phi_i(z))\cosh(\beta\Delta\phi_i(z)) \ , \tag{23}$$

Eq. (22) can be rewritten as

$$\frac{d^2\phi_i(z)}{dz^2} = A_i\sinh(\beta\Delta\phi_i(z)) + 2B_i\sinh(\beta\Delta\phi_i(z))\cosh(\beta\Delta\phi_i(z)) + a_i \ . \tag{24}$$

Multiplying Eq. (24) by

$$2d\phi_i = 2\frac{d\phi_i(z)}{dz}dz \ , \tag{25}$$

and integrating, we have

$$
\begin{aligned}
&\int 2\frac{d^2\phi_i(z)}{dz^2}\frac{d\phi_i(z)}{dz}dz = \\
&\int 2A_i \sinh\left(\beta\Delta\phi_i(z)\right) d\phi_i + \\
&\int 4B_i \sinh\left(\beta\Delta\phi_i(z)\right)\cosh\left(\beta\Delta\phi_i(z)\right) d\phi_i + \\
&\int 2a_i d\phi_i \ ,
\end{aligned}
\tag{26}
$$

whose solution is

$$
\begin{aligned}
&\left(\frac{d\phi_i(z)}{dz}\right)^2 = \frac{2A_i\cosh\left(\beta\Delta\phi_i(z)\right)}{\beta} + \\
&\frac{2B_i\cosh^2\left(\beta\Delta\phi_i(z)\right)}{\beta} + 2a_i\phi_i(z) + \\
&W_i \ ,
\end{aligned}
\tag{27}
$$

where W_i is a constant of integration for region i.

To further simplify symbolic representation of the equations, considering Eqs. (6) and (21), we denote

$$
\begin{aligned}
&Q_{m_i} = 2A_i \ , \ Q_{d_i} = 2B_i \ , \text{ and,} \\
&g_i = 2a_i \ .
\end{aligned}
\tag{28}
$$

Eq. (27) is thus expressed as

$$
\begin{aligned}
&\left(\frac{d\phi_i(z)}{dz}\right)^2 = \frac{Q_{m_i}\cosh\left(\beta\Delta\phi_i(z)\right)}{\beta} + \\
&\frac{Q_{d_i}\cosh^2\left(\beta\Delta\phi_i(z)\right)}{\beta} + g_i\phi_i(z) + \\
&W_i \ .
\end{aligned}
\tag{29}
$$

We can rewrite Eq. (29) as

$$
\frac{d\phi_i(z)}{dz} = \sqrt{\xi_i(z) + g_i\phi_i(z) + W_i} \ , \tag{30}
$$

where

$$
\begin{aligned}
&\xi_i(z) = \frac{Q_{m_i}\cosh\left(\beta\Delta\phi_i(z)\right)}{\beta} + \\
&\frac{Q_{d_i}\cosh^2\left(\beta\Delta\phi_i(z)\right)}{\beta} \ .
\end{aligned}
\tag{31}
$$

Equation (30) is the Poisson-Boltzmann equation for the electric potential in any region i (Cortez et al., 2008; Pinto, 2010).

2.1.2. Solution of the Poisson-Boltzmann Equation for the Extracellular Region ($i = ext$)

In the extracellular region, the effect of fixed charges is negligible ($\rho_{f\,ext} = 0$ and $g_{ext} = 0$), and the solution of Eq. (30) therefore only considers the electrolytic charges. Moreover, the electric potential in $z = -\infty$ is constant and we can write

$$
\left.\frac{d\phi_{ext}(z)}{dz}\right|_{(z=-\infty)} = 0 \ . \tag{32}
$$

In order to use Eq. (30) to calculate the potential in the extracellular region, we must find the value of W_{ext}. We thus consider an imaginary surface $S_{-\infty}$, perpendicular to the $z-$axis, at $z_1 \ll (-h_g - h/2)$, where $\rho_{f\,ext} = 0$. We then integrate Eq. (30) from another position $z_2 < z_1$ to z_1. Since both z_1 and z_2 are in the $-\infty$ region, $\phi_{-\infty} = \phi_{ext}(z_1) = \phi_{ext}(z_2) = \phi_{S_{-\infty}}$, and $\Delta\phi_{ext}(z_2) = \phi_{ext}(z_2) - \phi_{S_{-\infty}} = 0$. We can then substitute Eq. (32) and $\Delta\phi_{ext}(z_2) = 0$ in Eq. (30), to calculate W_{ext} as

$$
\begin{aligned}
&0 = \frac{Q_{m_{ext}}}{\beta}\cosh(0) + \frac{Q_{d_{ext}}}{\beta}\cosh^2(0) + \\
&W_{ext} \ ,
\end{aligned}
\tag{33}
$$

and

$$
W_{ext} = \frac{-Q_{m_{ext}} - Q_{d_{ext}}}{\beta} \ . \tag{34}
$$

We then substitute Eq. (34) in Eq. (30) to obtain the differential equation for $\phi_{ext}(z)$, for any position $z < (-h_g - h/2)$, in the extracellular region

$$
\frac{d\phi_{ext}(z)}{dz} = \sqrt{\lambda_{ext}(z) + \sigma_{ext}(z)} \ , \tag{35}
$$

where

$$
\begin{aligned}
&\lambda_{ext}(z) = \frac{Q_{m_{ext}}\left[\cosh\left(\beta\Delta\phi_{ext}(z)\right) - 1\right]}{\beta} \ , \\
&\sigma_{ext}(z) = \frac{Q_{d_{ext}}\left[\cosh^2\left(\beta\Delta\phi_{ext}(z)\right) - 1\right]}{\beta} \ , \\
&\text{and, } \Delta\phi_{ext}(z) = \phi_{ext}(z) - \phi_{-\infty} \ .
\end{aligned}
\tag{36}
$$

Equation (35) can be simplified to

$$
\frac{d\phi_{ext}(z)}{dz} = \sqrt{\chi_{ext}(z) + \omega_{ext}(z)} \ , \tag{37}
$$

where

$$
\begin{aligned}
&\chi_{ext}(z) = 2\frac{Q_{m_{ext}}\sinh^2\left(\frac{\beta}{2}\Delta\phi_{ext}(z)\right)}{\beta} \ , \\
&\text{and,} \\
&\omega_{ext}(z) = \frac{Q_{d_{ext}}\sinh^2\left(\beta\Delta\phi_{ext}(z)\right)}{\beta} \ .
\end{aligned}
\tag{38}
$$

2.1.3. Solution of the Poisson-Boltzmann Equation for the Cytoplasmic Region ($i = c$)

Because, in the cytoplasmic region, the potential in $z = +\infty$ is also constant,

$$\left.\frac{d\phi_c(z)}{dz}\right|_{(z=+\infty)} = 0 \ . \tag{39}$$

As we did for the extracellular region, to calculate the potential in the cytoplasmic region using Eq. (30), we must first find the value of W_c. We thus consider an imaginary surface $S_{+\infty}$, perpendicular to the $z-$axis, at $z_3 \gg (h/2)$. We then integrate Eq. (30) from another position $z_4 > z_3$ to z_3. As both z_3 and z_4 are in the $+\infty$ region, $\phi_{+\infty} = \phi_c(z_3) = \phi_c(z_4) = \phi_{S_{+\infty}}$, and $\Delta\phi_c(z_4) = \phi_c(z_4) - \phi_{S_{+\infty}} = 0$. We thus substitute Eq. (39) and $\Delta\phi_c(z_4) = 0$ in Eq. (30), to obtain W_c as

$$\begin{aligned} 0 = {} & \frac{Q_{m_c}}{\beta}\cosh(0) + \frac{Q_{d_c}}{\beta}\cosh^2(0) + \\ & g_c\phi_{+\infty} + W_c \ . \end{aligned} \tag{40}$$

The constant of integration W_c is

$$W_c = \frac{-Q_{m_c} - Q_{d_c}}{\beta} - g_c\phi_{+\infty} \ . \tag{41}$$

We then substitute Eq. (41) in Eq. (30) to obtain the differential equation for $\phi_c(z)$, for any $z > (h/2)$, in the cytoplasmic region

$$\frac{d\phi_c(z)}{dz} = \sqrt{\lambda_c(z) + \sigma_c(z) + g_c\Delta\phi_c(z)} \ , \tag{42}$$

where

$$\begin{aligned} \lambda_c(z) &= \frac{Q_{m_c}\left[\cosh\left(\beta\Delta\phi_c(z)\right) - 1\right]}{\beta} \ , \\ \sigma_c(z) &= \frac{Q_{d_c}\left[\cosh^2\left(\beta\Delta\phi_c(z)\right) - 1\right]}{\beta} \ , \\ \text{and,} \ \ & \Delta\phi_c(z) = \phi_c(z) - \phi_{+\infty} \ . \end{aligned} \tag{43}$$

Equation (42) can be simplified to

$$\frac{d\phi_c(z)}{dz} = \sqrt{\chi_c(z) + \omega_c(z) + g_c\Delta\phi_c(z)} \ , \tag{44}$$

where

$$\begin{aligned} \chi_c(z) &= 2\frac{Q_{m_c}\sinh^2\left(\frac{\beta}{2}\Delta\phi_c(z)\right)}{\beta} \ , \ \text{and,} \\ \omega_c(z) &= \frac{Q_{d_c}\sinh^2\left(\beta\Delta\phi_c(z)\right)}{\beta} \ . \end{aligned} \tag{45}$$

2.1.4. Solution of the Poisson-Boltzmann Equation for the Glycocalyx Region ($i = g$)

We consider that the potential $\phi_{S_{eg}}$ on the surface S_{eg} is

$$\left.\frac{d\phi_g(z)}{dz}\right|_{(z=-h_g-h/2)} \hat{z} = \vec{E}_g|_{S_{eg}} \ , \tag{46}$$

where $\hat{z}$ is the unit vector in the z direction, and $\vec{E}_k|_{S_{ij}}$ is the electric field in region k, $\vec{E}_k(z_{ij})$, at z_{ij}, the position of surface S_{ij} between regions i and j, e.g., $\vec{E}_g|_{S_{eg}} = \vec{E}_g(-h_g - h/2)$ is the electric field in the glycocalyx region at the position of surface S_{eg}.

In order to use Eq. (30) to calculate the potential in the glycocalyx region, we need to find the value of W_g. We thus solve Eq. (30) at $z = -h_g - h/2$, on the surface S_{eg}, and take $\phi_g(-h_g - h/2) = \phi_{S_{eg}}$, and $\Delta\phi_g(-h_g - h/2) = \phi_g(-h_g - h/2) - \phi_{S_{eg}} = 0$. We can then substitute Eq. (46) and $\Delta\phi_g(-h_g - h/2) = 0$ in Eq. (30), to calculate W_g as

$$\begin{aligned} \left(\vec{E}_g|_{S_{eg}}\right)^2 = {} & \frac{Q_{m_g}}{\beta}\cosh(0) + \\ & \frac{Q_{d_g}}{\beta}\cosh^2(0) + \\ & g_g\phi_{S_{eg}} + W_g \ . \end{aligned} \tag{47}$$

The constant of integration W_g, for the glycocalyx region, is therefore

$$\begin{aligned} W_g = {} & \left(\vec{E}_g|_{S_{eg}}\right)^2 - \left(\frac{Q_{m_g} + Q_{d_g}}{\beta}\right) - \\ & g_g\phi_{S_{eg}} \ . \end{aligned} \tag{48}$$

We then substitute Eq. (48) in Eq. (30) to obtain the differential equation for $\phi_g(z)$, for any position $(-h_g - h/2) < z < (-h/2)$, in the glycocalyx region

$$\frac{d\phi_g(z)}{dz} = \sqrt{\lambda_g(z) + \sigma_g(z) + g_g\Delta\phi_g(z) + \vec{E}_g|^2_{S_{eg}}} \ , \tag{49}$$

where

$$\begin{aligned} \lambda_g(z) &= \frac{Q_{m_g}\left[\cosh\left(\beta\Delta\phi_g(z)\right) - 1\right]}{\beta} \ , \\ \sigma_g(z) &= \frac{Q_{d_g}\left[\cosh^2\left(\beta\Delta\phi_g(z)\right) - 1\right]}{\beta} \ , \\ \text{and,} \ \ & \Delta\phi_g(z) = \phi_g(z) - \phi_{S_{eg}} \ . \end{aligned} \tag{50}$$

Equation (49) can be further simplified to

$$\frac{d\phi_g(z)}{dz} = \sqrt{\chi_g(z) + \omega_g(z) + g_g\Delta\phi_g(z) + \vec{E}_g|^2_{S_{eg}}} , \tag{51}$$

where

$$\chi_g(z) = 2\frac{Q_{m_g}\sinh^2\left(\frac{\beta}{2}\Delta\phi_g(z)\right)}{\beta}, \text{ and,}$$

$$\omega_g(z) = \frac{Q_{d_g}\sinh^2\left(\beta\Delta\phi_g(z)\right)}{\beta} \ . \qquad (52)$$

2.1.5. *Solution of the Poisson-Boltzmann Equation for the Bilayer* $(i = b)$

As mentioned earlier, because the bilayer is highly hydrophobic, $\rho_b(z) = 0$ (Cortez and Bisch, 1993; Cortez et al., 2008). Equation (2) assumes the form (Cortez et al., 2008)

$$\nabla^2\phi_b(x, y, z) = 0 \ , \qquad (53)$$

and its solution is a family of linear functions. The electric field within the bilayer (see Eq. (58)), $\vec{E}_b$, is therefore (Cortez et al., 2008)

$$\vec{E}_b = \frac{\phi_{S_{gb}} - \phi_{S_{bc}}}{h}\hat{z} \ . \qquad (54)$$

2.2. *Surface Potentials*

In order to solve the differential Eqs. (37), (44) and (51) for the extracellular, cytoplasmic and glycocalyx regions of the neuronal membrane, respectively, we must know the values of the surface potentials $\phi_{S_{eg}}$, $\phi_{S_{gb}}$ and $\phi_{S_{bc}}$. Although membrane surface potentials in cells cannot be measured experimentally, it is possible to obtain analytical predictions for the values of $\phi_{S_{eg}}$, $\phi_{S_{gb}}$ and $\phi_{S_{bc}}$, from basic electrostatic relations, as we will now show.

Considering the surface densities of electric charges, Gauss' law, and the discontinuity of the electric field vector on the surfaces S_{eg}, S_{gb} and S_{bc}, we obtain (Cortez et al., 2008; Pinto, 2010)

$$\epsilon_g\vec{E}_g|_{S_{eg}} - \epsilon_{ext}\vec{E}_{ext}|_{S_{eg}} = 4\pi Q_{S_{eg}}\hat{z} \ , \qquad (55)$$

$$\epsilon_b\vec{E}_b|_{S_{gb}} - \epsilon_g\vec{E}_g|_{S_{gb}} = 4\pi Q_{S_{gb}}\hat{z} \ , \text{ and} \qquad (56)$$

$$\epsilon_c\vec{E}_c|_{S_{bc}} - \epsilon_b\vec{E}_b|_{S_{bc}} = 4\pi Q_{S_{bc}}\hat{z} \ , \qquad (57)$$

respectively, where $\vec{E}_b|_{S_{gb}} = \vec{E}_b|_{S_{bc}} = \vec{E}_b$ (see Eq. (54)). In the above, $Q_{S_{eg}}$, $Q_{S_{gb}}$ and $Q_{S_{bc}}$ stand for the charge density on the S_{eg}, S_{gb} and S_{bc} surfaces, respectively.

As

$$\vec{E}_i = -\vec{\nabla}\phi_i(z) = -\frac{d\phi_i(z)}{dz}\hat{z} \ , \qquad (58)$$

in order to determine the discontinuity of the electric field vector on the surfaces S_{eg}, S_{gb} and S_{bc}, we substitute Eq. (58) in Eqs. (55), (56) and (57), and obtain

$$\vec{E}_g|_{S_{eg}} = \frac{4\pi Q_{S_{eg}} - \epsilon_{ext}\frac{d\phi_{ext}(z)}{dz}|_{(z=-h_g-h/2)}}{\epsilon_g}\hat{z} \ , \qquad (59)$$

$$\vec{E}_b = \frac{4\pi Q_{S_{gb}} - \epsilon_g\frac{d\phi_g(z)}{dz}|_{(z=-h/2)}}{\epsilon_b}\hat{z} \ , \text{ and} \qquad (60)$$

$$\vec{E}_b = \frac{-4\pi Q_{S_{bc}} - \epsilon_c\frac{d\phi_c(z)}{dz}|_{(z=h/2)}}{\epsilon_b}\hat{z} \ . \qquad (61)$$

As we have previously obtained the expression that determines the electric field within the bilayer, $\vec{E}_b$, we substitute Eq. (54) into Eqs. (60) and (61), and obtain

$$\phi_{S_{bc}} = \phi_{S_{gb}} - \frac{h}{\epsilon_b}\left(4\pi Q_{S_{gb}} - \epsilon_g\frac{d\phi_g(z)}{dz}|_{(z=-h/2)}\right) \ , \qquad (62)$$

$$\phi_{S_{gb}} = \phi_{S_{bc}} - \frac{h}{\epsilon_b}\left(4\pi Q_{S_{bc}} + \epsilon_c\frac{d\phi_c(z)}{dz}|_{(z=h/2)}\right) \ , \qquad (63)$$

respectively.

Substituting Eqs. (51) and (59) in Eq. (62), we determine the expression to calculate the surface potential $\phi_{S_{bc}}$

$$\phi_{S_{bc}} = \phi_{S_{gb}} - \frac{4\pi Q_{S_{gb}}h}{\epsilon_b} + \frac{\epsilon_g h}{\epsilon_b}\sqrt{\alpha} \ , \qquad (64)$$

where

$$\alpha = \chi_g(-h/2) + \omega_g(-h/2) + g_g\Delta\phi_g(-h/2) + \left(\frac{4\pi Q_{S_{eg}} - \epsilon_{ext}\frac{d\phi_{ext}(z)}{dz}|_{(z=-h_g-h/2)}}{\epsilon_g}\right)^2 \qquad (65)$$

and here, $\Delta\phi_g(-h/2) = \phi_{S_{gb}} - \phi_{S_{eg}}$. In the same manner, substituting Eq. (44) in Eq. (63), we determine the expression to calculate the surface potential $\phi_{S_{gb}}$

$$\phi_{S_{gb}} = \phi_{S_{bc}} - \frac{4\pi Q_{S_{bc}}h}{\epsilon_b} - \frac{\epsilon_c h}{\epsilon_b}\sqrt{\kappa} \ , \qquad (66)$$

where

$$\kappa = \chi_c(h/2) + \omega_c(h/2) + g_c\Delta\phi_c(h/2) \ , \qquad (67)$$

and here, $\Delta\phi_c(h/2) = \phi_{S_{bc}} - \phi_{+\infty}$.

The electric potential on the surface S_{eg}, $\phi_{S_{eg}}$, is determined from electrophoresis experiments (Dolgaya and Mironov, 1984; Dolgaya et al., 1985; Mironov and Dolgaya, 1985) and the Helmholts-Smoluchowski equation (Cortez and Bisch, 1993)

$$\mu = \frac{\epsilon_i \zeta_i}{4\pi\nu_i} \ , \tag{68}$$

where μ is the electrophoretic mobility; $\zeta_i = \phi_{S_{eg}} - \phi_{-\infty}$ is the zeta potential; and ν_i is the viscosity of region i. As, in our model, we define the potential $\phi_{-\infty} = 0$, the surface potential $\phi_{S_{eg}}$ is

$$\phi_{S_{eg}} = \frac{4\pi\nu_i\mu}{\epsilon_i} \ . \tag{69}$$

3. Model Calculations for Spinal Ganglion Neurons and Neuroblastoma Cells

We have used data obtained from experimental observations (Dolgaya and Mironov, 1984; Dolgaya et al., 1985; Mironov and Dolgaya, 1985) for values of parameters, in order to solve the first order ordinary differential equations, obtained from the Poisson-Boltzmann Eq. (30), for the different regions of the membrane. Some experimental values were obtained from electrophoretic experiments. Since each kind of cell presents a specific electrophoretic mobility, the values of some parameters are different for the spinal ganglion neuron and the neuroblastoma, in our calculations. Tables (1) and (2) show all experimental values of the parameters used to solve the equations for the spinal ganglion neuron and the neuroblastoma. The difference $\phi_{+\infty} - \phi_{-\infty}$ is called the transmembrane potential and is denoted as ϕ_R in the resting state, and ϕ_A in the AP state. We have defined $\phi_{-\infty} = 0$ in our calculations, so that $\phi_R = \phi_{+\infty}$ in the resting state, and $\phi_A = \phi_{+\infty}$ in the AP state. We have thus examined the influence of parameters representing electric properties of the membrane, on the resting and AP states, and analyzed the differences between the healthy spinal ganglion neuron and a neuroblastoma cell.

We implemented an approximate heuristic for finding roots of functions, to calculate $\phi_{S_{gb}}$ and $\phi_{S_{bc}}$ from Eqs. (64) and (66) (see Appendix A). As mentioned earlier, the potential $\phi_{S_{eg}}$ was calculated with Eq. (69), from data obtained from electrophoretic experiments.

As we included the density of charges fixed onto proteins within the membrane regions in the Poisson Eq. (1), we obtained a non-linear Poisson-Boltzmann Eq. (30), whose analytical solution has not been found (Cortez and Bisch, 1993; Cortez et al., 2008). We therefore calculated values of the potential profiles with Eqs. (37), (44) and (51) numerically, using the Runge-Kutta method.

4. Results from Simulations

With our mathematical model, we first investigate the effect of $Q_{S_{bc}}$ and ρ_{fc} on the electric potential on the surfaces of the neuronal membranes of the spinal ganglion and the neuroblastoma. However, there is little information in the literature, regarding experimentally obtained quantities related to electric charges, fixed within biological membranes. This is mainly due to the difficulties involved in obtaining these experimental measurements. Therefore, we estimate values for fixed charges in the cytoplasm ($Q_{S_{bc}}/Q_{S_{eg}}$ and ρ_{fc}/ρ_{fg}), as a function of known experimental data for fixed electric charges in the glycocalyx, and examine the behaviour of the potentials $\phi_{S_{gb}}$ and $\phi_{S_{bc}}$.

Figure (2) shows the behavior of $\phi_{S_{gb}}$ and $\phi_{S_{bc}}$ as a function of variations in $Q_{S_{bc}}$. We notice that for both the resting and AP states, a negative increase of $Q_{S_{bc}}$ has almost no effect on the surface potentials of both neuronal membranes. These variations in $Q_{S_{bc}}$ only determine a small gradual decay of $\phi_{S_{bc}}$ during the resting state of the cells. Values for $\phi_{S_{gb}}$ and $\phi_{S_{bc}}$ are different between these types of cells, due to their specific membrane properties. We also observe that $\phi_{S_{gb}}$ remains constant at -34.97 mV and -25.17 mV, respectively for the spinal ganglion and neuroblastoma cells, when they switch from the resting to AP states, and vice versa. Moreover, during the AP state, $\phi_{S_{bc}}$ assumes values near the transmembrane potentials (Fig. (2B)).

We also examine the electric potential on the surfaces of the membranes of the healthy and the cancerous cells, in response to variations in the densities of charges fixed onto proteins of the cytoplasm. Figure (3) presents the resulting $\phi_{S_{gb}}$ and $\phi_{S_{bc}}$ as a function of variations in ρ_{fc}. For both the resting and AP states, $\phi_{S_{gb}}$ remains constant when values of ρ_{fc} vary. However, a decrease in ρ_{fc} (more negative values, corresponding to increasing values of ρ_{fc}/ρ_{fg}) causes an expressive fall of $\phi_{S_{bc}}$, for both types of cells, at resting and AP states. At the AP state, $\phi_{S_{bc}}$ presents a quick drop when $\rho_{fc}/\rho_{fg} < 20$

Parameter	Symbol	Value	Value in CGS[1]	References
Dielectric constant in region b	ϵ_b	2	2	(Cortez and Bisch, 1993; Cortez et al., 2008)
Dielectric constant in region i ($i = ext, g, c$)	ϵ_i	81	81	(Cortez et al., 2008)
Glycocalyx width	h_g	2.5 nm	2.50×10^{-7} cm	(Cortez et al., 2008; Dolgaya and Mironov, 1984; Dolgaya et al., 1985)
Bilayer thickness	h	7.5 nm	7.50×10^{-7} cm	(Cortez and Bisch, 1993; Cortez et al., 2008; Dolgaya and Mironov, 1984; Dolgaya et al., 1985)
Ionic concentration of monovalent ions on S_{eg}	$\eta_{1,S_{eg}}$	0.154 M	9.27×10^{19} cm^{-3}	(Clay and Shrier, 2001; Dolgaya and Mironov, 1984; Inoue, 2002; Mironov and Dolgaya, 1985)
Ionic concentration of monovalent ions on S_{gb}	$\eta_{1,S_{gb}}$	0.154 M	9.27×10^{19} cm^{-3}	(Clay and Shrier, 2001; Dolgaya and Mironov, 1984; Inoue, 2002; Mironov and Dolgaya, 1985)
Ionic concentration of divalent ions on S_{eg}	$\eta_{2,S_{eg}}$	0.002 M	1.20×10^{18} cm^{-3}	(Clay and Shrier, 2001; Dolgaya and Mironov, 1984; Inoue, 2002; Mironov and Dolgaya, 1985)
Ionic concentration of divalent ions on S_{gb}	$\eta_{2,S_{gb}}$	0.002 M	1.20×10^{18} cm^{-3}	(Clay and Shrier, 2001; Dolgaya and Mironov, 1984; Inoue, 2002; Mironov and Dolgaya, 1985)
Ionic concentration of monovalent ions on S_{bc}	$\eta_{1,S_{bc}}$	0.154 M	9.27×10^{19} cm^{-3}	(Clay and Shrier, 2001; Inoue, 2002; Rosenheck, 1998)
Ionic concentration of divalent ions on S_{bc}	$\eta_{2,S_{bc}}$	0.0004 M	2.41×10^{17} cm^{-3}	(Clay and Shrier, 2001; Inoue, 2002)
Potential in $-\infty$, the extracellular region	$\phi_{-\infty}$	0 mV	0 statV	(Cortez and Bisch, 1993; Cortez et al., 2008)
Temperature	T	310 K	310 K	(Cortez et al., 2008)
Boltzmann's constant	K	1.38×10^{-23} J/K	1.38×10^{-16} erg/K	(Walker et al., 2011)
Absolute value of electron charge	e	1.60×10^{-19} C	4.80×10^{-10} statC	(Walker et al., 2011)
Viscosity of region i	ν_i	0.1 Pa $\cdot$ s	1 P	(Cortez and Bisch, 1993)

Table 1: Values of parameters used for calculations for the spinal ganglion neuron and the neuroblastoma cell.

Parameter	Symbol	Spinal Ganglion Neuron			Neuroblastoma		
		Value	Value in CGS	Reference	Value	Value in CGS	Reference
Fixed charge density in glycocalyx	ρ_{fg}	-0.12 e/nm^3	-5.76×10^{10} statC/cm^3	(Dolgaya and Mironov, 1984)	-0.2 e/nm^3	-9.61×10^{10} statC/cm^3	(Dolgaya et al., 1985)
Charge density on S_{eg}	$Q_{S_{eg}}$	-0.012 e/nm^2	-5.76×10^{2} statC/cm^2	(Dolgaya and Mironov, 1984)	-0.02 e/nm^2	-9.61×10^{2} statC/cm^2	(Dolgaya et al., 1985)
Charge density on S_{gb}	$Q_{S_{gb}}$	$-1/1000$ e/Å^2	-4.80×10^{3} statC/cm^2	(Becchetti et al., 1992)	$-1/385$ e/Å^2	-1.25×10^{4} statC/cm^2	(Becchetti et al., 1992)
Resting trans-membrane potential	ϕ_R	-69 mV	-2.30×10^{-4} statV	(Dolgaya and Mironov, 1984; Rosenthal and Bezanilla, 2002)	-64 mV	-2.13×10^{-4} statV	(Hernandez et al., 1996)
Action trans-membrane potential	ϕ_A	40 mV	1.33×10^{-4} statV	(Guyton and Hall, 1997)	30 mV	1.00×10^{-4} statV	(Tosetti et al., 1999)
Electrophoretic mobility	μ	-1.40 μm.cm/V.s	-4.20×10^{-2} cm^2/statV.s	(Dolgaya and Mironov, 1984; Dolgaya et al., 1985)	-1.80 μm.cm/V.s	-5.40×10^{-2} cm^2/statV.s	(Dolgaya et al., 1985)

Table 2: Values of parameters used for calculations for the spinal ganglion neuron and the neuroblastoma cell.

and tends to an asymptotic value, for decreasing values of ρ_{fc}, for both types of cells.

Besides investigating the effect of fixed charges on the potential on the surfaces of these membranes, we study how the electric potential profile changes across the membranes of spinal ganglion neurons and neuroblastoma cells, for the resting and AP states (Figs. (4) and (5), respectively, considering $Q_{S_{bc}} = 30 Q_{S_{eg}}$ and $\rho_{fc} = 20 \rho_{fg}$). For both natural states of these cells, we verify an accentuated decrease of the potential along the z axis, from the extracellular region to the surface of the glycocalyx. This decay is slightly more expressive for the neuroblastoma than for the spinal ganglion neuron, although the shapes of both curves are very similar.

In the spinal ganglion neuron, the potential maintains an expressive drop across the glycocalyx. Interestingly, this phenomenon does not occur for the cancerous cells, whose electric potential remains almost unchanged in this region. We observe linear variations of the potential across the bilayer of these cells, for both resting and AP states. During rest,

---

[1] CGS is the centimeter-gram-second system of units.

the electric potential assumes much lower values on S_{bc} than the asymptotic value in the bulk cytoplasmic region, while during the AP state, these values are similar. Before reaching the transmembrane potential value, the intracellular potential exponentially increases from the inner surface of the membrane to the bulk cytoplasmic region, during the resting condition, while during the AP state, we see no alterations in the electric potential in the cytoplasm, for both cells.

5. Conclusions

Our simulations demonstrate that variations in the electric charges fixed onto the inner surface of the membrane have a small effect on the electric potential of the surfaces that compose the neuronal membranes (Fig. (2)). We observe only a gentle gradual drop in $\phi_{S_{bc}}$ of the spinal ganglion and the neuroblastoma cells during the resting state, as charges fixed on S_{bc} decrease (more negative values). However, our model shows that decreasing the density of charges fixed onto proteins of the cytoplasm (increasing $|\rho_{fc}|$ and ρ_{fc}/ρ_{fg}) results in an expressive decay of $\phi_{S_{bc}}$, in both cells (Fig. (3)).

Nonetheless, variations of intracellular charges fixed on the membrane and on the cytoplasmic proteins have no effect on the potential on S_{gb} (Figs. (2) and (3)). This is related to the fact that the membrane plays a role in electrically isolating the intracellular and extracellular regions, due to the absence of charges within the lipidic bilayer (see Eq. (53)).

The results we have obtained for the spinal ganglion and the neuroblastoma cells match those obtained for the squid axon membrane, by Cortez et al. (2008). These authors used a similar model to the one we used in this study, and also observed gentle variations of the surface potentials, in response to variations of charges fixed on S_{bc}.

An interesting result of our calculations is that, in the spinal ganglion neuron, the electric potential across the glycocalyx decreases, and this does not occur in the neuroblastoma cell. This reveals an important discrepancy of the electric fields in the glycocalyx of both types of cells (Figs. (4) and (5)), and may explain the difference between their electrophoretic behavior, which was observed in experiments by Dolgaya and Mironov (1984) and Dolgaya et al. (1985). As expected, the electric potential presents a linear behavior within the bilayer of the membrane during the resting and AP states, due to the absence of electric charges in this region.

The strong negative electric potential on S_{bc} is a characteristic of the potential profile in the resting state, and this probably occurs for all types of neuronal cells (Fig. (4)). The steep increase of the potential from S_{bc} towards the bulk cytoplasmic region is regulated by the negative charges spatially distributed in the cytoplasm. Even though the net value of charges of proteins is predominantly negative in the cytoplasm (Cortez et al., 2008), our simulations indicate that the contribution of these charges to the intracellular potential profile is much smaller than the effect of charges fixed on S_{bc}. This is shown by the curvature of the potential in the cytoplasmic region.

The neuroblastoma cells, like all cancerous cells, multiply themselves quickly. Alterations of the dynamics of cellular multiplication mediate changes in the synthesis, structure and degradation of the membrane components (Dehlinger and Schimke, 1971), which result in deformations on the structure and composition of the surfaces of membranes (Schubert et al., 1971). These deformations provoke changes in the composition of electric charges on the membrane. Our results indicate that the alteration of these charges and of those within the cells may influence the behavior of the potential on the inner surface of the neuroblastoma cells.

Experimental observations have suggested that the resting state and the generation of action potentials in human neuroblastoma cells depend on the degree of the morphologic differentiation of the cell. Some of these cells are relatively non-excitable (Gèrard et al., 1998; Kuramoto et al., 1981). Kuramoto et al. (1977) stimulated the growth of SK-N-SH human neuroblastoma cells under standard culture conditions. These cancerous cells remained morphologically undifferentiated, partially responded to injections of pulses of electric current, and presented deficiency of the depolarizing component of the mechanism that generates the action potential. In our simulations, the results shown in Fig. (5) corroborate these experimental findings, where depolarization of the electric potential in the neuroblastoma, during generation of the action potential, is less intense than in the healthy spinal ganglion neuron. The neuroblastoma should generate a less intense firing pattern in response to its input excitation. We conclude that these properties may affect the transmission of signals through networks of these neurons and their functions of

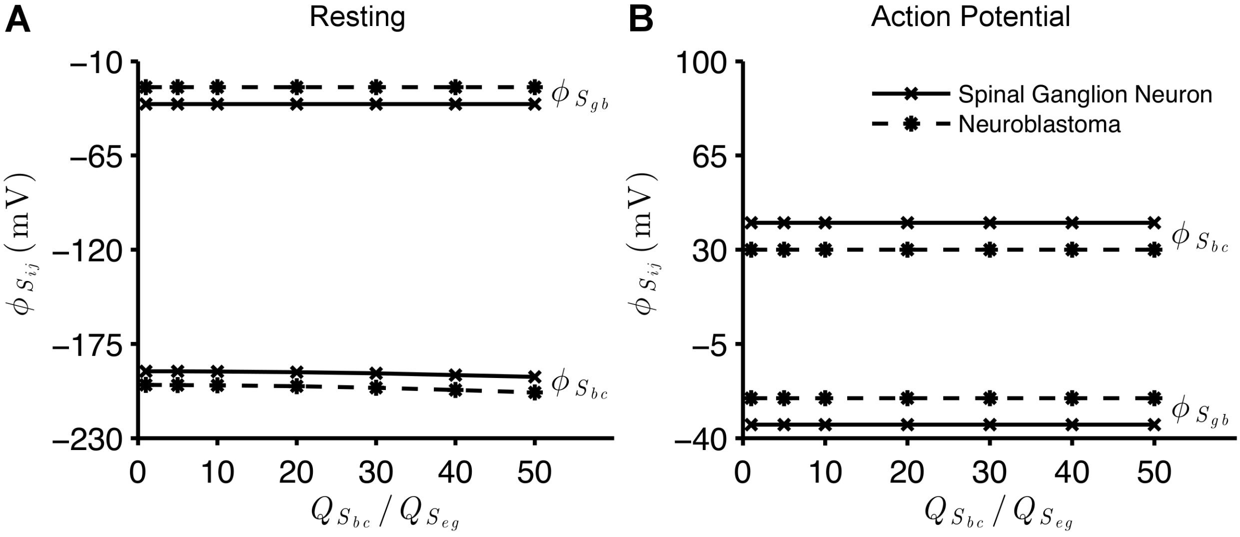

Figure 2: Electric potential on the surfaces of regions of the membranes of the spinal ganglion neuron (×) and the neuroblastoma cell ($*$), as a function of the ratio of charge density, $Q_{S_{bc}}/Q_{S_{eg}}$, as $Q_{S_{eg}}$ is kept constant. Results for the resting potential are depicted in (A) and for the AP state, in (B). In both graphs, $\rho_{fc} = 20\rho_{fg}$.

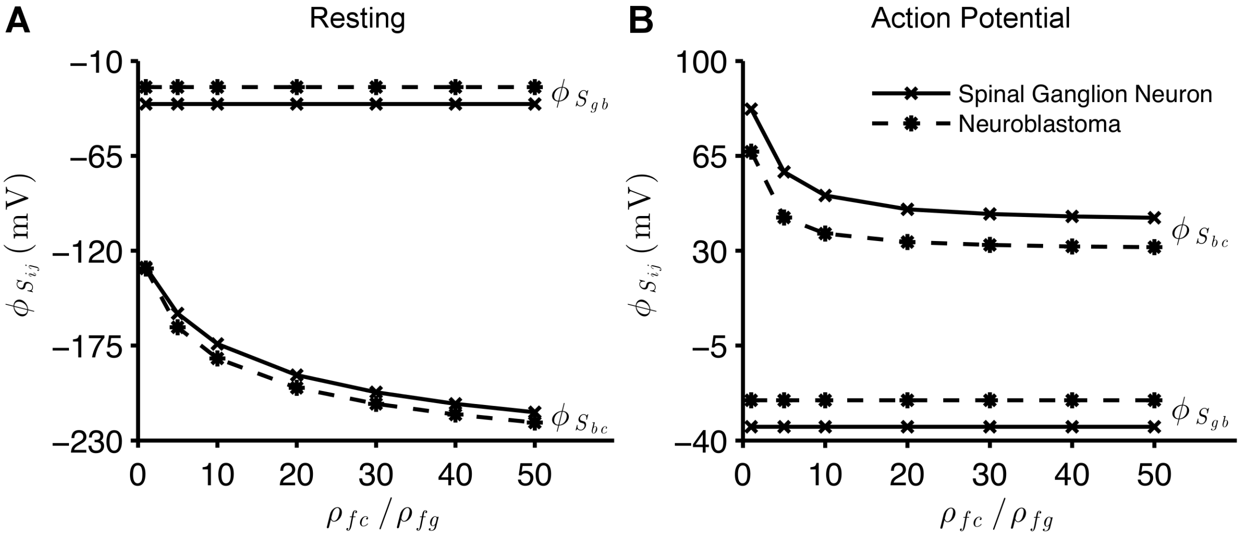

Figure 3: Electric potentials $\phi_{S_{bc}}$ and $\phi_{S_{gb}}$ as a function of ρ_{fc}/ρ_{fg}, as ρ_{fg} is kept constant, for the spinal ganglion neuron (×) and the neuroblastoma cell ($*$). Results for the resting potential are depicted in (A) and for the AP state, in (B). In both graphs, $Q_{S_{bc}} = 30Q_{S_{eg}}$.

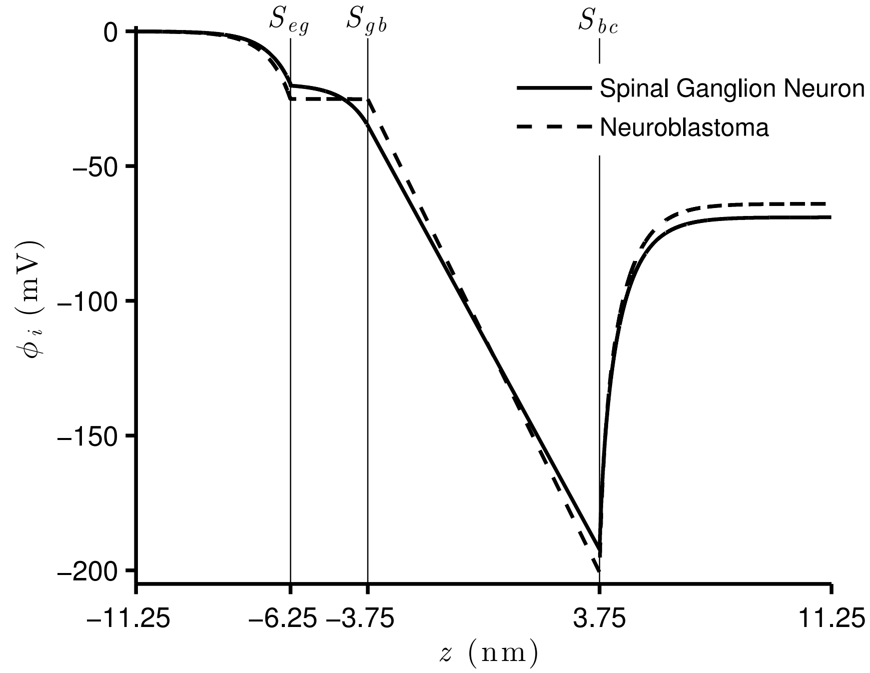

Figure 4: Electric potential profile across the membranes of the spinal ganglion neuron (solid) and the neuroblastoma cell (dashed), during the resting state. For the spinal ganglion neuron, $\phi_{S_{eg}} = -19.52$ mV, $\phi_{S_{gb}} = -34.97$ mV, and $\phi_{S_{bc}} = -192.22$ mV. For the neuroblastoma cell, $\phi_{S_{eg}} = -25.10$ mV, $\phi_{S_{gb}} = -25.17$ mV, and $\phi_{S_{bc}} = -200.66$ mV. For all simulations, $Q_{S_{bc}} = 30Q_{S_{eg}}$ and $\rho_{fc} = 20\rho_{fg}$.

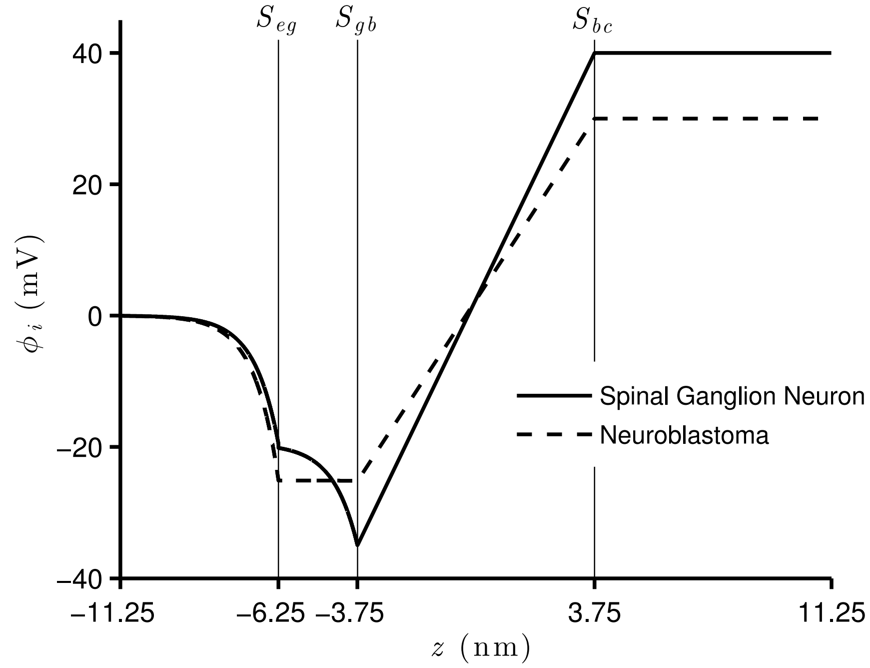

Figure 5: Electric potential profile across the membranes of the spinal ganglion neuron (solid) and the neuroblastoma cell (dashed), during the AP state. For the spinal ganglion neuron, $\phi_{S_{eg}} = -19.52$ mV, $\phi_{S_{gb}} = -34.97$ mV, and $\phi_{S_{bc}} = 39.99$ mV. For the neuroblastoma cell, $\phi_{S_{eg}} = -25.10$ mV, $\phi_{S_{gb}} = -25.17$ mV, and $\phi_{S_{bc}} = 29.99$ mV. For all simulations, $Q_{S_{bc}} = 30Q_{S_{eg}}$ and $\rho_{fc} = 20\rho_{fg}$.

storage and communication of information.

Mironov and Dolgaya (1985) have suggested that the outer electric charges for the neuroblastoma cells and erythrocytes are similar, but the spinal ganglion neurons strongly differ from these cells. Therefore, the molecular structure (and the resulting constitution of charges) on the outer surface of the membrane of the neuroblastoma cells would be similar to the erythrocytes, and may be constituted by $\simeq 40\%$ of peripheral proteins and $\simeq 60\%$ of gangliosides. Our results illustrate that the drop of the potential across the glycocalyx for the neuroblastoma cell is much smaller than for the spinal ganglion neuron, during both resting and AP states. This corroborates previous studies which show a smaller decay of the potential for the erythrocyte in the glycocalyx than for the neuron (Cortez et al., 2008; Cruz et al., 2000; Heinrich et al., 1982). The different behaviour of the potential across the glycocalyx, for the neuroblastoma and the spinal ganglion neuron, should indicate important differences among these cells, of the properties that enable the transmission of electric signals through the membrane. This occurs due to the fact that different molecular structures of these membranes interact differently with (i) the outer electric field, which is responsible for the orientation of the charged particles that are closer to the membrane, and (ii) the potential on the outer surface of the membrane. The nature of these interactions are crucial for many cell processes, such as the beginning of the process of triggering of the action potential, which depends on the opening of specific Na^+ channels.

Our results may also contribute to the understanding of the resistance of the neuroblastoma to certain chemotherapeutic treatments (Lindskog et al., 2004; Michaelis et al., 2001). The smaller change of the potential, in response to changes in properties of cellular cultures (pH values, for instance) and to the amount of fixed charges present in the membrane due to alterations in its composition and structure, may be an electric property responsible for the low pharmacological response.

Appendix A. Roots of the System of Non-linear Equations

Because there is no experimental method to directly measure values of the surface potentials, $\phi_{S_{gb}}$ and $\phi_{S_{bc}}$, we use Eqs. (64) and (66) that form a system of non-linear equations with two variables, $\phi_{S_{gb}}$ and $\phi_{S_{bc}}$, to determine these values. Some research work (Cortez and Bisch, 1993; Cortez et al., 2008; Mironov and Dolgaya, 1985; Dolgaya and Mironov, 1984; Dolgaya et al., 1985) indicates that the values of these potentials in real cells are in a limited region of the $\phi_{S_{gb}} \times \phi_{S_{bc}}$ plane. This means that we are looking for one of the roots of Eqs. (64) and (66), in a known region.

We can write the system of Eqs. (64) and (66) as

$$\begin{aligned} \phi_{S_{gb}} &= G\left(\phi_{S_{bc}}\right) \\ \phi_{S_{bc}} &= F\left(\phi_{S_{gb}}\right) \ . \end{aligned} \tag{A.1}$$

Our simple method for finding the roots of this system consists in the steps described in *Algorithm_Roots*, shown in Fig. (A.1). At the resting state, $min = -250$ mV and $max = -50$ mV, while, at the AP state, $min = 10$ mV and $max = 100$ mV.

```
Algorithm Algorithm_Roots
  Step 0: $\delta_{\phi_{min}} = 10^{-4}$ mV
  Step 1: Choose an initial value for $\phi_{S_{bc}}$
          in $min < \phi_{S_{bc}} < max$
  Step 2: $\delta_\phi = 20$ mV
  Step 3: While $\delta_\phi > \delta_{\phi_{min}}$ do
            begin
              $\phi_{S_{gb}} = G(\phi_{S_{bc}})$
              $\phi^*_{S_{bc}} = F(\phi_{S_{gb}})$
              If $|\phi_{S_{bc}} - \phi^*_{S_{bc}}| < \delta_\phi$ then
                $\delta_\phi = |\phi_{S_{bc}} - \phi^*_{S_{bc}}|$
                $\phi_{S_{bc}} = \phi^*_{S_{bc}}$
              else
                return to Step 1
              end if
            end While
```

Figure A.1: Algorithm for determining $\phi_{S_{gb}}$ and $\phi_{S_{bc}}$, for the spinal ganglion neuron and the neuroblastoma cell.

With the $\phi_{S_{bc}}$ value found with this procedure, we use Eq. (66) to obtain the corresponding $\phi_{S_{gb}}$ value. The surface potentials $\phi_{S_{gb}}$ and $\phi_{S_{bc}}$ for the spinal ganglion neuron and the neuroblastoma cell, whose values are shown in Section 4, were obtained with *Algorithm_Roots*.

References

Becchetti, A., Arcangeli, A., Del Bene, M., Olivotto, M., Wanke, E., 1992. Intra and extracellular surface charges near Ca2+ channels in neurons and neuroblastoma cells. Biophys. J. 63 (4), 954–965.

Belan, P., Dolgaya, E., Mironov, S., Tepikin, A., 1987. Relation between the surface potential of mouse neuroblastoma clone c1300 cells and the phase of the cell cycle. Neirofiziologiya 19 (1), 130–133.

Clay, J., Shrier, A., 2001. Action potentials occur spontaneously in squid giant axons with moderately alkaline intracellular ph. Biol. Bull. 201, 186.

Cortez, C., Bisch, P., 1993. The effect of ionic strength and outer surface charge on the membrane electric potential profile: a simple model for the erythrocyte membrane. Bioelectroch. Bioener. 32, 305–315.

Cortez, C., Cruz, F., Silva, D., Costa, L., 2008. Influence of fixed electric charges on potential profile across the squid axon membrane. Physica B 403, 644–652.

Cruz, F., Vilhena, F., Cortez, C., 2000. Solution of non-linear Poisson-Boltzmann equation for erythrocyte membrane. Braz. J. Phys. 30, 403–409.

Dehlinger, P., Schimke, R., 1971. Size distribution of membrane proteins of rat liver and their relative rates of degradation. J. Biol. Chem. 246 (8), 2574–2583.

Dolgaya, E., Mironov, S., 1984. Investigation of surface properties of rat spinal ganglion neuron by microelectrophoresis. Neirofiziologiya 16 (2), 176–182.

Dolgaya, E., Mironov, S., Pogorelaya, N., 1985. Changes in surface charge of mouse neuroblastoma cells during growth and morphological differentiation of the cell population. Neirofiziologiya 17 (2), 168–174.

Gèrard, V., Rouzaire-Dubois, B., Dilda, P., Dubois, J., 1998. Alterations of ionic membrane permeabilities in multidrug-resistant neuroblastoma x glioma hybrid cells. J. Exp. Biol. 201, 21–31.

Guyton, A., Hall, J., 1997. Human physiology and mechanisms of disease, sixth Edition. W.B. Saunders Co., Philadelphia.

Heinrich, R., Gaestel, M., Glaser, R., 1982. The electric potential profile across the erythrocyte membrane. J. Theor. Biol. 96 (2), 211–231.

Hernandez, M., Kisaalita, W., Farmer, M., 1996. Assessment of murine neuroblastoma (N1E-115) resting membrane potential by confocal microscopy. J. Fluoresc. 6 (2), 77–82.

Iglic, A., Brumen, M., Svetina, S., 1997. Determination of the inner surface potential of erythrocyte membrane. Bioelectroch. Bioener. 43, 97–107.

Inoue, H., 2002. Transport of 125I and 36Cl across an anion-exchange paper membrane. Appl. Radiat. Isot. 56, 659–665.

Kuramoto, T., Perez-Polo, J., Haber, B., 1977. Membrane properties of a human neuroblastoma. Neurosci. Lett. 4 (3-4), 151–159.

Kuramoto, T., Werrbach-Perez, K., Perez-Polo, J., Haber, B., 1981. Membrane properties of a human neuroblastoma II: Effects of differentiation. J. Neurosci. Res. 6 (4), 441–449.

Lindskog, M., Spenger, C., Jarvet, J., Graslund, A., Kogner, P., 2004. Predicting resistance or response to chemotherapy by proton magnetic resonance spectroscopy in neuroblastoma. J. Natl. Cancer Inst. 96 (19), 1457–1466.

Michaelis, M., Cinatl, J., Vogel, J., Pouckova, P., Driever, P., Cinatl, J., 2001. Treatment of drug-resistant human neuroblastoma cells with cyclodextrin inclusion complexes of aphidicolin. Anticancer Drugs 12 (5), 467–473.

Mironov, S., Dolgaya, E., 1985. Surface charge of mammalian neurones as revealed by microelectrophoresis. J. Membrane Biol. 86, 197–202.

Pinto, T., 2010. Modelagem do potencial elétrico através da membrana do neurônio ganglionar e células de neuroblastoma: Efeitos das cargas superficiais. Master's thesis, Universidade do Estado do Rio de Janeiro, Rio de Janeiro.

Rosenheck, K., 1998. Evaluation of the electrostatic field strength at the site of exocytosis in adrenal chromaffin cells. Biophys. J. 75, 1237.

Rosenthal, J., Bezanilla, F., 2002. A comparison of propagated action potentials from tropical and temperate squid axons: different durations and conduction velocities correlate with ionic conductance levels. J. Exp. Biol. 205, 1819–1830.

Schubert, D., Humphreys, S., de Vitry, F., Jacob, F., 1971. Induced differentiation of a neuroblastoma. Dev. Biol. 25 (4), 514–546.

Tosetti, P., Taglietti, V., Toselli, M., 1999. Action-potential-like depolarizations relieve opioid inhibition of N-type Ca2+ channels in NG108-15 cells. Pflug. Arch. Eur. J. Phy. 437 (3), 441–448.

Verwey, E., Overbeek, J., 1948. Theory of the stability of lyophobic colloids. Elsevier, Amsterdam.

Walker, J., Halliday, D., Resnick, R., 2011. Fundamentals of Physics, sixth Edition. Hoboken, NJ: Wiley.